Crystallization of monodisperse gold ultrasmall icosahedral nanoparticles : nucleation/growth mechanism study using microfluidic chips

Ezgi Yildirim

Université Fédérale
Toulouse Midi-Pyrénées

THÈSE

En vue de l'obtention du
DOCTORAT DE L'UNIVERSITÉ DE TOULOUSE

Délivré par l'Université Toulouse 3 - Paul Sabatier

Présentée et soutenue par

Ezgi YILDIRIM

Le 23 mars 2023

Crystallization of Monodisperse Gold Ultrasmall Icosahedral Nanoparticles: Nucleation/Growth Mechanism Study Using Microfluidic Chips

---

Ecole doctorale : **SDM - SCIENCES DE LA MATIERE - Toulouse**

Spécialité : **Chimie Organométallique et de Coordination**

Unité de recherche :
LPCNO-IRSAMC - Laboratoire de Physique et Chimie des Nano-Objets

Thèse dirigée par
Guillaume VIAU et Lise-Marie LACROIX

Jury

Mme Lorette SICARD, Rapporteure
Mme Fabienne TESTARD, Rapporteure
Mme Marianne IMPEROR, Examinatrice
M. Nicolas COMBE, Examinateur
M. Guillaume VIAU, Directeur de thèse
Mme Lise Marie LACROIX, Co-directrice de thèse

To my dear husband...

Acknowledgments

As no journey is completed alone, I want to take this opportunity to thank some people for their valuable support in the course of my PhD project.

I would like to express my foremost gratitude to my supervisors, Prof. **Guillaume Viau** and Maître de conférences **Lise-Marie Lacroix** for their time, effort, endless professional support throughout the project and understanding in helping me succeed in my thesis. They have been incredible mentors to me. Our journey is started in 2019 with an internship. From that day until today, I learnt every day from them. I strongly believe that their students are really lucky to have them in the university. Their valuable knowledge and experience have inspired me throughout my studies. They always supported me to go to summer programs, conference to develop my skills such as HERCULES. I will always remember that they have even changed the travel plans for off-site experiments when we learnt I had been chosen for the best oral presentation at CNano 2020. I never forget it, thank you! During my writing period, they never let me alone. I am really grateful to them. Thanks to their generosity and encouragement, my time spent studying has been truly rewarding. I am grateful to be in our gold team for being such a wonderful group of people, both in and out of the laboratory.

I express my gratitude to Directeur de recherche **Fabienne Testard** and Maître de conférences **Lorette Sicard** who accepted to evaluate my thesis. To Directeur de recherche **Marianne Imperor**, Prof. **Nicolas Combe** and Maître de conférences **Sébastien Teychené** a special thank you for accepting to be part of the jury.

My special thanks also go to Dr. **Raj Kumar Ramamoorthy**. He was always with me to help and teach me with his great knowledge. His valuable feedback and encouragement greatly influenced how I conducted my experiments and interpreted my results. The data of this project would have been incomplete without his knowledge and support. Generally, we were in the same shift during the synchrotron, his behavior to the problems was impressive and a good guidance to me. Raj, I truly wish you the best professional opportunities in life. I hope you will find a good opportunity in India and be close to your family one day. I am quite sure that your students will be lucky and guided to become the best in the world.

I owe special thanks to **Dr. Pierre Roblin**, the king of the SAXS! I ‘d like to offer my thanks to him to being part of our gold team. I am always impressed of his knowledge about the SAXS. He was always shocked about our number of samples to measure. I know you have waited patiently almost 4 years to speak French with me. It was the time to speak but I am graduating :).

I'd like to express my gratitude to Maître de conférences **Sébastien Teychené** and Dr. **Isaac Rodríguez-Ruiz** for their excellent instructions, ideas, support and help to fabricate the microfluidic chips, nice collaboration and synchrotron experiments. I believe it was a good team to work on and produce the chips. They were really friendly when I was working in the laboratory. Our coffee times were very good and interesting, that I kept learning from their experiences. I was very lucky that I have worked with a such a great people for my project.

I'd like to thank to Prof. **Valeri Petkov** for sharing his great knowledge of XRD with us. And I want to thank for him valuable moral support when he was in Toulouse.

I am extremely thankful to all of my colleagues in the **NCO team** in the LPCNO. My lab mates are all appreciated for the fun times we had working and socializing together.

I am thankful to **Angélique Gillet, Adeline Pham, Simon Cayez, Francis Chouzenoux** and **Nicolas Ratel-Ramond** for their help for both the training and technical support. Adeline and Nicolas, I never forget your help to find capillaries for me. That day was very hard for me and you saved my life. I would like to thank the technical and support staff of LPCNO. Since we have travelled a lot, **Brice Altman** was always doing booking and travel planning with me. Even the airline lost my luggage in Canada during my conference, he helped getting it back. Your support facilitated all the challenges I was facing!

I would like to thank the LPCNO for providing me the resources to pursue my study. I'd like to thank the Ministère de l'Enseignement Supérieur et de la Recherche et de l'Innovation for the funding of my project. It is very important for me that women are able to advance in their career and I could start my journey in France thanks to the scholarship.

To conclude, I 'd like to thank my husband. I am extremely grateful to my husband for his patience, compromise, continuous moral support and understanding during the last four years in which most of my time and energy was devoted to the completion of this project. It would have been impossible to finish my studies without his moral support needed for the continuation of the PhD over the past years. He always encouraged me for the success and inspired for research. Also, I would like to thank to my family for their unlimited support during the time of my thesis even from thousands of kilometers away!

Abstract

The recent challenge on size reduction of metallic nanoparticles for diverse applications such as catalysis, generates a broad diversity of objects with tunable morphology and properties. Ultra-small metal nanoparticles with a mean diameter below 2 nm have gained considerable attention because of their unique structural and chemical properties. At such small sizes, metal particles can present an atomic structure which differs from the bulk one. This different atomic structure results from electronic effects, surface energy or nucleation mechanism during the nanoparticle formation.

We have studied the synthesis of ultra-small Au NPs through a liquid-phase approach in organic solvent (hexane). The reduction of $HAuCl_4$ was ensured by trialkylsilanes in presence of oleylamine (OY) under ambient conditions. Though it could seem fairly simple since it involves only few reagents, the optimization of the synthesis requires to understand the nucleation and growth mechanisms involved.

The first chapter present a brief overview of the state of the art on the Au NP synthesis, the nucleation/growth models and the in-situ studies. Then, the dedicated microfluidic set-up designed to get access to the short reaction time during which the nucleation occurred, and the different characterization techniques used are presented in chapter 2. The formation of NPs in presence of a very large excess of reducing agent (tri-isopropylsilane (TIPS)) is studied in chapter 3. A non-classical nucleation mechanism involving the presence of prenucleation clusters (PNCs) was evidenced by combining in-situ Small Angle X-Ray Scattering (SAXS) and X-Ray Absorption Spectroscopy (XAS). High Energy X-Ray Diffraction (HE-XRD) revealed that the 2 nm NPs exhibit an icosahedral structure.

The effect of the reducing agent concentration was presented in chapter 4. In presence of low reducing agent concentration, a competition between the direct reduction of the PNCs and the crystallization of a lamellar Au(I) complex which favors the growth of larger fcc particles was evidenced. The reaction kinetic could be determined both by in-situ UV-Visible or XAS spectroscopies and could be modulated by tuning the TIPS concentration from 1 M down to the stoichiometric 30 mM.

Chapter 5 describes the effect of two other experimental parameters: the reaction temperature and the strength of the reducing agent. The direct reduction was favored for fast reaction rates, leading to monodispersed icosahedral NPs. Finally, a general discussion on the two competitive pathways is reported in chapter 6, highlighting the experimental condition allowing for the simple synthesis of monodisperse Au icosahedral NPs.

Résumé

Le récent défi de la réduction de la taille des nanoparticules (NPs) métalliques pour optimiser leurs propriétés pour différentes applications telles que la catalyse, a conduit à une grande diversité d'objets à la morphologie et aux propriétés ajustables. Les nanoparticules métalliques ultra petites, d'un diamètre moyen inférieur à 2 nm, ont suscité un intérêt considérable en raison de leurs propriétés structurelles et chimiques uniques. À des tailles aussi petites, les particules métalliques peuvent présenter une structure atomique différente de celle du massif. Cette structure peut résulter d'effets électroniques et de minimisation d'énergie (notamment l'énergie de surface), ou du mécanisme de nucléation pendant la formation des nanoparticules.

Nous avons étudié la synthèse de NP d'or ultra-petites par une approche en phase liquide dans un solvant organique (hexane). La réduction de $HAuCl_4$ a été assurée par des trialkylsilanes en présence d'oleylamine (OY) dans des conditions ambiantes. Bien que cette synthèse puisse sembler assez simple puisqu'elle ne fait intervenir que peu de réactifs, son optimisation nécessite de comprendre les mécanismes de nucléation et de croissance impliqués.

Le premier chapitre présente un bref aperçu de l'état de l'art sur la synthèse des NPs d'or, les modèles de nucléation/croissance et les études in-situ. Ensuite, le montage microfluidique dédié, conçu pour accéder au temps court de réaction pendant lequel la nucléation se produit, et les différentes techniques de caractérisation utilisées sont présentés dans le chapitre 2. La formation de NPs en présence d'un très grand excès d'agent réducteur (tri-isopropylsilane (TIPS)) est étudiée dans le chapitre 3. Un mécanisme de nucléation non-classique impliquant la présence de clusters moléculaires (PNCs) a été mis en évidence en combinant la diffusion in-situ de rayons X aux petits angles (SAXS) et la spectroscopie de rayons X (XAS). La diffraction des rayons X à haute énergie a révélé que les NPs finales de 2nm présentent une structure icosaédrique.

L'effet de la concentration de l'agent réducteur a été présenté dans le chapitre 4. En présence d'une faible concentration, une compétition entre la réduction directe des PNCs et la cristallisation d'un complexe Au(I) lamellaire qui favorise la croissance de plus grandes particules fcc a été mise en évidence. La cinétique de la réaction a pu être déterminée à la fois par des spectroscopies UV-Visible ou XAS in-situ et a pu être modulée en jouant sur la concentration de TIPS entre 1M et 30 mM, qui correspond à la stoechiométrie.

Le chapitre 5 décrit l'effet de deux autres paramètres expérimentaux : la température de réaction et la force de l'agent réducteur. La réduction directe a été favorisée avec des vitesses de réaction rapides,

conduisant à des NPs icosaédriques monodisperses. Enfin, une discussion générale sur les deux voies compétitives est rapportée au chapitre 6, mettant en évidence la condition expérimentale permettant la synthèse simple de NPs icosaédriques d'or.

Table of Contents

Chapter 2 Microfluidic Tools and Characterization Techniques for In Situ Studies

Chapter 3 From Prenucleation clusters to nanospheres

Chapter 4 Synthesis of Au NPs with TIPS: Influence of the Reducing Agent Concentration

Chapter 5 Optimization of Monodisperse Ultra-Small Au NPs

Chapter 6 Pre-Nucleation Clusters (PNCs)

Conclusions

Introduction

The recent efforts on the size reduction of metallic nanoparticles gives rise to a wide variety of objects with tunable morphology and properties. Besides the size and the shape of nanoparticles, the control of the crystalline structures is also very important to properly tune the chemical or physical properties of the nanoparticles. In particular, preparing monodisperse metal nanoparticles with a low symmetry crystalline structure is very important fundamentally[1] and technologically for their paramount properties which qualify them for optical[2], catalytic[3], and electronics applications[4].

Size-selected clusters with controlled atomic structures, such as icosahedra, decahedra or cuboctahedra were prepared using gas phase synthesis methods.[5] Icosahedral particles are of particular interest for catalysis since they exhibit 20 triangular facets and 2-fold, 3-fold and 5-fold symmetry axis[6]. These particles, energetically favored only at very small sizes due to the important strain induced, could be specifically obtained thanks to size selection but only in limited quantities.

Alternatively, chemical synthesis in liquid phase allow producing large amount of nanoparticles in a single batch. Thanks to intensive researches in the past decades, nanoparticles with fairly controlled size and shapes could be obtained thanks to the proper addition of ligands. These molecules help stabilizing the nanoparticles by modifying the surface energy and thus the size at which a given crystalline structure may become stable[7].

The ligands not only stabilize the final nanoparticles but they can also interfere with the metal precursor to form stable complexes, affecting drastically the reaction kinetics. Thus, to prepare monodisperse nanoparticles with a specific atomic structure requires the proper identification of the complexes formed in-situ and a deep understanding of the nucleation and growth mechanism involved.

Up to date the formation of metal nanoparticles has been described by the classical nucleation theory (CNT)[8]. In terms of CNT, when atoms in solution exceed the solubility limit, they aggregate and generate stable-nuclei after crossing the energetic barrier imposed by the volume and surface energies. After that, they grow by an atom by atom addition process. The size of the final nanoparticle is inversely proportional to the supersaturation ratio which is the ratio of the actual and the equilibrium concentration of the precursors[9,10]. But recent observations, using advanced characterization techniques, [11,12,13,14,15] pointed out the existence of non-crystalline intermediate states such as oligomers or pre-nucleation clusters (PNCs).

Among the different metal of interest, we have focused on gold. Fairly resistant against the oxidation, Au NPs exhibit good catalytic, electronic and optical properties. Previous studies performed in the group showed that ultrathin nanowires could be easily obtained by the reduction of a gold chloride salt in presence of a long chain amine (oleylamine) in organic solvent. These wires, exhibiting a sub-2nm diameter and a micrometric length, possess a tetragonally closed packed crystalline structure, which strongly differs from the bulk fcc structure.[16]

Interestingly, by varying the oleylamine to gold ratio, ultrasmall nanoparticles below 2 nm could be quantitatively produced. Combining in situ high energy X-ray diffraction and scanning transmission electron microscopy, the particles were proven to exhibit an icosahedral structure but the reaction pathway was not known.

In this thesis, we studied the synthesis of ultra-small icosahedral Au NPs thanks to time-resolved in situ studies, namely wide angles X-ray scattering,[16] X-ray absorption spectroscopy (XAS)[17] and UV-Visible spectroscopy using dedicated microfluidic setup in order to access short reaction times.

The PhD thesis will present the main results of our study and is divided into 6 chapters.

Chapter 1 presents a partial overview of the extended research works on Au NPs synthesis methods. A particular focus is given on the mechanistic studies using in-situ techniques. Classical nucleation theory (CNT) is briefly introduced along with the non-classical pathways recently proposed. Finally, our studied system which consists in the synthesis of Au NPs using silanes as reducing agent in presence of oleylamine is detailed.

Chapter 2 gives a description of the specific microfluidic tools developed and the characterization techniques used to study the synthesis of Au NPs. The access to short reaction time, typically in the sub seconds range, was essential to capture the very first events of the reaction and in particular the nucleation stage.

Chapter 3 investigates the synthesis of Au NPs prepared with a large excess of triisopropylsilane (TIPS), which was commonly used as reducing agent in such systems. After characterizing the final nanoparticles obtained from a morphological and structural point of view, time-resolved studies combining Small Angle X-Ray Scattering (SAXS) and X-Ray Spectroscopy (XAS) were performed. While preliminary results were obtained in capillaries, the use of the microfluidic chips allowed to gain a clearer picture of the three stages involved in the reaction, namely the induction, the nucleation and the growth stages.

Chapter 4 presents the effect of the reducing agent concentration on the Au NPs formation. For the first time, the presence of an intermediate phase which tends to crystallize under slow reaction is

evidenced. The relation between this stable lamellar phase, which contains Au(I) species, and the presence of larger NPs is proposed.

Chapter 5 presents the optimization of the reaction parameters to yield monodisperse ultra-small Au NPs. To fasten the reaction kinetic and thus prevent the crystallization of the lamellar phase, the influence of the reaction temperature and the strength of the reducing agent were studied. Interestingly, highly monodisperse NPs exhibiting the icosahedral structure could be prepared using a less bulky reducing agent, namely trietoxysilane (TES).

Chapter 6 propose a general discussion on the ensemble of results obtained and a confrontation with the classical nucleation theory is proposed. Though it is still an hypothesis, non-classical pathways could apply in the formation of Au NPs using silane. In this framework, the role of the pre-nucleation clusters, as long as their chemistry, nature and size are discussed.

Finally, a conclusion and some perspectives of this work are given.

Bibliography

(1) Polte, J. Fundamental Growth Principles of Colloidal Metal Nanoparticles – a New Perspective. *CrystEngComm* **2015**, *17* (36), 6809–6830. https://doi.org/10.1039/C5CE01014D.

(2) Kwon, K.; Lee, K. Y.; Lee, Y. W.; Kim, M.; Heo, J.; Ahn, S. J.; Han, S. W. Controlled Synthesis of Icosahedral Gold Nanoparticles and Their Surface-Enhanced Raman Scattering Property. *The Journal of Physical Chemistry C* **2007**, *111* (3), 1161–1165.

(3) Mikami, Y.; Dhakshinamoorthy, A.; Alvaro, M.; García, H. Catalytic Activity of Unsupported Gold Nanoparticles. *Catal. Sci. Technol.* **2012**, *3* (1), 58–69. https://doi.org/10.1039/C2CY20068F.

(4) Maurer, J. H. M.; González-García, L.; Reiser, B.; Kanelidis, I.; Kraus, T. Sintering of Ultrathin Gold Nanowires for Transparent Electronics. *ACS Appl. Mater. Interfaces* **2015**, *7* (15), 7838–7842. https://doi.org/10.1021/acsami.5b02088.

(5) Plant, S. R.; Cao, L.; Palmer, R. E. Atomic Structure Control of Size-Selected Gold Nanoclusters during Formation. *J. Am. Chem. Soc.* **2014**, *136* (21), 7559–7562. https://doi.org/10.1021/ja502769v.

(6) Huang, L.; Shan, A.; Li, Z.; Chen, C.; Wang, R. Phase Formation, Magnetic and Optical Properties of Epitaxially Grown Icosahedral Au@Ni Nanoparticles with Ultrathin Shells. *CrystEngComm* **2013**, *15* (13), 2527–2531. https://doi.org/10.1039/C3CE26980A.

(7) Baletto, F.; Ferrando, R. Structural Properties of Nanoclusters: Energetic, Thermodynamic, and Kinetic Effects. *Rev. Mod. Phys.* **2005**, *77* (1), 371–423. https://doi.org/10.1103/RevModPhys.77.371.

(8) Thanh, N. T. K.; Maclean, N.; Mahiddine, S. Mechanisms of Nucleation and Growth of Nanoparticles in Solution. *Chem. Rev.* **2014**, *114* (15), 7610–7630. https://doi.org/10.1021/cr400544s.

(9) Leffler, V.; Ehlert, S.; Förster, B.; Dulle, M.; Förster, S. Nanoparticle Heat-Up Synthesis: In Situ X-Ray Diffraction and Extension from Classical to Nonclassical Nucleation and Growth Theory. *ACS Nano* **2021**, *15* (1), 840–856. https://doi.org/10.1021/acsnano.0c07359.

(10) Kashchiev, D.; van Rosmalen, G. M. Review: Nucleation in Solutions Revisited. *Crystal Research and Technology* **2003**, *38* (7–8), 555–574. https://doi.org/10.1002/crat.200310070.

(11) Watzky, M. A.; Finke, R. G. Transition Metal Nanocluster Formation Kinetic and Mechanistic Studies. A New Mechanism When Hydrogen Is the Reductant: Slow, Continuous Nucleation and Fast Autocatalytic Surface Growth. *J. Am. Chem. Soc.* **1997**, *119* (43), 10382–10400. https://doi.org/10.1021/ja9705102.

(12) Ramamoorthy, R. K.; Yildirim, E.; Barba, E.; Roblin, P.; Vargas, J. A.; Lacroix, L.-M.; Rodriguez-Ruiz, I.; Decorse, P.; Petkov, V.; Teychené, S.; Viau, G. The Role of Pre-Nucleation Clusters in the Crystallization of Gold Nanoparticles. *Nanoscale* **2020**, *12* (30), 16173–16188. https://doi.org/10.1039/D0NR03486J.

(13) Mikhlin, Y.; Likhatski, M.; Karacharov, A.; Zaikovski, V.; Krylov, A. Formation of Gold and Gold Sulfide Nanoparticles and Mesoscale Intermediate Structures in the Reactions of Aqueous HAuCl4 with Sulfide and Citrate Ions. *Phys. Chem. Chem. Phys.* **2009**, *11* (26), 5445–5454. https://doi.org/10.1039/B823539B.

(14) Mikhlin, Y.; Karacharov, A.; Likhatski, M.; Podlipskaya, T.; Zubavichus, Y.; Veligzhanin, A.; Zaikovski, V. Submicrometer Intermediates in the Citrate Synthesis of Gold Nanoparticles: New Insights into the Nucleation and Crystal Growth Mechanisms. *J Colloid Interface Sci* **2011**, *362* (2), 330–336. https://doi.org/10.1016/j.jcis.2011.06.077.

(15) Loh, N. D.; Sen, S.; Bosman, M.; Tan, S. F.; Zhong, J.; Nijhuis, C. A.; Král, P.; Matsudaira, P.; Mirsaidov, U. Multistep Nucleation of Nanocrystals in Aqueous Solution. *Nat Chem* **2017**, *9* (1), 77–82. https://doi.org/10.1038/nchem.2618.

(16) Vargas, J. A.; Petkov, V.; Nouh, E. S. A.; Ramamoorthy, R. K.; Lacroix, L.-M.; Poteau, R.; Viau, G.; Lecante, P.; Arenal, R. Ultrathin Gold Nanowires with the Polytetrahedral Structure of Bulk Manganese. *ACS Nano* **2018**, *12* (9), 9521–9531. https://doi.org/10.1021/acsnano.8b05036.

(17) Abécassis, B.; Testard, F.; Kong, Q.; Francois, B.; Spalla, O. Influence of Monomer Feeding on a Fast Gold Nanoparticles Synthesis: Time-Resolved XANES and SAXS Experiments. *Langmuir* **2010**, *26* (17), 13847–13854. https://doi.org/10.1021/la1020274.

Chapter 1 Bibliography

1.1 Introduction

The Au NPs with size in the range 1.5 nm -100 nm are the most widely worked system compared to other nanostructured materials. Because of their unique properties such as great chemical stability, surface plasmon resonance effect, biocompatibility and catalytic activity they find applications in biomedical research[1] like cancer treatment, drug delivery, imaging, DNA sequencing, electronics[2], information storage[3], catalysis[4] and photovoltaic devices[5]. These properties depend on the preparation of the Au NPs and in particular of the control of their size and shapes and also on the different functionalities that can be added through surface modification. One interest is that Au NPs can be easily prepared in solution from gold ions salts or complexes using reducing agents such as amines[6], hydrides[7], alcohols[8], polymers[9] or fungus[10]. In addition to that, several capping ligands such as thiols[11], amines[6] and polymers[12] can be used to control the shape and the stability of the colloidal suspensions.

Different methods have been used in order to produce gold nanoparticles with various shapes and structures as shown in figure 1.1 including nanospheres, nanocubes, nanorods, nanoclusters, nanostars…. To prepare such a broad variety of gold nanoparticles, the top-down and bottom-up techniques[13] are used. The nanoparticle synthesis by top-down techniques comprises several approaches such as laser ablation, sputtering, pyrolysis, lithography and ball milling. The bottom-up technique involves chemical synthesis, radiation induced synthesis and microemulsion synthesis. In this chapter we will focus mostly on the chemical synthesis of gold nanoparticles in liquid phases.

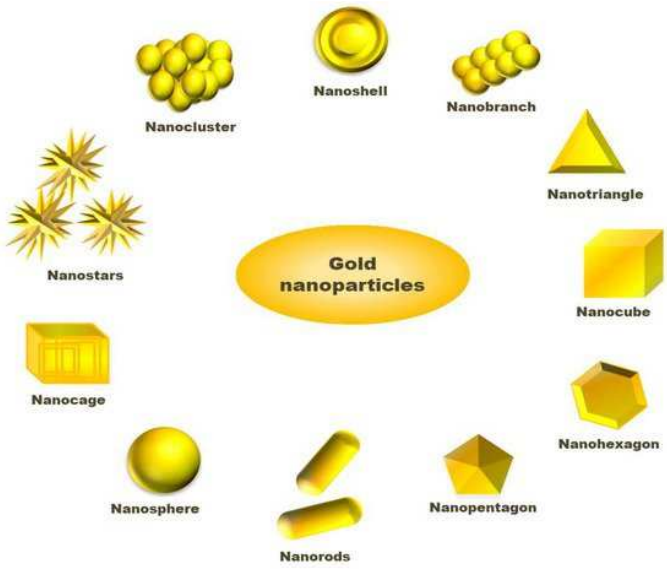

Figure 1.1 The different morphologies of the gold nanoparticles. Reprinted from the reference[14].

In this chapter firstly, different methods for the liquid-phase preparation of the Au NPs and their atomic structure will be discussed. After that, some elements of the classical nucleation and growth mechanism of NP formation in solution will be recalled and examples of studies using *in situ* techniques will be discussed. At the end of this chapter, a state of the art of the synthesis of Au nanoparticles using silane as reducing agent in presence of oleylamine, which is the method we used, will be described.

1.2 Chemical synthesis of Au NPs

This approach basically consists in the chemical reduction of a precursor, a gold salt or a gold complex, in solution thanks to a reducing agent, in the presence of stabilizing agents to stabilize a nanometric size, using suitable reaction parameters (such as pressure, temperature…).

-the gold precursors are ionic salts such as halides, nitrates, acetate, acetylacetonate, or complex with phosphine. The oxidation states of the gold precursors are Au^{+1} or Au^{+3}. The final state of the Au NPs is Au^0. Basically, Au^{+1} or Au^{+3} are reduced to Au^0 using reducing agents.

-the solvents are functional hydrocarbons (oleylamine), polar molecules like water, ethanol, methanol, ethylene glycol, polyethylene glycol or non-polar molecules like hexane, toluene, chloroform, depending on the gold precursor that have been chosen.

-the stabilizing agents depend on the polarity of the solvent. In polar solvent, trisodium citrate dihydrate, hydrophilic polymers such as poly(vinylpyrrolidone) (PVP), or surfactants such as cetyltrimethylammonium bromide (CTAB) are commonly used. In apolar solvents, long chain alkylthiolates, phosphine ligands or amines are often chosen. Their role is to stabilize the Au NPs in the suspension inhibiting the agglomeration by repulsive force that can be either steric or electrostatic. As we will further describe later, they also can affect the growth rate of the nanoparticles.

-the reducing agents are silanes, borohydrides, citric and oxalic acids, hydrogen peroxide, sulfites, polyols, H_2 gas and many others. They supply electrons in order to reduce the gold ions, Au^{3+} and Au^{+} to Au^0. In some studies, the stabilizing agent can also be the reducing agent[15]

The different reaction parameters such as the temperature, the pH, as long as the reactants and the solvent play an important role in controlling the size, the shape and the structure of the gold nanoparticles.

A wide range of methods has been developed in the past in order to control the shape[16], the size[17–19] and the surface functionality[20–23] of metal nanoparticles. In 1951, Turkevich *et al.* developed a synthesis which is now the most widely used one to prepare spherical Au NPs in water with a size in the range

of 15-50 nm[24]. Basically, the hydrogen tetrachloroaurate ($HAuCl_4$) is reduced by citric acid in boiling water. In this synthesis, the citrate is used as reducing agent for the reduction of gold ions (Au^{3+}) to gold atoms (Au^0) as well as stabilizing agent (figure 1.2.a). In 1973, this method was modified by Frens[25] in order to control the particle size over a wider range by changing the gold to citrate ratio. This refinement of the Turkevich method allowed to prepare Au NPs with a size in the range 16-147 nm. This Au NPs stabilized by citrate can be functionalized by replacing the citrate shell by thiolate ligands but one can face irreversible aggregation during the ligand exchange. Several methods have been improved in order to prevent aggregation using a surfactant such as Tween 20[26] or thioctic acid (lipoic acid) [27]. A highly diluted medium is generally required which can be an issue for large scale production.

Another very popular method to prepare Au NPs was developed in 1994 by Brust *et al*[11]. Organic suspensions of Au NPs with the size range of 1.5-5.2 nm stabilized with alkanethiol were prepared by a two-phase reaction. The basic principle of this method is to extract the gold precursor from the aqueous solution to an organic solvent (toluene) using a phase transfer reagent (tetraoctylammonium bromide). The biphasic reduction is carried out with sodium borohydride ($NaBH_4$) (figure 1.2.b). This method provides spherical Au NPs with a size in the range 1.5 to 5 nm depending on the reaction parameters such as the gold to thiol ratio, the reduction rate and the reaction temperature[28]. Love *et al*[29] found that these Au NPs stabilized alkanethiol exhibit a high stability because of the strong thiol-gold bond and the strong van der Waals attractions between the ligands. They proposed that these Au NPs can be the starting material for further functionalization since these NPs do not aggregate during the drying and the redispersion procedures.

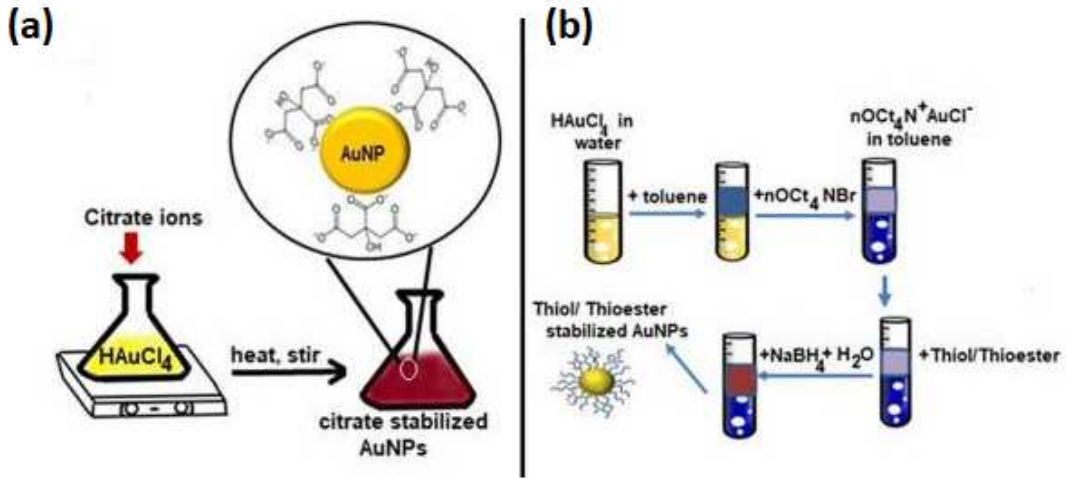

Figure 1.2 Schematic picture of the (a) Turkevich method and (b) Brust method for the synthesis of Au NPs. Reprinted from the reference[30].

Besides these approaches, the seed-mediated growth[31,32] is commonly used to synthesize other shapes of Au NPs , such as rods and cubes (figure 1.3). In this technique, firstly, the seeds are produced by reduction of the gold salt using sodium borohydride ($NaBH_4$) and citrate ions as stabilizing agents. For the next step, generally, the seeds are introduced in the medium that contains the gold precursor and a mild reducing agent such as hydroxylamine or ascorbic acid. The seeds provide nucleation centers on reactive sites, which allows to have an heterogenous nucleation and finally to control the size and shape of the Au NPs. The size of the particles ranges from 5 to 40 nm and the shape depends on the concentration of the reducing agent, the nature of the seeds[33] and the nature of the stabilizing agent used in the second step. Multi-twinned seeds such as decahedra are used to grow nanorods with a selective growth along the 5-fold axis of the decahedra.

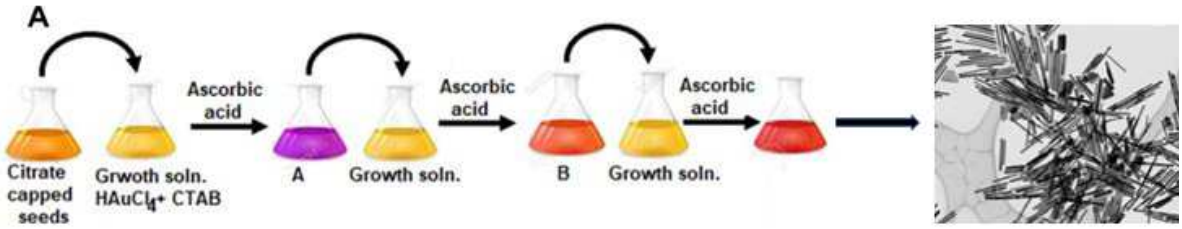

Figure 1.3 Schematic picture of a three-step seed-mediated synthesis of long gold nanorods. Reprinted from the reference[34].

1.3 Structural studies

Most of the noble-metal crystallize with the *fcc* structure, as in the bulk state. As a consequence, the noble-metal nanocrystals with a single crystal structure exhibit cubic, cuboctahedra, octahedral or tetrahedral shapes[35]. However, as mentioned above, there is also a great interest to grow twinned nanocrystals to have new shapes and improved properties[36] (figure 1.4). These multi-twinned particles are decahedra, icosahedra and rods with a pentagonal cross section. Icosahedral shaped multi-twinned particles are really attractive because of their high symmetry and physicochemical properties. An icosahedral nanocrystal includes 20 triangular {111} facets and 2-, 3- and 5-fold rotational symmetry axis.

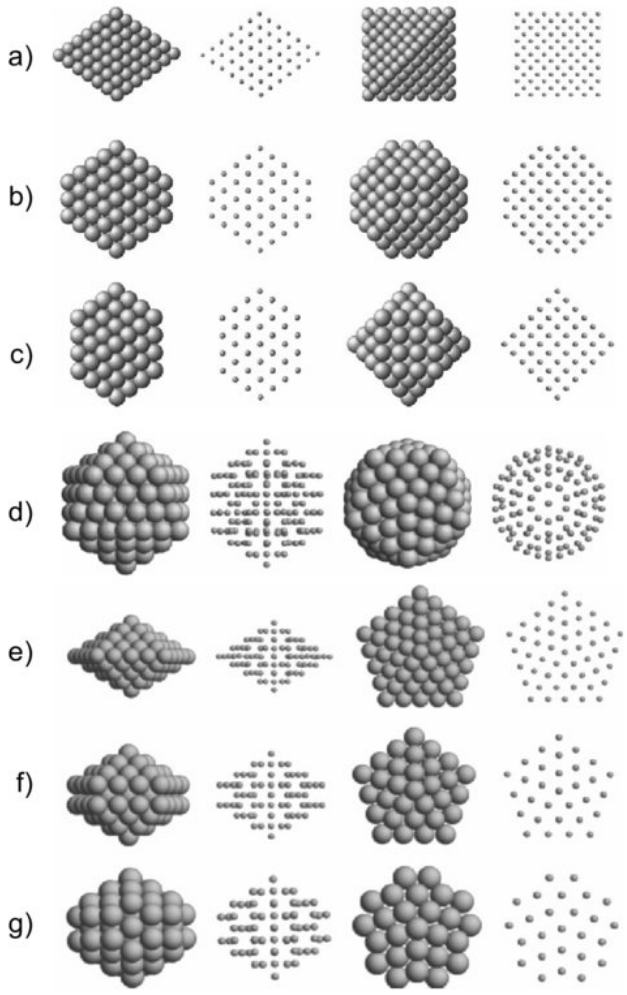

Figure 1.4 Face-centered-cubic clusters: (a) octahedron; (b) truncated octahedron; (c) cuboctahedron; icosahedral cluster: (d) Mackay icosahedron; decahedral clusters: (e) regular decahedra; (f) Ino truncated decahedra and (g) Marks truncated decahedra. Reprinted from the reference[37].

Research groups have demonstrated the advantage of the surface strain for improving properties of the nanoparticles. For example, icosahedral noble metal nanoparticles such as Pt_3Ni and Pd have better performance for the oxygen redaction reaction[38] and electrocatalytic activity[39] compared to other nanoparticles. In addition to that, icosahedral Cu, Ag and Au nanoparticles increased the signal intensity in surface-enhanced Raman scattering (SERS) applications[40]. For most of noble metals, the icosahedral structure is only energetically favored at very small sizes, their synthesis requires a kinetic control, or the use of specific capping agents and/or seeds[37].

The Au NPs crystallize as three main structures, icosahedron, decahedron and face-centered cubic (*fcc*) polyhedra. In bulk state, the thermodynamic stable phase of Au is the *fcc* structure and the more stable

shape can be given by the Wulf calculation if the surface energy of the different (*hkl*) facets are known. Decreasing the particle size favors first the decahedral structure and then the icosahedral structure below critical sizes[37]. Barnard et al[41 42] generated a quantitative phase diagram for the Au nanoparticles to demonstrate the relation between the crystal structure, size in the range of 2.5-30 nm and temperature in the range 0-1500 K . This diagram given figure 1.5 shows that the icosahedral structure is favored for the small NP size and at low temperature. Icosahedra have a larger internal strain and lower surface energy than decahedra and *fcc* nanocrystals. Experimentally, icosahedra are stable at room temperature below a critical size which is 1.6 nm, 1.2 nm and 2 nm for Au, Pt and Pd, respectively[37 43 44].

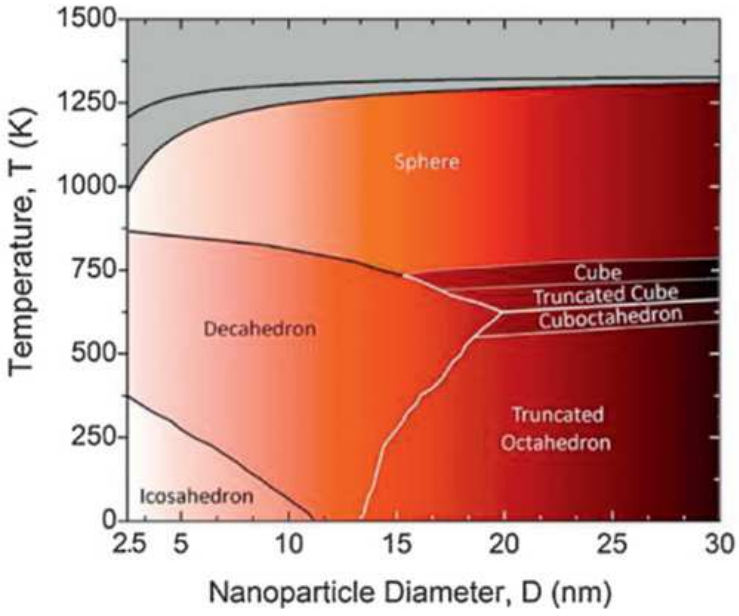

Figure 1.5 Phase diagram based on thermodynamic calculations giving the nanoparticle shape and structure as a function of the diameter and temperature. Reprinted from the reference[42].

Interestingly, it is also possible to grow icosahedral nanoparticles above this critical size providing that the reaction is kinetically controlled rather than thermodynamically. Large icosahedra are metastable structures due the strain energy. A transformation towards more stable structures like decahedra or cuboctahedra requires however to overpass an activation energy which can be very high. In the next sections we will present the different methods reported for the synthesis of icosahedral Au NPs.

1.4 Examples of Au NP synthesis with controlled structure

There are a lot of method to prepare Au NPs with controlled size and shape. For example, oleylamine is used in organic solvents (toluene, chloroform) to prepare icosahedral NPs. OY is a primary amine with a long alkyl chain and a double bond in the middle of the chain (figure 1.6). Oleylamine is often used as a stabilizing agent for the NPs but can also stabilize Au complexes.

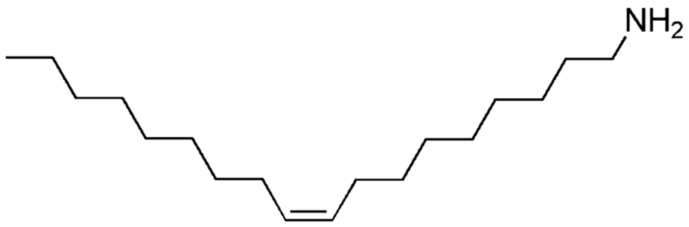

Figure 1.6 Oleylamine

For example, Lu et al[45] showed that the coordination of AuCl with oleylamine in chloroform leads to a [AuCl(oleylamine)] complex. Then the thermolysis of this complex at 60°C gave Au NPs with a mean size of 12.7 nm with a standard deviation of 8 % as shown in figure 1.7.a. The high-resolution TEM image of the nanoparticles showed a multiply twinned structure (figure 1.7.b). The UV/Vis spectra of the Au NPs formed at different reaction times revealed a fairly slow reaction (figure 1.7.c). An absorbance peak at λ= 530 nm, which is characteristic of the localized surface plasmon resonance for Au NPs, appears after 3h. Its intensity further increases with time. The absence of any extra reducing agent let us think that oleylamine was also playing this role, as previously described in other synthesis.

Replacing oleylamine with octadecylamine leads to larger nanoparticles with a size of ~100 nm. The authors invoked a lower stability of the complex formed in presence of octadecyl amine compared with oleylamine. The authors also modified the halide used, starting from AuBr instead of AuCl. The reaction was faster, a mixture of nanospheres and nanorods was obtained after solely 3h, instead of the 24 h needed in presence of -Cl.

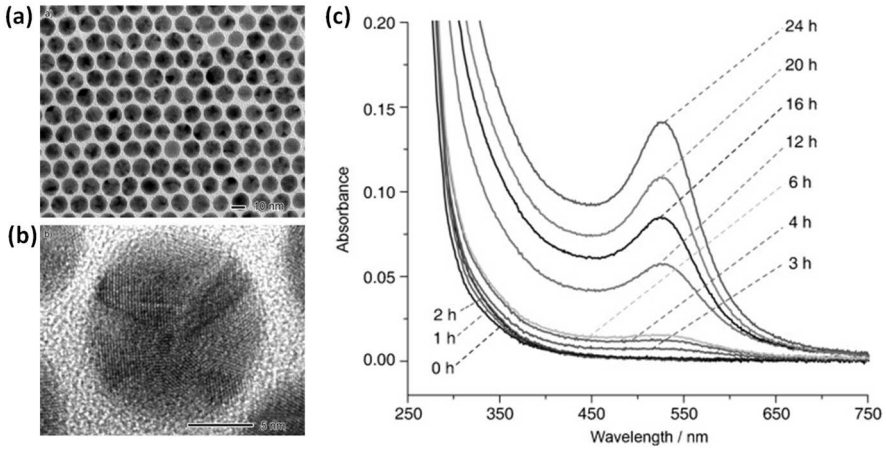

Figure 1.7 (a) TEM image of Au NPs obtained at 60 °C from the AuCl and oleylamine in $CHCl_3$, (b) HRTEM image of the Au NPs and (c) UV/Vis absorption spectra for the Au NPs formation at 60 °C from the AuCl and oleylamine in $CHCl_3$. Reprinted from the reference[45].

In another work, Lee et al.[46] have prepared fcc, decahedral and icosahedral nanoparticles varying the gold salt concentration ($HAuCl_4$) in 4-tert-butyl toluene as shown in the figure 1.8. 1,2-hexadecanediol was used as reducing agent. They showed that the oleylamine increased the solubility of $HAuCl_4$ in organic media allowing to reach high Au (III) salt concentration, which leads to icosahedral NPs.

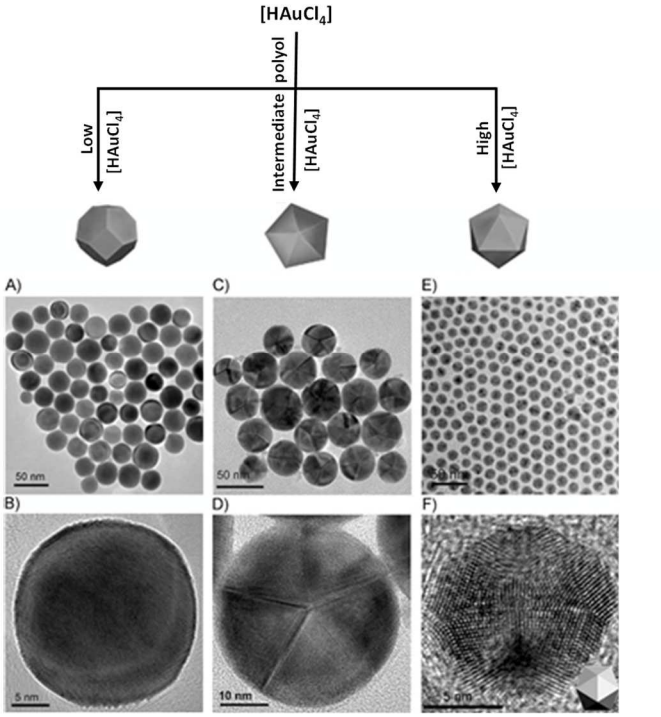

Figure 1.8 TEM and HRTEM images of A,B) fcc, C,D) decahedral and E,F) icosahedral Au NPs. Reprinted from the reference[46].

Using tert-butyl aminoborane (TBAB) as reducing agent Peng et al. prepared Au NPs with different sizes in the range 2.4 – 9.5 nm playing on the temperature of reaction in the range 2 - 40 °C[47]. The lower the temperature, the larger the particles obtained (figure 1.9). The NPs with a mean diameter d_m = 2.4 nm exhibited a XRD pattern which cannot be indexed by a *fcc* structure, the main peak being shifted towards high *q*. In contrast, the particles with a diameter above 5 nm exhibited an icosahedral outer shape but a *fcc* structure (figure 1.10). These particles are multi-twinned particles. The effect of the temperature on their size was interpreted in the framework of the classic LaMer theory: the higher the temperature, the faster the reduction rate, the higher the number of nuclei in the medium and thus the smaller the final particles. As a matter of fact, the induction time varied from 5 min to a few seconds when the temperature was increased from 2°C to 25°C.

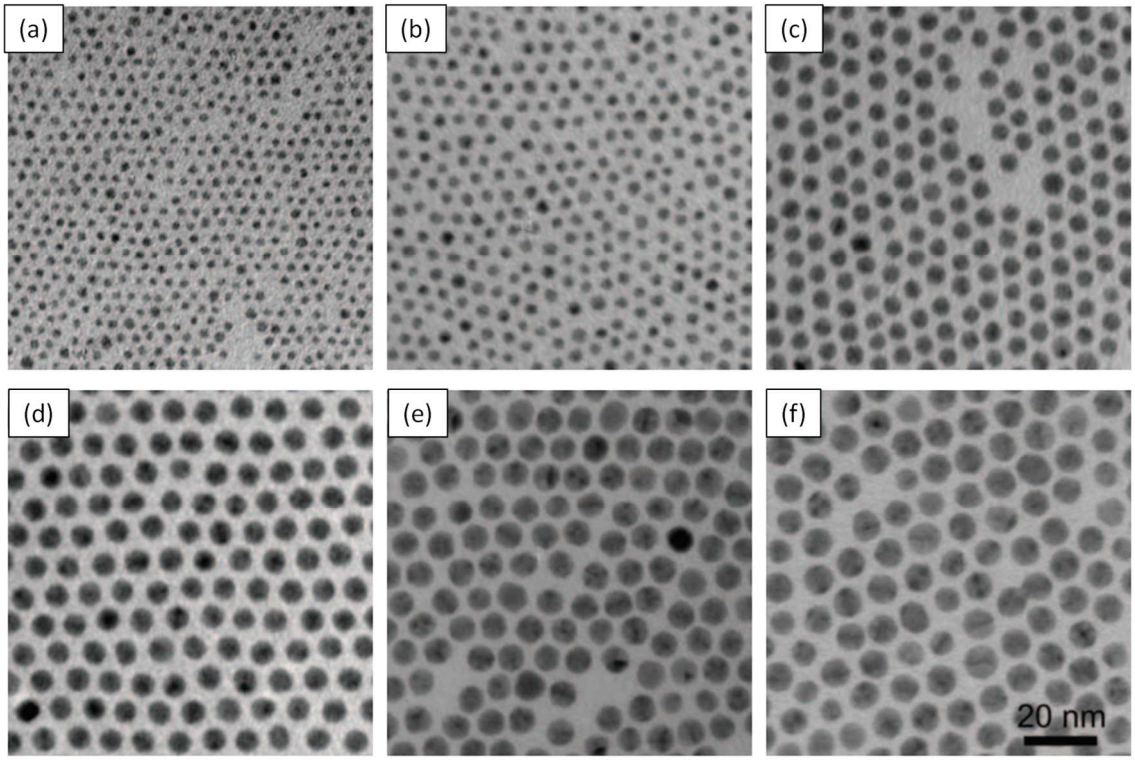

Figure 1.9 TEM images of the Au NPs synthesized at different temperatures: (a) 40 °C, (b) 35 °C, (c) 25 °C, (d) 15 °C, (e) 10 °C, and (f) 2 °C. Reprinted from the reference[47].

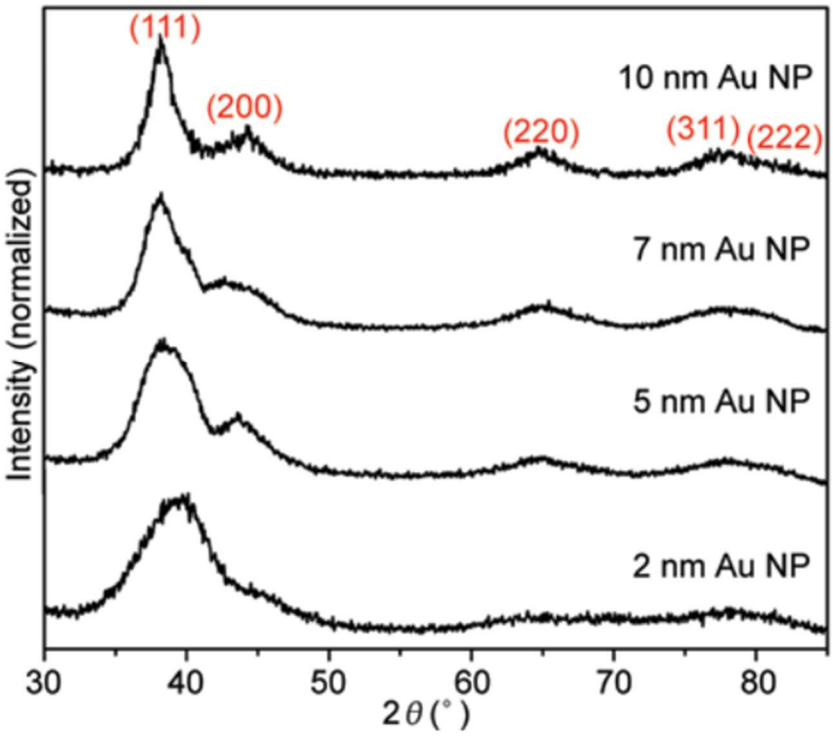

Figure 1.10 XRD patterns of the Au NPs of different sizes. The size was measured from the respective TEM images (figure 1.9). Reprinted from the reference[47].

1.5 Nucleation and growth mechanisms

Generally, the nucleation of nanoparticles grown in solution is described by the Classical Nucleation Theory (CNT). According to this theory, when the monomer atoms in the solution exceed the solubility limit, the atoms continuously aggregate to form embryos. These embryos disintegrate until they reach a critical size (r_c). The high surface energy of the embryos imposes indeed a barrier against the formation of stable nuclei. The nucleation occurs when a crystalline nucleus is stable enough to further grow. After that, the nuclei start to grow and reach the final structure of nanoparticles by an atom by atom addition. The nucleation rate which is the rate at which crystalline nuclei are produced in solution depends on the thermodynamic barrier and on the kinetics of addition of the monomer atoms. According to the CNT, the crystallization is a phase transition that involves the surface energy of the crystal in solution (Figure 1.11).

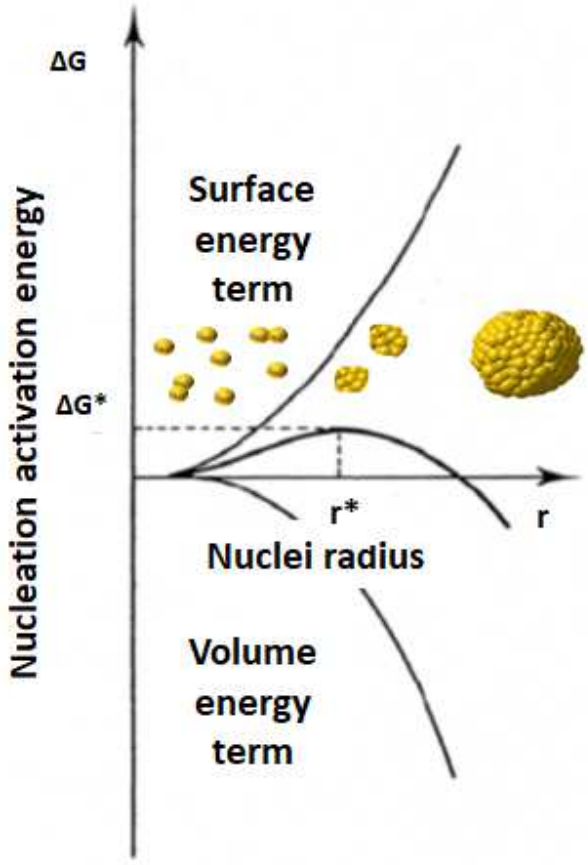

Figure 1.11 Free energy diagram for classical nucleation theory. Reprinted from the reference[48].

The driving force of crystallization of a solid in solution is the supersaturation *S* which is the ratio between the concentration of the monomers in solution and the solubility of the solid, also called the saturation concentration, c_S:

$$S = \frac{c}{c_s} \qquad \text{(Eq. 1.1)}$$

The free enthalpy of a spherical solid particle of radius *r* in a liquid is :

$$\Delta G(r) = 4\pi r^2\gamma + \frac{4}{3}\pi r^3 \frac{1}{v_m}\Delta\mu \qquad \text{(Eq. 1.2)}$$

with γ the surface tension of the solid particle in the liquid, v_m the molar volume and $\Delta\mu$ the difference of chemical potentials of the monomers in the solid and in solution. The first term of the sum

represents the surface term and the second one the volume term. The difference of chemical potentials is related to the supersaturation as:

$$\Delta\mu = -\mathrm{kTln}S \qquad \text{(Eq. 1.3)}$$

The volume term is negative for monomer concentrations higher than the saturation while the surface term is always positive (Figure 1.11). If we plot ΔG as a function of r, the curve presents a maximum for a given critical radius *r**. The expression of *r** is deduced from the derivative of ΔG :

$\frac{\partial \Delta G}{\partial r} = 2 \times 4\pi r\gamma + 4\pi r^2 \frac{1}{v_m}\Delta\mu = 2 \times 4\pi r\gamma - 4\pi r^2 \frac{\mathrm{kTln}S}{v_m}$ and for *r* = *r**, $\left(\frac{\partial \Delta G}{\partial r}\right)_{r=r*} = 0$

So, the critical radius is:

$$r^* = \frac{2\gamma v_m}{kTlnS} \qquad \text{(Eq. 1.4)}$$

This is the basics of the classical nucleation theory. Particles with a diameter below *r** are not stable in solution because $\frac{\partial \Delta G}{\partial r} > 0$ and thus they dissolve. The nuclei become stable and can grow when they reach the critical radius *r**. It is important to note that *r** increases with γ and decreases with *S*. Basically, when the surface energy is very high, the critical radius is bigger. On the other hand, the critical size decreases when the supersaturation or the temperature increase.

The value of the free enthalpy for *r* = *r** is:

$$\Delta G^*_{r=r^*} = \frac{16}{3}\pi v_m^2 \frac{\gamma^3}{(kTlnS)^2} \qquad \text{(Eq. 1.5)}$$

This energy barrier $\Delta G^*_{r=r^*}$ can be seen as an activation energy determining the kinetic of nucleation.

An Arrhenius law defines the nucleation constant k_N:

$$k_N = \beta \times \exp\left[-\frac{\Delta G^*_{r=r^*}}{kT}\right] \qquad \text{(Eq. 1.6)}$$

where, β is the frequency of the monomer attachment. The nucleation rate $J_{nucl.}$ writes as:

$$J_{nucl.}(t) = \beta[M]\frac{V}{v_0}\exp\left[-\frac{\Delta G^*_{r=r^*}}{kT}\right] \qquad \text{(Eq. 1.7)}$$

where, M is the concentration of the monomer and $\frac{V}{v_0}$ is the Zeldovich factor. The energy barrier is lower and the nucleation rate higher when: (i) the surface tension γ is low; (ii) the supersaturation S is high; or (iii) the reaction temperature T is high. So, in these conditions, the nucleation is faster and the size of the stable nuclei is smaller. For a given concentration of monomers the final particle size is expected to be smaller since more nuclei are formed.

The LaMer's model[49] considers the concentration of the monomer as a function of time during the nanocrystal formation (figure 1.12). When the concentration of the monomer increases, it reaches first the solubility but nothing occurs. When it is higher than the solubility we should see the precipitation of the solid, but the concentration has to reach a critical value called critical supersaturation (C_{min}) for the nucleation to start. During the nucleation stage, the monomers are consumed, leading to a decrease of the concentration. When it drops below the critical supersaturation concentration, nucleation of stable nuclei can no longer form. The growth then takes place on the existing nuclei. The LaMer's model is often invoked to describe the formation of monodisperse particles. According to this model, nucleation must be short and consume enough monomer not to overlap with the growth stage.

The growth of a nuclei is often modelled as a two-steps process: the diffusion of the monomer from the solution to the surface of the nuclei and the reaction at the surface of the nuclei.

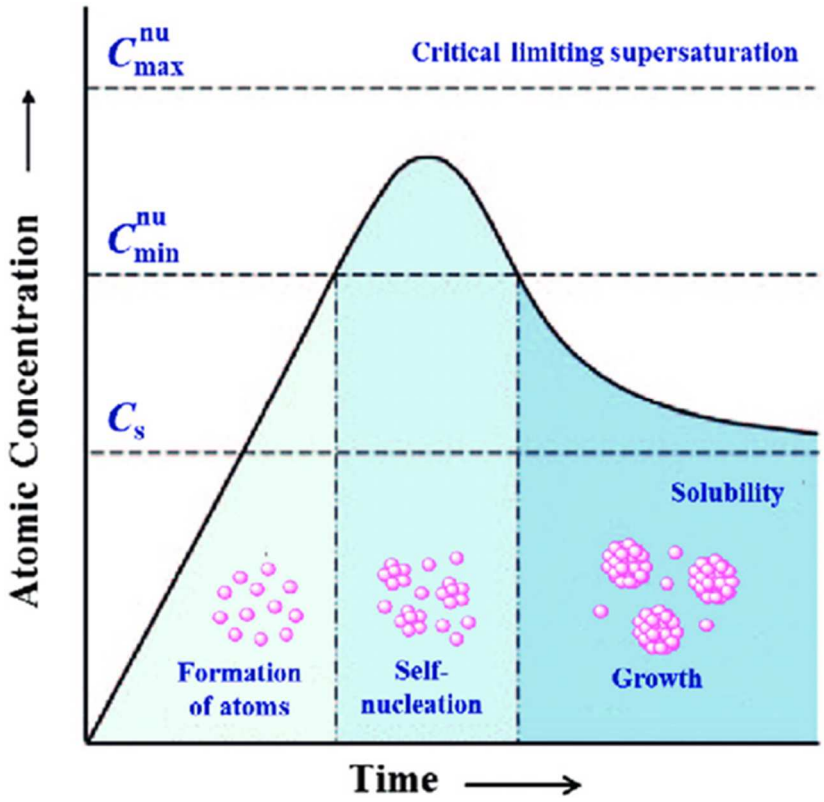

Figure 1.12 The LaMer model of the formation of atoms, nucleation and growth of nanocrystals as a function of reaction time. Reprinted from the reference[50]. C_s : solubility limity, C_{min} and C_{max} : minimal and maximal critical supersaturation.

Recent studies propose that the nanoparticle formation may evolve different pathways (see figure 1.13) i.e through one or several non-crystalline intermediate states instead of crystalline nuclei[51,52]. These non-crystalline intermediate states are oligomers, complexes, liquid droplets or amorphous nanoparticles. Such non-classical mechanism has been proposed for several systems, mainly oxides, but more rarely for metal nanoparticles. Capturing the crystallization pathways is challenging because of the length and time scales at which the object appears firstly during the reaction. For this reason, in-situ time resolved experiments are needed.

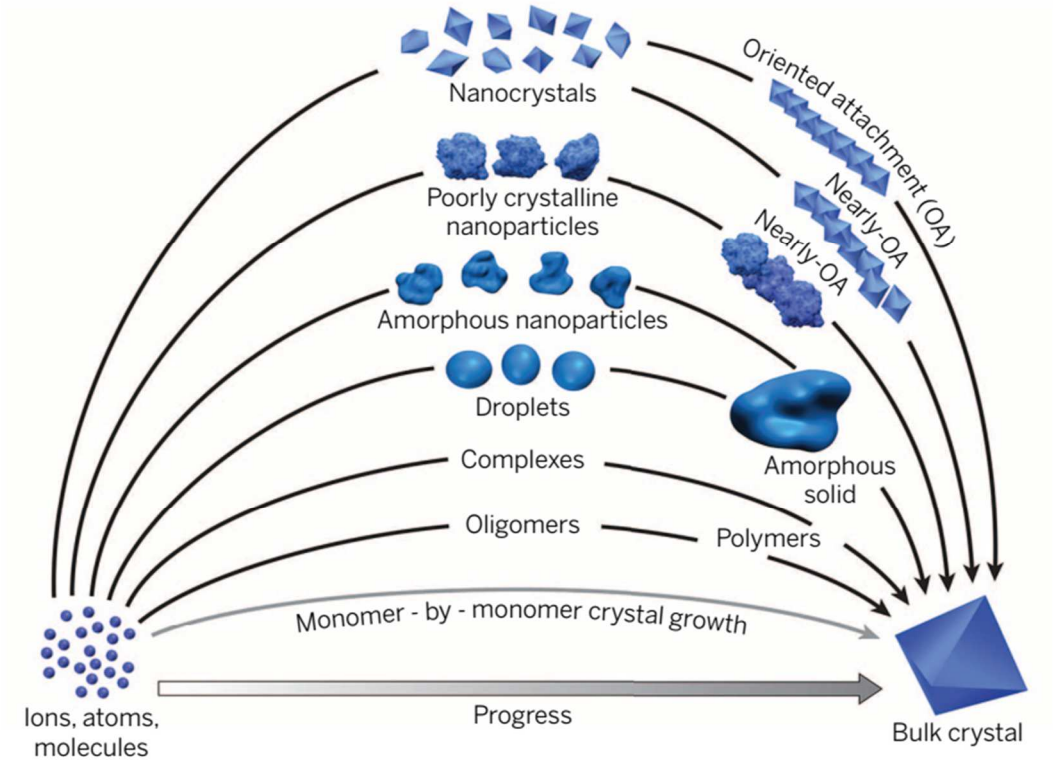

Figure 1.13 Pathways to crystallization by particle attachment. Reprinted from the reference[51].

1.6 *In situ* studies

Time-resolved *in situ* techniques such as *in situ* X-ray scattering and absorption spectroscopy studies[53–55] using synchrotron radiation are very useful to catch the formation of nanoparticles pathways[56,57].

Abécassis et al[58,59]. have studied the nucleation and growth mechanism of gold nanoparticles using *in situ* small angle X-ray scattering (SAXS), X-ray absorption near edge spectroscopy (XANES) and UV-Vis spectroscopy.

The Au NPs were prepared from the reduction by a borohydride (BH_4^-) of an $AuCl_3$ salt solubilized in toluene using a cationic surfactant (DDAB) in presence of long chain ligands such as decylamine or decanoic acid. To ensure the proper mixing of the gold salt with the reducing agent-ligand solutions, they have used a fast-mixing stopped-flow device, leading to a 3 to 200 ms time resolution depending on the characterization techniques. Since the Au NPs are formed in a few seconds, such time resolution and fast mixing was essential to capture the beginning of the reaction. In-situ UV-vis experiments were first used to check qualitatively the formation of the Au NPs prepared with decanoic acid. At the beginning of the reaction they have observed a band at λ=400 nm, which corresponds to Au (III)-DDAB.

The intensity of this band decreased over 150 ms indicating the reduction of Au (III). Up to 400 ms, the UV-vis spectrum was constant. The surface plasmon band at λ=544 nm appears after 400 ms, showing that the Au NPs were forming. When they changed the ligand with the decylamine, a faster reaction was observed. The transition stage was only of 50 ms, revealing that the nature of the ligand plays an important role on the kinetic of the Au NPs formation.

The size of the Au nanoparticles could be deduced from in-situ SAXS. Au NPs of 3.5 nm and 1.4 nm were formed in presence of acid ("slow" reaction) or amine ligands (faster reaction), respectively.

In addition, XANES gave an information about the chemical state of Au during the formation of the NPs. From this technique, it was possible to deduce the concentration of the Au (III), Au (I) and Au (0) during the reaction which is required to understand the chemical pathways. In figure 1.14, the first spectrum at 104 ms was found similar to the Au (I) reference. The final spectrum (t = 20 s) is very close to the Au (0) reference. So, the reduction of Au (III) occurs through Au (I), which then evolves toward Au (0). Reactions rates could be deduced with this technique. Regarding the acid ligand and amine ligand case at 298 K, the growth rate found 4 x 10^{-4} ($m.s^{-1}$) and 2.2 x 10^{-4} ($m.s^{-1}$), respectively.

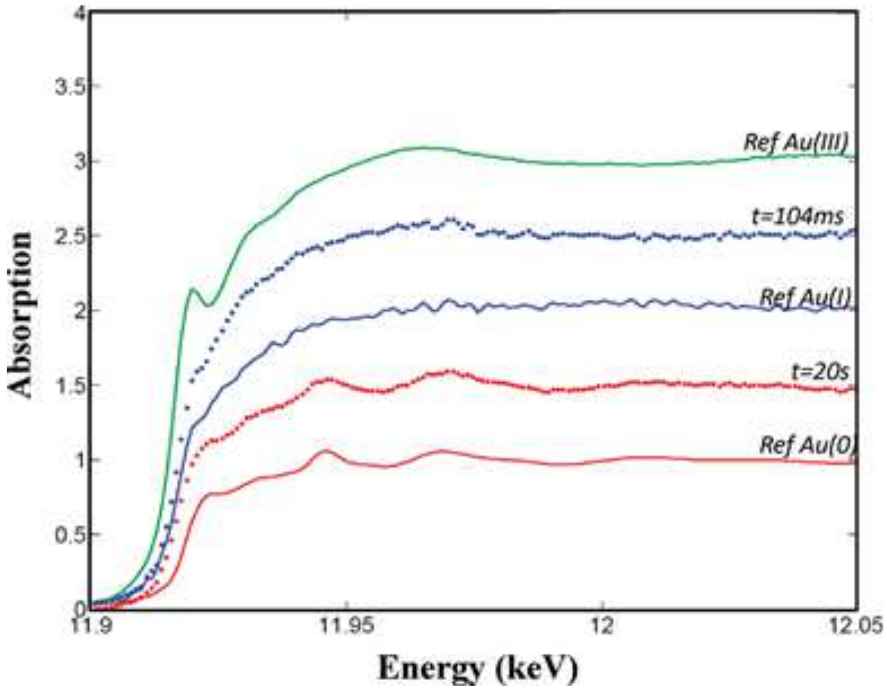

Figure 1.14 XANES spectrum at the gold L_{III} edge recorded during the synthesis of Au NPs with the acid ligand at t =104 ms and 20 s. Comparison with the XANES spectra of Au(III), Au(I) and Au(0) references. Reprinted from the reference[59].

Abecassis[58,59] et al. concluded that the results of the *in situ* studies on the synthesis of Au NPs were in agreement with the classical nucleation theory, the faster the reaction, the smaller the NPs. And also, since the ration between the surface reaction constant and diffusion coefficient of the monomer is bigger than 1, the growth stage was controlled by the surface reaction and not by the diffusion of the monomer from the solution to the surface of the nuclei.

Another study, reported by Chen et al[60]. was devoted to unravel the nucleation and growth mechanism of Au NPs using *in situ* time resolved techniques such as SAXS, WAXS and UV-vis along with a stopped-flow microfluidic device shown in figure 1.15. The mixing of the solutions of gold salt and reducing agent was ensured using a fast mixer, as in the previous study, but the dead time corresponding to the transfer of the solutions in the measurement cell was minimized.

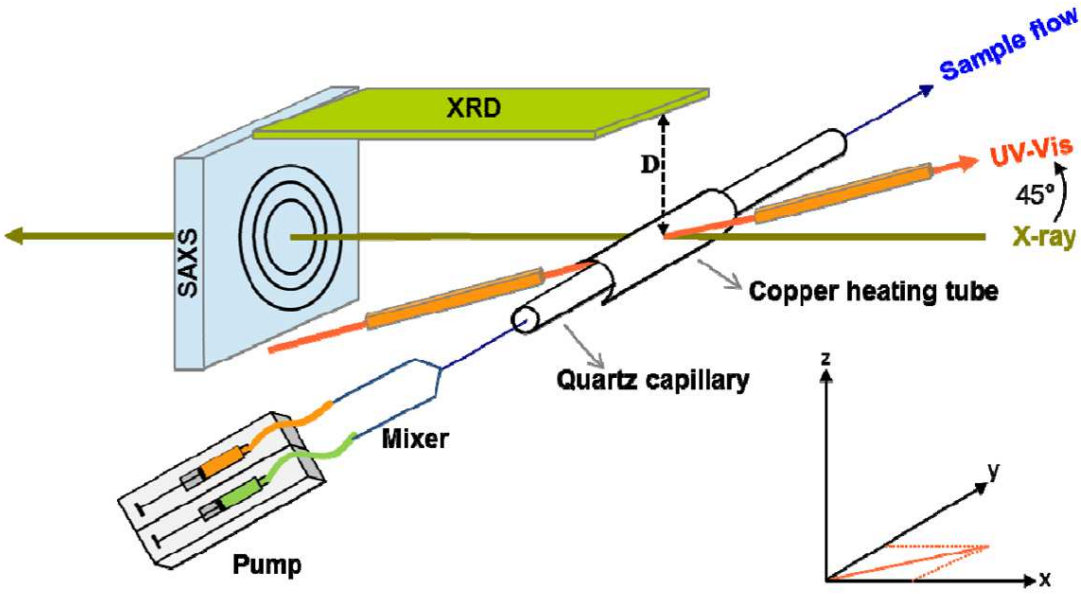

Figure 1.15 Schematic image of the experimental setup to perform *in situ* experiment. Reprinted from the reference[60].

The Au NPs were prepared by the reduction of gold (I) salt using t-butylamineborane (TBAB) in toluene in the presence of dodecanethiol (DDT). The authors have studied the influence of the precursor concentration, the temperature and the ligand on the Au NPs formation. Figure 1.16.a shows a TEM image of the Au NPs taken at the end of the in-situ analysis. Spherical Au NPs with a mean diameter of 5.9 nm and a narrow size distribution were observed. UV-vis spectra recorded during the Au NPs formation shows the appearance of an absorbance maximum at the characteristic λ=530 nm (figure

1.16.b). SAXS scattering curves were also recorded during the Au NPs formation (figure 1.16.c). During the first 30 min, they have observed the evolution of the Guinier-plateau in the range 0.4 nm^{-1}-1.0 nm^{-1} and a strong decrease of the scattering intensity at high q. This demonstrates the formation of small Au NPs, with a radius below 1.5 nm. With time, they have observed the form factor oscillation at high q, with a shift of the knee, revealing the growth of monodisperse Au NPs. Thanks to *in situ* WAXS measurements, the crystalline nature of the Au NPs was determined as a function of time. Two main peaks corresponding to the (111) and (200) reflections of the Au *fcc* lattice were observed (figure 1.16.d). The increase of the (111) peak and the decrease of the full-width at half-maximum (FWHM) show that the crystallite size was increasing during the growth of the Au NPs.

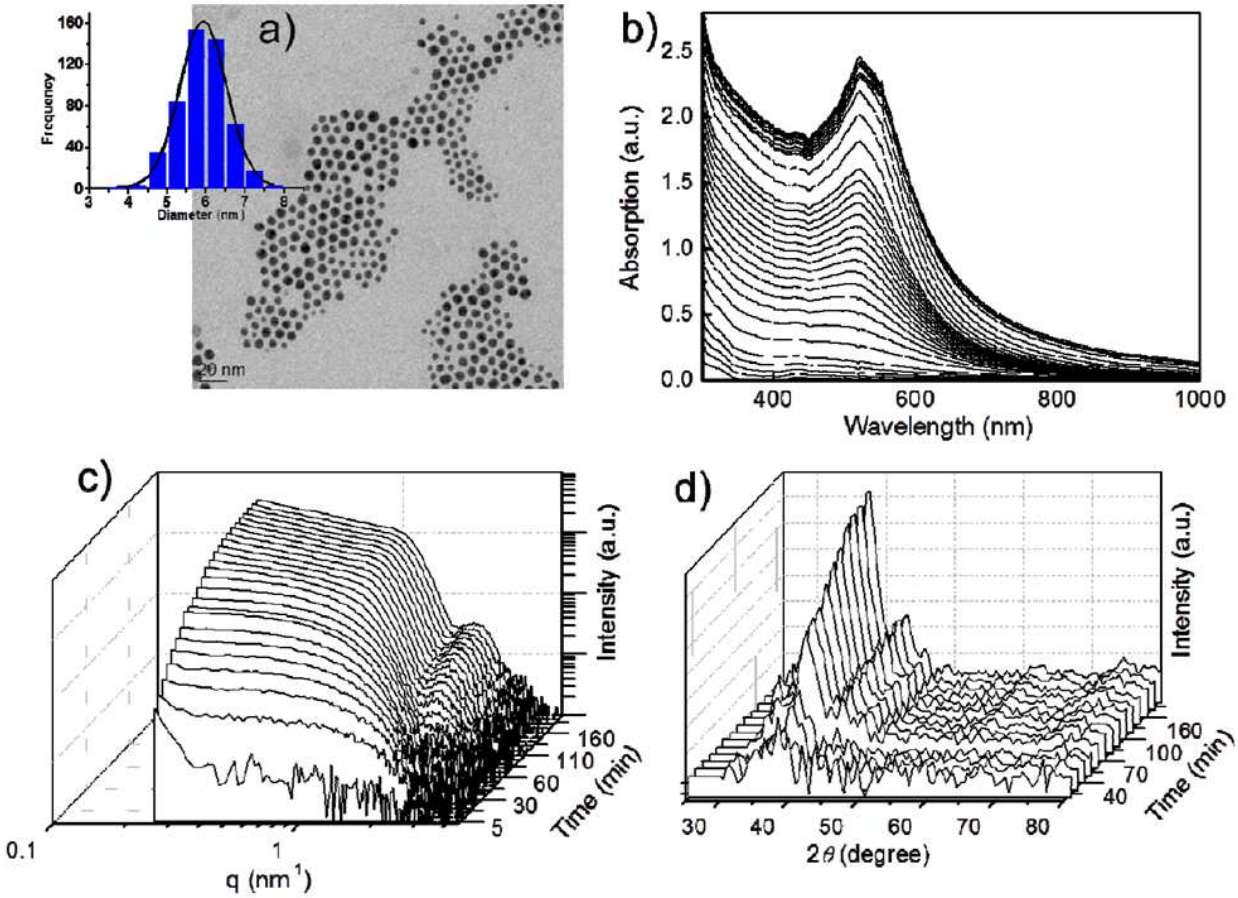

Figure 1.16 (a) TEM image of the Au NPs taken from in-situ measurement and the size distribution, (b) UV-Vis spectrum as a function of time, (c) Time resolved SAXS curves and (d) WAXS curve recorded during the crystallization of Au NPs by the reduction of gold (I) salt using t-butylamineborane (TBAB). Reprinted from the reference[60].

Chen et al[60]. concluded that their results can be explained by the classical nucleation and growth theory. They observed a rapid formation of small nuclei and subsequent slow growth until the completely consumption of the precursor. They have found that the precursor concentration, the temperature and the ligand concentration had an effect on the different steps of nucleation and growth of the Au NPs. The precursor reaction rate constant increased from 1.7 x 10^{-3} to 6.7 x 10^{-3} L/mol.s with and precursor concentration decreasing from 12.5 to 5 mM. But the growth rate constant didn't change. They have observed the temperature has strong effect on the kinetics and the final particle size. The reaction was then occurred faster at the higher temperature. They have observed an increase in reduction rate constant from 1.7 x 10^{-3} to 6.7 x 10^{-3} L/mol.s and strong change of the growth rate from 1.4 x 10^{-6} to 1.7 x 10^{-5} L/mol.s with increasing temperature from 295 to 318 K. When they have worked on the ligand effect, they have found that the growth is completed earlier at higher concentration with comparing to experiment at lower ligand concentration. In addition to that, the ligand concentration has an effect on the precursor reaction rate constant. It increased when the higher concentration of ligand was used. As observed for precursor concentration effect, the growth rate constant didn't change with the change in the ligand concentration.

1.7 Synthesis of Au nanoparticles using silane as reducing agent in presence of oleylamine

The objective of this section is to describe the state of the art on the synthesis of Au NPs in organic solvent using silane as reducing agent. The originality of the shape and atomic structure of the particles obtained by these methods will be presented and the role of the OY and the silane discussed. This section is based on the previous studies reported in the literature and in our group as well as on preliminary results I have obtained during my Master internship at LPCNO.

Silanes are a particular class of reducing agent that are not so often used for the synthesis of metal NPs, compared to sodium borohydride or amino borane. The general formula of the silanes is R_3SiH (Figure 1.17.a-b). These molecules are soluble in organic solvents. The silanes can be considered as hydrides so each silane can be oxidized and release 2 electrons and one proton to form the R_3Si^+ cation. It is however unlikely that such cation forms in organic solvents. It is more likely that the silane transforms into a silicon chloride R_3SiCl. The first step of the reduction can be seen as the exchange of the Si-H bond by a Si-Cl bond. The reduction of Au (III) into Au (0), which requires 3 electrons, must involve 1.5 eq. of R_3Si-H. The Cl in excess will lead to the formation of oleylammonium chloride, thus requiring 2.5 eq. of oleylamine as reagent.

The reduction can be written as:

$$HAuCl_4 + \frac{3}{2}R_3SiH + \frac{5}{2}C_{18}H_{35}NH_2 \rightarrow Au(0) + \frac{3}{2}R_3SiCl + \frac{5}{2}C_{18}H_{35}NH_3^+Cl^- \qquad \text{Eq. 1.8}$$

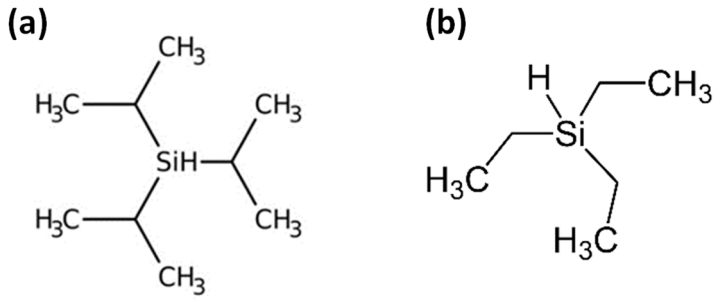

Figure 1.17: (a) Tri-isopropyl Silane (TIPS) and (b) Tri-ethyl Silane

The very first report of such reduction by Feng et al. consists in the reduction of $HAuCl_4.3H_2O$ by tri-isopropyl silane (TIPS) in hexane[61]. The reduction can be carried out at room temperature. This method is very simple and offers a great variety of shape by changing the reaction parameters such as the Au precursor concentration, the OY concentration or the solvent. As it will be described below one great interest of this method is that monodisperse particles can be produced using fairly high concentration of gold, typically 10 or 20 mM. Therefore, large amount of particles can be produced in a single batch and such large concentrations facilitate the *in-situ* studies, allowing to decrease the acquisition time.

1.7.1 Nanospheres and nanowires: influence of [OY] on the particle shape

Experimentally, the synthesis of Au nanoparticles with silanes consists in:

1) dissolving $HAuCl_4.3H_2O$ in hexane by the addition of OY and sonication;

2) mixing at room temperature the solution of Au (III) with a solution containing TIPS in hexane.

All the previous Au NPs syntheses using silanes were done with a very large excess of TIPS.[59] Indeed, 1M of TIPS was used, leading to a [TIPS]/[Au] = 50 well above the 1.5 stoichiometric ratio needed (Eq.1.8).

Several parameters were previously studied in the team to control the particle size and shape. The main parameter to tune the particle shape is the OY concentration. In the following I will present the syntheses of Au nanospheres and nanowires that have been obtained with two different [OY]/[Au] ratio. In both syntheses the gold concentration was 20 mM, the OY concentration was either 50 or 400 mM.

Nanospheres with [OY]/[Au] =2.5. The solubilization of $HAuCl_4.3H_2O$ in hexane by the addition of OY and sonication resulted in a pale yellow solution. Then the reducing agent solution was added quickly and induced a color change, which is characteristic of Au (0) formation, within only few seconds. The reaction was let undisturbed for 3h to ensure the complete reduction. The NPs finally obtained are presented in Figure 1.18a. Well dispersed spherical NPs with a mean diameter of 2 nm and with a ratio σ/d_m =11% were observed.

Nanowires with [OY]/[Au] =20. In presence of an excess of OY (400 mM), the dissolution of $HAuCl_4.3H_2O$ in hexane is easier and leads to a dark orange solution. The reduction once the TIPS solution is added is however much slower than for [OY] = 50 mM. The red color appears after only about 3 hours. The reaction is pursued for 24 h and yield ultrathin Au NWs with a diameter of 2 nm and a length of several micrometers (Figure 1.18b). The diameter of the wires is very monodisperse with a ratio σ/d_m= 11%. The length distribution is however very difficult to estimate from the TEM images because generally the wires are not seen entirely on the images.

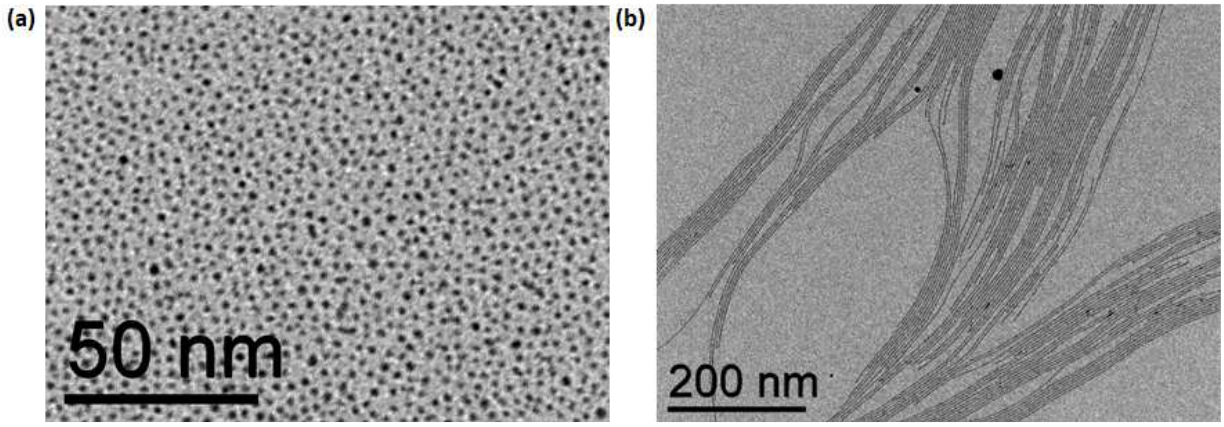

Figure 1.18: TEM images of nanospheres and nanowires prepared with [OY] of (a) 50 mM and b) 400 mM.

In both cases the reduction by silane leads to ultrasmall nanoparticle with a well-defined shape. The obtained solutions are stable, no coalescence was observed neither on the NPs nor on the NWs despite the high concentration of gold.

1.7.2 Atomic structure

The structure of the particles was analyzed by X-ray Diffraction (XRD). In the figure 1.19 are shown the *ex situ* XRD patterns of the final nanoparticles and nanowires prepared by the reduction of $HAuCl_4.3H_2O$ with a large excess of TIPS in presence of [OY] = 50 mM and 400 mM, respectively. Several drops of the colloidal suspensions were deposited on a zero-background Si substrate and the solvent was evaporated in air. For both type of Au nano objects, the XRD patterns exhibited very broad bands in agreement with the very small diameter of the particles.

The dashed lines in the figure 1.19 indicates the different reflections expected for the *fcc* structure of bulk Au. In both cases, the structure differs from the bulk. For the nanowires, the main peak is very asymmetric and the (200) line is absent. For the nanospheres, prepared with the ratio [OY]/[Au] = 2.5, the main peak is shifted to high angle compared to the (111) reflection and the (200) peak is also absent. A shoulder at higher angles, around 58 °, can be seen but it does not match with any reflection of the *fcc* Au.

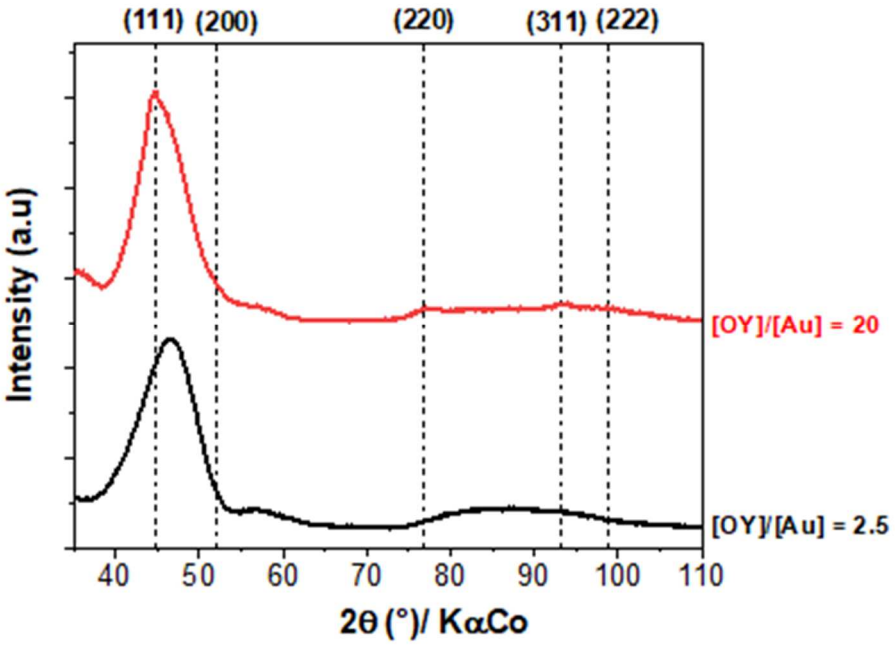

Figure 1.19: *Ex situ* XRD patterns of final nanoparticles prepared with different OY concentrations. In black: [OY]/[Au] = 2.5, in red: [OY]/[Au] = 20 recorded after a reaction of 3h and 24h, respectively.

High-energy X-Ray diffraction (HE-XRD) using synchrotron radiation and pair distribution function (PDF) analysis were performed to have a better understanding on the crystalline structure of Au NPs prepared with TIPS [62].

The experimental PDFs are given on Figure 1.20 along with the best fits using atomic models. The first neighbor Au-Au pair distance is obtained at around 2.86 Å, which is slightly smaller than the Au-Au bonding distance in bulk Au (2.88 Å) and can be related to the small particle size. The PDF of the nanospheres prepared with [OY] = 50 mM, is well fitted using a model of distorted icosahedra.

The nanowires displayed a tetrahedrally close packed structure close to the α-Mn structure. This structure is very original since the Au lattice does not present any octahedral sites but only tetrahedral ones hence the name of tetrahedrally close packed structure. This can be seen on the PDF by the absence of Au-Au neighbors at the distance of 4.08 Å which is the distance of the octahedral sites. The Au coordination polyhedra integrate distorted icosahedra and larger size coordination polyhedra, as reported in the previous work dedicated to the structural study of the ultrathin nanowires prepared with silanes[62].

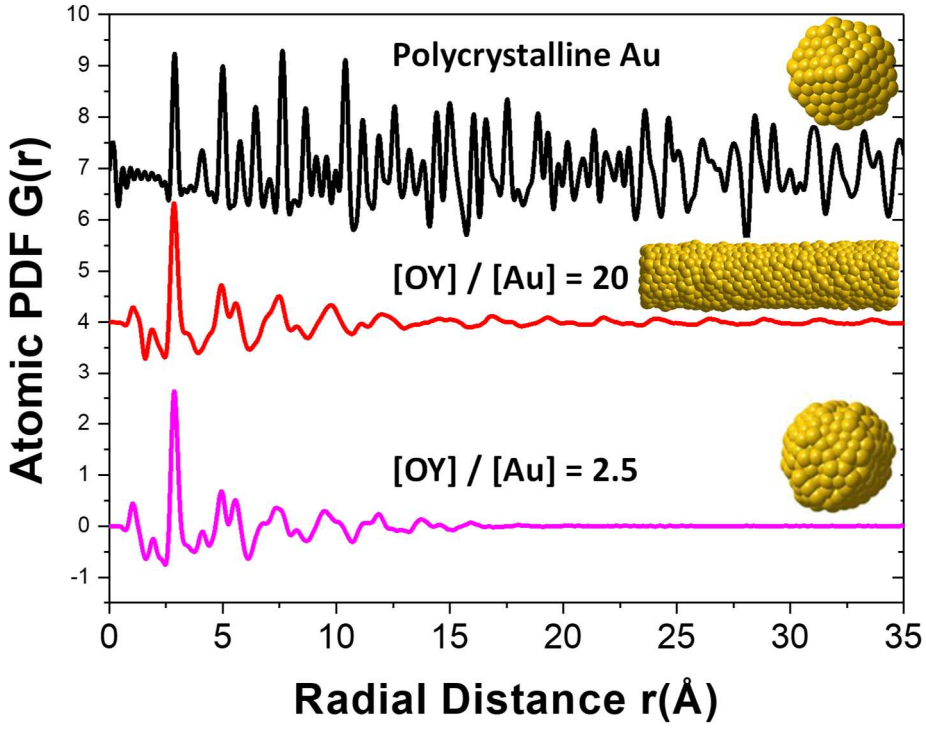

Figure 1.20: *In situ* atomic pair distribution function of Au nanoparticles prepared with different [OY]/[Au] ratios and best fits to the experimental curves: distorted icosahedron for [OY] / [Au] =2.5 and wire with α-Mn-type crystal structure. Reprinted from the reference[62].

1.7.3 Surface chemistry

X-ray Photoelectron Spectroscopy (XPS) measurements provide the value of the binding energy and relative atomic percentage of the different elements present at the surface of the samples.

XPS experiments were performed on Au nanospheres and nanowires[63] deposited on a Si substrate. The final gold suspensions were concentrated in ethanol by centrifugation (5000 rpm, 5min) and redispersed in small volume of hexane before deposition on the substrate.

On the survey scans the following binding energies were detected: Si_{2p}, O_{1s}, N_{1s}, C_{1s}, Cl_{2p} and Au_{4f}. Si and O elements are coming from the silicon substrate.

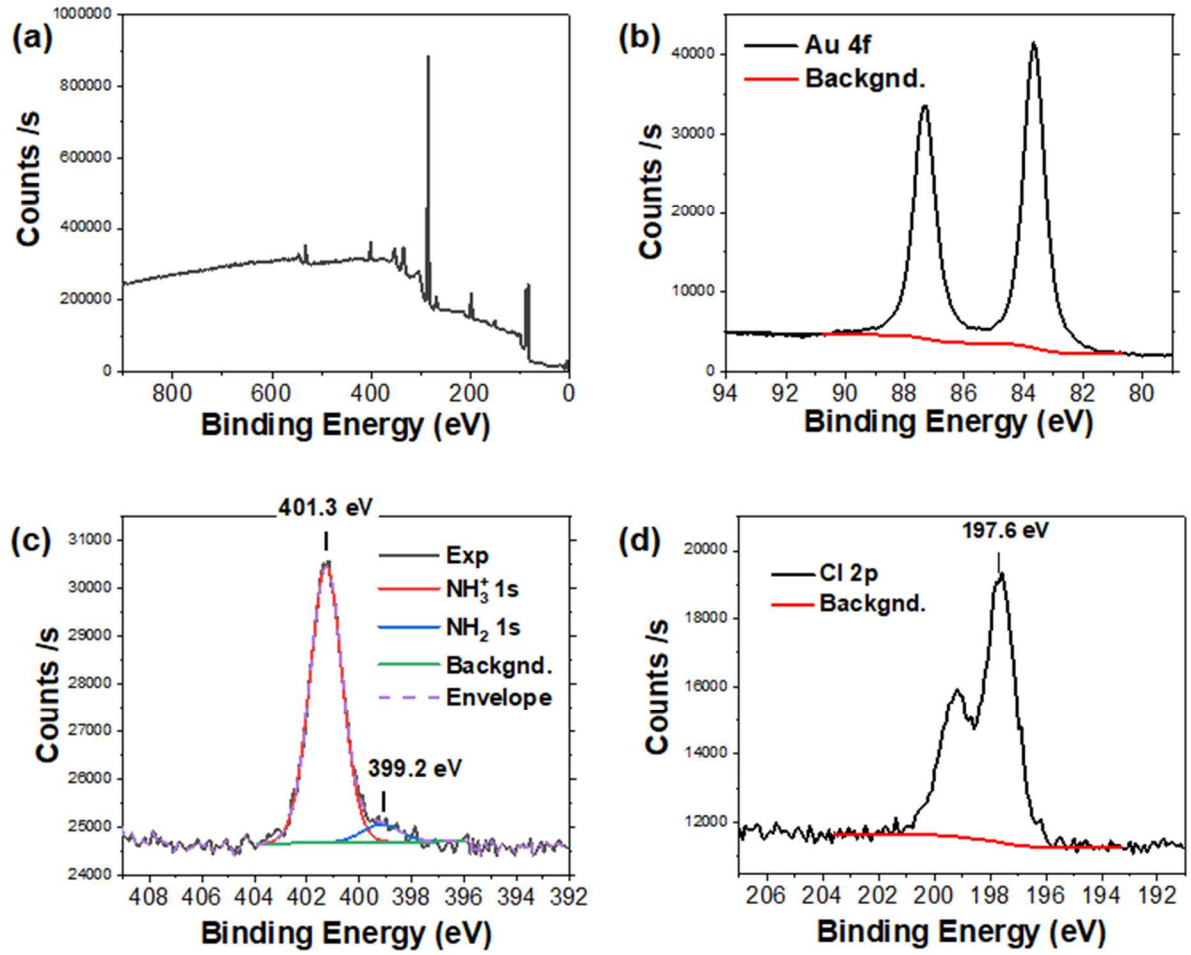

Figure 1.21 High resolution XPS spectra of Au nanoparticles prepared with [OY]/[Au]= 2.5: (a) survey scan, (b) Au 4f peak, (c) N 1s peak and (d) Cl 2p peak. Reprinted from the reference[64].

For the Au nanospheres the binding energy Au $4f_{7/2}$ was found in the range 83.3 – 83.9 eV which corresponds to Au in zero valent state, Au^0, according to the NIST database[65]. No oxidation of gold atoms at the surface was detected (figure 1.21.b). The binding energy C 1s was found at 285 eV. This energy corresponds to $–CH_2–$ groups coming from the oleylamine carbon chain. In figure 1.21.c is given the N1s binding energy region. Two peaks were identified: the main one at 401.3 eV and a minor peak at 399.2 eV, corresponding to oleylammonium (RNH_3^+) and oleylamine (RNH_2) groups, respectively. The relative amount of ammonium /amine was calculated from the surface area of each peak. A ratio = 93/7 was found, showing the very large excess of ammonium at the vicinity of NSs. Cl 2p binding energy was found in the range 197.65 – 197.73 eV which corresponds to chloride ions, Cl^- (figure 1.21.d). The ratio NH_3^+/Cl^- is equal to 1, evidencing that oleylammonium chloride is present at the NP surface. The ratio C/N_{total} is 20, so very close to 18 the value expected for oleylamine or oleylammonium ($OY=C_{18}H_{37}N$).

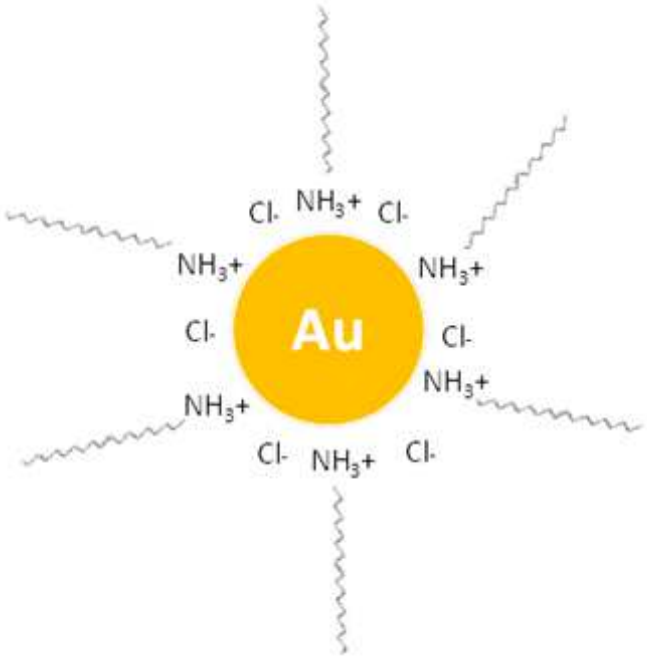

Figure 1.22 Schematic representation of the ligand shell of oleylammonium chloride monolayer on the surface of the nanospheres prepared with the ratio [OY]/[Au] = 2.5

These results are in very good agreement with the Eq. 1.8. In presence of a stoichiometric ratio [OY]/[Au] = 2.5 used for the preparation of the nanospheres, OY should be totally converted into oleylammonium chloride (OY^+Cl^-). The NSs surface is thus stabilized by oleylammonium chloride (OY^+Cl^-), as depicted in figure 1.22.

For the Au nanowires, the major peaks on the survey scan of XPS were found as Au 4f, C 1s, N 1s, and Cl 2p at 84, 285, 400, and 198 eV, respectively. The Au high-resolution spectra were fitted well with the Au (0) peaks. The peaks of N were found at 399 and 401 eV corresponding to N 1s of nitrogen atoms in the OY and OY^+Cl^-, respectively. The ratio NH_3^+/Cl^- was found very close to 1 indicating again the formation of (OY^+Cl^-). Differently from the Au nanospheres, the ratio N(OY)/N(OY^+) was calculated close to 1, showing that the surface of the Au NWs is capped by a mixture of oleylamine and oleylammonium chloride.

1.7.4 Evidence of a bilayer of ligand around the nanowires

The gold nanowires prepared with TIPS in hexane were characterized by *ex situ* x-ray diffraction at small angles with a standard diffractometer in order to examine their organization as a powder. One drop of the NW suspension was dried on the zero background Si substrate and characterized for 2θ varying in the range 1-10 °. Bragg peaks were observed (Figure 1.23) showing the organization of the nanowires into a hexagonal superlattice as previously reported[63].

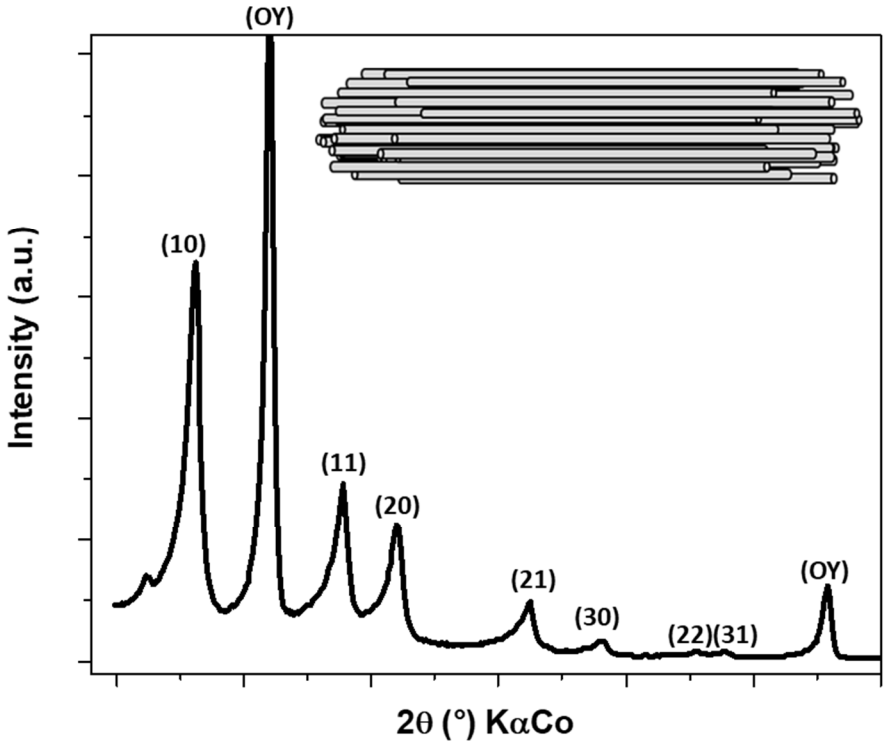

Figure 1.23 SAXS data of the hexagonal phase of nanowires

The gold nanowires tend to align parallel to each other, along the c axis of an hexagonal superlattice. As the NWs are “infinite”, the unit cell is bidimensional. The lattice planes are therefore defined only by two miller indices, h and k. For such 2D hexagonal array the interplanar spacing d_{hk} is given by the formula:

$$d_{hk} = \frac{a}{\sqrt{\frac{4(h^2+k^2+hk)}{3}}} \qquad \text{Eq.1.9}$$

with *a* the parameter of the hexagonal phase, corresponding to the distance between the wire (center to center) shown in figure 1.24.

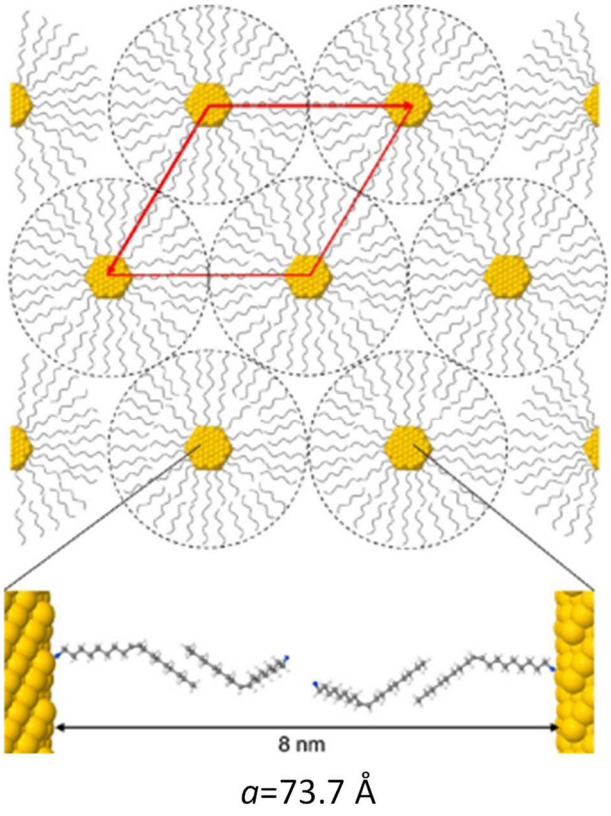

Figure 1.24 Schematic representation of the ligand shell of the Au NWs prepared with the ratio [OY]/[Au] = 20: oleylammonium chloride + oleylamine bilayer on the surface of the nanowires. Reprinted from the reference[63].

In the case of a 2D hexagonal lattice, according to Eq. 1.9, the ratio $(d_{10}/d_{hk})^2$ follow the sequence 1, 3, 4, 7, 9, 12, 13. In the table 1.1 we have compared experimental and theoretical ratios. The agreement is very good showing that all the peaks can be indexed as d_{hk} reflection of the hexagonal phase. The parameter *a* of the hexagonal phase was deduced from this indexation, an average value of 73.7 Å being found, in agreement with previous work[66].

Two additional peaks were observed, corresponding to pure oleylamine. The colloidal suspension of nanowires containing a large excess of OY ([OY]/[Au] =20 while 2.5 are needed), OY crystallizes beside the hexagonal phase of nanowires during the solvent evaporation.

Ratio of interplanar spacing	**theoretical**	**experimental**	**a (Å)**
$\mathbf{(d_{10}/d_{10})^2}$	1	1	73.0
$\mathbf{(d_{10}/d_{11})^2}$	3	2,9	73.7
$\mathbf{(d_{10}/d_{20})^2}$	4	3,9	73.8
$\mathbf{(d_{10}/d_{21})^2}$	7	6,8	73.9
$\mathbf{(d_{10}/d_{30})^2}$	9	8,8	73.8
$\mathbf{(d_{10}/d_{22})^2}$	12	11,7	73.8
$\mathbf{(d_{10}/d_{31})^2}$	13	12,6	74.0

Table 1.1. Interplanar spacing in theoretical and experimental

The gold nanowires prepared with TIPS in hexane were characterized by *in situ* SAXS. The gold nanowires were synthesized and after 24 h introduced in the capillary. With time, the nanowires self-assemble in suspension to form bundles crystallizing with a hexagonal structure.

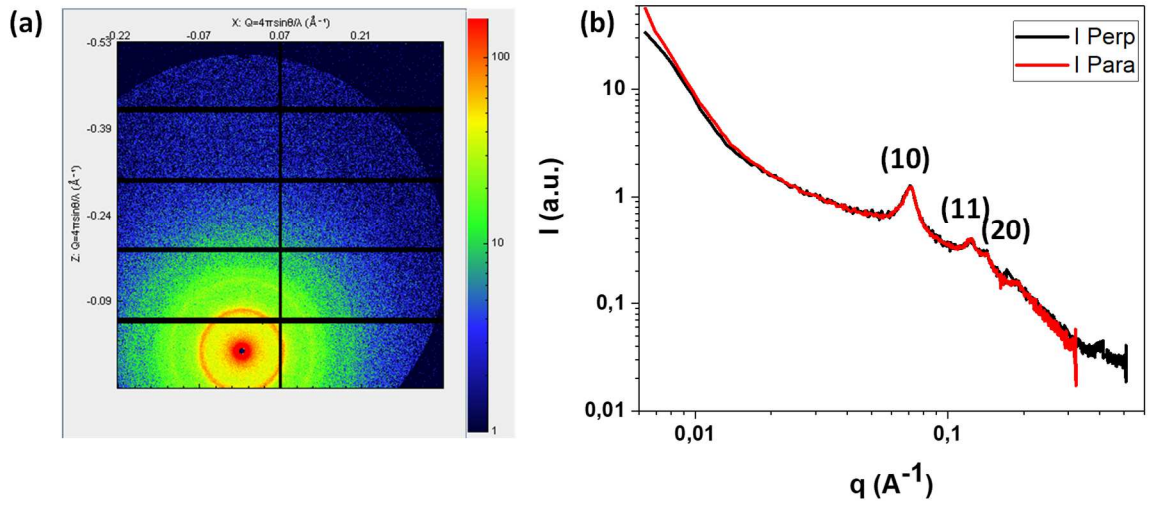

Figure 1.25: Isotropic SAXS of bundles of nanowires with hexagonal structure and the corresponding (a) 2D SAXS image; (b) I(q) for ψ = 0° (intensity along X) and ψ = 90° (intensity along Z)

In figure 1.25, 2D image and SAXS pattern were shown, respectively. The SAXS patterns of the suspensions exhibit Bragg peaks that can be indexed as an hexagonal phase according to the relative position of the 3 first peaks. In this case the peaks of OY were not observed because the suspension was not dried. The main difference of the hexagonal phase characterized *in situ* compared to the ex situ is the value of the parameter a. The value measured *in situ* was 10.2 Å which is significantly longer than the value measured ex situ. As the mean diameter of the wires is well estimated from the TEM images it is possible to calculate the spacing between the wires by subtracting the diameter to the parameter a. The distance (edge to edge) between the wire was then 54 Å in the dried state and 82 Å in suspensions. These distances are very long compared to the length of the oleylamine chain which is around 21 Å. The previous studies conclude then that a monolayer of OY around each wire cannot account for these very large distances. Otherwise, the distance maximum would be 42 Å. It has been concluded[63] that a bilayer of OY and OY^+Cl^- surrounded the wires; *in situ* the distance of 80 Å is well explained by such a bilayer. The distance measured ex situ is shorter because the bundles are dried and the OY chains are probably folded. The evidence of such a bilayer is very important for the understanding of the anisotropic growth. A reason for the anisotropic growth could be due to the formation of cylindrical micelles when the OY concentration is high enough.

1.7.5 The multiple roles of OY

The previous studies dealing with the synthesis of Au nanoparticles with silanes as reducing agent in organic solution containing OY have shown that the role of OY is much more complex than only a stabilizing agent.

First of all, as mentioned OY is necessary to dissolve $HAuCl_4.3\ H_2O$ in non-polar solvent like hexane. The formation of an ion pair $OY^+AuCl_4^-$ could be an explanation for the solubilization. However, as mentioned above (see section 1.7.1) the color of the solution is very dependent on the molar ratio [OY]/[Au]. The solution is yellow for a ratio of 2.5 and orange for a ratio of 20. This difference is certainly due to a change of the Au (III) coordination sphere with the presence of OY as ligand when the concentration is high enough. To the best of our knowledge no spectroscopic study has been done on this topic.

As primary amine, the second role of OY is the role of base. It has been described above that when OY is added in the medium in the stoichiometry of Eq. 1.8, it was totally converted into OY^+Cl^-. As a consequence, the role of OY as stabilizing agent is seriously questioned. In the case of the nanospheres prepared with 2.5 eq. of OY with respect to Au, OY cannot play the role of stabilizing agent of the final particles since it has disappeared of the medium. Even in the case of the nanowires, the presence of a mixture of OY^+Cl^- and OY, as evidenced by XPS, makes possible that the species at the surface of the wires could be the oleylammonium chloride. This hypothesis was reinforced by the nanoxerography experiments performed by Moutet et al[67]. on a suspension of purified Au NWs. The directed and selective assembly onto positive charged patterns revealed that the nanowires' surfaces were negatively charged.

Finally, the most spectacular role of OY in these syntheses is that above a given concentration, it favors growth of ultrathin nanowires. OY (or the mixture OY and OY^+Cl^-) has very likely a role in the structuration of the medium favoring the 1D growth of the Au particles, as previously proposed by Loubat et al[68]..

1.7.6 Kinetic studies on the nanowire's nucleation and growth

Thanks to a collaboration with Marianne Imperor and Brigitte Pansu, in situ SAXS studies were performed by the group during the synthesis of nanowires[63]. At that time, the reactions were performed with [Au] = 10 mM and the temperature was set at 40°C to fasten the reaction kinetic. The

evolution of the scattering curves with time is shown in figure 1.26. Ex-situ TEM was also performed. The SAXS patterns were analyzed using the form factors of two contributions as observed on the TEM images: a) polydisperse spheres and b) nanowires. Best fitting was obtained by adjusting several tunable parameters like the diameter, the polydispersity and the volume fraction of gold nanospheres and nanowires.

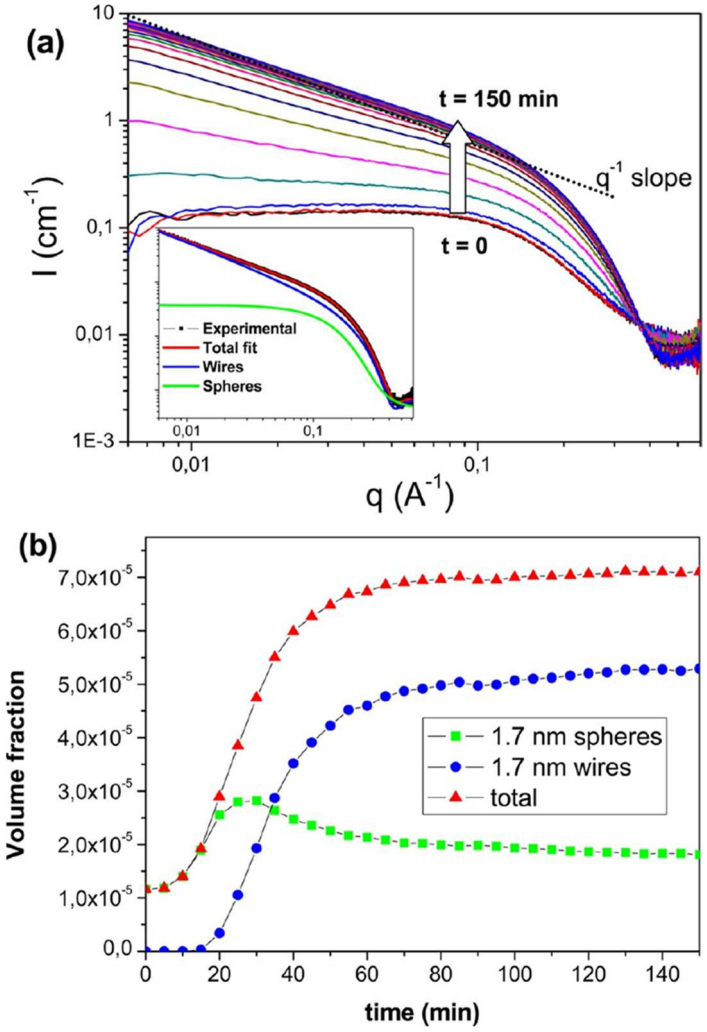

Figure 1.26: (a) SAXS pattern; (b) Volume fraction deduced from the SAXS modelling as a function of time. Reprinted from the reference[63].

At t=0, polydisperse (>30%) spheres with a diameter of 1.7 nm were observed. Until 80 min, an increase of the intensity was detected. At this point, the scattering profile was following a q^{-1} law (Figure 1.26.a) which is the signature of nanowires. Fairly monodisperse (2% distribution) nanowires with a diameter

of 1.7 nm and length of 100 nm were observed. In Figure 1.26.b, the evolution of the volume fraction of the spheres and nanowires as a function of time was plotted. While NSs are observed very rapidly, NWs were only observed after 20 min. At t=30 min, the volume fraction of the spheres reached a maximum and the NW growth rate was the fastest. The volume fraction of spheres and nanowires reached a plateau after 80 min, corresponding to volume fractions of 1.8×10^{-5} and 5.3×10^{-5}, respectively. The total volume fraction of 7.1×10^{-5} was in agreement with the expected value for the 10 mM solution, thus revealing a complete consumption of the Au atoms introduced in the reaction.

In absence of any spectroscopic studies, the results presented in 2015 by Loubat et al. were fairly convincing. A relative ratio of Au nanowires of 73% was determined while a complete reduction was supposed. In the following chapters, these interpretations will be questioned. For instance, we have recently attributed the signal observed at short times not to Au nanosphere but rather to pre-nucleation clusters (PNCs).

1.8 Conclusion

In conclusion, the synthesis of Au nanoparticles using tri isopropyl silane in non-polar solvents containing OY is very simple to carry out and has already proven its interest to synthesize ultrasmall nanoparticles with a narrow size distribution. One originality of these syntheses is the unusual atomic structure of the particles, very different for the *fcc* structure of the bulk.

While several aspects regarding the formation of the particles and the actual role of OY in the shaping of the particles have been already studied, some points on the nucleation and growth mechanism deserve to be addressed in more detail. The growth of the nanowires has solely been studied by *in situ* SAXS.[63,69] Following the synthesis of the small nanospheres prepared with [OY] = 50 mM with complementary techniques such as *in situ* X-ray absorption spectroscopy (XAS) *or in situ* X-ray diffraction (XRD) could give additional information about the different chemical steps of the reaction and the crystallization of the gold particles.

From an experimental point of view, the high concentration of Au used will facilitate the *in situ* studies, the sensitivity of the different techniques being not a limitation. However, the reaction is very fast in the case of the nanosphere: the characteristic color change is observed after only few seconds. Thus, to study properly *in situ* the crystallization of the nanospheres, a special microfluidic setup with fast mixing is required. In the next chapter, the conception and realization of such home-made microfluidic setup will be explained.

Bibliography

(1) Cabuzu, D.; Cirja, A.; Puiu, R.; Grumezescu, A. M. Biomedical Applications of Gold Nanoparticles. *Curr. Top. Med. Chem.* **2015**, *15* (16), 1605–1613. https://doi.org/10.2174/1568026615666150414144750.

(2) Dadosh, T.; Gordin, Y.; Krahne, R.; Khivrich, I.; Mahalu, D.; Frydman, V.; Sperling, J.; Yacoby, A.; Bar-Joseph, I. Measurement of the Conductance of Single Conjugated Molecules. *Nature* **2005**, *436* (7051), 677–680.

(3) Tseng, R. J.; Huang, J.; Ouyang, J.; Kaner, R. B.; Yang, Y. Polyaniline Nanofiber/Gold Nanoparticle Nonvolatile Memory. *Nano Lett.* **2005**, *5* (6), 1077–1080. https://doi.org/10.1021/nl050587l.

(4) Suchomel, P.; Kvitek, L.; Prucek, R.; Panacek, A.; Halder, A.; Vajda, S.; Zboril, R. Simple Size-Controlled Synthesis of Au Nanoparticles and Their Size-Dependent Catalytic Activity. *Sci. Rep.* **2018**, *8* (1), 4589. https://doi.org/10.1038/s41598-018-22976-5.

(5) Hasobe, T.; Imahori, H.; Kamat, P. V.; Ahn, T. K.; Kim, S. K.; Kim, D.; Fujimoto, A.; Hirakawa, T.; Fukuzumi, S. Photovoltaic Cells Using Composite Nanoclusters of Porphyrins and Fullerenes with Gold Nanoparticles. *J. Am. Chem. Soc.* **2005**, *127* (4), 1216–1228. https://doi.org/10.1021/ja047768u.

(6) Leff, D. V.; Brandt, L.; Heath, J. R. Synthesis and Characterization of Hydrophobic, Organically-Soluble Gold Nanocrystals Functionalized with Primary Amines. *Langmuir* **1996**, *12* (20), 4723–4730. https://doi.org/10.1021/la960445u.

(7) Kameo, A.; Suzuki, A.; Torigoe, K.; Esumi, K. Fiber-like Gold Particles Prepared in Cationic Micelles by UV Irradiation: Effect of Alkyl Chain Length of Cationic Surfactant on Particle Size. *J. Colloid Interface Sci.* **2001**, *241* (1), 289–292. https://doi.org/10.1006/jcis.2001.7706.

(8) Ayyappan, S.; Gopalan, R. S.; Subbanna, G. N.; Rao, C. N. R. Nanoparticles of Ag, Au, Pd, and Cu Produced by Alcohol Reduction of the Salts. *J. Mater. Res.* **1997**, *12* (2), 398–401. https://doi.org/10.1557/JMR.1997.0057.

(9) Hoppe, C. E.; Lazzari, M.; Pardiñas-Blanco, I.; López-Quintela, M. A. One-Step Synthesis of Gold and Silver Hydrosols Using Poly(N-Vinyl-2-Pyrrolidone) as a Reducing Agent. *Langmuir ACS J. Surf. Colloids* **2006**, *22* (16), 7027–7034. https://doi.org/10.1021/la060885d.

(10) Mukherjee, P.; Ahmad, A.; Mandal, D.; Senapati, S.; Sainkar, S. R.; Khan, M. I.; Parishcha, R.; Ajaykumar, P. V.; Alam, M.; Kumar, R.; Sastry, M. Fungus-Mediated Synthesis of Silver Nanoparticles and Their Immobilization in the Mycelial Matrix: A Novel Biological Approach to Nanoparticle Synthesis. *Nano Lett.* **2001**, *1* (10), 515–519. https://doi.org/10.1021/nl0155274.

(11) Brust, M.; Walker, M.; Bethell, D.; Schiffrin, D. J.; Whyman, R. Synthesis of Thiol-Derivatised Gold Nanoparticles in a Two-Phase Liquid–Liquid System. *J. Chem. Soc. Chem. Commun.* **1994**, No. 7, 801–802. https://doi.org/10.1039/C39940000801.

(12) Corbierre, M. K.; Cameron, N. S.; Sutton, M.; Mochrie, S. G.; Lurio, L. B.; Rühm, A.; Lennox, R. B. Polymer-Stabilized Gold Nanoparticles and Their Incorporation into Polymer Matrices. *J. Am. Chem. Soc.* **2001**, *123* (42), 10411–10412. https://doi.org/10.1021/ja0166287.

(13) Habibullah, G.; Viktorova, J.; Ruml, T. Current Strategies for Noble Metal Nanoparticle Synthesis. *Nanoscale Res. Lett.* **2021**, *16* (1), 47. https://doi.org/10.1186/s11671-021-03480-8.

(14) *Green Synthesis of Gold Nanoparticles (AuNPs) from Plants*. https://encyclopedia.pub/entry/15584 (accessed 2022-11-26).

(15) Kimling, J.; Maier, M.; Okenve, B.; Kotaidis, V.; Ballot, H.; Plech, A. Turkevich Method for Gold Nanoparticle Synthesis Revisited. *J. Phys. Chem. B* **2006**, *110* (32), 15700–15707. https://doi.org/10.1021/jp061667w.

(16) Grzelczak, M.; Pérez-Juste, J.; Mulvaney, P.; Liz-Marzán, L. M. Shape Control in Gold Nanoparticle Synthesis. *Chem. Soc. Rev.* **2008**, *37* (9), 1783–1791. https://doi.org/10.1039/B711490G.

(17) Sardar, R.; Shumaker-Parry, J. S. Spectroscopic and Microscopic Investigation of Gold Nanoparticle Formation: Ligand and Temperature Effects on Rate and Particle Size. *J. Am. Chem. Soc.* **2011**, *133* (21), 8179–8190. https://doi.org/10.1021/ja107934h.

(18) Hussain, I.; Graham, S.; Wang, Z.; Tan, B.; Sherrington, D. C.; Rannard, S. P.; Cooper, A. I.; Brust, M. Size-Controlled Synthesis of near-Monodisperse Gold Nanoparticles in the 1-4 Nm Range Using Polymeric Stabilizers. *J. Am. Chem. Soc.* **2005**, *127* (47), 16398–16399. https://doi.org/10.1021/ja055321v.

(19) Jana, N. R.; Gearheart, L.; Murphy, C. J. Seeding Growth for Size Control of 5−40 Nm Diameter Gold Nanoparticles. *Langmuir* **2001**, *17* (22), 6782–6786. https://doi.org/10.1021/la0104323.

(20) Daniel, M.-C.; Astruc, D. Gold Nanoparticles: Assembly, Supramolecular Chemistry, Quantum-Size-Related Properties, and Applications toward Biology, Catalysis, and Nanotechnology. *Chem. Rev.* **2004**, *104* (1), 293–346. https://doi.org/10.1021/cr030698+.

(21) Wilton-Ely, J. D. E. T. The Surface Functionalisation of Gold Nanoparticles with Metal Complexes. *Dalton Trans.* **2007**, No. 1, 25–29. https://doi.org/10.1039/B714144K.

(22) Roux, S.; Garcia, B.; Bridot, J.-L.; Salomé, M.; Marquette, C.; Lemelle, L.; Gillet, P.; Blum, L.; Perriat, P.; Tillement, O. Synthesis, Characterization of Dihydrolipoic Acid Capped Gold Nanoparticles, and Functionalization by the Electroluminescent Luminol. *Langmuir ACS J. Surf. Colloids* **2005**, *21* (6), 2526–2536. https://doi.org/10.1021/la048082i.

(23) Ackerson, C. J.; Jadzinsky, P. D.; Kornberg, R. D. Thiolate Ligands for Synthesis of Water-Soluble Gold Clusters. *J. Am. Chem. Soc.* **2005**, *127* (18), 6550–6551. https://doi.org/10.1021/ja046114i.

(24) Turkevich, J.; Stevenson, P. C.; Hillier, J. A Study of the Nucleation and Growth Processes in the Synthesis of Colloidal Gold. *Discuss. Faraday Soc.* **1951**, *11* (0), 55–75. https://doi.org/10.1039/DF9511100055.

(25) Frens, G. Controlled Nucleation for the Regulation of the Particle Size in Monodisperse Gold Suspensions. *Nat. Phys. Sci.* **1973**, *241* (105), 20–22. https://doi.org/10.1038/physci241020a0.

(26) Aslan, K.; Pérez-Luna, V. H. Quenched Emission of Fluorescence by Ligand Functionalized Gold Nanoparticles. *J. Fluoresc.* **2004**, *14* (4), 401–405. https://doi.org/10.1023/B:JOFL.0000031821.74706.ea.

(27) Abad, J. M.; Mertens, S. F. L.; Pita, M.; Fernández, V. M.; Schiffrin, D. J. Functionalization of Thioctic Acid-Capped Gold Nanoparticles for Specific Immobilization of Histidine-Tagged Proteins. *J. Am. Chem. Soc.* **2005**, *127* (15), 5689–5694. https://doi.org/10.1021/ja042717i.

(28) Templeton, A. C.; Hostetler, M. J.; Warmoth, E. K.; Chen, S.; Hartshorn, C. M.; Krishnamurthy, V. M.; Forbes, M. D. E.; Murray, R. W. Gateway Reactions to Diverse, Polyfunctional Monolayer-Protected Gold Clusters. *J. Am. Chem. Soc.* **1998**, *120* (19), 4845–4849. https://doi.org/10.1021/ja980177h.

(29) Love, J. C.; Estroff, L. A.; Kriebel, J. K.; Nuzzo, R. G.; Whitesides, G. M. Self-Assembled Monolayers of Thiolates on Metals as a Form of Nanotechnology. *Chem. Rev.* **2005**, *105* (4), 1103–1169. https://doi.org/10.1021/cr0300789.

(30) Amina, S. J.; Guo, B. A Review on the Synthesis and Functionalization of Gold Nanoparticles as a Drug Delivery Vehicle. *Int. J. Nanomedicine* **2020**, *15*, 9823–9857. https://doi.org/10.2147/IJN.S279094.

(31) Piella, J.; Bastús, N. G.; Puntes, V. Size-Controlled Synthesis of Sub-10-Nanometer Citrate-Stabilized Gold Nanoparticles and Related Optical Properties. *Chem. Mater.* **2016**, *28* (4), 1066–1075. https://doi.org/10.1021/acs.chemmater.5b04406.

(32) Carbó-Argibay, E.; Rodríguez-González, B. Controlled Growth of Colloidal Gold Nanoparticles: Single-Crystalline versus Multiply-Twinned Particles. *Isr. J. Chem.* **2016**, *56* (4), 214–226. https://doi.org/10.1002/ijch.201500032.

(33) Niu, J.; Zhu, T.; Liu, Z. One-Step Seed-Mediated Growth of 30–150 Nm Quasispherical Gold Nanoparticles with 2-Mercaptosuccinic Acid as a New Reducing Agent. *Nanotechnology* **2007**, *18* (32), 325607. https://doi.org/10.1088/0957-4484/18/32/325607.

(34) Hinman, J. G.; Stork, A. J.; Varnell, J. A.; Gewirth, A. A.; Murphy, C. J. Seed Mediated Growth of Gold Nanorods: Towards Nanorod Matryoshkas. *Faraday Discuss.* **2016**, *191* (0), 9–33. https://doi.org/10.1039/C6FD00145A.

(35) Ruditskiy, A.; Peng, H.-C.; Xia, Y. Shape-Controlled Metal Nanocrystals for Heterogeneous Catalysis. *Annu. Rev. Chem. Biomol. Eng.* **2016**, *7* (1), 327–348. https://doi.org/10.1146/annurev-chembioeng-080615-034503.

(36) Gilroy, K. D.; Peng, H.-C.; Yang, X.; Ruditskiy, A.; Xia, Y. Symmetry Breaking during Nanocrystal Growth. *Chem. Commun.* **2017**, *53* (33), 4530–4541. https://doi.org/10.1039/C7CC01121K.

(37) Baletto, F.; Ferrando, R. Structural Properties of Nanoclusters: Energetic, Thermodynamic, and Kinetic Effects. *Rev. Mod. Phys.* **2005**, *77* (1), 371–423. https://doi.org/10.1103/RevModPhys.77.371.

(38) Wu, J.; Qi, L.; You, H.; Gross, A.; Li, J.; Yang, H. Icosahedral Platinum Alloy Nanocrystals with Enhanced Electrocatalytic Activities. *J. Am. Chem. Soc.* **2012**, *134* (29), 11880–11883. https://doi.org/10.1021/ja303950v.

(39) Lv, T.; Wang, Y.; Choi, S.-I.; Chi, M.; Tao, J.; Pan, L.; Huang, C. Z.; Zhu, Y.; Xia, Y. Controlled Synthesis of Nanosized Palladium Icosahedra and Their Catalytic Activity towards Formic-Acid Oxidation. *ChemSusChem* **2013**, *6* (10), 1923.

(40) Kelly, K. L.; Coronado, E.; Zhao, L. L.; Schatz, G. C. The Optical Properties of Metal Nanoparticles: The Influence of Size, Shape, and Dielectric Environment. *J. Phys. Chem. B* **2003**, *107* (3), 668–677. https://doi.org/10.1021/jp026731y.

(41) Barnard, A. S.; Young, N. P.; Kirkland, A. I.; van Huis, M. A.; Xu, H. Nanogold: A Quantitative Phase Map. *ACS Nano* **2009**, *3* (6), 1431–1436. https://doi.org/10.1021/nn900220k.

(42) González, A. L.; Noguez, C.; Barnard, A. S. Map of the Structural and Optical Properties of Gold Nanoparticles at Thermal Equilibrium. *J. Phys. Chem. C* **2012**, *116* (26), 14170–14175. https://doi.org/10.1021/jp3047906.

(43) Baletto, F.; Mottet, C.; Ferrando, R. Microscopic Mechanisms of the Growth of Metastable Silver Icosahedra. *Phys. Rev. B* **2001**, *63* (15), 155408. https://doi.org/10.1103/PhysRevB.63.155408.

(44) Baletto, F.; Ferrando, R.; Fortunelli, A.; Montalenti, F.; Mottet, C. Crossover among Structural Motifs in Transition and Noble-Metal Clusters. *J. Chem. Phys.* **2002**, *116* (9), 3856–3863. https://doi.org/10.1063/1.1448484.

(45) Lu, X.; Tuan, H.-Y.; Korgel, B. A.; Xia, Y. Facile Synthesis of Gold Nanoparticles with Narrow Size Distribution by Using AuCl or AuBr as the Precursor. *Chem. – Eur. J.* **2008**, *14* (5), 1584–1591. https://doi.org/10.1002/chem.200701570.

(46) Zhang, Q.; Xie, J.; Yu, Y.; Yang, J.; Lee, J. Y. Tuning the Crystallinity of Au Nanoparticles. *Small* **2010**, *6* (4), 523–527. https://doi.org/10.1002/smll.200902033.

(47) Peng, S.; Lee, Y.; Wang, C.; Yin, H.; Dai, S.; Sun, S. A Facile Synthesis of Monodisperse Au Nanoparticles and Their Catalysis of CO Oxidation. *Nano Res.* **2008**, *1* (3), 229–234. https://doi.org/10.1007/s12274-008-8026-3.

(48) Veesler, S.; Puel, F.; Fevotte, G. Polymorphism in Processes of Crystalization in Solution. *STP Pharma Prat.* **2003**, *13*, 1–32.

(49) Whitehead, C. B.; Özkar, S.; Finke, R. G. LaMer's 1950 Model of Particle Formation: A Review and Critical Analysis of Its Classical Nucleation and Fluctuation Theory Basis, of Competing Models and Mechanisms for Phase-Changes and Particle Formation, and Then of Its Application to Silver Halide, Semiconductor, Metal, and Metal-Oxide Nanoparticles. *Mater. Adv.* **2021**, *2* (1), 186–235. https://doi.org/10.1039/D0MA00439A.

(50) Jana, S. Advances in Nanoscale Alloys and Intermetallics: Low Temperature Solution Chemistry Synthesis and Application in Catalysis. *Dalton Trans. Camb. Engl. 2003* **2015**, *44*. https://doi.org/10.1039/c5dt03699b.

(51) De Yoreo, J. J.; Gilbert, P. U. P. A.; Sommerdijk, N. A. J. M.; Penn, R. L.; Whitelam, S.; Joester, D.; Zhang, H.; Rimer, J. D.; Navrotsky, A.; Banfield, J. F.; Wallace, A. F.; Michel, F. M.; Meldrum, F. C.; Cölfen, H.; Dove, P. M. Crystallization by Particle Attachment in Synthetic, Biogenic, and Geologic Environments. *Science* **2015**, *349* (6247), aaa6760. https://doi.org/10.1126/science.aaa6760.

(52) Gebauer, D.; Völkel, A.; Cölfen, H. Stable Prenucleation Calcium Carbonate Clusters. *Science* **2008**, *322* (5909), 1819–1822. https://doi.org/10.1126/science.1164271.

(53) Hubert, F.; Testard, F.; Thill, A.; Kong, Q.; Tache, O.; Spalla, O. Growth and Overgrowth of Concentrated Gold Nanorods: Time Resolved SAXS and XANES. *Cryst. Growth Des.* **2012**, *12*, 1548–1555. https://doi.org/10.1021/cg2016116.

(54) Polte, J.; Erler, R.; Thünemann, A. F.; Sokolov, S.; Ahner, T. T.; Rademann, K.; Emmerling, F.; Kraehnert, R. Nucleation and Growth of Gold Nanoparticles Studied via in Situ Small Angle X-Ray Scattering at Millisecond Time Resolution. *ACS Nano* **2010**, *4* (2), 1076–1082. https://doi.org/10.1021/nn901499c.

(55) Koerner, H.; MacCuspie, R. I.; Park, K.; Vaia, R. A. In Situ UV/Vis, SAXS, and TEM Study of Single-Phase Gold Nanoparticle Growth. *Chem. Mater.* **2012**, *24* (6), 981–995. https://doi.org/10.1021/cm202633v.

(56) Jensen, H.; Bremholm, M.; Nielsen, R. P.; Joensen, K. D.; Pedersen, J. S.; Birkedal, H.; Chen, Y.-S.; Almer, J.; Søgaard, E. G.; Iversen, S. B.; Iversen, B. B. In Situ High-Energy Synchrotron Radiation

Study of Sol–Gel Nanoparticle Formation in Supercritical Fluids. *Angew. Chem. Int. Ed.* **2007**, *46* (7), 1113–1116. https://doi.org/10.1002/anie.200603386.

(57) Beale, A. M.; Eerden, A. V. D.; Jacques, S. D. M.; Leynaud, O.; O'Brien, M. G.; Meneau, F.; Nikitenko, S.; Bras, W.; Weckhuysen, B. M. A Combined SAXS/WAXS/XAFS Setup Capable of Observing Concurrent Changes across the Nano-to-Micrometer Size Range in Inorganic Solid Crystallization Processes. *J. Am. Chem. Soc.* **2006**, *128* (38), 12386–12387. https://doi.org/10.1021/ja062580r.

(58) Abécassis, B.; Testard, F.; Spalla, O.; Barboux, P. Probing in Situ the Nucleation and Growth of Gold Nanoparticles by Small-Angle X-Ray Scattering. *Nano Lett.* **2007**, *7* (6), 1723–1727. https://doi.org/10.1021/nl0707149.

(59) Abécassis, B.; Testard, F.; Kong, Q.; Francois, B.; Spalla, O. Influence of Monomer Feeding on a Fast Gold Nanoparticles Synthesis: Time-Resolved XANES and SAXS Experiments. *Langmuir* **2010**, *26* (17), 13847–13854. https://doi.org/10.1021/la1020274.

(60) Chen, X.; Schröder, J.; Hauschild, S.; Rosenfeldt, S.; Dulle, M.; Förster, S. Simultaneous SAXS/WAXS/UV–Vis Study of the Nucleation and Growth of Nanoparticles: A Test of Classical Nucleation Theory. *Langmuir* **2015**, *31* (42), 11678–11691. https://doi.org/10.1021/acs.langmuir.5b02759.

(61) Feng, H.; Yang, Y.; You, Y.; Li, G.; Guo, J.; Yu, T.; Shen, Z.; Wu, T.; Xing, B. Simple and Rapid Synthesis of Ultrathin Gold Nanowires, Their Self-Assembly and Application in Surface-Enhanced Raman Scattering. *Chem. Commun.* **2009**, No. 15, 1984–1986. https://doi.org/10.1039/B822507A.

(62) Vargas, J.; Petkov, V.; Nouh, E. S. A.; Ramamoorthy, R.-K.; Lacroix, L.-M.; Poteau, R.; Viau, G.; Lecante, P.; Arenal, R. Ultrathin Gold Nanowires with the Polytetrahedral Structure of Bulk Manganese. *ACS Nano* **2018**, *12* (9), 9521–9531. https://doi.org/10.1021/acsnano.8b05036.

(63) Loubat, A.; Impéror-Clerc, M.; Pansu, B.; Meneau, F.; Raquet, B.; Viau, G.; Lacroix, L.-M. Growth and Self-Assembly of Ultrathin Au Nanowires into Expanded Hexagonal Superlattice Studied by in Situ SAXS. *Langmuir* **2014**, *30* (14), 4005–4012. https://doi.org/10.1021/la500549z.

(64) Ramamoorthy, R. K.; Yildirim, E.; Barba, E.; Roblin, P.; Vargas, J. A.; Lacroix, L.-M.; Rodriguez-Ruiz, I.; Decorse, P.; Petkov, V.; Teychené, S.; Viau, G. The Role of Pre-Nucleation Clusters in the Crystallization of Gold Nanoparticles. *Nanoscale* **2020**, *12* (30), 16173–16188. https://doi.org/10.1039/D0NR03486J.

(65) Powell, C. X-Ray Photoelectron Spectroscopy Database XPS,Version 4.1, NIST Standard Reference Database 20, 1989. https://doi.org/10.18434/T4T88K.

(66) Maurer, J. H. M.; González-García, L.; Reiser, B.; Kanelidis, I.; Kraus, T. Sintering of Ultrathin Gold Nanowires for Transparent Electronics. *ACS Appl. Mater. Interfaces* **2015**, *7* (15), 7838–7842. https://doi.org/10.1021/acsami.5b02088.

(67) Moutet, P.; Lacroix, L.-M.; Robert, A.; Impéror-Clerc, M.; Viau, G.; Ressier, L. Directed Assembly of Single Colloidal Gold Nanowires by AFM Nanoxerography. *Langmuir ACS J. Surf. Colloids* **2015**, *31* (14), 4106–4112. https://doi.org/10.1021/acs.langmuir.5b00299.

(68) Loubat, A.; Lacroix, L.-M.; Robert, A.; Impéror-Clerc, M.; Poteau, R.; Maron, L.; Arenal, R.; Pansu, B.; Viau, G. Ultrathin Gold Nanowires: Soft-Templating versus Liquid Phase Synthesis, a Quantitative Study. *J. Phys. Chem. C* **2015**, *119* (8), 4422–4430. https://doi.org/10.1021/acs.jpcc.5b00242.

(69) Pschunder, F.; Puig, J.; Giovanetti, L. J.; Huck-Iriart, C.; Requejo, F. G.; Buceta, D.; Hoppe, C. E.; Ramallo-López, J. M. New Insights into the Growth Mechanism of Ultrathin Au Nanowires from Combined in Situ EXAFS and SAXS Studies. *J. Phys. Chem. C* **2018**, *122* (50), 29051–29061. https://doi.org/10.1021/acs.jpcc.8b10449.

Chapter 2 Microfluidic Tools and Characterization Techniques for *In Situ* Studies

The main objectives of the work presented in this manuscript was to study the nucleation and growth of gold nanoparticles obtained by the reduction of a gold precursor with a trialkyl silane in the presence of oleylamine. As it has been described in the previous chapter, the reduction of Au (III) precursor by silane in organic media is strongly affected by the amine concentration, lasting from few seconds for low concentration to few hours for a large excess. To get a clear picture of the nucleation and growth mechanism, one needs to study with a good accuracy the evolution of the reaction mixture in-situ and in real time combining different techniques. In this chapter, we will first briefly introduce the basics of three of these technics: small angle X-ray scattering (SAXS) to determine the size and shape of the particle formed; X-ray absorption spectroscopy (XAS) to follow in-situ the gold speciation and UV-visible spectroscopy to track the appearance of Au (0) NPs in the media using in-house facilities.

For the nanowires formation the reaction is very slow and classical set-ups such as glass capillaries can be used. On the other hand, for the nanospheres prepared with a stochiometric amine concentration, the reduction is very fast. It thus requires special set-ups to gain access to very short times (few tens of milliseconds). The development of dedicated microfluidic setups compatible with harsh organic solvent was a major technological barrier. The fabrication process of ostemer-based chip and the specific designs to ensure a sufficient signal over noise ratio for each characterization techniques are described in the second part of the chapter.

Part A Methods for *In Situ* Studies

2.1 Small angles X-ray scattering (SAXS)

2.1.1. General information

Small-Angle X-Ray Scattering (SAXS) is a very useful technique to investigate nanometer-scale structures, characterizing the size, shape and size distribution of colloidal systems in suspension or once precipitated. This technique has indeed several advantages among which one can list[1]:

- Being non-destructive
- Inducing no preparation artifact
- Being suitable for liquids and solids characterization

From SAXS experiments, we can deduce a lot of information like the size, the shape and the surface nature (dense, fractal…)[2] and the volume fraction.[1] As it can be carried out in situ it is also very helpful

to study growth kinetics and mechanism[3]. Furthermore, the structure of dense suspensions and the interparticle interactions in the system can be examined using SAXS[4]. Thanks to the small angle range, SAXS allows measuring the signal scattered by nano-objects, typically in the size range 1-100 nm.

Photons interact with electrons and give information about the fluctuations of electron densities in the matter. So, a good electronic density contrast, between the particles and the solvent in case of colloidal suspensions or between the precipitates and the matrix in solids, is the first requirement to obtain a SAXS signal. A typical experimental set-up is shown on Figure 2.1. A monochromatic beam of incident wave vector k_i interacts with the sample. The scattered intensity is collected as a function of the scattering angle 2θ on the 2D detector. The interactions that are interesting for the analysis correspond to elastic scattering and thus are characterized by zero energy transfers, which means that the wave vector k_s of the scattered beam has the same modulus as k_i. The scattering vector: $\vec{q} = \overrightarrow{k_s} - \overrightarrow{k_i}$ allows analyzing these interactions. The relationships between q and θ, and between q and the distance in the real space d are given by:

$$q = \frac{4\pi \sin\theta}{\lambda} = \frac{2\pi}{d} \qquad \text{Eq. 2.1}$$

Where θ is the scattering angle and λ is the wavelength of the incident beam[5] [6].

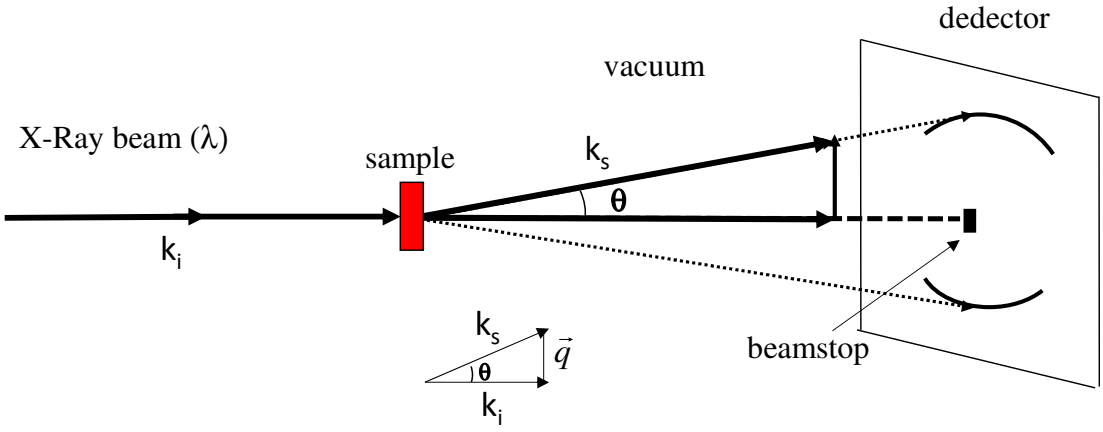

Figure 2.1: Schematic representation of Small Angle X-ray Scattering experiment

The inelastic scattering gives an additional background which is subtracted from the SAXS signal before analysis.

There are two significant terms obtained from a SAXS measurement: the form factor (*P(q*)) and the structure factor (*S(q*)) of the objects. These two terms contribute to the intensity, *I(q)*, which is plotted as a function of *q*. For isotropic sample the intensity depends only on the norm of the vector *q*:

$$I(q) \propto P(q).S(q) \qquad \text{Eq. 2.2}$$

The structure factor is the scattering intensity resulting from the correlation between the particles. If there are some interaction between the particles, the structure factor allows evaluating the characteristic length of the interparticle distance. In the case of nanoparticle superlattices, the structure factor corresponds to the Bragg peaks which arisen from the X-ray diffraction of the nanoparticle array. Since we will work mostly with diluted suspension, we will not observe any correlation between NPs. The structure factor *S(q)* will therefore be constant and equal to 1, except in the chapter 5 when we describe the SAXS of a thin film of particles.

In diluted suspension, the form factor will govern the intensity. To give some insights, small angle scattering patterns of objects with different shapes (disks in red, rods in green and spheres in blue) are given in the figure 2.2. From a first glance, strong difference appears between the different shapes both at the low-*q* and high-*q* regions. The SAXS profile is conventionally divided into three regions: Guinier, Fourier, and Porod. These three regions were highlighted for the sphere in Figure 2.2 by the yellow, green and grey colors, respectively. For the disk and rod, these regions are separated by the vertical grey line.

At small *q* there is a plateau which is called the Guinier's regime and ends at the so-called knee position. One can determine the radius of gyration (R_g) of the particles from this plateau. Moreover, the inverse of the knee position allows determining the size of the object, these patterns being in reciprocal space. At high *q* range, we see the Porod's region which is characteristic of the specific interface between the objects and the surrounding media. In between, the Fourier's region allows to extract the shape of the objects. SAXS intensity follows a power law with an exponent which is related to the dimensionality of the particle. For instance, spherical object takes a slope of 4, while disk and rod follow a slope of 2 and 1, respectively.

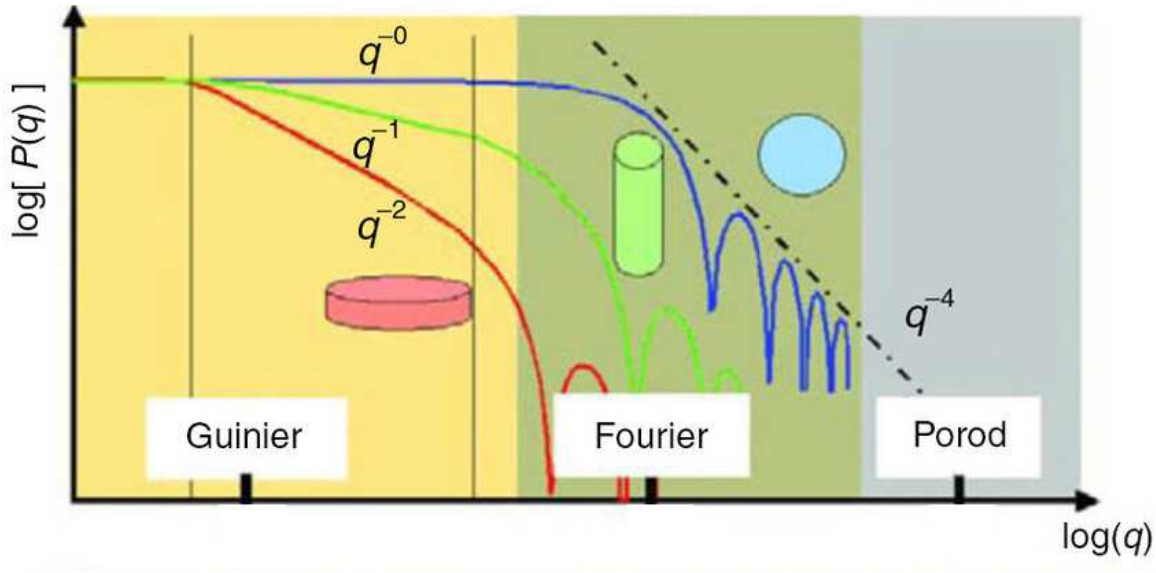

Figure 2.2: Schematic SAXS profile with the Guinier, Fourier and Porod regions colored in yellow, green and grey, respectively for the sphere (blue line), separated by vertical grey line for the disk (red line) and rod (green line). Dashed line: asymptotic q^{-4} behavior. Reprinted from reference[7].

2.1.2 Form factor of nanospheres

Since most of our studies will deal with Au nanosphere dispersed in hexane, we present here their specific scattering intensity which can be described by the general equation:

$$I_{NS}(q) = n\left(\rho_{gold} - \rho_0\right)^2 P(q)S(q) \qquad \text{Eq. 2.3}$$

where ρ_{gold} and ρ_0 are the scattering length densities of gold and hexane, respectively. $P(q)$ and $S(q)$ are the form and structure factors, respectively. n is the number density of the spheres, i.e. the number of spheres per unit volume which can be written as:

$$n = \Phi/V \qquad \text{Eq. 2.4}$$

where Φ is the volume fraction and *V* is the volume of the sphere ($V = 4/3\ \pi r^3$, r is a radius of the sphere).

In our studies, the systems being highly diluted we consider that the structure factor $S(q) = 1$, The form factor of the sphere is:

$$P_{sphere}(q) = F_s^2(q) \qquad \text{Eq. 2.5}$$

where, $F_S(q)$ is the amplitude form factor which can be written as:

$$F_s(q) = \frac{3V[\sin(qr) - qr\cos(qr)]}{(qr)^3} \qquad \text{Eq. 2.6}$$

Figure 2.3 displays the simulated SAXS patterns of monodisperse spherical particles with different sizes varying from 2 to 20 nm[8]. Some important points can be highlighted. First, when the particle size increases, the total intensity increases at low *q*, in the Guinier's region. The knee position shifts towards lower *q*, in agreement with the Eq.2.1. Finally, since in this simulation the particles have a single size, oscillations were observed at high *q*, revealing the monodispersity of the system.

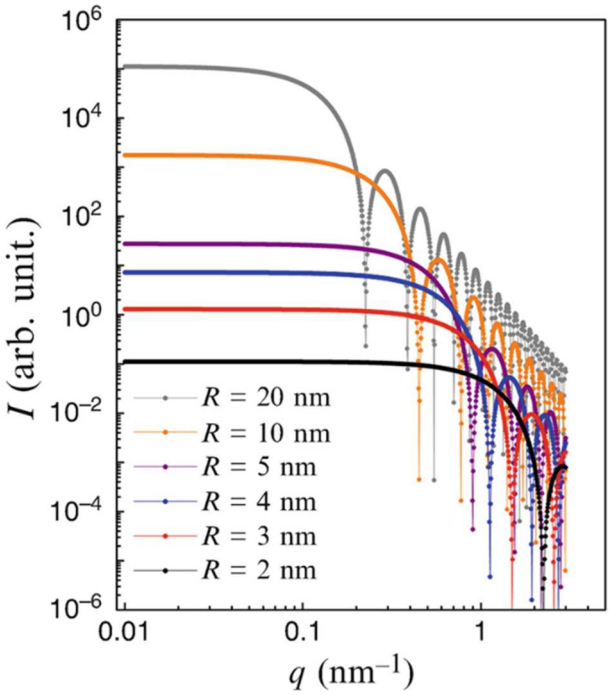

Figure 2.3: Form factor of different spheres calculated considering a single size of 2 nm (black), 3 nm (red), 4 nm (blue), 5 nm (purple), 10 nm (orange) and 20 nm (grey). Reprinted from reference[8]

2.1.3 Experimental acquisition parameters

We have used two different apparatus for SAXS depending on the experiments performed:

-The SAXS of the colloidal suspensions of gold nanoparticles were recorded at the LGC laboratory on a XEUSS 2.0 instrument equipped with a pixel detector PILATUS 1 M (DECTRIS) and a Cu Kα X-ray source provided by GeniX3D (λ = 1.54 Å). The sample to detector distance was fixed to record the SAXS signal in the *q* range 0.015 - 1 $Å^{-1}$ which allows to access the size range of 0.6 nm - 42 nm. Depending on our requirements for the measurement, the acquisition time was set from 30 sec to 10 min.

- For the time-resolved in situ SAXS experiments at synchrotron, SWING beamline (SOLEIL, France) and c-SAXS beamline at the Swiss Light Source (PSI, Switzerland) were used. Further details will be given in chapter 3.

2.1.4 Fitting of the SAXS patterns using SASVIEW 4.2.2

To extract some quantitative information from the SAXS patterns, the experimental scattering intensity profiles can be fitted. For that, we have used SASVIEW,[9] which is a very useful free software. Different models of form factor are available including the form factor of spheres.

In SASVIEW, the SAXS scattering intensity $I(q)$ of a sphere in the absence of structure factor is given by the formula, derived from equations 2.2 to 2.6:

$$I(q) = \frac{scale}{V}[3V(\Delta(\rho).\frac{sin(qr)-qrcos(qr)}{(qr)^3}]^2 + background \qquad \text{Eq. 2.7}$$

with *scale* corresponding to the volume fraction and *background* an adjustable value which represents the inelastic scattering.

From SASVIEW we can investigate how good the chosen model fits the experimental data thanks to the value chi-square (x^2, *'Chi2'*) which should be close to 1. This term is given by:

$$chi - square = \sum((I(Q)_{meas} - I(Q)_{calc})^2 / E(Q)^2) / (N_{pts} - N_{params}) \quad \text{Eq. 2.8}$$

Where $I(Q)$ is the scattering intensity, $E(Q)$ is the error on the intensity value, N_{pts} is the number of data points in the dataset and N_{params} is the number of model parameters being optimized.

In SASVIEW, one can also play with the polydispersity. It is really important to have information about the population of the particles with different sizes. Basically, SASVIEW calculates the average intensity for a population of particles with a given size distribution. Then the intensity is normalized by the average particle volume. The form factor reads:

$$P(q) = \frac{scale}{V} < F * F > + background \quad \text{Eq. 2.9}$$

Where F is the scattering amplitude and $< F * F >$ shows an average over the distribution $f(x, \bar{x}, \sigma)$. Including the polydispersity, the form factor can be rewritten as:

$$P(q) = \frac{scale}{V} \int f(x; \bar{x}, \sigma) F^2(q, x) dx + background \quad \text{Eq. 2.10}$$

Where x and σ are the center value and the width parameter, respectively. These components are required for the characterization of the distribution. There are several distribution functions but we choose the gaussian distribution as shown in figure 2.4. The gaussian distribution is written:

$$f(x) = \frac{1}{Norm} exp(-\frac{(x-x)^2}{2\sigma^2}) + background \quad \text{Eq. 2.11}$$

where *Norm* is a normalization factor that is coming from the numerical calculation.

The polydispersity in models is given by

$$PD = {}^{\sigma}/_{x} \qquad \text{Eq. 2.12}$$

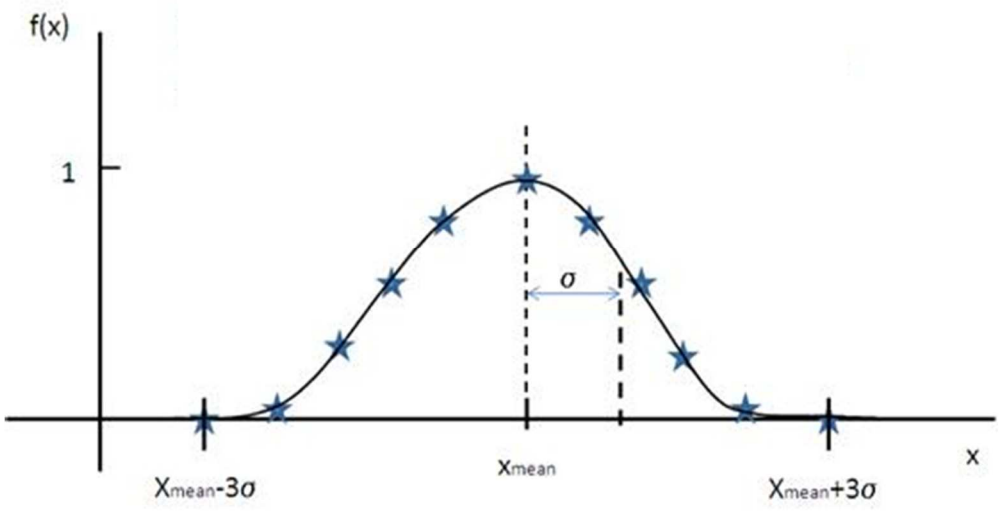

Figure 2.4: Representative image for the Gaussian distribution,[9] σ the standard deviation and x_{mean} the mean value. The blue stars represent the 11 points considered in the simulation to reproduce the Gaussian distribution.

2.2 X-Ray absorption spectroscopy (XAS)

2.2.1. General information

X-ray absorption spectroscopy (XAS)[10,11] allows to have an information about the local and chemical environment of atoms. The general principle is to measure the absorption at the energy corresponding to the K-, L- or M-edges of atoms. The absorption edge contains electronic and structural information such as oxidation state, coordination geometry and local disorder.

The energy of the absorption edge is unique for each element. So, we can choose which element to look at by playing with the incident energy. On figure 2.5 is shown a representative X-ray absorption spectrum.

The XAS spectrum is divided into two regions highlighted by the blue and orange circles in the figure 2.5:

-X-ray Absorption Near Edge Structure (XANES). XANES corresponds to the electronic transitions from the atomic core level considered to final states in the energy region just above the ionization energy. The wavelength of the photoelectron is larger than the interatomic distance between the absorbing atom and its first neighbor atoms. This region contains qualitative information on the local geometry, oxidation states and electronic structure of the species.

-Extended X-ray Absorption Fine Structure (EXAFS). EXAFS is an interference pattern coming from the interaction of the photoelectron wave outgoing from the absorbing atom with the wave back scattered from the neighbor atoms. From this region of the XAS pattern we can gather quantitative information such as coordination number, bond length and distortion.

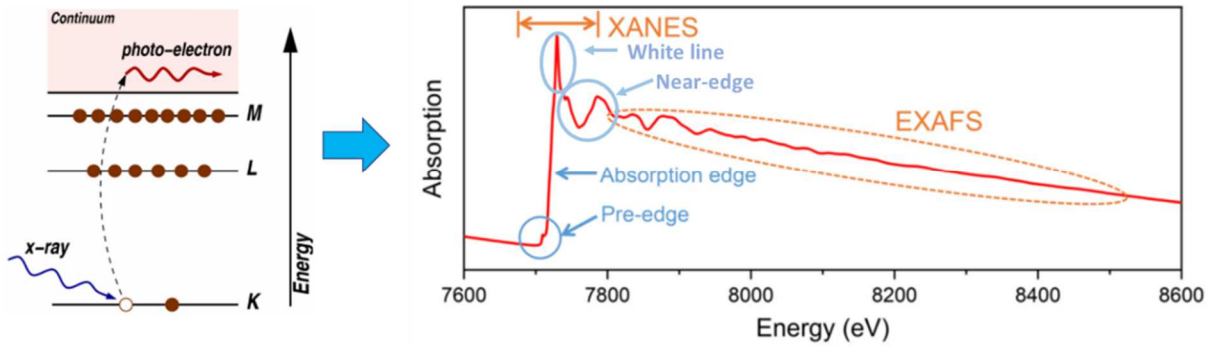

Figure 2.5: Representative image of the basic physical process in XAS and XAS spectrum including the pre-edge, absorption edge, white line, near edge, XANES and EXAFS regions[12 13]

2.2.2. Analyzing of the XAS data

For the XANES data, a linear combination analysis (LCA) is the way to measure the relative proportion of different constituents in the solution if they exhibit different features on the edge. This analysis is based on the interpretation of data by comparison with references or standards. Basically, in the chemical reaction of formation of nanoparticles, different complex at different oxidation states can be found in the system. If we can measure the spectra of the pure components beforehand, the XAS spectra can be analyzed by a linear combination of these relevant references. Thanks to LCA analysis,

we can determine the concentration of these components at each particular step of our reaction. The main difficulty consists in identifying the proper reference compounds so which species could be in the solution.

To give an example, Lengke et al.[14] have studied the mechanism of gold (III) chloride reduction in cyanobacteria. These authors have used XAS to understand the mechanism of gold bioaccumulation by bacteria. In figure 2.6. is given a XAS spectra at the Au L_{III}-edge recorded after different reaction times. Each XAS spectrum was fitted by a linear combination using three references, Au foil for the Au(0) state, $AuCl_3$ in water for the Au(III) state and Au sulfide for the Au(I) state (Figure 2.6b). The evolution of the concentration of each species as a function of time was then obtained (Figure 2.6c).

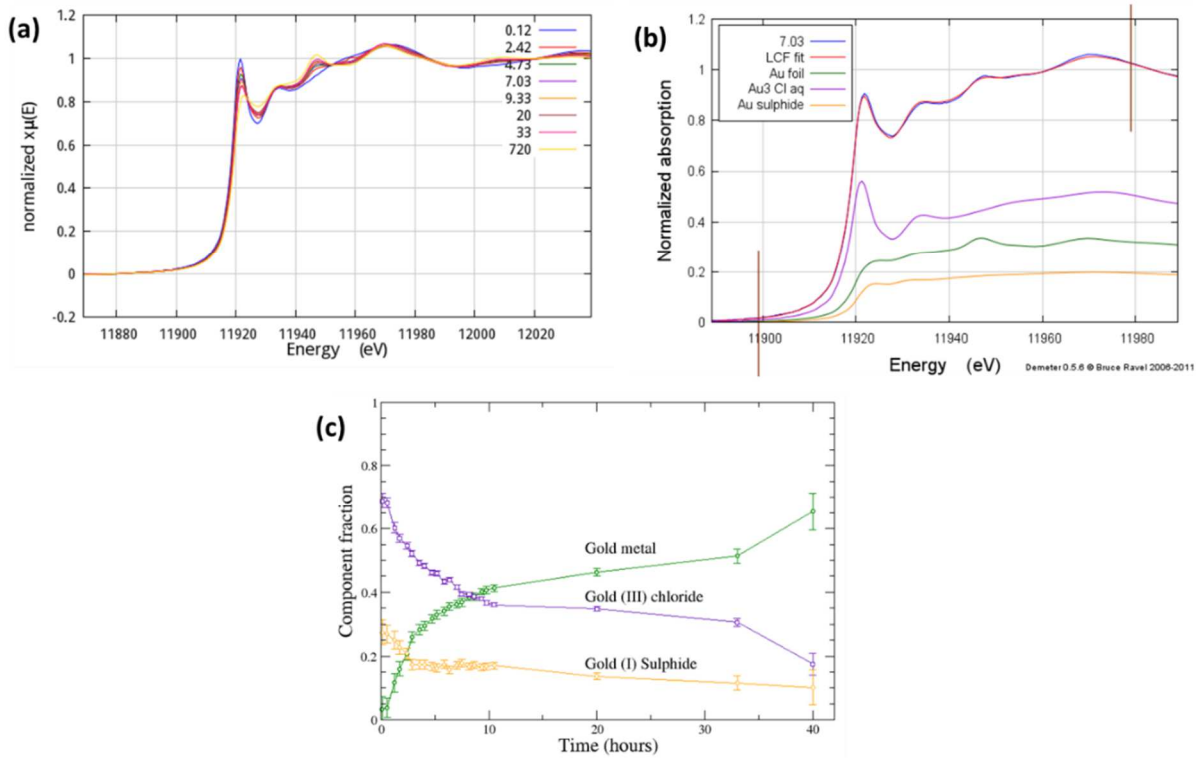

Figure 2.6: (a) XAS spectra at the Au L_{III}-edge recorded during the reaction (b) XANES L_{III}-edge spectrum and an example of an LCA fit at t = 7.03 s. The weighted components are displayed below the fit, (c) Evolution of the gold oxidation states and species with time in solution. Reprinted from reference [14].

In chapter 3, 4 and 5 we have employed LCA to get access to the evolution of the different oxidation states of Au during the reduction and crystallization of the particles.

The EXAFS analysis consists in the analysis of the interference pattern first in the energy space (*q*-space) and then in the real space (*r*-space) to deduce the number and the nature of atoms in the first coordination shell and sometimes in the second shells. Raj Kumar Ramamoorthy, a post doc in the group, was in charge of this analysis. Few results will be presented in chapter 6 regarding the coordination shell of the Au complex involved in the pre-nucleation clusters.

2.2.3. Experimental acquisition parameters

Time-resolved experiments were performed at the beam line ODE of the synchrotron Soleil on cuvettes and at the SuperXAS beamline of the PSI synchrotron. In this last case the beam size was well adapted to the size of the channel of the microfluidic chips. More details are given in chapter 3.

2.3 Ultraviolet-Visible (UV-Vis) spectroscopy

2.3.1. General information

Ultraviolet-Visible spectroscopy (UV-Vis)[15,16] is a common technique to study the electronic transitions in molecules, solids or nanomaterials. This method is well-known, inexpensive, fast and fairly simple to implement in the laboratory. In case of nanoparticles in suspension, UV-Vis is used to have an information about their size, concentration and aggregation state. UV-vis spectroscopy consists in measuring the transmittance of a sample in the ultraviolet, visible and near infrared region corresponding to the ranges 190-380 nm, 380-750 nm and 750-2500 nm, respectively. The transmittance is defined as $T = {I}/{I_0}$

with I_0 the incident intensity and *I* the intensity coming out from sample. The absorbance of a sample (*A*) is defined as $A = \log\left(\frac{I_0}{I}\right) = -\log T$. In case of molecules or nanoparticles in suspension, the absorbance of the solvent is generally subtracted from the experimental value to obtain the absorbance of the solute.

The Beer-Lambert law (Eq. 2.13) describes the linear relationship between the absorbance *A* of a substance in solution and its concentration (*C* in mol/L), its molar absorption coefficient (ε in $L \cdot mol^{-1} \cdot cm^{-1}$) and the path length in solution (*l* in cm).

$$A = \varepsilon c l \qquad \text{Eq. 2.13}$$

The UV-Vis spectroscopy allows to determine the wavelength λ_{max} at which the sample has strongest photon absorption, corresponding to a maximum absorbance (Abs_{max}). The Beer-Lambert law is generally used for electronic transitions and is valid when the concentration of the solute is not too high.

Every material absorbs specifically some wavelength, depending on its nature. In metal nanoparticles, the interaction with the electromagnetic radiation creates electronic transitions from the ground state to a higher energy state. These transitions can be either inter-band *d*-to-*s*, intra-band *s*-to-*s* or specific surface plasmon resonance (SPR).

Plasmons[17] are coherent oscillations of conduction electrons in metals. SPR are strong and broad optical absorption bands coming from a confinement of surface plasmon in nanoparticles. Noble metal nanoparticles, and more precisely Au and Ag show strong SPR in the visible range. Several parameters affect the Abs_{max} and λ_{max} of SPR of nanoparticles such as the size, shape, composition, interparticle interactions, and the dielectric constant of the medium.

In figure 2.7, the UV-vis spectra of Au NPs[18] with different sizes is given as an example. In this graph, we see the strong SPR absorption band. The maximum wavelength λ_{max} of the plasmon peak is found around 520 nm whatever the NP size. However, the intensity of the SPR band decreases when the NP size is reduced and its broadening increases. The SPR is very damped for a size of 2.5 nm and finally vanishes at very small size (1.9 nm).

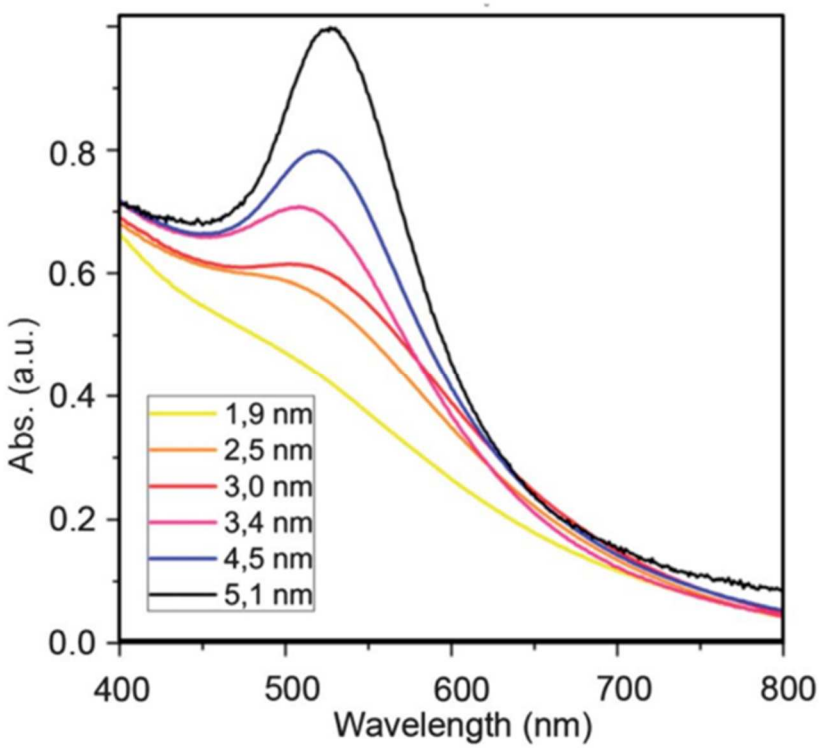

Figure 2.7 UV-vis absorption spectra of toluene suspension of dodecanethiol-covered gold nanoparticles of 1.9 nm (yellow), 2.5 nm (orange), 3.0 nm (red), 3.4 nm (pink), 4.5 nm (blue) and 5.1 nm (black). Reprinted from reference [19]

Figure 2.8 shows the *in-situ* UV-vis spectra recorded during the synthesis of Au nanoparticle in water using ascorbic acid as reductant. In this graph we see the Au (III) and ascorbic acid (AA) bands in the ultraviolet region (λ: 200-300 nm). With time, these peaks shades indicating their consumption. Meanwhile, the plasmon band at 520 nm is appearing, revealing the formation of Au nanoparticles within the 3s time scale of the measurements.

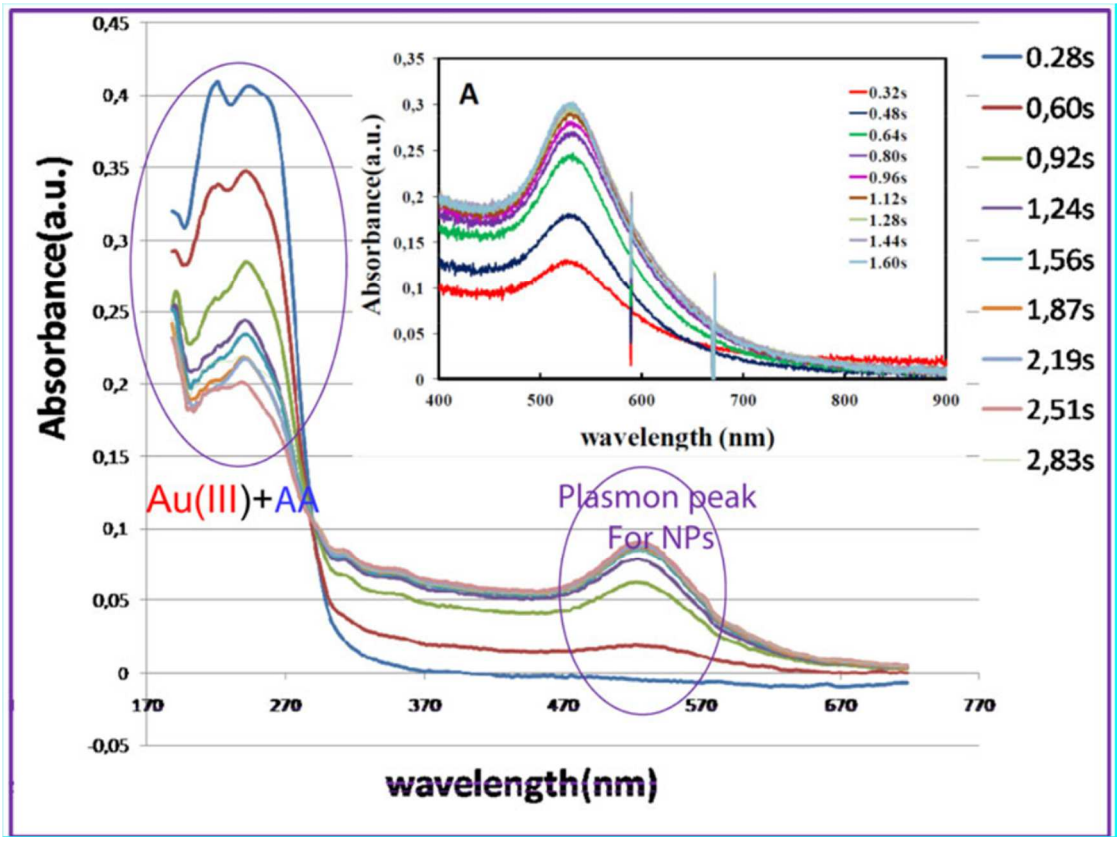

Figure 2.8 In-situ UV-vis spectrum of the formation of gold nanoparticles in water, reprinted from reference[20].

Similar studies have been performed in organic media. For instance, Chen *et al*[21] followed the synthesis of Au NPs stabilized by dodecanethiol (DDT) in toluene. The *in situ* UV-vis spectra recorded after the addition of the t-butylamineborane, TBAB, which serves as reducing agent, are presented in figure 2.9. The evolution of the absorbance maximum in the range λ = 510 - 530 nm, corresponding to the plasmon resonance, is probed and reported as inset. In addition to the SPR band, a peak was observed in the ultraviolet-region, at around λ = 320 nm. The authors have identified this peak as an inter-band transitions for gold clusters, in agreement with Tsukuda *et al*[22].

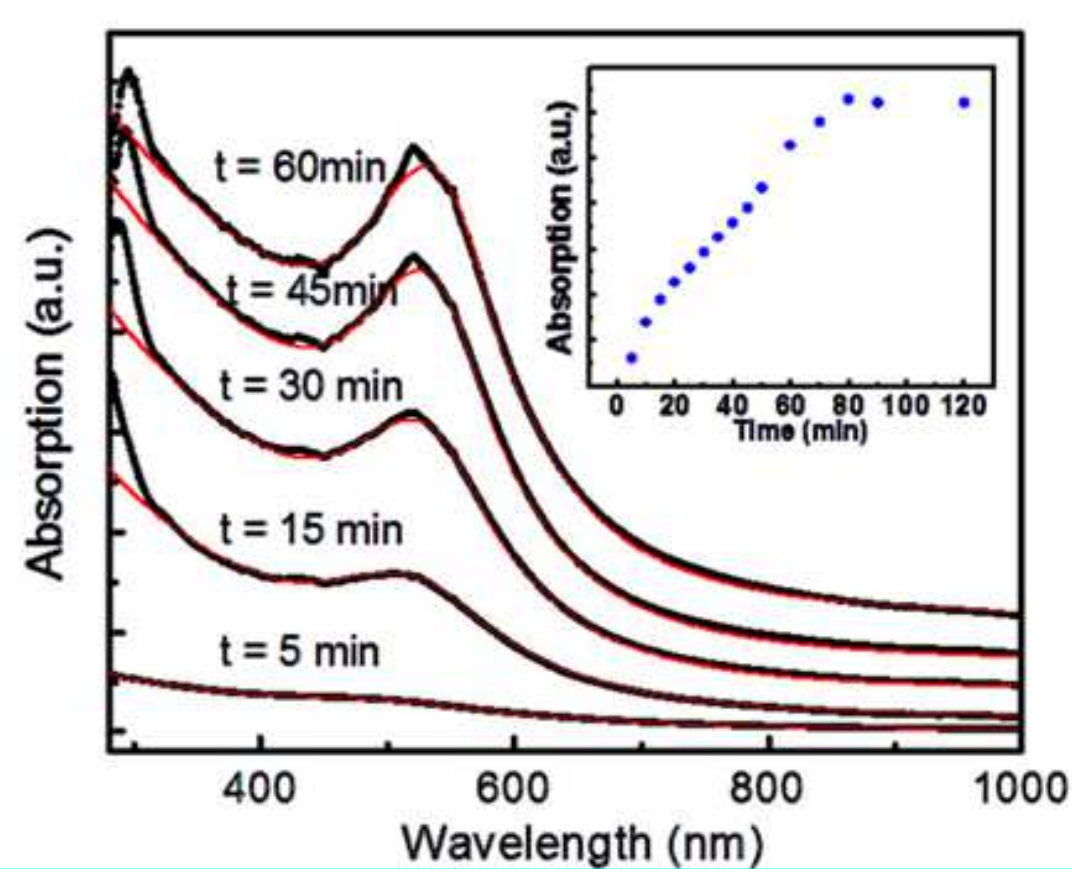

Figure 2.9 UV-vis spectrum of gold nanoparticles formation with borane complex (t-butylamineborane, TBAB) in toluene in the presence of dodecanethiol (DDT) as function of time, reprinted from reference[21]. As inset: the evolution of the absorbance maximum in the range 510 - 530 nm.

As both the intensity and the broadening of the plasmon resonance peak varies with the particle size, it is not always easy to directly deduce accurately the evolution of the Au(0) concentration. Moreover, in the case of very ultra-small particles, the resonance plasmon may be absent or very damped. The increase of the inter- and intra-band intensity can however be used to follow the increase of the Au(0) concentration as a function of time.

2.3.2 Experimental acquisition parameters

UV-vis spectroscopy experiments were performed at the laboratory bench at LGC laboratory. Kinetic measurements were performed by measuring the absorbance of a sample on a large wavelength window. For the experiments, deuterium and halogen lamp sources were used to cover the UV (190-370 nm) and visible light-near infra-red wavelengths (320-1100 nm), respectively.

The acquisition time was set at 1-3 ms with a 10 times repetition for averaging. So, the total measurement time was varying between 10-30 ms. The experiments were performed as follow :

First, the transmitted intensity was measured for two references (hexane and the starting solution) and the Au NPs as shown in figure 2.10.a. One can see that the transmitted intensity of the starting solution, consisting of the Au (III) precursor + OY + TIPS in hexane is fairly similar to the one of pure hexane. Therefore, the reference intensity I_0 was chosen as the starting solution.

The corresponding absorbance was calculated as a function of time using $A = -\log\left(\frac{I}{I_0}\right)$ (Figure 2.10.b).

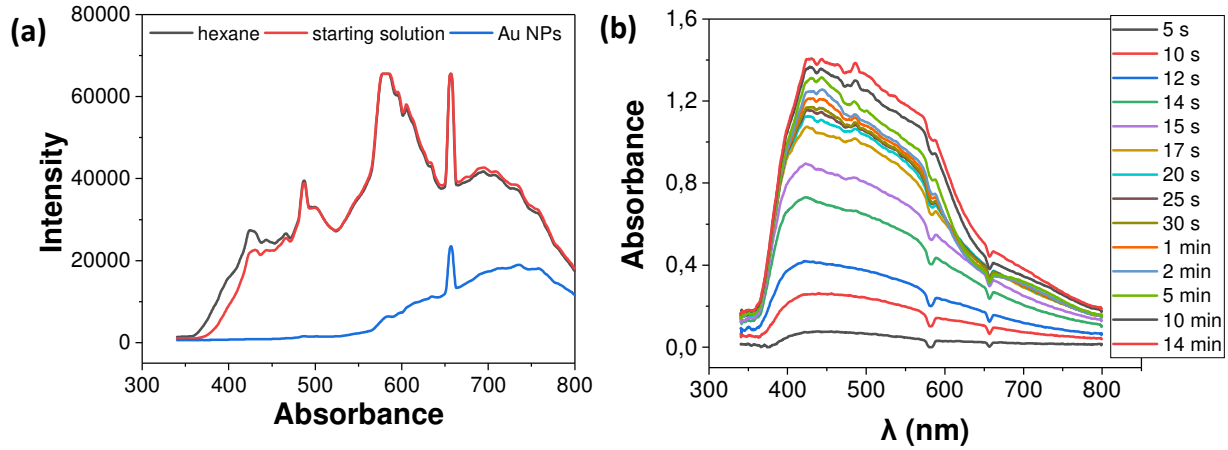

Figure 2.10 (a) UV-vis transmission spectra and (b) UV-vis absorption spectra of the Au NPs ([TIPS]= 1 M) formation

As we will further detail in the part B of this chapter, the microfluidic chip used for these measurements was made from ostemer which absorbs in the UV range. Therefore, we could not get have information below 380 nm, masking the potential region of interest for Au(III) and Au(I).

However, we can study the whole visible region at the exception of λ = 580 nm and 660 nm due to the deuterium lamp. Due to the small size of our nanoparticles, we never observed the SPR at λ = 520 nm but a general increase of the absorbance in the visible range. We believe that it is mainly due to inter- and intra-band transitions. In the chapter 4, we have chosen to plot the Absorbance as a function of time at λ = 520 nm.

Part B Microfluidic Cells Fabrication

2.4. Introduction

Microfluidic cells have been widely developed in the past decades to achieve multiplexing and high-throughput sorting for biomedical applications. The efficient mixing, transport and separation of fluids within microscale channels was also really attractive to investigate the matter combining advanced characterization methods like X-ray absorption spectroscopy (XAS), small angle X-ray scattering (SAXS) and UV-visible absorption spectroscopy. The microfluidic systems have a lot of advantages such as:

- Use of small volumes of samples and reagents that reduces the chemical consumption
- Limited exposure to hazardous chemicals.
- Efficient and precise mixing
- Accurate measurements thanks to high spatial resolution combined with sensitive characterization techniques.

Generally, the microfluidic chip fabrication[23,24,25] can be adjusted depending on the experimental requirements such as:

i) the characterization methods which may require larger optical path,

ii) the chemical substances used which impose restrictions on the polymer for chip fabrication,

iii) the reaction kinetic which may need ultra-fast and efficient mixing elements and sub-second time resolution.

In most cases, the microfluidic chips are prepared using soft lithography and cast molding techniques taken into consideration all the experimental constraints.

Then, a pump is of course mandatory to push the solution into the chip, large capillary forces being encountered in microfluidic channels.

Recently, people have used microfluidic chips to perform kinetic studies on chemical synthesis, combining advanced characterization techniques either in-house or at synchrotron facilities. A lot of studies have been reported on the crystallization process using droplet-based microfluidics[23,26]. For example, Pham et. al.[23] have worked on the protein crystallization within aqueous droplets in oil. Using only a few mg of protein they could study a large number of crystallization conditions and study them by SAXS. In figure 2.11 (left), the design of the chip and the full-set up with the synchrotron beam-line is shown. The recorded SAXS pattern, shown in figure 2.11 (right), were fitted with different models

and software to characterize the degree of crystallization and thus, determine the best experimental parameters.

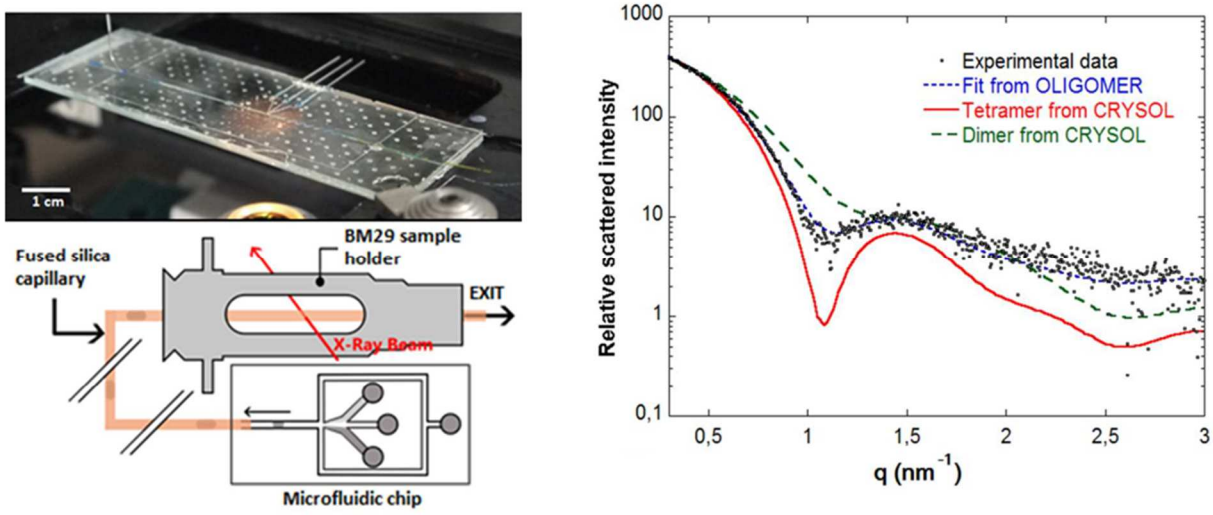

Figure 2.11 Microfluidic design, microfluidic platform, and connection to the beam line sample holder (left), the scattering intensity as a function of the scattering vector (right), reprinted from reference [23]

Vitry et. al. [27] have been working on the fast nucleation kinetics by using droplet based microfluidic devices along with a microscope equipped with a fast camera which is used to record the optical images. By adjusting the chip design to specifically decouple the nucleation from the mixing, they could measure fast nucleation rates such as 7.68 x 10^{13} $m^{-3}s^{-1}$ for neodymium oxalate.

In our case, we have fabricated microfluidic chips according to the procedure previously established by the LGC team to perform experiments in synchrotron facilities and laboratory bench[28]. However, the design of the cell has been adjusted in order to follow precisely the gold nanoparticles formation in organic media using XAS, SAXS and UV-vis spectroscopy as a function of time.

2.5 Design of the microfluidic chips

The design of the microfluidic chip depends on the specific requirements of each applications. In our case, we have previously seen in batch experiments that the mixing of the gold precursor with the reducing agent was of paramount importance to control reproducibility. Therefore, an efficient mixing part was designed and reproduced within the different chip designs. To insure a very fast (within 200 µs) and an homogeneous mixing of the reactants, a butterfly-shaped micromixer of cross-section 20 µm x 50 µm was chosen, based on the literature[29]. Schematics of the microfluidic cell is shown in figure 2.12. The structure includes two inlets (labelled as 1 and 2 in figure 2.12): one for the gold precursor solution, the second one for the reducing agent solution. A bypass (label 4) was added in the structure to avoid any back flow when we switch to a stop-flow mode. It is followed by the channel part where we monitor the reaction and a final outlet (label 5).

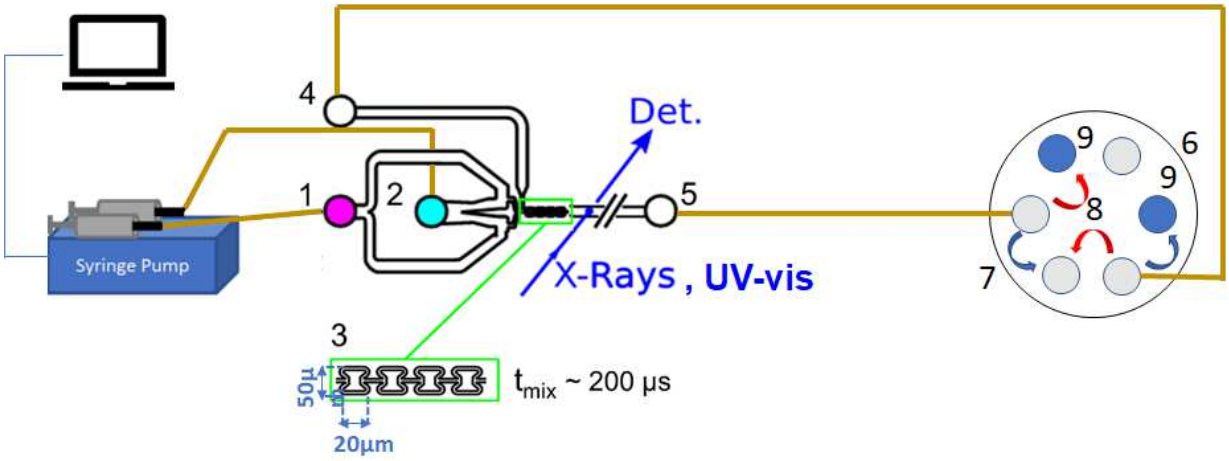

Figure 2.12: (a) Schematics of the microfluidic cells, comprising two outlets for reagent injection (1, 2), a fast passive butterfly-shaped micromixer of cross-section 20 µm x 50 µm (3) and a subsequent interrogation channel for X-ray or UV-visible beam. The mixer and subsequent channel are connected by their two extremes to a bypass (4) and an outlet channel (5), both controlled with a switch HPLC valve (6) (two positions are plugged (9)) , in a way that it can be operated as a continuous flow reactor (7) by continuously injecting the reagent solutions (for *in situ* and *in operando* probing at short reaction times), or as a stop-flow cell (8) (for longer reaction times) if the flowrates are stopped and the outlet is closed simultaneously.

Since we want to follow kinetics at different time scale, from few tens of milliseconds to tens of minutes, the chip needs to be versatile enough to allow for such study. Flowing the reactants in continuous mode (so called lost flow), one can reach temporal resolution by scanning the length of the channel, the further from the mixing part, the later it is in the reaction. The time step can be precisely calculated considering the channel dimension, the flow speed and the spatial step resolution. Total time duration of ~5 seconds can be obtained in this mode. In the stop flow mode, the time is no longer given only by the position but also by the switching time, there are no restrictions regarding the maximum time length of the experiments (figure 2.12).

Time-resolved information is calculated in continuous operation as a function of reagent flow rates and the thickness of the interrogating X-Ray beam. Reagent flow rates pumped into the microfluidic chip were controlled by high precision homemade syringe pumps, shown in figure 2.13, coupled to 5 mL glass syringes. This syringe pump system was fully instrumented to be remotely controlled during the reaction. This is of paramount importance for synchrotron measurements, since you cannot enter into the hutch to operate the syringe pump when the experiment is running. Thanks to this system, we can inject the volume of reagents needed, with the proper flow rate and switch from continuous flow to stop-flow mode whenever we want.

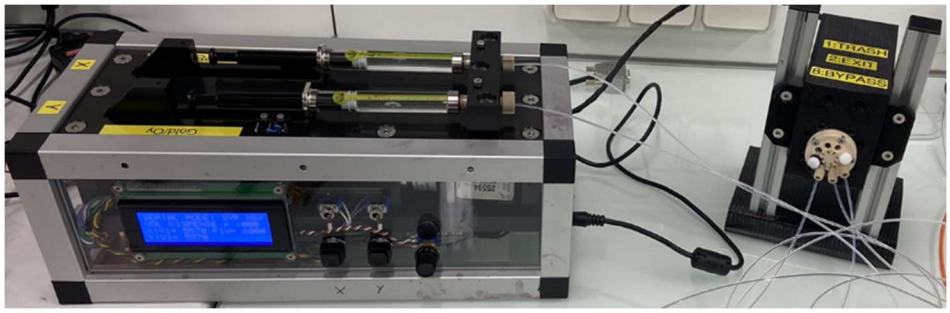

Figure 2.13: Homemade syringe pump system

2.5.1 Mixing tests

A fluorescent dye was used to probe the homogeneity of the mixture. To do this test, DI water was injected in the first inlet and a solution of fluorescent dye in the second one. The fluorescence level was followed inside the channel width as a function of the flow rate, using fluorescence microscopy. The corresponding optical images and fluorescent intensity profiles are reported on the figure 2.14.

At reduced flow rates of 1 and 2 µL/s, very heterogeneous profiles were observed. For flow rates of 4, 8 and 12 µL/s, the mixing was homogeneous. Thus, for the SAXS, XAS and UV-VIS experiments, flow rates ≥ 4 µL/s were used to ensure a proper mixing of the gold precursor and reducing agent solutions.

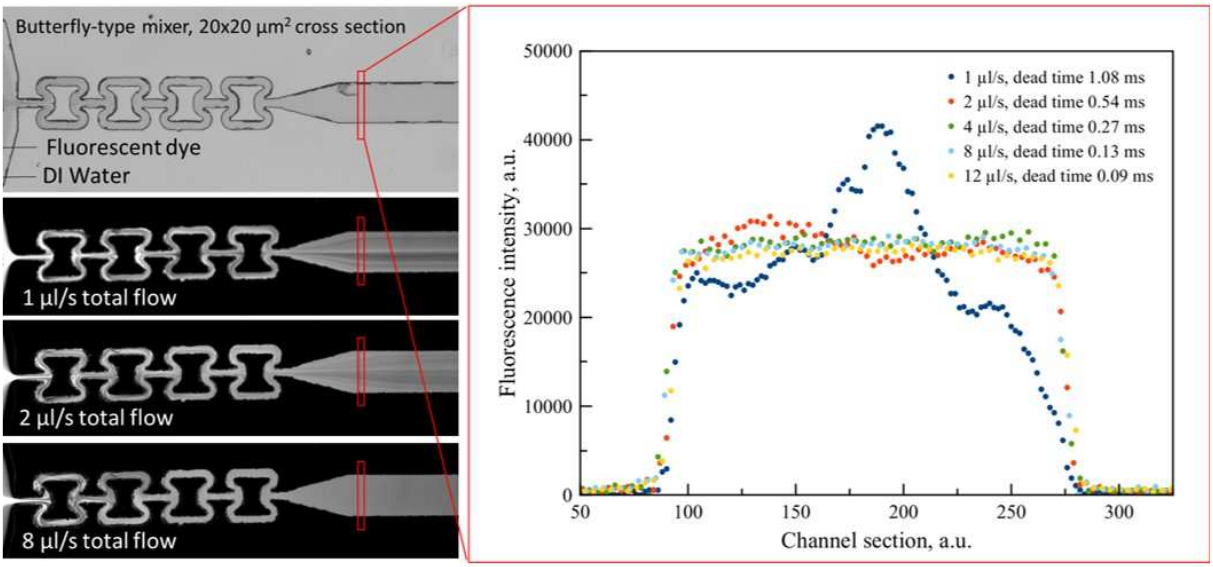

Figure 2.14: Mixing test of the butterfly structure mixer

2.5.2 Specific designs of the microfluidic chips for the characterization techniques

The microfluidic chips were designed according to the specific requirements of each characterization technique. In order to have a good signal from the experiments performed with the microfluidic chips, we should consider of course the probability for the photons to interact with the sample, but also the radiation damage to reach a proper signal to noise ratio.

If we increase the optical path length, through the channel width, or the concentration of the sample, the probability of interaction with the sample increases, so, the signal to noise ratio is improved. In our case, the gold concentration was kept constant at 20 mM for the all techniques. For this reason, we only played with the channel dimensions as listed in table 2.1.

The chip for the SAXS experiment was designed with the 200 µm x 3.1 cm x 370 µm interrogation channel shown in figure 2.15.a. The chip for the XAS experiment was designed with a much larger interrogation channel of 2 mm x 7.6 cm x 2 mm as shown in figure 2.15.b in order to have a sufficient

absorption at the Au-L_{III} edge. As one could see, pillars were designed all around the channel to help for beam alignment.

The chip for the UV-vis experiment was designed with a 500 µm x 3 cm x 250 µm interrogation channel to get a sufficient transmitted intensity (figure 2.15.c). The pillars around the channel were used to insert the optical fibers, connected to the lamps and the UV-Vis spectrometer.

technique	Channel dimensions		
	width	**length**	**thickness**
SAXS	200 µm	3.1 cm	370 µm
XAS	2 mm	7.6 cm	2 mm
UV-VIS	500 µm	3 cm	250 µm

Table 2.1: The channel dimensions of the microfluidic chips used in different techniques.

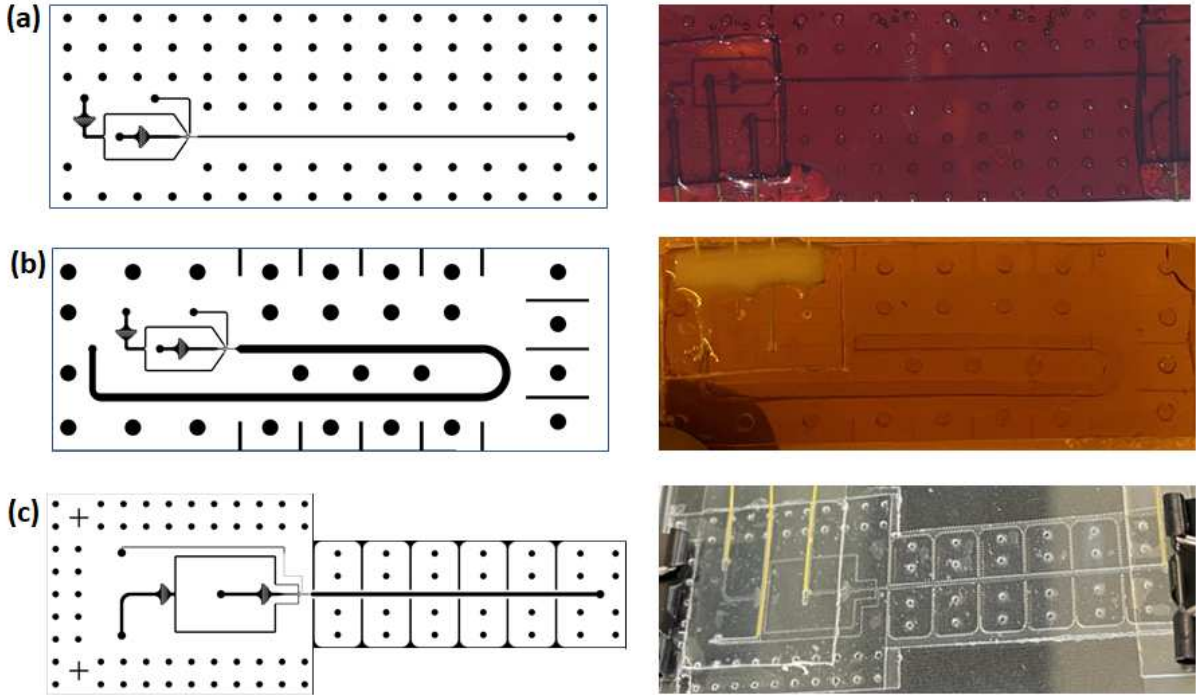

Figure 2.15: The microfluidic chips used for (a) SAXS, (b) XAS and (c) UV-vis experiments. The schematic (1st column) and experimental picture (2nd column) are shown.

A global view of the microfluidic chips within the SAXS, XAS and UV-Vis experiments is shown in the figure 2.16. Depending on the experimental set up, the microfluidic chips are placed either horizontally or vertically, without altering its efficiency.

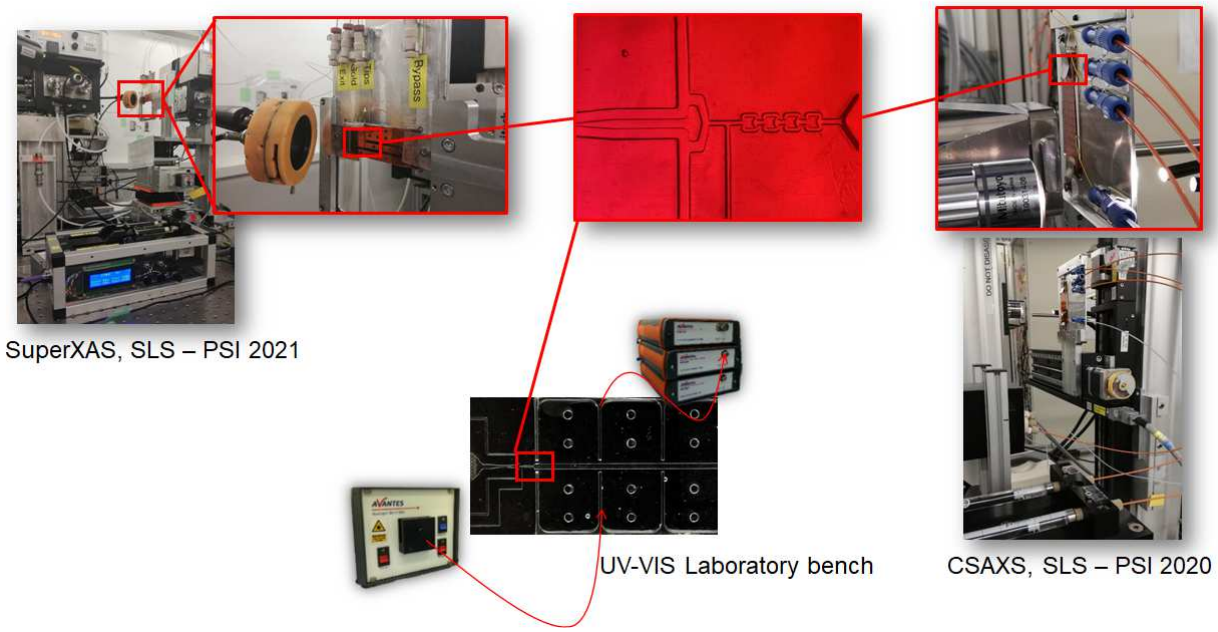

Figure 2.16: The microfluidic chip applications in the synchrotron facilities and laboratory bench: SuperXAS, SLS-PSI, CSAXS, SLS – PSI and UV-VIS Laboratory bench.

2.6. Preparation of the microfluidic chip

The synthesis of Au nanoparticles is made in hexane, a fairly harsh organic solvent for polymers. Therefore, ostemer was preferred to the conventional PDMS for the final microfluidic chip. This material was selected for its flexible properties, low cost, chemical resistance, adjustable wetting properties and high-pressure resistance.

The chip fabrication consists in a fairly low-cost yet efficient three-step process based on the replication of a master. A first mold is made from dry-films using photolithography. PDMS replicates are then prepared from it to serve as soft templates for the final ostemer injection. The details of these different steps are briefly described hereafter.

2.6.1 Mold fabrication using photoresist dry-films

The very first step of the chip preparation consist in making a permanent dry film mold. For that, the dry film was laminated on a glass substrate using pressurized hot roll (Figure 2.17.a). To achieve the desired thickness, a multistep lamination using additional dry-film layers was made (experimental details on Table 2.2).

The patterning of the dry-film was performed by conventional photolithography. A dedicated mask was designed and used during the UV exposure, the dry-films being a positive photoresist (Figure 2.17b-c and Table 2.2). The development leads to the dissolution of the insolated areas.

Since one wants to reproduce this mold, it is finally treated with a solution which contains fluorinated ketones in order to obtain an hydrophobic surface.

2.6.2 Preparation of soft replica

The second step consists in preparing a soft replica from the dry-film mold using polydimethylsiloxane (PDMS) which is a silicone elastomer often used in microfluidic applications.

For that, a mixture of elastomer and curing agent with a 10:1 ratio was poured on the dry film mold after being carefully mixed and degassed in a vacuum chamber. After a 4h curing at 65°C, the PDMS mold was peeled off carefully and put in a vacuum chamber in order to remove all the air from the polymer. Then, the PDMS surface was treated with the same solution as the dry-film mold to become hydrophobic and thus, favor the future demolding.

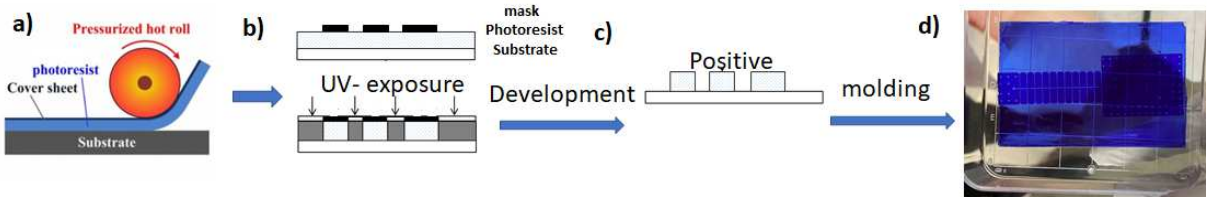

Figure 2.17 Schematic overview of the first two steps of the fabrication process: (a) Lamination of the dry film using hot-rolls, (b) UV exposure through the dedicated mask depicted in black. Grey: exposed areas of the dry-films, (c) positive development using K_2CO_3 solution, leading to the dissolution of the exposed areas, (d) Final PDMS replicate obtained after PDMS deposition and curing

Steps	**Details**
Lamination of 1 st layer	Thickness of the layer= 100 µm, T= 96°C
UV exposure	Duration= 7 seconds
Annealing using hot plate	Duration= 1 min, T= 110°C
Lamination 2 st layer	Thickness of the layer= 300 µm, T= 96°C
Put mask-1 and UV exposure	Duration= 18 seconds
Annealing using hot plate	Duration= 1 min, T= 110°C
Development	With K_2CO_3 solution
Rinse and dry	With water and air
Annealing using hot plate	Duration= 1 min, T= 110°C
Lamination 3 st layer	Thickness of the layer= 50 µm, T= 96°C
Put mask-2 and UV exposure	Duration= 4 seconds
Annealing using hot plate	Duration= 1 min, T= 110°C
Development	With K_2CO_3 solution
Rinse and dry	With water and air
Annealing using hot plate	Duration= 1 min, T= 110°C
Apply novec	Duration= 1-2-hour, T= 110°C

Table 2.2 General parameters of laminating and processing by soft lithography procedure for fabrication of a dry film mold

2.6.3 Injection molding

The third step is ostemer injection to have the final microfluidic chip. To prepare ostemer (crystal clear), two different components which are the monomer and the curing agent were carefully mixed using a ratio 1.1:1 and degassed in a vacuum chamber.

The PDMS replica, which will serve as mold was mounted and clamped with a flexible substrate between two glass slides, as shown in figure 2.18.I. Several holes were carefully opened in the PDMS to inject the ostemer using syringes (Figure 2.18.II). The presence of any air bubbles, which can then lead to channel unconformity or solution leaking, was tracked under microscope. After UV curing and removal of the glass slides, the ostemer, along with the flexible substrate was peeled off from the PDMS mold resulting in a solid, but flexible and yet sticky polymer (Figure 2.18.IV).

The functional chip, which must contain all the connections (inlets and outlets) to allow for fluid circulation, is prepared from the patterned ostemer (Figure 2.18.V and VI).

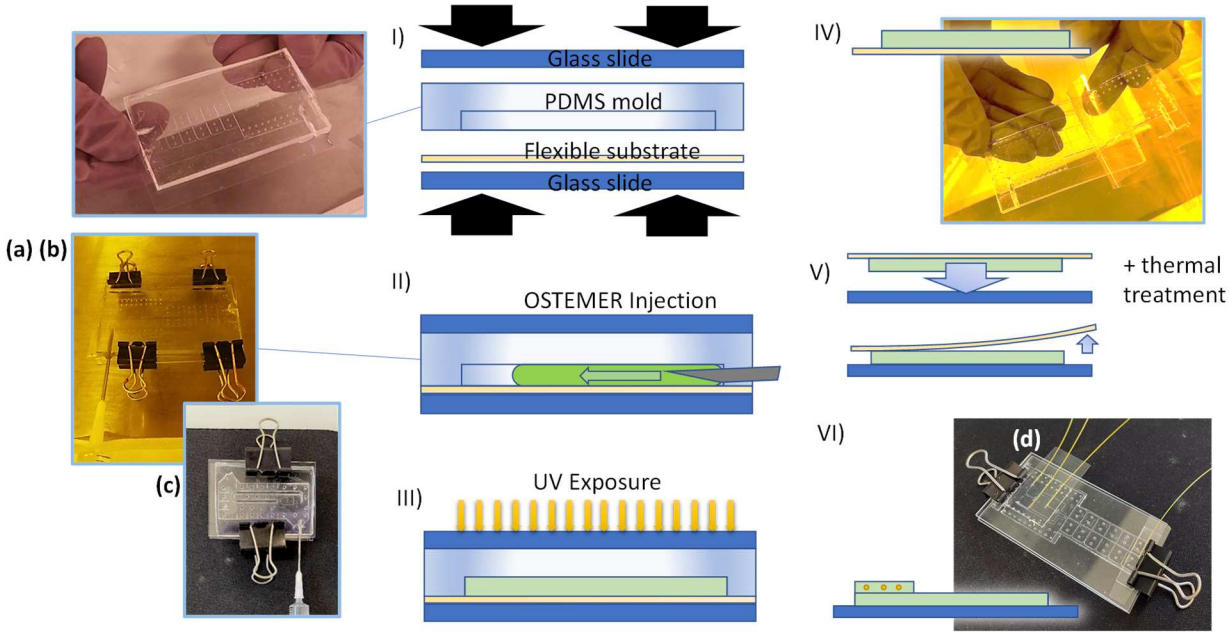

Figure 2.18 (I) PDMS replicate (a) is sandwiched between two glass slides with a flexible substrate on one side and the sandwich is clamped (b), (II) OSTEMER injection (c), (III) UV exposure to cure the OSTEMER polymer, (IV) OSTEMER chip on the flexible substrate, (V) Transfer of the OSTEMER chip onto a glass slide, (VI) Another OSTEMER part including connecting channels is placed on top (d), the tubings being finally inserted and glued

Bibliography

(1) Maes, J.; Castro, N.; De Nolf, K.; Walravens, W.; Abécassis, B.; Hens, Z. Size and Concentration Determination of Colloidal Nanocrystals by Small-Angle X-Ray Scattering. *Chem. Mater.* **2018**, *30* (12), 3952–3962. https://doi.org/10.1021/acs.chemmater.8b00903.

(2) Castro, N.; Bouet, C.; Ithurria, S.; Lequeux, N.; Constantin, D.; Levitz, P.; Pontoni, D.; Abécassis, B. Insights into the Formation Mechanism of CdSe Nanoplatelets Using in Situ X-Ray Scattering. *Nano Lett.* **2019**, *19* (9), 6466–6474. https://doi.org/10.1021/acs.nanolett.9b02687.

(3) Abécassis, B.; Bouet, C.; Garnero, C.; Constantin, D.; Lequeux, N.; Ithurria, S.; Dubertret, B.; Pauw, B. R.; Pontoni, D. Real-Time in Situ Probing of High-Temperature Quantum Dots Solution Synthesis. *Nano Lett.* **2015**, *15* (4), 2620–2626. https://doi.org/10.1021/acs.nanolett.5b00199.

(4) Kikhney, A. G.; Svergun, D. I. A Practical Guide to Small Angle X-Ray Scattering (SAXS) of Flexible and Intrinsically Disordered Proteins. *FEBS Lett.* **2015**, *589* (19 Pt A), 2570–2577. https://doi.org/10.1016/j.febslet.2015.08.027.

(5) Als-Nielsen, J.; McMorrow, D. *Elements of Modern X-ray Physics*, 1st ed.; Wiley, 2011. https://doi.org/10.1002/9781119998365.

(6) *What is measured in a Small Angle X-ray Scattering (SAXS) ?*. IRAMIS. https://iramis.cea.fr/Phocea/Vie_des_labos/Ast/ast_sstechnique.php?id_ast=1065 (accessed 2022-10-12).

(7) Boldon, L.; Laliberte, F.; Liu, L. Review of the Fundamental Theories behind Small Angle X-Ray Scattering, Molecular Dynamics Simulations, and Relevant Integrated Application. *Nano Rev.* **2015**, *6*, 25661. https://doi.org/10.3402/nano.v6.25661.

(8) Moscoso Londoño, O.; Tancredi, P.; Rivas Rojas, P.; Muraca, D.; Socolovsky, L.; Knobel, M. Small-Angle X-Ray Scattering to Analyze the Morphological Properties of Nanoparticulated Systems. In *Handbook of Materials Characterization*; 2018; pp 37–75. https://doi.org/10.1007/978-3-319-92955-2_2.

(9) *Model Functions — SasView 5.0.5 documentation*. https://www.sasview.org/docs/user/qtgui/Perspectives/Fitting/models/index.html (accessed 2022-10-12).

(10) Fracchia, M.; Ghigna, P.; Vertova, A.; Rondinini, S.; Minguzzi, A. Time-Resolved X-Ray Absorption Spectroscopy in (Photo)Electrochemistry. *Surfaces* **2018**, *1* (1), 138–150. https://doi.org/10.3390/surfaces1010011.

(11) Kelly, S. D.; Hesterberg, D.; Ravel, B. Analysis of Soils and Minerals Using X-Ray Absorption Spectroscopy. In *Methods of Soil Analysis Part 5—Mineralogical Methods*; John Wiley & Sons, Ltd, 2008; pp 387–463. https://doi.org/10.2136/sssabookser5.5.c14.

(12) Newville, M. Fundamentals of XAFS, 2020. https://github.com/newville/Fundamentals-of-XAFS (accessed 2022-10-14).

(13) Zhang, N.; Wang, W.; Zhou, T.; Tian, Y.; Chu, W. Exploring Structure-Function Relationship of Two-Dimensional Electrocatalysts with Synchrotron Radiation X-Ray Absorption Spectrum. *Curr. Chin. Sci.* **2020**, *01*. https://doi.org/10.2174/2210298101999201008142619.

(14) Lengke, M. F.; Ravel, B.; Fleet, M. E.; Wanger, G.; Gordon, R. A.; Southam, G. Mechanisms of Gold Bioaccumulation by Filamentous Cyanobacteria from Gold(III)-Chloride Complex. *Environ. Sci. Technol.* **2006**, *40* (20), 6304–6309. https://doi.org/10.1021/es061040r.

(15) Kunkely, H.; Vogler, A. Photooxidation of N,N'-Bis(3,5-Di-Tert.-Butylsalicylidene)-1,2-Diamino Hexane-Manganese(III) Chloride (Jacobsen Catalyst) in Chloroform. *Inorg. Chem. Commun.* **2001**, *4* (12), 692–694. https://doi.org/10.1016/S1387-7003(01)00301-X.

(16) Quevedo, A. C.; Guggenheim, E.; Briffa, S. M.; Adams, J.; Lofts, S.; Kwak, M.; Lee, T. G.; Johnston, C.; Wagner, S.; Holbrook, T. R.; Hachenberger, Y. U.; Tentschert, J.; Davidson, N.; Valsami-Jones, E. UV-Vis Spectroscopic Characterization of Nanomaterials in Aqueous Media. *J. Vis. Exp.* **2021**, No. 176, 61764. https://doi.org/10.3791/61764.

(17) Englebienne, P.; Hoonacker, A. V.; Verhas, M. Surface Plasmon Resonance: Principles, Methods and Applications in Biomedical Sciences. *J. Spectrosc.* **NaN/NaN/NaN**, *17*, 255–273. https://doi.org/10.1155/2003/372913.

(18) Garitaonandia, J. S.; Insausti, M.; Goikolea, E.; Suzuki, M.; Cashion, J. D.; Kawamura, N.; Ohsawa, H.; Gil de Muro, I.; Suzuki, K.; Plazaola, F.; Rojo, T. Chemically Induced Permanent Magnetism in Au, Ag, and Cu Nanoparticles: Localization of the Magnetism by Element Selective Techniques. *Nano Lett.* **2008**, *8* (2), 661–667. https://doi.org/10.1021/nl073129g.

(19) Nealon, G. L.; Donnio, B.; Greget, R.; Kappler, J.-P.; Terazzi, E.; Gallani, J.-L. Magnetism in Gold Nanoparticles. *Nanoscale* **2012**, *4* (17), 5244–5258. https://doi.org/10.1039/C2NR30640A.

(20) Spalla, O.; Testard, F.; Han, J.; Abecassis, B.; Kong, Q. Cinétique et Mécanisme de Croissance de Nanoparticules d'or Suivis Par UV SAXS and XANES. **2013**. https://doi.org/10.1051/uvx/201301010.

(21) Chen, X.; Schröder, J.; Hauschild, S.; Rosenfeldt, S.; Dulle, M.; Förster, S. Simultaneous SAXS/WAXS/UV–Vis Study of the Nucleation and Growth of Nanoparticles: A Test of Classical Nucleation Theory. *Langmuir* **2015**, *31* (42), 11678–11691. https://doi.org/10.1021/acs.langmuir.5b02759.

(22) Shichibu, Y.; Negishi, Y.; Tsukuda, T.; Teranishi, T. Large-Scale Synthesis of Thiolated Au25 Clusters via Ligand Exchange Reactions of Phosphine-Stabilized Au11 Clusters. *J. Am. Chem. Soc.* **2005**, *127* (39), 13464–13465. https://doi.org/10.1021/ja053915s.

(23) Pham, N.; Radajewski, D.; Round, A.; Brennich, M.; Pernot, P.; Biscans, B.; Bonneté, F.; Teychené, S. Coupling High Throughput Microfluidics and Small-Angle X-Ray Scattering to Study Protein Crystallization from Solution. *Anal. Chem.* **2017**, *89* (4), 2282–2287. https://doi.org/10.1021/acs.analchem.6b03492.

(24) Pham, V. N.; Radajewski, D.; Rodríguez-Ruiz, I.; Teychene, S. Microfluidics: A Novel Approach for Dehydration Protein Droplets. *Biosensors* **2021**, *11* (11), 460. https://doi.org/10.3390/bios11110460.

(25) Martin, A.; Teychené, S.; Camy, S.; Aubin, J. Fast and Inexpensive Method for the Fabrication of Transparent Pressure-Resistant Microfluidic Chips. *Microfluid. Nanofluidics* **2016**, *20* (6), 1–9. https://doi.org/10.1007/s10404-016-1757-7.

(26) Gavira, J. A.; Rodriguez-Ruiz, I.; Martinez-Rodriguez, S.; Basu, S.; Teychené, S.; McCarthy, A. A.; Mueller-Dieckman, C. Attaining Atomic Resolution from in Situ Data Collection at Room Temperature Using Counter-Diffusion-Based Low-Cost Microchips. *Acta Crystallogr. Sect. Struct. Biol.* **2020**, *76* (8), 751–758. https://doi.org/10.1107/S2059798320008475.

(27) Vitry, Y.; Teychené, S.; Charton, S.; Lamadie, F.; Biscans, B. Investigation of a Microfluidic Approach to Study Very High Nucleation Rates Involved in Precipitation Processes. *Chem. Eng. Sci.* **2015**, *133*, 54–61. https://doi.org/10.1016/j.ces.2015.01.062.

(28) Rodríguez-Ruiz, I.; Charton, S.; Radajewski, D.; Bizien, T.; Teychené, S. Ultra-Fast Precipitation of Transient Amorphous Cerium Oxalate in Concentrated Nitric Acid Media. *CrystEngComm* **2018**, *20* (24), 3302–3307. https://doi.org/10.1039/C8CE00358K.

(29) Lu, Z.; McMahon, J.; Mohamed, H.; Barnard, D.; Shaikh, T. R.; Mannella, C. A.; Wagenknecht, T.; Lu, T.-M. Passive Microfluidic Device for Sub Millisecond Mixing. *Sens. Actuators B Chem.* **2010**, *144* (1), 301–309. https://doi.org/10.1016/j.snb.2009.10.036.

Chapter 3 From Prenucleation clusters to nanospheres

In this chapter we will describe the synthesis of gold particles using a large excess of triisopylsilane (TIPS). We start by describing the first *in situ* kinetic studies performed in capillaries or in vials and then we continue with the experiments carried out using the microfluidic chips.
The chapter is organized as follow: the experimental conditions of the synthesis, the size and structure characterization of the final particles are given first, then the different time-resolved *in situ* XAS and SAXS studies are presented. In the last section we will compare the results obtained with the microfluidic chips described in chapter 2 with the ones obtained with classical mixing procedures.

3.1. Size and structure of Au NPs prepared with large excess of TIPS

Ultra-small Au nanoparticles were synthesized by the reduction of $HAuCl_4.3H_2O$ in presence of oleylamine (OY) in hexane thanks to the addition of a concentrated solution of triisopropylsilane (TIPS) at 25°C. The final concentrations of Au, OY and TIPS were 20 mM, 50 mM and 1 M, respectively. According to Eq. 3.1, OY is added in the stoichiometric ratio while TIPS is added in a very large excess compared to the 30 mM needed to reduce completely the 20 mM of Au (III):

$$HAuCl_4 + \frac{3}{2}R_3SiH + \frac{5}{2}C_{18}H_{35}NH_2 \rightarrow Au(0) + \frac{3}{2}R_3SiCl + \frac{5}{2}C_{18}H_{35}NH_3^+Cl^- \qquad \text{Eq. 3.1}$$

When the precursor/OY and silane solutions were mixed manually in a vial, the pale-yellow color of the Au (III) complex solution turned to dark red/brown immediately after the addition of the TIPS solution. The reaction was let undisturbed for 3h at 25 °C to ensure completion. Particles were analyzed by Transmission Electron Microscopy (TEM) and SAXS to get their sizes.

Figure 3.1 shows two representative TEM images of Au NPs obtained after 3h. We observe mainly very small particles on the TEM grids as shown in Fig. 3.1.a. A size distribution of these very small particles was calculated over ~2000 NPs using ImageJ software and the image analysis available. We have found a mean diameter d_m = 1.8 ± 0.1 nm and a relative standard deviation σ/d_m = 14% (Fig. 3.1.c). Larger particles with a mean size of ~ 15 nm were also observed on some TEM images (Fig. 3.1.b). These big particles have a very low occurrence compared to the ultra-small ones. The estimation of the relative number of big particles, *i.e.* with a size larger than 10 nm, and small particles, *i.e.* with a size around 2 nm, was very difficult from the TEM images. High magnifications were indeed needed to observe the very small particles reducing the field of view and therefore limiting the number of big particles

observed. On the other hand, at low magnification we can clearly see the big particles but not the ultra-small ones anymore.

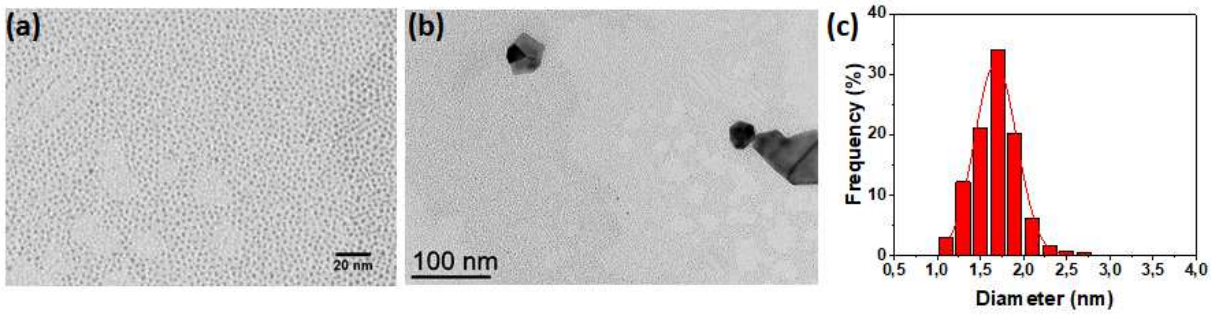

Figure 3.1. (a) (b) TEM image at different magnifications; (b) the corresponding number-weighted size distribution of the ultra-small Au NPs. The size distribution was calculated with the software Image J.

To have a better assessment of the particle size distribution we performed SAXS on the raw NP suspensions. A glass capillary with a diameter of 1.5 mm was filled with the suspension without any purification. The SAXS pattern was recorded by Pierre Roblin at LGC (Toulouse) on a XEUSS 2.0 instrument equipped with a pixel detector PILATUS 1 M (DECTRIS) and a Cu Kα X-ray source provided by GeniX3D (λ = 1.54 Å). The sample to detector distance was fixed to record the SAXS signal in the q range 0.015-1 $Å^{-1}$., corresponding to a size range of 0.6 to 41.9 nm The SAXS signal of the reference capillary containing OY and TIPS in hexane was subtracted from the NP signal. The SAXS of the Au NPs was analyzed using SASVIEW 4.2.2 software.

Figure 3.2.a shows a representative SAXS pattern of an as-prepared Au nanoparticle suspension. The global SAXS signal reminds the form factor of a sphere with a plateau at low q, a "knee" position at q ~ 0.25 $Å^{-1}$ and a Porod signal (q^{-4} law) at high q.

Our first try was to fit the SAXS signal with a single population of nanospheres. The function used was the form factor of a sphere (see chapter 2, Eq. 2.5) with as adjustable parameters the background, the scale and the radius R. We have included in the fit a polydispersity of the size distribution, choosing a Gaussian function. The polydispersity ratio defined as the ratio between the standard deviation, σ, and the mean radius was the 4th adjustable parameter. The result was not completely satisfactory especially at high-q region as it can be seen on figure 3.2.b.

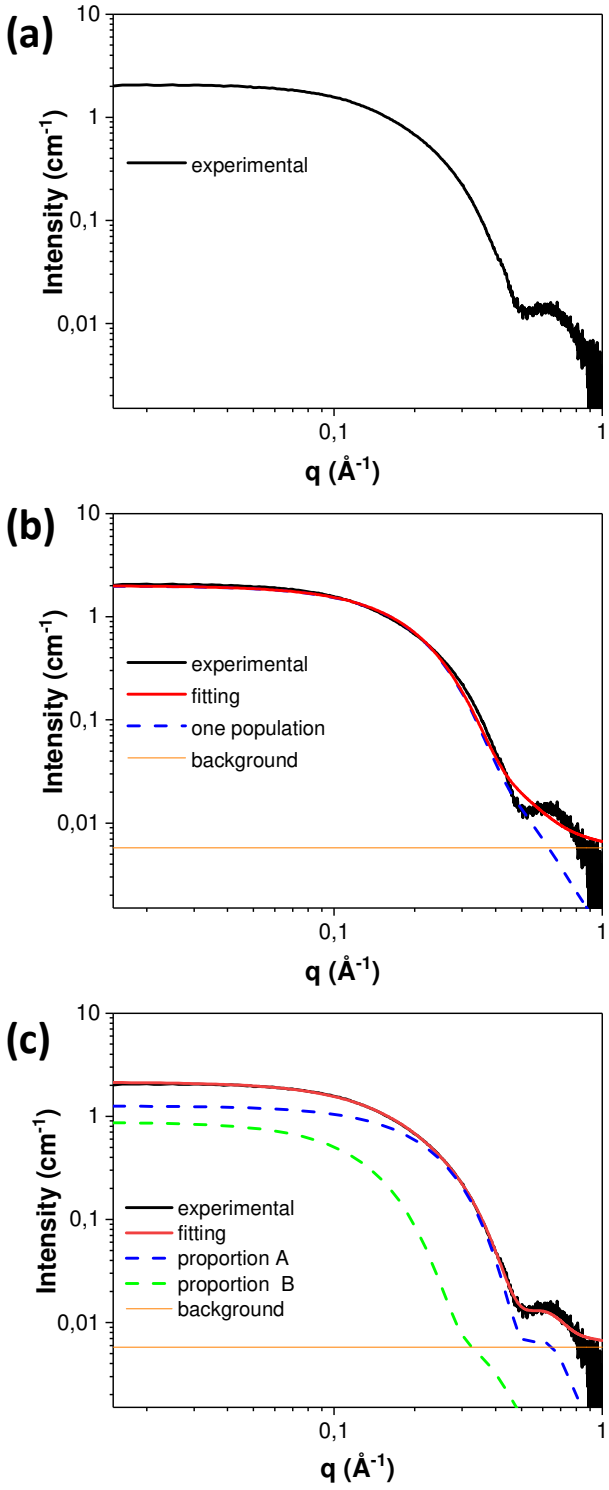

Figure 3.2. (a) SAXS pattern of suspension of Au nanoparticles obtained after 3h of reaction. Fit of the SAXS signal with (b) a single population or (c) two populations of nanospheres. In black: experimental data; red: the corresponding fit considering a constant background (orange) and one or two populations of nanospheres (blue / green dashed lines).

To improve the fit, we used in SASVIEW the model corresponding to a mixture of two populations of spheres. The intensity was thus fitted with a sum of two sphere form factors, including in both cases a polydispersity with a Gaussian function (Eq. 3.2):

$$I(q) = scale\left[\frac{scale_1}{V_1}\left[3V_1(\Delta(\rho).\frac{sin(qr_1)-qr_1cos(qr_1)}{(qr_1)^3}\right]^2 + \frac{scale_2}{V_2}\left[3V_2(\Delta(\rho).\frac{sin(qr_2)-qr_2cos(qr_2)}{(qr_2)^3}\right]^2\right] + background$$

The best fit is displayed in Figure 3.2.c. The diameter (d_m), polydispersity (σ/d_m), and the relative volume fractions for the two populations defined as $scale_1 / (scale_1 + scale_2)$ for population A and as $scale_2 / (scale_1 + scale_2)$ for population B are given in the Table 3.1.

Thus, the best fit evidenced two populations of nanospheres:

- population A (in blue) with a mean diameter of 1.7 nm, called later on the small particles;

- population B (in green) with a mean diameter of 2.6 nm, called later on the larger particles.

Population A				**Population B**				
d_m	**σ/d_m**	**% vol.**	**Scale1**	**d_m**	**σ/d_m**	**% vol.**	**Scale2**	**Total scale**
1.7	0.15	87	2.7×10^{-4}	2.6	0.23	13	4×10^{-5}	3.1×10^{-4}

Table 3.1. Fitting parameters of the two population of spheres used : d_m : mean diameter, σ/d_m polydispersity ratio with σ the standard deviation. Total scale = Scale 1 + Scale 2 and % vol. : is the relative volume fraction calculated as Scale i / Total scale (i=1 or 2)

The small particles are quite homogeneous in size with a polydispersity ratio of 0.15 while the larger ones are more polydisperse with a polydispersity ratio of 0.23. The relative proportion of the small particles and larger particles were 87 % and 13 %, respectively, showing that the small particles are in very large majority. The total scale, which corresponds to the volume fraction, is found around 3.1 x 10^{-4}. This value is larger than the theoretical volume fraction of 2 x 10^{-4} expected for [Au] = 20 mM. This is due to a calibration problem, in our firsts experiments we didn't perform a normalization with water and/or hexane.

According to the overall SAXS signal it seems that there are almost only particles with a size below 3 nm in suspension. We didn't detect by SAXS the very large particles of ~15 nm observed by TEM. The presence of such big particles in suspension would lead to an increased intensity at small *q*. Therefore, the largest particles observed by SAXS are much smaller than the very large particles observed by TEM.

This discrepancy can be explained by :

i) a very small volume fraction of the large particles (> 10 nm), below the detection limit of SAXS.

ii) An overestimation of the number of big particles by TEM. TEM is an ex-situ technique which may induce sampling issue with a proportion of big particles on the grid much higher than the reality. The other reason can be that the big particles appeared on the TEM grid when the suspension was dried because of aggregation, coalescence and recrystallization of small particles into bigger ones.

The atomic-scale structure of the Au NPs was characterized by high-energy X-ray diffraction (HE-XRD) using the synchrotron radiation. HE-XRD data were collected at the ID15A beamline (ESRF, France), using an X-ray beam with an energy of 69 keV (λ= 0.1797Å). Such a high energy allows to record the XRD over a very large *q* range which is necessary for the pair distribution function analysis. In this experiment, the X-ray scattering patterns were recorded using a Pilatus 2M detector in the *q*-range from 0.2 to 22 $Å^{-1}$, corresponding to distances in real space between 0.28 to 31.4 Å.

The nanoparticles in suspension in the mother liquor were sealed in a 1.5 mm diameter capillary. A representative XRD pattern of Au NPs is displayed in figure 3.3. The XRD pattern exhibits very broad bands, as expected for ultra-small particles. This confirms that very large NPs are only in minority, in agreement with SAXS. In the figure 3.3. the XRD pattern is compared to the theoretical bulk *fcc* Au pattern (dashed red line), showing significant differences. The main peak at *q* = 2.795 $Å^{-1}$ is shifted to high *q* compared to the (111) reflection of *fcc* Au (*q* =2.668 $Å^{-1}$). An additional band at *q* = 3.379 $Å^{-1}$ is observed in the XRD patterns while the (200) lines of *fcc* Au is expected at *q* = 3.081 $Å^{-1}$.

Such difference is not only due to a difference of lattice parameter. Indeed, the theoretical ratio $q_{(200)}/q_{(111)}$ for the *fcc* structure is equal to $\sqrt{4/3} = 1.15$ while the ratio between the *q* values of the two first peaks is 1.21, so significantly different. Thus, we can conclude that the Au nanoparticles do not crystallize in the *fcc* structure.

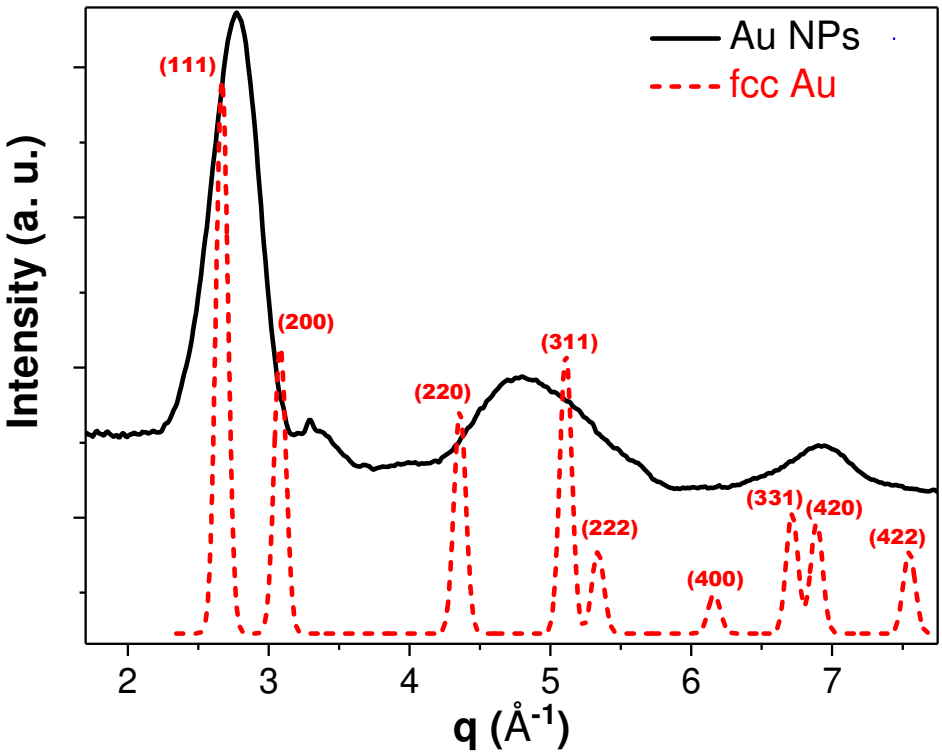

Figure 3.3. In situ high-energy X-Ray diffraction of gold nanoparticles (the dash red line corresponds to the theoretical XRD pattern of *fcc* Au with an arbitrary line broadening)

In order to have a better description of their atomic-scale structure, the pair distribution function (PDF) was extracted and compared with different models. This analysis was done by Valeri Petkov, professor at Central Michigan University, who collaborates with the team.

In figure 3.4.a the PDF of the Au NPs is displayed. The G(r) oscillations observed on the PDF is found to extend in the r-space till ~1.7 nm. The atomic correlation length is therefore close to the mean diameter measured by SAXS. The experimental PDF was compared with the theoretical PDFs of two particles containing 309 atoms (1.7 nm in diameter): a cuboctahedron with the *fcc* structure (CBO) and an icosahedron (ICO). The structure bears some similarities to that of bulk *fcc* Au, but the relative intensity of the peaks and the overall shape of the PDFs discard the CBO model, which confirms the non *fcc* structure of the particles. In contrast, the PDF of the 309 atoms ICO reproduces the experimental data reasonably well as shown in the figure 3.4.b.

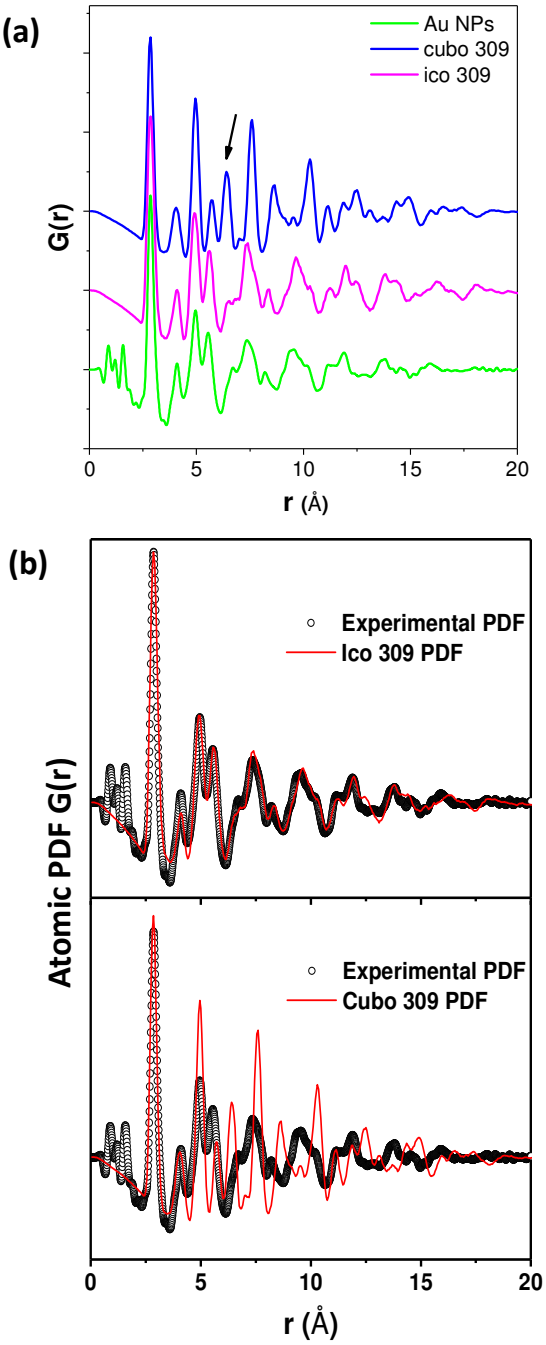

Figure 3.4. (a) in situ atomic pair distribution function and comparison with CBO is 309 atoms cuboctahedron with *fcc* structure, ICO is a 309 atoms icosahedron, (b) Comparison between experimental PDF of Au NPs (black circle) with atomic PDF of ICO (up) and PDF of CBO (bottom).

In conclusion, both SAXS and HE-XRD characterizations showed that we were able to reproduce the synthesis of monodisperse ultra-small Au nanoparticles that crystallize with an icosahedral structure as previously reported in the team.

3.2. *In situ* X-ray absorption spectroscopy: kinetic study

As previously described in chapter 2, XAS allows to get quantitative information about the Au speciation during the reaction. The time-resolved XAS spectra can indeed be fitted by a linear combination analysis (LCA) of three components, Au (III), Au (I) and Au (0) to determine their relative concentration during the reaction. Measuring this evolution is really important to have a better understanding of the chemical pathways of the Au NPs formation.

For the *in-situ* experiments 3 mL of a solution containing $HAuCl_4 \cdot 3H_2O$ (40 mM) and OY (100 mM, 200 mM or 800 mM) dissolved in hexane and 3 mL of a TIPS (2M) solution in hexane were prepared so as to obtain the concentrations classically used once the two solutions are mixed. The chemical reduction was achieved by injecting equal volumes of both solutions, at the rate of 10 $mL.min^{-1}$, in a T-micromixer (IDEX-HS P-712) using PHD 22/2000 syringe pumps (Harvard apparatus, Figure 3.5). The mixing time, estimated from the Falk and Commenge correlation, is 40 ms.[1]

In situ energy dispersive X-ray absorption spectroscopy (XAS) experiments were carried out at the ODE beamline (SOLEIL, France). XAS was recorded at the Au L_{III}-edge in transmission mode. Due to the low concentration of Au, a PMMA cuvette of 2.5 mL with a 10 mm optical path was employed for XAS studies. Due to the position of the X-Ray beam, a dead volume of 0.75 mL was faced (Figure 3.5). Since we used a total flow rate of 20 $mL.min^{-1}$, the dead volume was filled after 2.25 s. The first XAS spectrum was acquired 4 s after the mixing, time-resolved XAS signals were then recorded every 0.36 s.

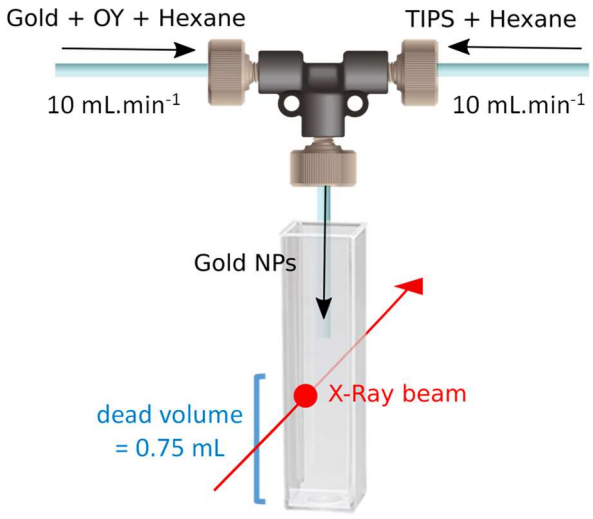

Figure 3.5. Set-up used for the XAS experiments at ODE beamline at SOLEIL. The gold and OY concentrations in the syringe on the left were 40 and 100 mM, the TIPS concentration in the syringe on the right was 2 M to lead to the final concentration of [Au] = 20 mM, [OY] = 50 mM and [TIPS] = 1M once mixed together.

The XAS spectra at the Au L_{III}-edge recorded from the first spectra (4 s) to 30 min are displayed in figure 3.6. One can clearly see an evolution of the XAS signal as a function of time.

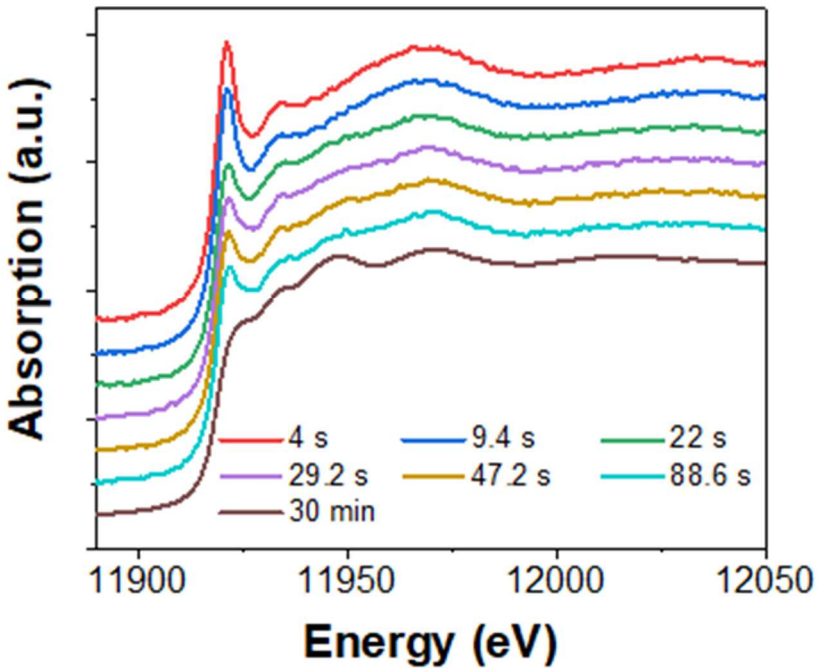

Figure 3.6. In situ XAS spectra at the Au L_{III}-edge recorded during the reduction of $HAuCl_4.3H_2O$ in OY/hexane by adding TIPS

To quantify and understand this evolution, XAS spectra at the Au L_{III}-edge were recorded for three relevant species exhibiting gold oxidation states of +3, +1 and 0. These three references were prepared as follow:

- the Au (III) reference was a fresh solution of the Au (III) precursor. It was prepared by dissolving $HAuCl_4.3H_2O$ in solution of OY in hexane. The concentrations of Au and OY were 20 mM and 50 mM, respectively.
- the Au (I) reference was the lamellar phase of formula OY-Au(I)-Cl. It was prepared according to a protocol previously established in the team.[2] $HAuCl_4{\cdot}3H_2O$ (20 mM) was dissolved in pure OY (5 mL) and left at room temperature for 48h. A white precipitate appeared which was the OY-Au(I)-Cl compound. It is used as prepared for the Au (I) XAS measurement.
- the Au (0) reference was the Au NPs suspension obtained after 3h of reaction in the classical conditions (20 mM of $HAuCl_4.3H_2O$, 50 mM OY and 1 M TIPS in hexane).

The Au L_{III}-edge XAS spectra of the three refences are given in figure 3.7. The XAS spectrum of the Au (III) reference exhibits an intense peak, called white line, at around 11921.2 eV (Figure 3.7.a). This energy is the signature of Au in the +3-oxidation state[3,4,5]. The XAS spectrum of the Au (I) is very different from the Au (III) compound (Figure 3.7.b) :

i) the edge is shifted to 11922.2 eV.

ii) the intensity of the white line is very attenuated compared to the Au (III) signal.

The edge energy and the shape of the XAS spectrum are both characteristic of an Au(I) compound[3,4,5].

The XAS spectrum of the Au NPs is fairly similar to the XAS spectrum of a gold foil (Figure 3.7.c). The two broad peaks at 11 948.5 eV and 11 970 eV, which do not appear in the XAS spectra of the Au(III) and Au(I) references, are characteristic of Au(0). We notice however that these two peaks are broader in the spectrum of the Au NPs.

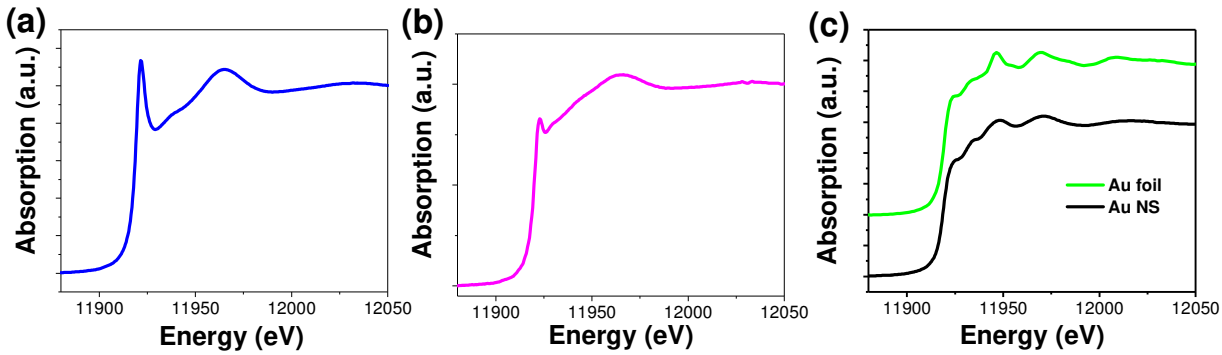

Figure 3.7. In situ Au L_{III}-edge XAS of the (a) Au (III) reference prepared by freshly dissolving $HAuCl_4$, $3H_2O$ with OY in hexane, (b) Au (I) reference obtained from the OY-Au(I)-Cl lamellar phase prepared in pure OY[2] and (c) Au (0) compounds consisting of Au foil (in green) and Au NPs obtained after 3h of reaction (in black) [6].

Coming back to the Figure 3.6, at first glance, the spectra clearly evidenced the reduction of the oxidized Au species, revealed by the characteristic white line at 11 921.2 eV, towards Au(0). After 30 min, the XAS spectrum is indeed similar to the one of Au NPs, indicating that most of Au(III) ions have been reduced to Au(0).

To assess quantitatively the gold speciation as a function of time, the time-resolved XAS spectra were fitted by a linear combination of the three references of figure 3.7. The linear combination analysis

(LCA) was performed using the software PrestoPronto. As an example, the fit of a representative XAS spectrum, recorded at t = 29 s, is shown in figure 3.8. A relative concentration of 38% of Au(III), 18% of Au(I) and 44% of Au(0) was found in that case.

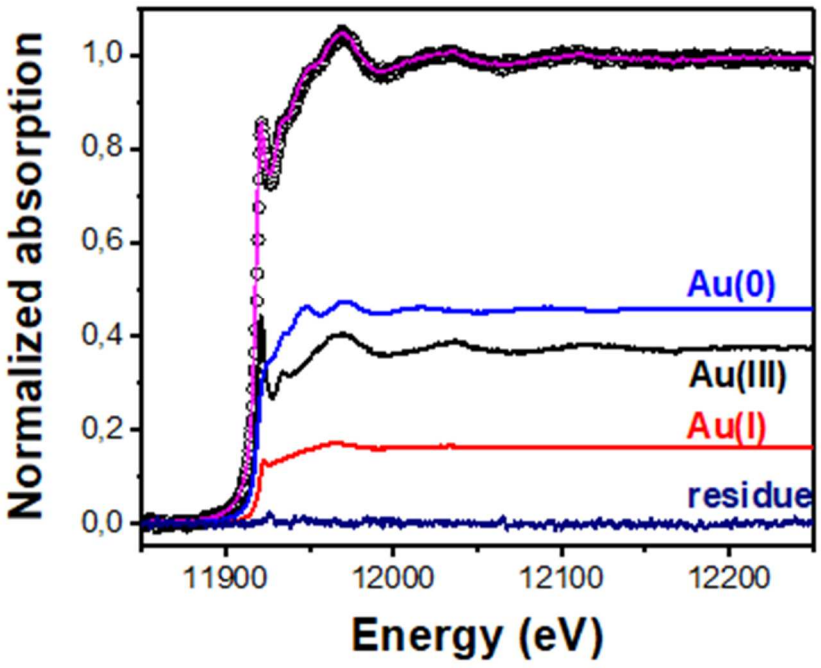

Figure 3.8. Fit of the experimental XAS spectrum recorded at t = 29 s after the mixing (open circle) by a linear combination of three components (magenta line) : Au (III) precursor (in black), Au (I) intermediate (in red) and the final Au (0) NPs (in blue)[6]. The residue, corresponding to the difference between the fit and the experimental values is indicated in dark blue.

The relative concentrations of Au (III), Au (I) and Au (0) deduced from the LCA as a function of time are plotted in Figure 3.9.a for short time range (from 4 to 120 s) and in Figure 3.9.b for longer time range (up to 25 min).

In the Figure 3.9.a, three stages can be defined: the induction period, the nucleation, and the growth stage. Straight after the addition of TIPS, Au(I) is observed in the medium. During the first 10 s, the reduction seems to be limited to Au(III) -> Au(I) since the Au(0) concentration remains fairly low. As a consequence, this first stage is referred to as the induction period. The second stage corresponds to the onset of Au(0) and its further steep increase. It is interpreted as the nucleation stage and is highlighted by a grey shaded area in figure 3.9.a. During this period, the Au(I) concentration reaches the maximum value of c.a. 35 %. After t = 30 s, the increasing of [Au(0)] is slowed down, which is interpreted as the end of the nucleation and the beginning of the growth stage. It is worth pointing

that 50% of the gold precursor has reacted during the first 30 s, and thus was involved in the nucleation. The remaining 50 % is reduced very progressively during the growth stage, over several tens of minutes.

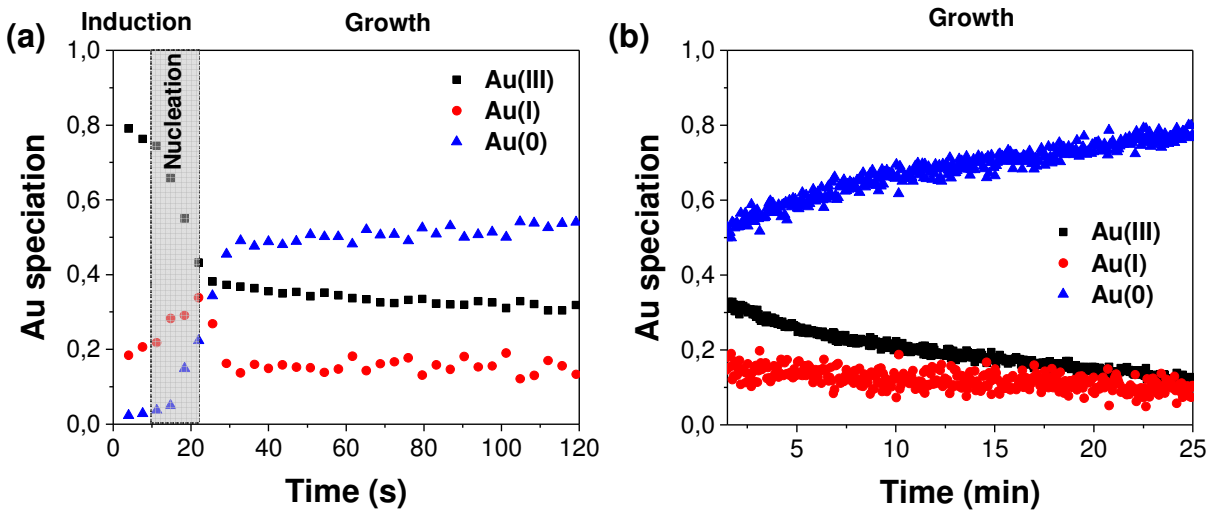

Figure 3.9. Relative Au (III), Au (I) and Au (0) concentrations obtained from the LCA analysis of the XAS spectra measured in situ during the reaction plotted (a) between 0 and 120 s, revealing the three different stages : induction, nucleation (in grey) and growth and (b) between 1.5 and 25 min to follow the reaction during the growth stage[6].

3.3. Comparison with XAS kinetic study using microfluidics

To further improve the time resolution and avoid the dead time of 4 s links with the filling of the PMMA cuvette, XAS studies were repeated using the home-made microfluidic chips, shown in figure 3.10, and previously described in chapter 2. The time-resolved experiments were carried out at the SuperXAS beamline at the Swiss Light Source, Paul Scherrer Institute (PSI) in Villigen (Switzerland). XAS was conducted at the Au L_{III}-edge in fluorescence mode.

Time-resolved XAS signals were collected in two configurations: continuous and stop flow modes.

In continuous flow, the response time depends on the position of the point being probed in the channel relative to the mixer. For that, the chip was moved steadily from a position close to the mixer to

positions further and further away to probe increasing reaction times. This allows to record XAS spectrum for reaction times varying between 100 ms and 30 s. Each acquisition lasted 0.1 s.

To probe reaction times longer than 30 s, the flow was stopped: the reaction was left to proceed homogeneously in the channel. The color change was then observed at a given point of the channel, corresponding to the length of the induction time, and further expand through the whole channel. The XAS signal was recorded up to a time of 1200 s, every 3 or 4 s. To avoid any possible radiation damage, the chip was moved continuously in order to change the beam position in the channel.

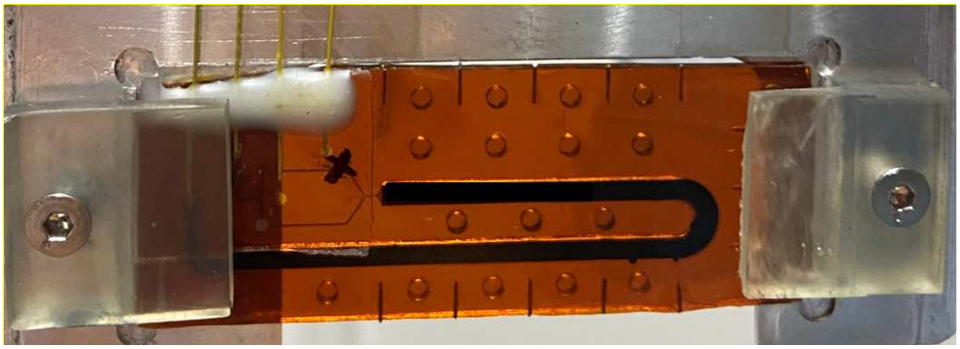

Figure 3.10. Representative image of the chip when using the stop flow mode

The Au(III) and Au(0) references were prepared in the same way as in part 3.2 but the Au(I) reference was prepared by a partial reduction of Au(III) by adding 10 mM of TIPS to a solution containing $HAuCl_4.3H_2O$ (20 mM) and OY (50 mM) in hexane. According to Eq. 3.1, the stoichiometry to reduce completely Au(III) in Au(I) is 1 equivalent of TIPS, i.e. 20 mM. However with such a concentration we noticed sometimes a pink color characteristic of Au(0). In presence of [TIPS] = 10 mM, the yellow color of the precursor solution progressively vanished with time, leading to a white precipitate. This solid phase was then separated from the solution by centrifugation and washed with hexane to discard any Au(III) species remaining. The chemical analysis of the purified precipitate, which will be detailed in chapter 4, revealed that it has indeed the OY-Au(I)-Cl composition.

This OY-Au(I)-Cl compound, which is prepared through a fairly similar reaction in presence of TIPS, has been preferred to the lamellar phase produced in pure oleylamine to serve as Au(I) reference.
The three references have been directly injected in the microfluidic channel to record the Au L_{III}-edge XAS spectra, presented in figure 3.11. As expected, the spectra of the Au(III) and Au(0) references are identical to the one used at SOLEIL. On the other hand, the XAS spectrum of the Au(I) reference was slightly different: the intensity of the white line is lower with this new preparation. One reason could

be that in the previous protocol a small part of Au(III) was not reduced and remained with the OY-Au(I)-Cl lamellar phase. As we will see later this difference does not change too much the results.

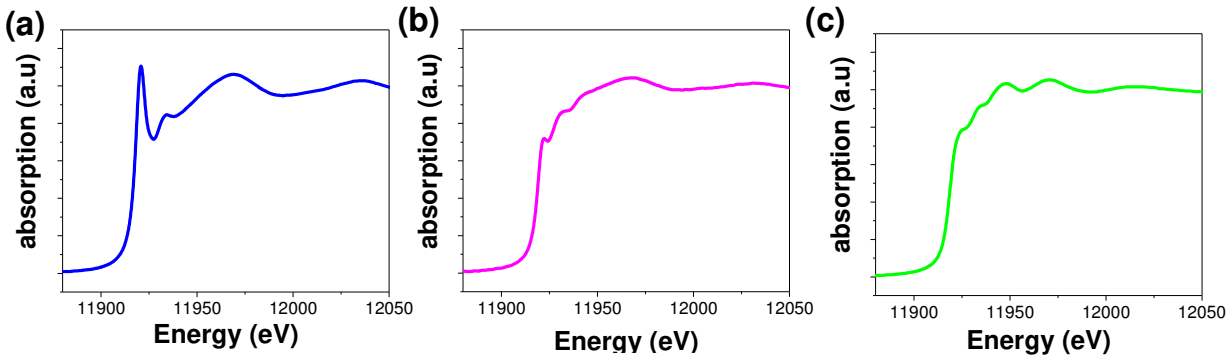

Figure 3.11. In situ Au L_{III}-edge XAS of the (a) Au (III), (b) Au (I) and (c) Au (0) compounds used as references for SuperXAS experiments.

The XAS spectra at the Au L_{III}-edge at different reaction times are displayed in figure 3.12.a with an example of a linear combination analysis for t = 30 s (figure 3.12.b). The Au speciation resulting from the LCA is similar to the one presented above. Thanks to the use of the microfluidic chip, the time resolution has been greatly improved. The Au(III) variation all over the induction and nucleation stages and Au(I) maximum are better defined with the microfluidic set-up. However, the measurements made at very short times, *i.e.* before 3 s were not satisfactory as one can see in figure 3.13.a. Indeed during the first 3 s, the Au(III) concentration is increasing while [Au(I)] is decreasing, which does not have any physical meaning. We can suppose that the flow of the solution close to the mixer is probably less homogeneous than expected because of the drastic change in the dimension. The mixing part corresponds indeed to a channel of 20 µm x 50 µm while the observation channel mandatory for XAS experiments is much larger (2 x 2 mm). Therefore, the reaction times close to the mixer are probably not the ideal ones given by the calculations.

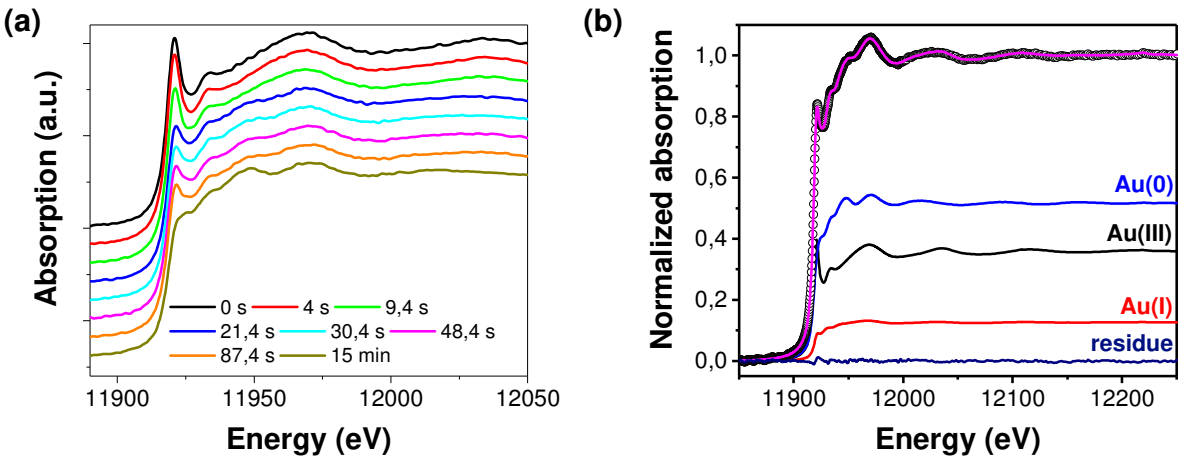

Figure 3.12. (a) In situ XAS spectra at the Au L_{III}-edge recorded during the reduction of $HAuCl_4.3H_2O$ in OY/hexane by adding TIPS; (b) fit of the XAS spectrum at 30 s by a linear combination of three components (magenta line): Au (III) precursor (black), Au (I) intermediate prepared by partial reduction with [TIPS] = 10 mM (red) and the final Au (0) NPs (blue), the residue is in dark blue.

Looking in details the evolution of the three Au species with times, the nucleation step can be observed at ~ 10 s. From 24 s onwards, we observe a clear break in the decrease of [Au(III)] and in the rate of the [Au(0)] increase. 24 s is also the time when the Au(I) concentration returns to a fairly constant value of ~12%, after having passed a maximum. At this time around 60 % of Au(III) has been reduced and 50 % of Au(0) has been formed. This study confirms that 50 % of Au is involved in the nucleation stage and 50 % remains for the growth stage.

All along the growth stage, *i.e.* for t > 24 s, it is noticeable that the Au(0) increase is almost linear. This observation will be analyzed in more details in the next chapters. The comparison of the results obtained previously at SOLEIL with the T-mixer and the PMMA cuvette and these ones, obtained with the microfluidic chip, shows that the nucleation stage occurred earlier. Indeed, the nucleation stage extended from 10 to 22 s in the microfluidic chip, while with the T-mixer/PMMA cuvette it extended from 15 s to 30 s (see Figure 3.9). This difference may be due to a faster mixing in the microfluidic chip.

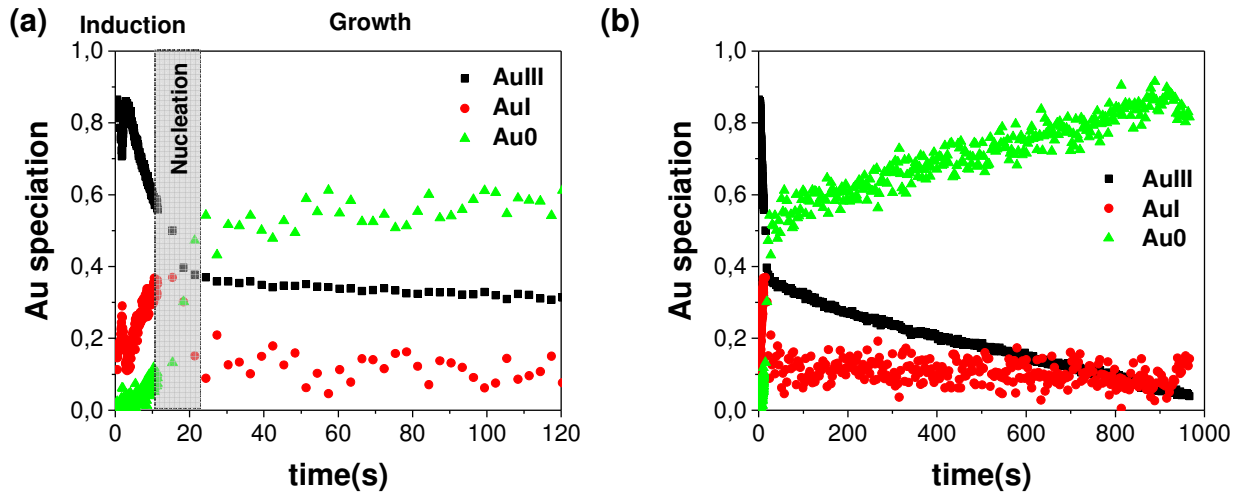

Figure 3.13. Relative Au (III), Au (I) and Au (0) concentrations obtained from the LCA analysis of the XAS spectra measured in situ during the reaction (a) plotted between 0 and 120 s and (b) between 0 and 1000 s.

In conclusion, the use of the microfluidic chip for the in situ XAS studies allowed to improve the time resolution which is very useful when we will try to fit the data with kinetic models. Further improvements on the design of the chip are however still necessary to catch the very short times.

3.4. In situ small angle X-ray scattering: from the precursor solution to a kinetic study

3.4.1. SAXS characterization of the precursor solution

The precursor solution containing $HAuCl_4.3H_2O$ (20 mM) and OY (50 mM) dissolved in hexane was first studied with the SAXS equipment at LGC in Toulouse. The SAXS signal ranging from q = 0.01 to 0.5 $Å^{-1}$ (d = 12 – 628 Å) is given in the Figure 3.14.a. Interestingly, scattering objects are already observed. The SAXS signal can be described by a Guinier regime with a plateau in the small-q range, a ''knee-feature'' at q ~ 0.1 $Å^{-1}$ and a Porod regime in the high-q region.

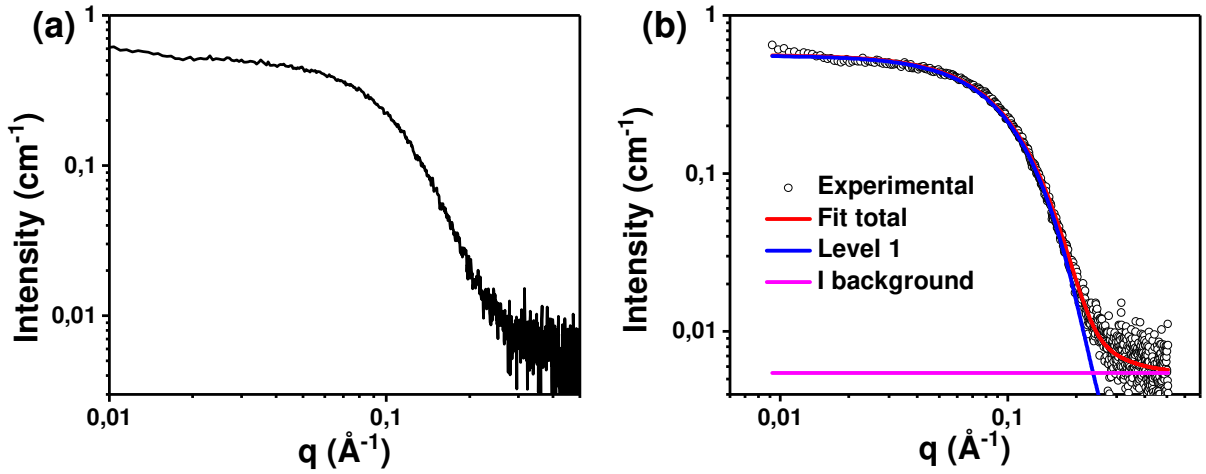

Figure 3.14. (a) SAXS pattern of the precursor solution containing $HAuCl_4.3H_2O$ (20 mM) and OY (50 mM) dissolved in hexane; (b) fit with a Beaucage equation (Eq. 3.3)[6].

In Table 3.2 are reported the scattering length density (SLD) of the different molecules present in the system and of several gold complexes. The SLD values of OY and hexane are very close. It means there is no contrast in the electronic density between OY and hexane. So, the scattering intensity of the precursor solution cannot come from the presence of organic molecules like OY. Such a significant scattering intensity indicates that we have molecular clusters involving gold in the precursor solution. These can be ion pairs consisting in the complex $[AuCl_4]^-$ and a protonated OY, $[Au(III)Cl_4]^-OYH^+$, or a neutral gold complex such as $Au(III)Cl_3$ – OY since their SLD are twice the one of hexane.

Name	Molecular formula	V_m (nm^3)	ρ^e ($e.nm^{-3}$)
Hexane	C_6H_{14}		230 [a]
Oleylamine (OY)	$C_{18}H_{37}N$	0.545	280 [a]
Triisopropylsilane (TIPS)	$C_9H_{22}Si$		266 [a]
Amine Au(III) trichloride	$AuCl_3NH_3$	0.134	1047 [b]
Sodium Au(III) tetrachloride	$AuCl_4Na$	0.161	983 [b]
Au(I) chloride	AuCl	0.049	1954 [b]
$TBA^+[Au(III)Cl_4]^-$	$C_{16}H_{36}N_4AuCl_4$	0.563	508 [b]
$OY^+[Au(III)Cl_4]^-$	$C_{18}H_{38}NAuCl_4$	0.679	442 [c]
OY-$Au(III)Cl_3$	$C_{18}H_{37}NAuCl_3$	0.679	415 [c]
OY-Au(I)Cl	$C_{18}H_{37}NAuCl$	0.594	417 [c]
Gold metal	Au(0)		4650 [b]

Table 3.2. Molecular volume (V_m) and electron density (number of electrons per unit volume, ρ^e) of the organic compounds used in the chemical synthesis. The scattering length density (SLD), ρ, is the product of the electron density by the classical radius of the electron $r_e = 2.81794 \times 10^{-15}$ m[6]. [a] values calculated from the molar mass and density; [b] values calculated from the crystallographic structure of the solid; [c] values estimated from the molar volume of oleylamine and $AuCl_3NH_3$ or AuCl.

The SAXS of the precursor solution was fitted with a Beaucage equation[7]:

$$I(q) = G \times exp\left(-\frac{q^2 R_g^2}{3}\right) + B\left(\frac{1}{q}\right)^p + I_{bg}(q) \qquad \text{(Eq. 3.3)}$$

where R_g is the radius of gyration of the scattering objects, p the exponent of the power law in the Porod regime, G a scaling factor and $I_{bg}(q)$ a background intensity corresponding to the incoherent scattering contribution. This work has been done by Raj Kumar Ramamoorthy, post-doc in the team.

The values of the radius of gyration and of the slope of the power law given by the best fitting shown in Figure 3.14.b were R_g = 17.1 Å and p = 3.5. Assuming spherical objects, the average diameter was calculated from the relation $D_{SAXS} = 2\sqrt{5/3}\,R_g$. D_{SAXS} was found equal to 4.4 nm.

The exponent the Porod law, p, contains information of the surface of the objects. For metal particles in suspension it is generally equal to 4. The exponent p = 3.5 reveals surface fractal objects, with an open shape and rough surface. This confirms the "molecular nature" of the clusters, presumably coordination polymer chains in folded conformation.

So, we can say that before introducing the reducing agent, a clustering of the Au (III) complexes was observed that forms scattering objects with a size around 4 nm. These objects will be called pre-nucleation clusters (PNCs) in the following.

3.4.2. *In situ* kinetic study in capillary

3.4.2.1. Experimental details

In situ SAXS synchrotron experiments were carried out at the SWING beamline (SOLEIL, France). SAXS measurements were performed in the transmission mode with X-ray source energy of 12.5 keV using glass capillary of 1.5 mm as container. Briefly, 3mL of a solution containing $HAuCl_4 \cdot 3H_2O$ (40 mM) and OY (100 mM) dissolved in hexane and 3 mL of a TIPS (2M) solution in hexane were prepared. The capillary was filled by injecting equal volumes of $HAuCl_4$/OY solution and TIPS solution, at the rate of 10 ml.min^{-1}, through a T-micromixer (IDEX-HS P-712) using PHD 22/2000 syringe pumps (Harvard apparatus) (Figure 3.15).

In situ SAXS signals were acquired every 2 s. Time-resolved SAXS signals were recorded at two distances of 6.07 m and 0.5 m using Eiger X 4M (Dectris). For further analysis, the two SAXS signals obtained from two different reactions were merged in the region q = 0.15 - 0.2 Å^{-1} in order to cover the full q range from 0.004 to 1.2 Å^{-1}, i.e. corresponding to sizes of 5 to 1570 Å.

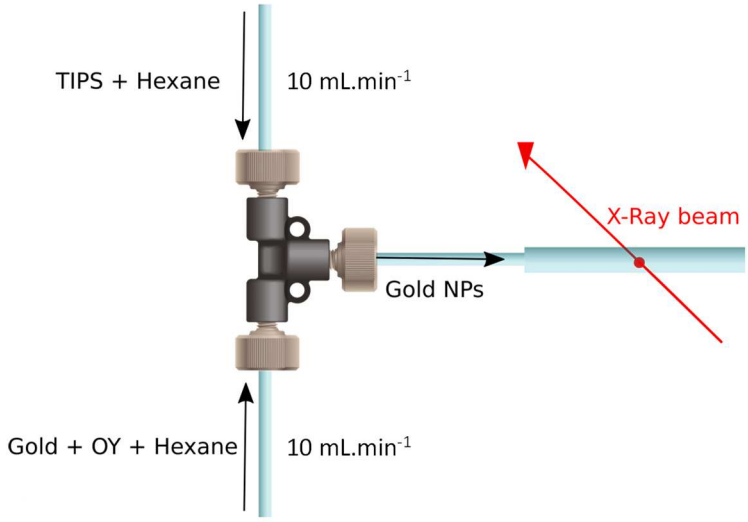

Figure 3.15. Schematic view of the set-up used for the SAXS experiments at SOLEIL (SWING beamline). The gold and OY concentrations in the lower syringe were 40 and 100 mM, respectively. The TIPS concentration in the upper syringe was 2 M.

3.4.2.2. *In situ* SAXS results

The in situ SAXS recorded at different reaction times are given in figure 3.16.a and b from 4 to 38 s and from 48 s to 30 min, for clarity. The nice overlap of the SAXS signals recorded from the two detector positions, all along the reaction time, indicated the reproducibility of the reaction.

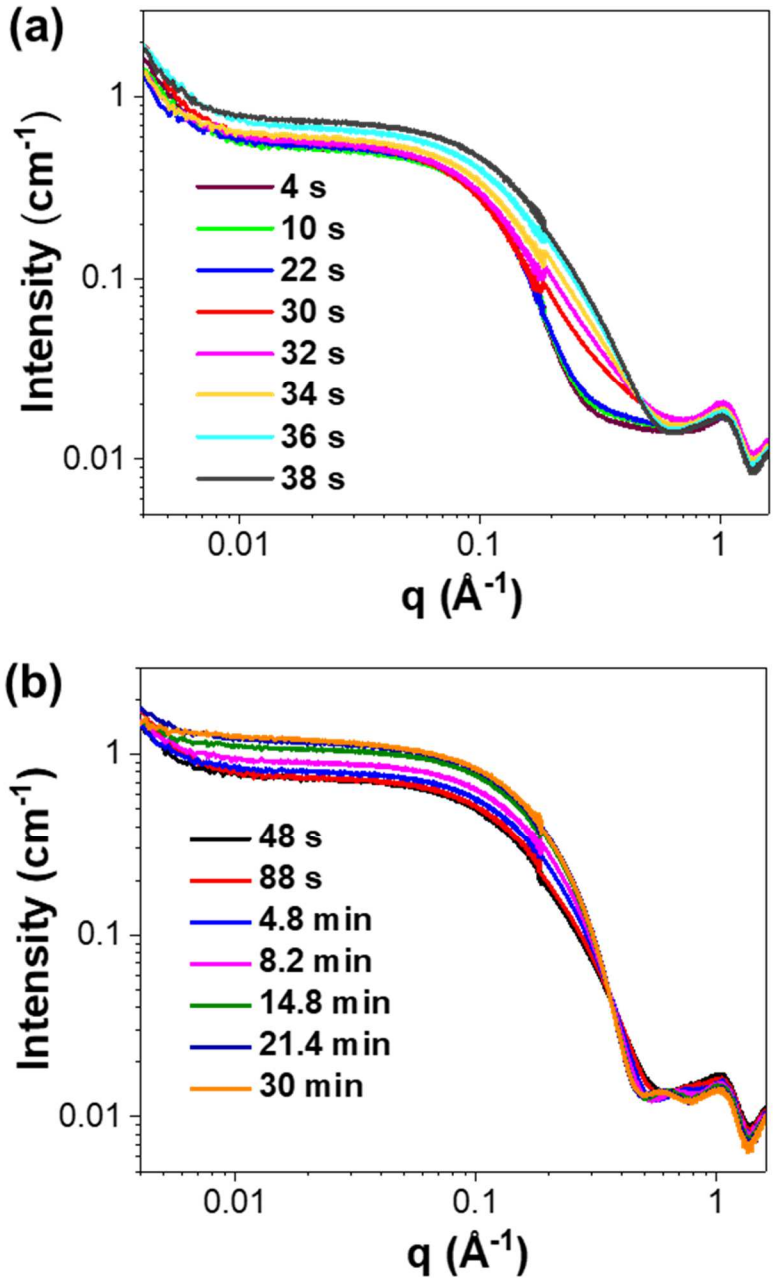

Figure 3.16. In situ SAXS pattern of the Au NPs formation (a) between 4 s and 38 s and (b) between 48 s and 30 min[6]

As we can see in the figure 3.16.a, the scattering intensity is almost constant from 4 s to 22 s. During this period, the SAXS signal is very similar to the pre-nucleation clusters (PNCs) which was observed before adding the TIPS (section 3.4.1). As in the case of the PNC, the SAXS was fitted with a Beaucage model with an additional contribution at very small *q* to consider the increasing intensity in this region. This increase could be due to the formation of bigger objects due to an association of the PNCs.

In our case, the Guinier region for these largest structures was out of the accessible *q* range and thus was not consider in the equation. The Beaucage model thus reads as follow :

$$I(q) = B_1 exp\left(-\frac{q^2 R_{g(2)}^2}{3}\right)\left(\frac{1}{q_1^*}\right)^{p_1} + G_2 exp\left(-\frac{q^2 R_{g(2)}^2}{3}\right) + B_2\left(\frac{1}{q_2^*}\right)^{p_2} + I_{bg}(q) \qquad \text{(Eq. 3.4)}$$

where $q_i^* = q[\mathrm{erf}(\frac{qR_g(i)}{\sqrt{6}})]^3$, B_i are the prefactors for the power law scattering regions, G_2 and R_{g2} are the prefactor for the Guinier region of the PNCs and their radius of gyration, respectively. p_i refers to the exponent corresponding to decay of scattering signal in the power law regions and $I_{bg}(q)$ refers to a background function corresponding to the incoherent scattering contribution.

An example of the resulting fit is given in Figure 3.17.

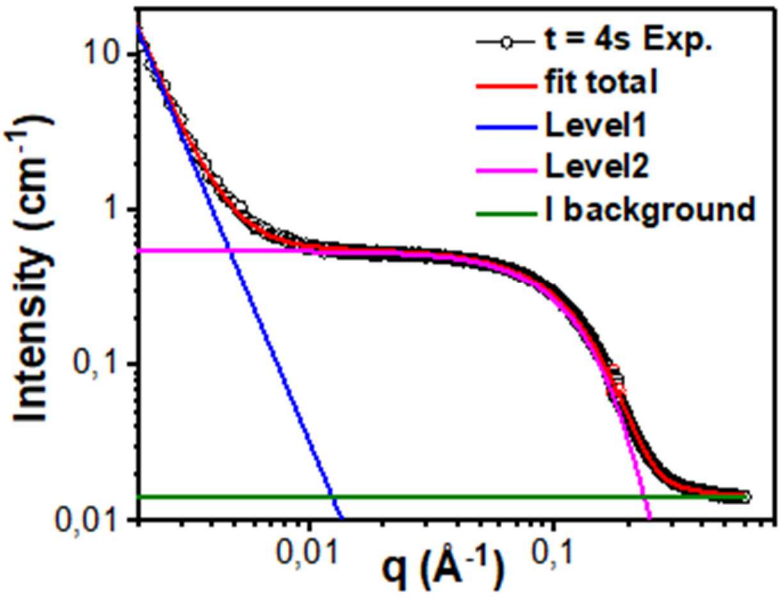

Figure 3.17. Fit of the SAXS signal recorded at t = 4 s, i.e. during the induction period. Open circle : experimental data, red : fit obtained considering diluted (pink) and assembled (blue) PNCs and a constant background corresponding to the incoherent scattering contribution (green)

The results of the fits at different times between 0 and 22 s are reported in Table 3.3. We can see that the diameter of the PNCs decreased a little bit at the beginning of the induction stage and then remained almost constant. The exponent of the power law at low-*q* was also fairly constant around 3.3.

Considering the previous results obtained by XAS (section 3.2), a progressive reduction of Au (III) to Au (I) was observed during the induction stage. By SAXS we can conclude that this partial reduction of Au(III) into Au(I) does not drastically affect the size (D_{SAXS}) nor the surface (indicated by p_2) of the PNCs.

Time	**Pre-nucleation clusters Induction stage**		
	R_{g2} (Å)	**D_{SAXS} (nm)**	**P_2**
0 s	17.1	4.4	3.5
2 s	16.5	4.2	3.5
4 s	14.9	3.8	3.2
10 s	14.8	3.8	3.1
22 s	15	3.9	3.4

Table 3.3. Radius of gyration, R_{g2}, diameter $D_{SAXS} = 2\sqrt{5/3}\,R_{g2}$ and exponent of the power law in the Porod regime p_2 deduced from the fit of the SAXS data using Eq. 3.4 for the induction period[6].

Between t = 22 s and 34 s, we can see on Figure 3.16.a that the scattering intensity changed suddenly with a shift of the ''knee-position'' toward high *q*. It indicates that the size of the objects was rapidly decreasing during this time period. Actually, during this period we have observed in the LCA-XAS analysis the onset and the fast increase of Au(0) with the highest [Au(0)] slope. This period was interpreted as the nucleation stage, and from the SAXS point of view corresponds to the shrinking of the PNCs and the potential appearance of Au(0) particles.

After that, a progressive increase of the intensity of the plateau in the intermediate-*q* range along with a shift of the knee position to low-*q* is observed in the time range t = 36 s - 30 min (Figure 3.16.b), revealing a slight increase of the size of the scattering objects. This time period corresponds to the growth stage previously determined by XAS.

The SAXS patterns in the growth stage was fitted by Raj Kumar Ramamoorthy with a sum of three contributions according to the following equation:

$$I(q) = \alpha \times I_{PNC}(q) + I_{NP}(q) + I_{bg}(q) \quad \text{(Eq. 3.5)}$$

with $I_{PNC}(q)$ the scattering intensity of the remaining precursors (PNCs) and α the weight of the PNC contribution, $I_{NP}(q)$ the scattering intensity of the metal nanoparticles and $I_{bg}(q)$ the background function. The scattering intensity at t = 22 s, i.e. at the end of the induction stage, was taken as reference for the PNC contribution. A Beaucage equation was used for the nanoparticle contribution:

$$I_{NP}(q) = G_{NP} exp\left(-\frac{q^2 R_g^2}{3}\right) + B_{NP}\left(\frac{1}{q}\right)^p + I_{bg}(q) \quad \text{(Eq. 3.6)}$$

The fitting parameters, G_{NP}, R_g, B_{NP} and p take the same meaning as above. An example of fit is given in Figure 3.18.

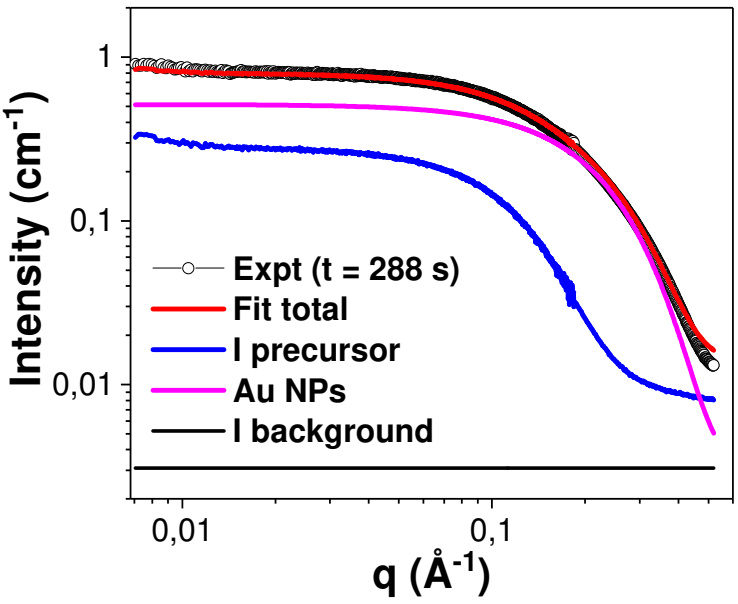

Figure 3.18. Fit of the SAXS signal recorded during the growth stage at t = 288 s. Open circle : experimental data, red : fit obtained considering the PNCs as lastly observed at the end of the induction stage (blue), Au(0) NPs (pink) and a constant background (black)

In Table 3.4 are reported the evolution of the fitting parameters used in the growth regime for reaction times between 36 s and 30 min. When the reaction proceeded, the weight of the PNC contribution decreased and the metal nanoparticle size increased from 1.9 to 2.4 nm. The exponent of the high-*q* Porod regime for the Au NPs was found of 3.7, thus close to 4 which is the expected value for metal particle with smooth surface in the suspension. As revealed by the XAS, the reduction was still not completely finished after 30 min. Thus, this small difference of *p* compared to the expected value could come from i) the disordered surface of the NPs or ii) the adsorption of unreduced species on the NPs surface.

Time	**Metal Nanoparticles Growth stage**			**Relative weight of PNCs**
	R_g (Å)	**D_{SAXS} (nm)**	**P**	**α**
36 s	7.5	1.9	3.7	0.67
48 s	7.6	2.0	3.7	0.65
88 s	7.7	2.0	3.7	0.61
288 s	8	2.1	3.7	0.51
488 s	8.4	2.2	3.7	0.47
688 s	8.8	2.3	3.7	0.37
1088 s	9.4)	2.4	3.7	0.34
1706 s	9.4	2.4	3.7	0.24

Table 3.4. Radius of gyration, R_g, diameter, DSAXS, and exponent of the Porod region, *p*, of the metal nanoparticles and relative weight of the PNCs, α, deduced from the fits of the SAXS data using Eq. 3.5 and 3.6 for the growth period[6].

The mean diameter, D_{SAXS}, of the PNCs during the induction stage and of the Au(0) NPs during the growth stage is plotted in the figure 3.19. On the same figure is also plotted the relative weight of the PNC, α, all over the kinetic deduced from the SAXS fits.

- During the induction stage, the size of the PNCs was almost constant;
- During the nucleation stage, there was a fast shrinkage of the particle size and the relative weight of the PNCs drops rapidly;
- During the growth stage, the mean size of the Au NPs increases slowly and the relative weight of the PNCs decreases slowly.

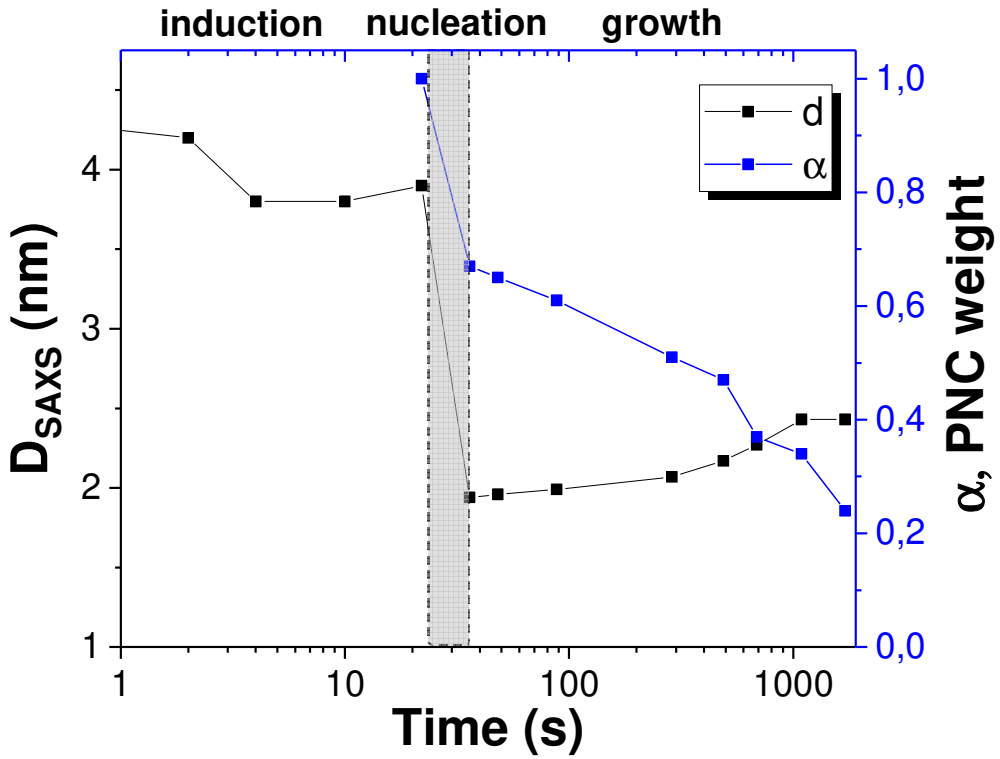

Figure 3.19. Particle mean diameter, $D_{SAXS,}$ as a function of time (black). The particles correspond to the PNCs during the induction period, and to Au NPs during the growth period. The time evolution of the relative weight of the PNCs deduced from Eq. 3.5 is given in blue[6].

3.4.3. In-situ kinetic study using the microfluidic chip

The SAXS experiments in the microfluidic chips were carried out in transmission mode at the c-SAXS beamline at the Swiss Light Source, Paul Scherrer Institute (PSI) in Villigen (Switzerland). X-rays with an energy of 11.5 keV and a beam size of 30 µm x 50 µm (vertical x horizontal) were shine on the sample. The scattered X-ray intensities were recorded at a distance of 2.17 m using a PILATUS 2M detector giving a *q* range from to 0.01 to 0.7 $Å^{-1}$ (corresponding to d = 9 to 628 Å). As previously described for the XAS experiments, short reaction times were acquired in continuous flow while, for the longer reaction time the flow was stopped.

The in situ SAXS recorded at different times during the formation of the Au NPs formation are displayed in figure 3.20. We observed an evolution of the SAXS signal very similar to the one observed in capillary. The scattering intensity of the PNC was constant during the first period from 0 to 16 s. A shift of the "knee" position was observed at 18 s interpreted as the formation of small Au NPs. After 18 s the intensity is increasing both at low and high-*q* values. After 90 s the SAXS signal is almost constant.
In comparison with the SAXS in capillary (Figure 3.16) the shift of the knee position appeared earlier. It confirms what we observed on the XAS data that the reaction is faster in the channel of the microfluidic chip.

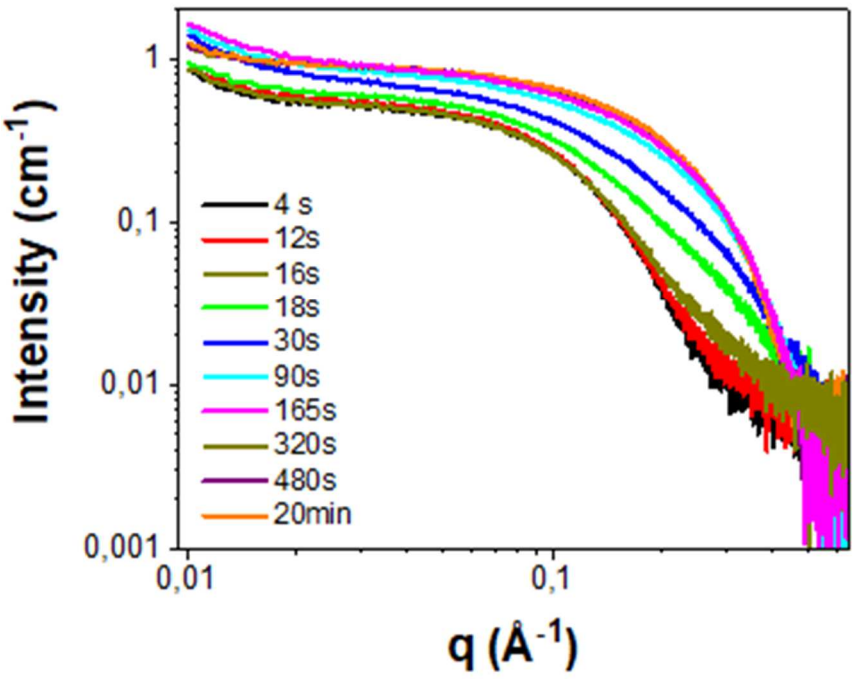

Figure 3.20. In situ SAXS patterns recorded during the Au NPs formation in the microfluidic chip.

3.5. Summary and conclusion

The XAS and SAXS measurements allowed us to define three stages in the formation of the Au NPs, the induction, nucleation and growth stages. Depending on the specificity of each methods the three stages were defined differently.

- With the XAS measurements the induction stage is the period during which we observed only the reduction of Au (III) to Au(I). The nucleation stage starts with the onset of Au (0) and continue with the fast increase of [Au (0)]. We have considered that the nucleation stage stops when we observed a break in the slope with a much lower reduction rate. The nucleation stage extended from 10 s to 22 s when the chip is used while with the T-mixer/PMMA cuvette it extended from 15 to 30 s.
- With the SAXS experiments, only a very slight variation of the SAXS signal was observed during the induction stage. The nucleation stage starts with the shift of the SAXS signal towards the high-*q* values. During the Au NP growth stage the scattering intensity increases and the signal is slightly shifted to the low-*q* values because of a slight increase the mean particle size.

In the figure 3.21 we plotted in the same figure the size measured by SAXS and the different stages identified by XAS[6]:

- induction stage: Firstly, non-reduced pre-nucleation clusters (PNCs) were formed. Secondly, the Au (III) atoms in the PNCs were progressively reduced to Au (I), leading to Au (III) - Au (I) PNCs precursors, without affecting the PNC size.

-nucleation stage: A fast shrinkage of the PNCs' size was observed, leading to small Au(0) metal nuclei. This shrinkage is interpreted as the transition from molecular clusters to metal NPs.

-growth stage: A slow increase of the metal NPs' mean size is observed. The final Au (0) NPs were formed by the reduction of Au (III) and Au (I) PNCs.

From our in-situ studies on the formation of the gold nanoparticles, we showed that the classical nucleation theory can be questioned. Abecassis *et al*[8]. and Chen *et al*[9]. have studied the chemical reduction of gold chloride, using borohydride or borane as reducing agents. They reported that Au(0) free monomers were progressively associated into small Au (0) clusters, leading eventually to stable Au (0) nuclei in agreement with the classical nucleation theory. In our case, the starting solution is not a classical solution of monomers since this gold complex form these aggregates that give a strong signal in SAXS and that we called pre-nucleation clusters. The shrinkage of the pre-nucleation clusters into small Au (0) metal particles seems to indicate that the nucleation is an internal reduction within the

pre-nucleation clusters. In the following chapters we have extended this study to different experimental conditions by varying the concentration of the reducing agent and/or its nature in order to have more data to compare our syntheses with the classical nucleation theory.

One goal of this chapter was to compare the microfluidic set-up with classical mixing conditions. The experiments carried out with the microfluidic chips reproduced well the experiments carried out in capillaries and in cuvettes but the time resolution has been increased. However, at very short times (below 2.5s) we noticed an artefact in the Au speciation calculated from the XAS experiments. This can be due to a mixing issue in the large channel of the chip. This problem will have to be analyzed in detail in the future.

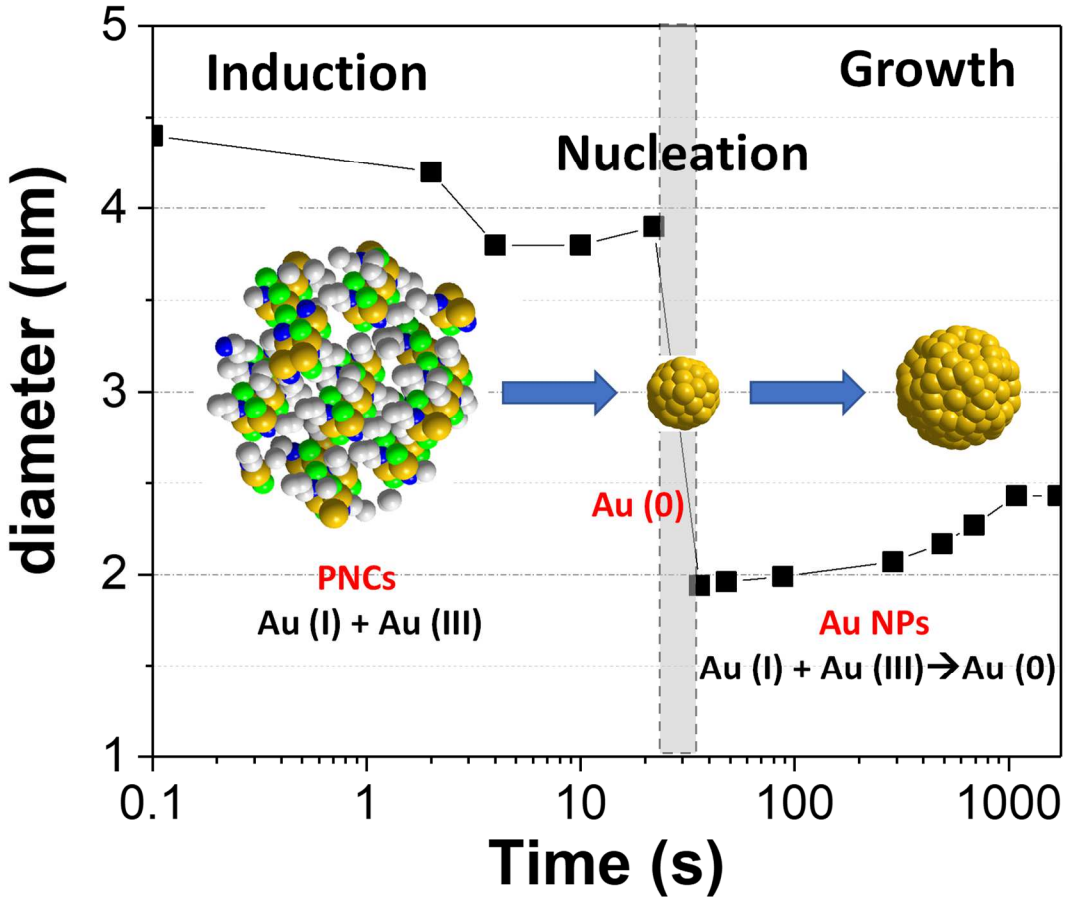

Figure 3.21. Time evolution of the particle mean size as determined by SAXS along with the evolution of the Au speciation, determined by XAS. The grey shaded area shows the nucleation period, determined from the XAS results[6].

Bibliography

(1) Commenge, J.-M. J.-Marc. C.-Lorraine. F.; Falk, L. Performance Comparison of Micromixers. *Chemical Engineering Science* **2010**, *65* (1), 405–411. https://doi.org/10.1016/j.ces.2009.05.045.

(2) Loubat, A.; Lacroix, L.-M.; Robert, A.; Impéror-Clerc, M.; Poteau, R.; Maron, L.; Arenal, R.; Pansu, B.; Viau, G. Ultrathin Gold Nanowires: Soft-Templating versus Liquid Phase Synthesis, a Quantitative Study. *J. Phys. Chem. C* **2015**, *119* (8), 4422–4430. https://doi.org/10.1021/acs.jpcc.5b00242.

(3) Lengke, M. F.; Ravel, B.; Fleet, M. E.; Wanger, G.; Gordon, R. A.; Southam, G. Precipitation of Gold by the Reaction of Aqueous Gold(III) Chloride with Cyanobacteria at 25–80 °C — Studied by X-Ray Absorption Spectroscopy. *Can. J. Chem.* **2007**, *85* (10), 651–659. https://doi.org/10.1139/v07-024.

(4) Parsons, J.; Aldrich, M.; Gardea-Torresdey, J. Environmental and Biological Application of Extended X-Ray Absorption Fine Structure (EXAFS) and X-Ray Absorption near Edge Structure (XANES) Spectroscopies. *APPLIED SPECTROSCOPY REVIEWS Vol. 37* **2002**, *No. 2*, 187–222. https://doi.org/10.1081/ASR-120006044.

(5) Giorgetti, M.; Aquilanti, G.; Ballarin, B.; Berrettoni, M.; Cassani, M.; Fazzini, S.; Nanni, D.; Tonelli, D. Speciation of Gold Nanoparticles by Ex Situ EXAFS and XANES. *Analytical Chemistry* **2016**, *88*. https://doi.org/10.1021/acs.analchem.6b01524.

(6) Ramamoorthy, R. K.; Yildirim, E.; Barba, E.; Roblin, P.; Vargas, J. A.; Lacroix, L.-M.; Rodriguez-Ruiz, I.; Decorse, P.; Petkov, V.; Teychené, S.; Viau, G. The Role of Pre-Nucleation Clusters in the Crystallization of Gold Nanoparticles. *Nanoscale* **2020**, *12* (30), 16173–16188. https://doi.org/10.1039/D0NR03486J.

(7) Beaucage, G. Small-Angle Scattering from Polymeric Mass Fractals of Arbitrary Mass-Fractal Dimension. *J Appl Cryst* **1996**, *29* (2), 134–146. https://doi.org/10.1107/S0021889895011605.

(8) Abécassis, B.; Testard, F.; Spalla, O.; Barboux, P. Probing in Situ the Nucleation and Growth of Gold Nanoparticles by Small-Angle X-Ray Scattering. *Nano Lett* **2007**, *7* (6), 1723–1727. https://doi.org/10.1021/nl0707149.

(9) Chen, X.; Schröder, J.; Hauschild, S.; Rosenfeldt, S.; Dulle, M.; Förster, S. Simultaneous SAXS/WAXS/UV–Vis Study of the Nucleation and Growth of Nanoparticles: A Test of Classical Nucleation Theory. *Langmuir* **2015**, *31* (42), 11678–11691. https://doi.org/10.1021/acs.langmuir.5b02759.

Chapter 4 Synthesis of Au NPs with TIPS: Influence of the Reducing Agent Concentration

We have described in the chapter 3 the synthesis of ultra-small Au NPs from the reduction of a solution of $HAuCl_4.3H_2O$ in hexane ([Au] = 20 mM) in presence of a stoichiometric concentration of OY (50 mM) and a large excess of TIPS (1M). This synthesis is fairly simple to carry out from an experimental point of view but exhibits a complex reaction pathway with the presence of pre-nucleation clusters in the starting Au(III) solution.

As described in the chapter 1, previous studies have shown that the OY concentration plays a key role on the shape control of the NPs: ultra-small nanospheres are obtained at low OY concentration ([OY] < 100 mM) while ultrathin nanowires are stabilized in presence of OY excess. The objective of this chapter is to study the effect of the reducing agent's concentration in the condition of formation of the nanospheres (OY/Au = 2.5), which is so far unknown. Therefore, synthesis with different TIPS concentrations were performed and characterized:

- Firstly, at the final state, to study the impact on the morphology, size and size distribution of the final NPs, using TEM and SAXS.
- Secondly, during the reaction using *in-situ* UV-Vis, XAS and SAXS to understand the influence of the reducing agent concentration on the NP formation.

4.1 Influence of the TIPS concentration on the size distribution

Several batches of Au nanoparticles were prepared by the reduction of $HAuCl_4.3H_2O$ in solution of OY in hexane using TIPS ([Au] = 20 mM; [OY] = 50 mM). The TIPS concentration was varied from 62 mM to 1 M, *i.e.* from a slight to a large excess compared to the stoichiometry, keeping all the other parameters constant and the same protocol.

Briefly, two vials were prepared: the first one containing the precursor solubilized in hexane thanks to OY, the second one containing the TIPS solution in hexane. The vials were placed in a thermostatic bath at 25 °C during 5 min before mixing in order to have an homogenous temperature, identical for both solutions. The reducing agent solution was then added onto the precursor solution. The reaction was manually shaken for few seconds and let to react at 25 °C for 3 h.

In every reaction, the color of the solution turned from pale yellow to dark brown, revealing the onset of the Au particle formation in suspension. The time at which the color change was observed varied with the TIPS concentration from about 3 min, for [TIPS] = 62 mM, to few seconds for [TIPS] = 1M. The final Au NPs were characterized using transmission electron microscopy (TEM). Figure 4.1 shows representative TEM images and the size distributions of Au NPs prepared with [TIPS] = 62, 250 and 500

mM. For a comparison, the TEM images of the Au NPs prepared with [TIPS] = 1M and previously reported in the chapter 3 are also included. Whatever the TIPS concentration, two populations were observed:

- A main population of ultra-small particles with a mean size varying between 1.7 and 1.9 nm and a polydispersity ration σ/dm around 10 % (see Table 4.1)
- Few bigger particles with a mean size of 7.3 nm, 13.0 nm, 10.2 nm and 14.6 nm for [TIPS] = 62 mM, 250 mM, 500 mM and 1 M, respectively

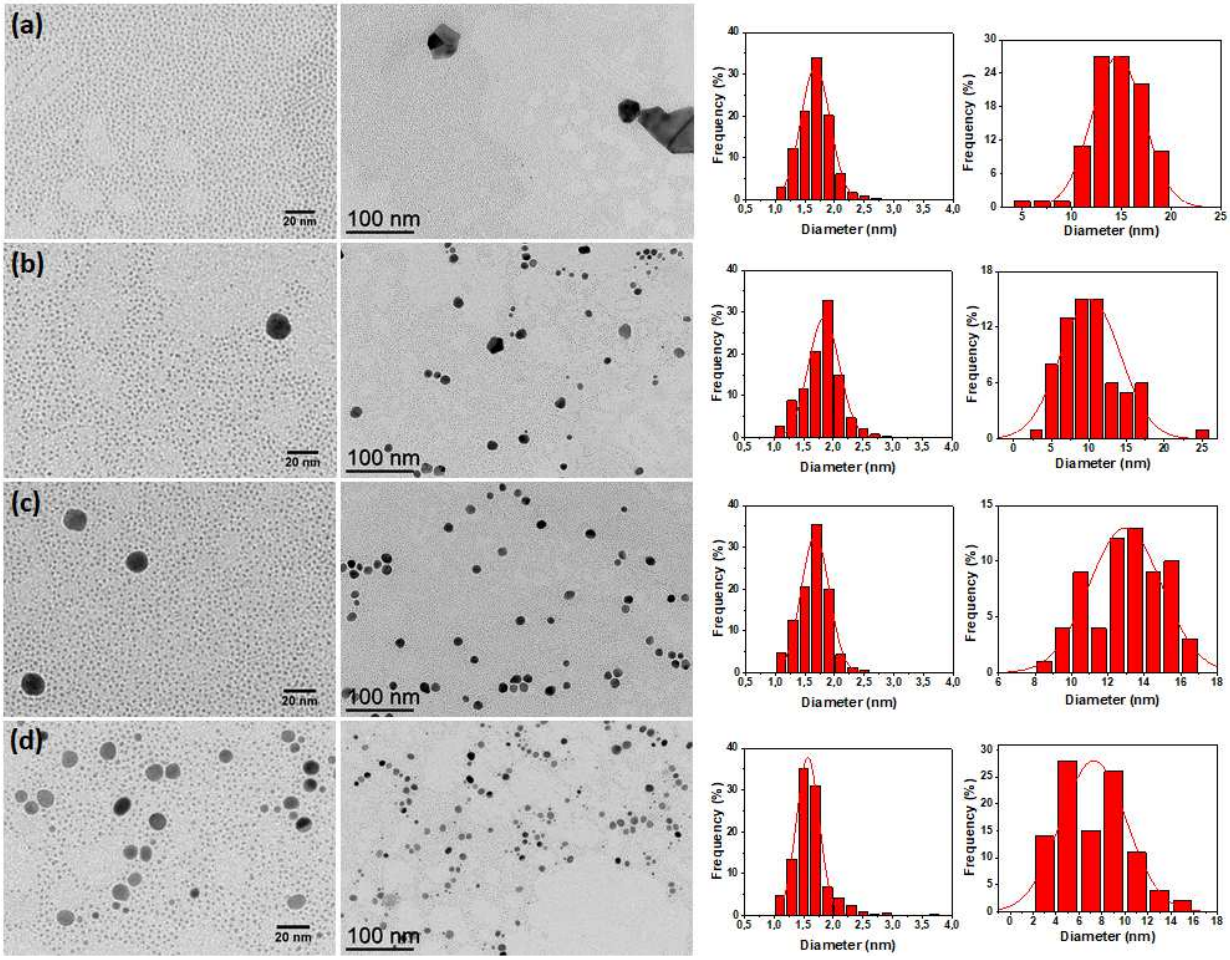

Figure 4.1 TEM images at different magnifications (1st and 2nd column) and the corresponding number-weighted size distribution for the main ultra-small population (3rd column) and bigger NPs (4th column) obtained after 3h of reaction for [TIPS] = (a) 1M, (b) 500 mM, (c) 250 mM and (d) 62 mM. The size distributions were calculated with the ImageJ software over > 2000 NPs for the main population and > 100 NPs for the bigger NPs.

	Main population		**Minor population**	
[TIPS]	**dm**	**σ/d_m**	**Dm**	**σ/d_m**
62 mM	1.7 nm	9 %	7.3 nm	39 %
250 mM	1.8 nm	10 %	13 nm	15 %
500 mM	1.9 nm	8 %	10.2 nm	39 %
1 M	1.8 nm	14 %	14.6 nm	18 %

Table 4.1. Mean size (d_m) and the standard deviation (σ/dm) for the main ultra-small NP population and the minor population of bigger NPs deduced from the TEM images. These values were extracted from the gaussian distribution used to fit the experimental size distributions determined automatically over > 2000 NPs for the main population and manually over 100 NPs for the minor one.

When we have a look at the overall TEM images, the number of big particles on the grids seem to increase when the TIPS concentration decreased but it is very difficult to estimate from the TEM images the relative proportion of the two populations due to sampling issues. Therefore, we have performed SAXS experiment to know more precisely the size, shape and polydispersity of the NPs from *in situ* measurements, the statistics being obtained on a much larger number of particles in suspension in their mother liquor.

In that aim, 1.5 mm glass capillaries were filled with the colloidal suspensions directly obtained after 3h of reaction, without any further purification. Figure 4.2 shows the SAXS patterns of the as-prepared Au nanoparticle suspensions. At first sight, differences can be observed between the different SAXS patterns. For [TIPS] = 62 mM and 250 mM (Figure 4.2 a-b), a two-step curve was observed, indicating the presence of a bimodal distribution of nanoparticles. At higher TIPS concentration, 500 mM and 1M, the curves smoothen (Figure 4.2 c-d).

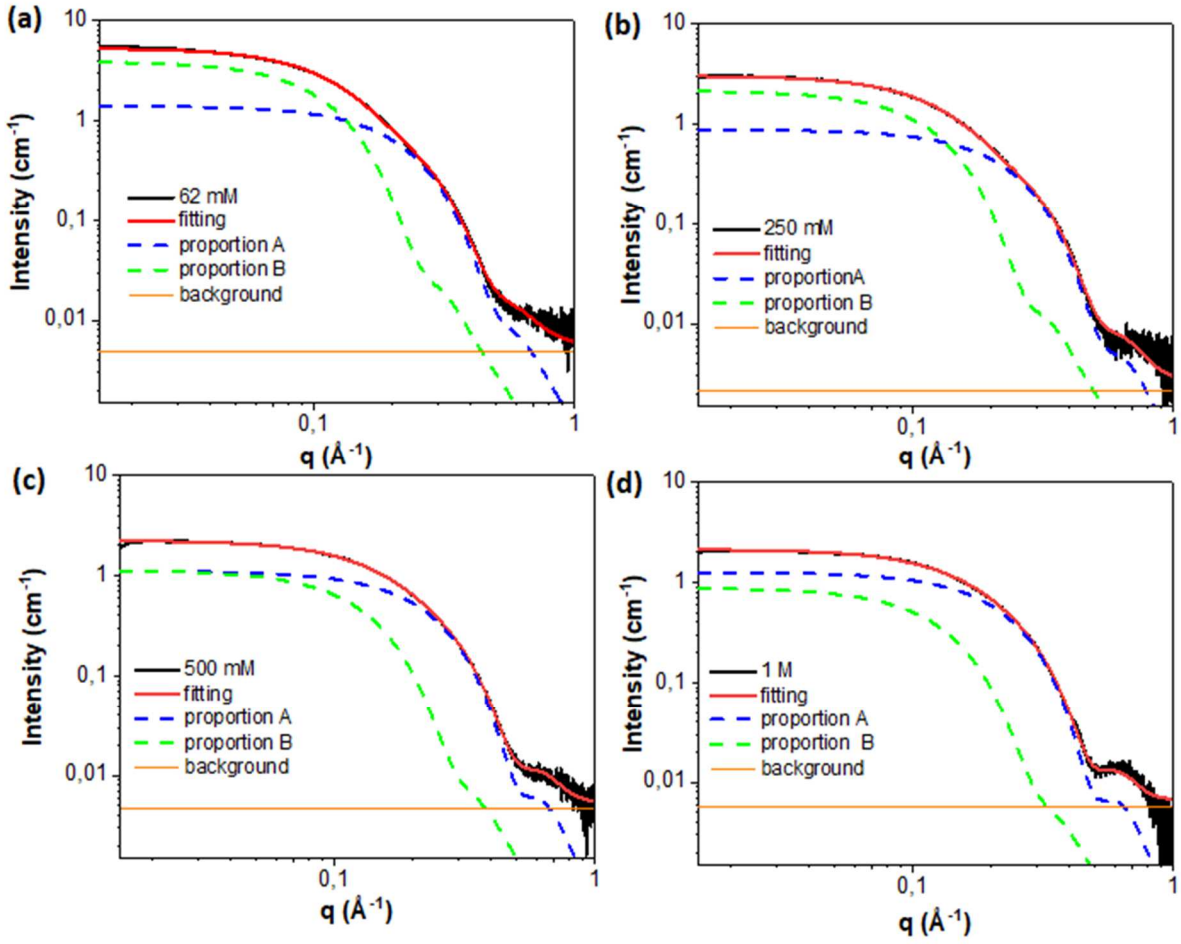

Figure 4.2 SAXS patterns of suspensions of Au nanoparticles obtained after 3h of reaction of $HAuCl_4.3H_2O$ in OY/hexane ([Au] = 20 mM; [OY] = 50 mM) using TIPS as reducing agent, in different concentrations: (a) [TIPS] = 62 mM; (b) [TIPS] = 250 mM; (c) [TIPS] = 500 mM and (d) [TIPS] = 1 M. In black: experimental data; red: the corresponding fit considering two populations of nanosphere (blue and green dashed lines) and a constant background (orange).

[TIPS]	Population A				Population B				
	d_m	σ/d_m	% vol.	scale	d_m	σ/d_m	% vol.	scale	Total scale
62 mM	1.8	0.17	64	$2.6x10^{-4}$	3.5	0.15	26	$1.4x10^{-4}$	$4.0x10^{-4}$
250 mM	1.6	0.19	75	$2.3x10^{-4}$	2.9	0.21	25	$7.6x10^{-5}$	$3.1x10^{-4}$
500 mM	1.6	0.17	83	$2.5x10^{-4}$	2.6	0.23	17	$5.0x10^{-5}$	$3.0x10^{-4}$
1 M	1.7	0.15	87	$2.7x10^{-4}$	2.6	0.23	13	$4.0x10^{-5}$	$3.1x10^{-4}$

Table 4.2 Summary of the adjustable parameters of the two gaussian distribution used to properly adjust the experimental SAXS pattern of Au nanoparticle suspensions obtained after 3h of reaction using different reaction parameters. Mean diameter, d_m, and polydispersity expressed as σ/d_m, with σ the standard deviation of the gaussian distribution.

Interestingly, all the experimental curves were nicely fitted using SASVIEW considering two gaussian distributions: a major one (referred to as population A) with a mean diameter of less than 2 nm and a second one (population B) with a larger diameter (2.6 nm or more) as reported in table 4.2. The total scale, which corresponds to the volume fraction, is found around 3×10^{-4} for every TIPS concentration, except 62 mM, where a volume fraction of 4×10^{-4} is found. Those values are larger than the theoretical volume fraction of 2×10^{-4} expected for [Au] = 20 mM. This is due to a calibration problem, in our firsts experiments we didn't perform a normalization with water and/or hexane. However, the facts that i) the volume fraction is fairly consistent and ii) the reaction with [TIPS] = 1M was over after 3h of reaction, as detailed in the chapter 3, make us believe that the reaction yields are the same, which is an important point to compare the results.

Figure 4.3 shows the corresponding volume-weighted size distribution determined from the fit. It clearly revealed that the relative proportion between the populations A and B depends on the TIPS concentration. The smallest nanoparticles (population A) increased significantly from 64 % for [TIPS]= 62 mM to 87 % for [TIPS]= 1 M but their mean diameter remained fairly constant at ~ 1.7 nm. Population B, which corresponds to the largest NPs detected by SAXS, have a mean diameter of solely ~ 3 nm, which is significantly smaller than the big particles observed by TEM (d > 10 nm). As previously discussed in the chapter 3, this discrepancy can be due to i) the very small volume fraction of the 10 nm NPs in solution or to ii) an aggregation artefact of Au NPs on the TEM carbon grid which could occur either during the drop casting or under the electron beam.

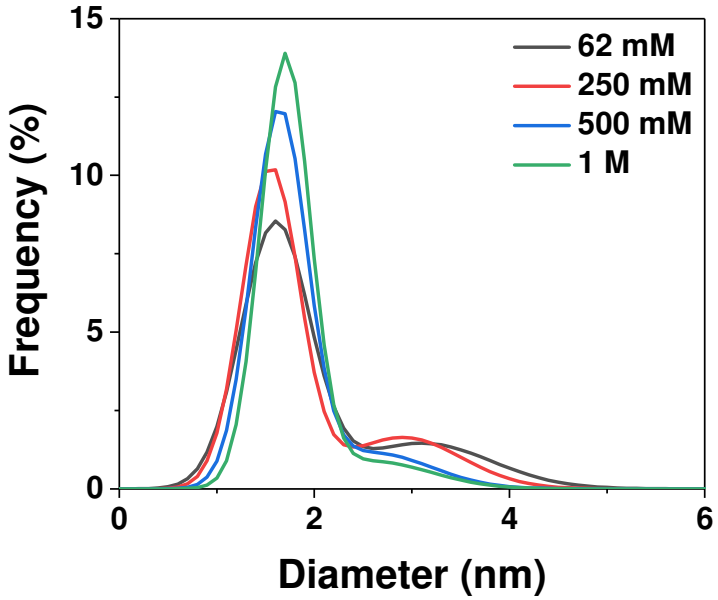

Figure 4.3 Volume-weighted distribution determined from the fit of the *in situ* SAXS of the final Au NPs obtained after 3 h of reaction at 25°C in presence of [TIPS] = 62 mM (black), 250 mM (red), 500 mM (blue) and 1M (green).

4.2 *In situ* UV-Vis

In order to follow the gold NPs formation and to compare the influence of the TIPS concentration on the kinetic, first at the laboratory scale, UV-Visible absorption spectroscopy experiments were performed *in situ* using the microfluidic set-up described in the chapter 2.

From an experimental point of view, the precursor solution and the reducing agent solution were prepared separately as in the previous reactions to obtain finally [Au] = 20 mM and [OY] = 50 mM, while the TIPS concentration was varied between 62 mM and 1M. The two solutions were injected through the microfluidic chip using a syringe pump system, mixed thanks to the ultrafast butterfly mixer and flowed through the channel. The reaction was then followed at a given position in the channel once the flow has been switched off. For that, the transmitted intensity in the wavelength range 380 to 1000 nm was measured. The color change from pale yellow to dark brown inside the channel indicated the formation of Au (0) NPs.

The time evolution of the absorbance of the solution at 520 nm as a function of the different TIPS concentrations is plotted in figure 4.4. In this graph, we see clearly that the time at which Au (0) NPs

appears strongly depends on the TIPS concentration: the Au (0) onset varies from 185 s ± 5 s for [TIPS] = 62 mM down to 10.5 s ± 0.5 s for [TIPS] = 1 M as summarized in table 4.3.

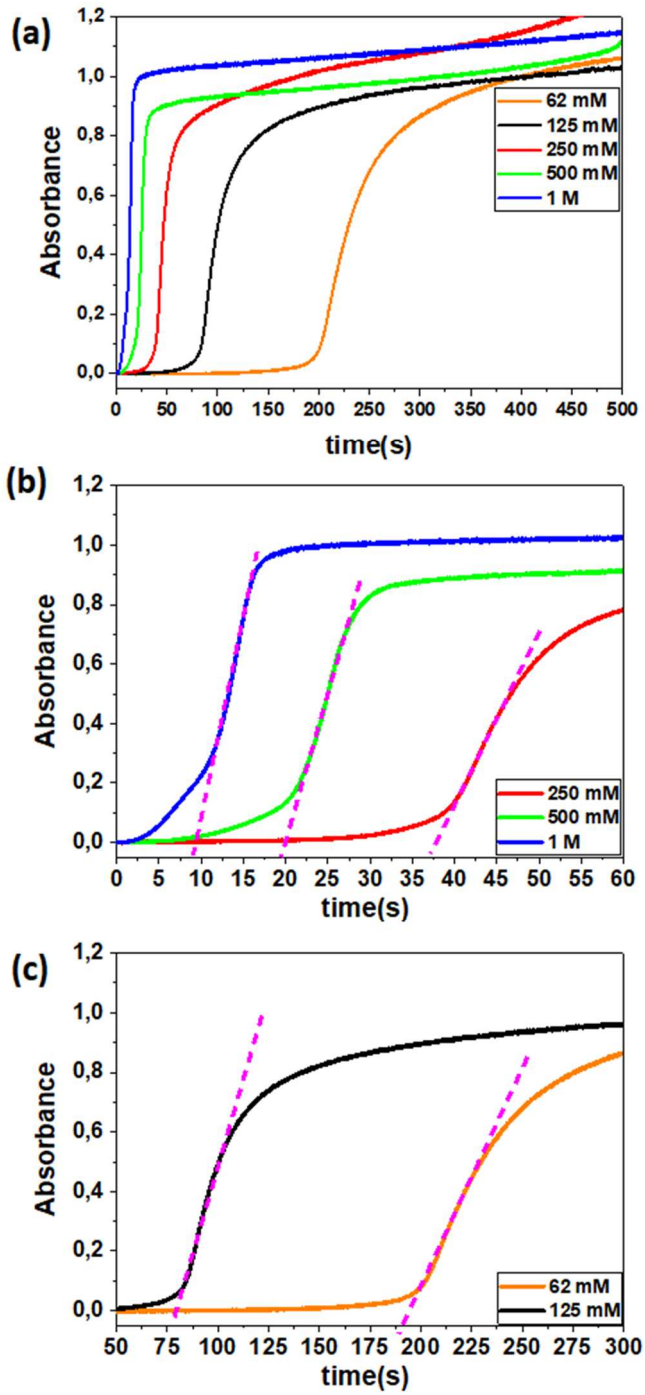

Figure 4.4 (a) Absorbance at λ = 520 nm vs time measured in the channel of a microfluidic chip during the reduction of $HAuCl_4$ (20 mM) with [TIPS]= 62 mM, 125 mM, 250 mM, 500 mM and 1M (b) zoom on the first 60 s and (c) from 50 s to 300 s. Pink dashed lines: linear fit of the absorption slope, determination of the onset time and reaction rate.

	UV-vis	
[TIPS]	**Au (0) onset (s)**	**Reaction rate (s^{-1})**
62 mM	185 ± 5	0.011 ± 10^{-3}
125 mM	74 ± 8	0.024 ± 2x10^{-3}
250 mM	40 ± 2	0.048 ± 8x10^{-3}
500 mM	23 ± 3	0.105 ± 5x10^{-3}
1 M	10.5 ± 0.5	0.123 ± 2x10^{-3}

Table 4.3 The summary of the Au (0) onset and reaction rate obtained from the UV-Vis spectra measured *in situ* during the reaction using [TIPS] from 62 mM to 1 M

These values are in good agreement with the qualitative observation made on the batch reactions in the laboratory bench.

In figure 4.5.a-b, the induction time and reaction rate were plotted as a function of $[TIPS]^{-1}$ and [TIPS], respectively. The plot of the induction time as a function of $[TIPS]^{-1}$ is well fitted with a linear function (χ^2 = 0.994). From this plot the Au (0) onset is therefore found inversely proportional to the [TIPS]. As one could expect, the higher the TIPS concentration, the faster the Au(0) onset appears.
The reaction rate was deduced from the linear fit of the absorption slope, depicted by the pink dashed line in figures 4.4 b and c. The reaction rate is increasing with the TIPS concentration by one order of magnitude (see figure 4.5.b). If we don't consider the [TIPS]=1 M, this increasing seems linear (χ^2 = 0.999).

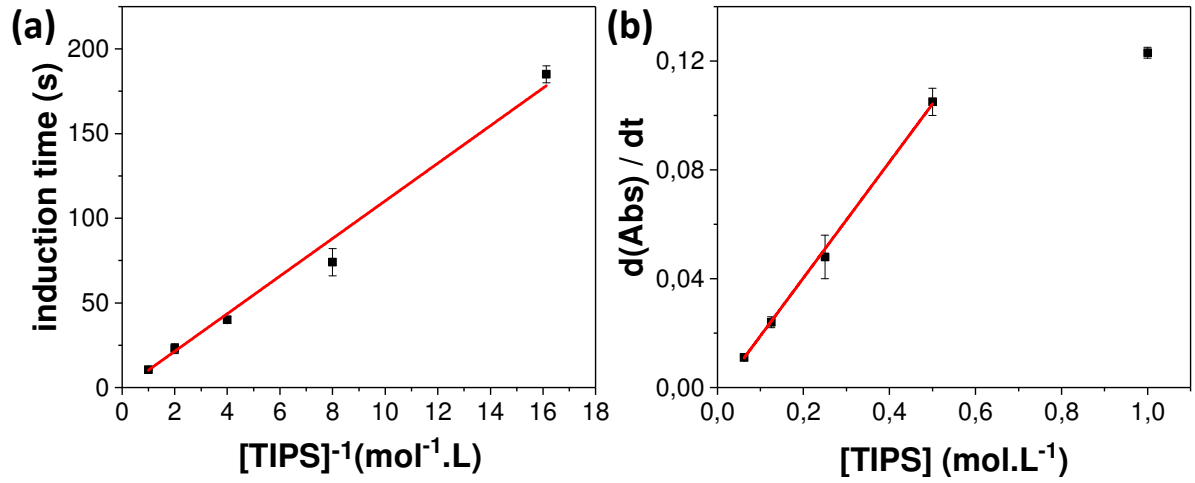

Figure 4.5 Kinetics data deduced from the time evolution of the UV-visible absorption at 520 nm (a) The time of Au (0) onset as a function of $[TIPS]^{-1}$, (b) The reaction rate (s^{-1}) as a function of [TIPS] obtained from the UV-vis spectra

4.3 *In situ* X-ray absorption spectroscopy

Since the ostemer polymer used for the microfluidic chip absorbs the UV light up to 380 nm, we could not follow the Au (III) and Au (I) species by UV spectrometry. To go beyond these results, we have performed X-Ray Absorption spectroscopy (XAS) at synchrotron to study the Au speciation all over the reaction.

The time-resolved XAS spectra were fitted by a linear combination (LCA) of three components, Au (III), Au (I) and Au (0), as described in the chapters 2 and 3. Figure 4.6 shows the evolution of the gold speciation, determined by the LCA, as a function of time during the nanoparticle synthesis in presence of [TIPS] = 62 mM and 250 mM. The curve obtained with [TIPS] = 1M, already described in the chapter 3, was added for comparison.

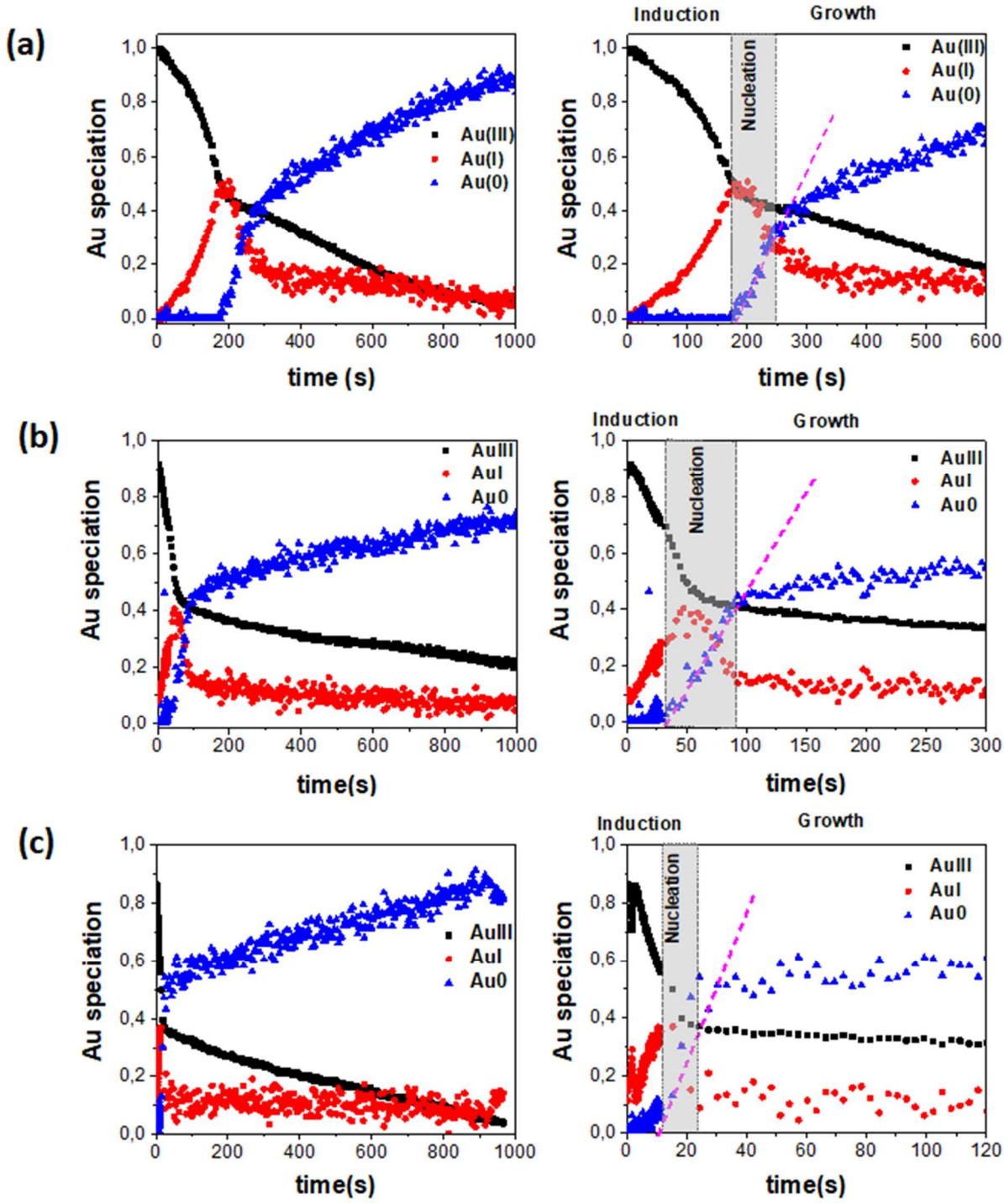

Figure 4.6 Relative Au (III), Au (I) and Au (0) concentrations deduced from the linear combination analysis of the XAS spectra measured *in situ* during the reaction using (a) [TIPS]= 62 mM, (b) [TIPS]= 250 mM and (c) 1 M. Pink dashed line: linear fit of the first Au (0) slope, determination of the onset time and nucleation rate.

The gold speciation follows a similar trend. In every case, three stages can be defined: the induction period, the nucleation, and the growth stage. The main difference between the three kinetics concerns the nucleation rate and the onset time. As summarized in Table 4.4: the higher the TIPS concentration, the faster the reaction is. For instance, the induction stage, which corresponds to the reduction of Au (III) to Au (I) lasts 178 ± 2 s for [TIPS] = 62 mM but only 7.6 s ± 1.0 s for [TIPS] = 1 M.

In addition, the maximum concentration of Au(I), which is concomitant with the Au (0) onset, varies with the [TIPS]. It reached 50 %, 40 % and 36 % for the 62 mM, 250 mM and 1 M, respectively. The nucleation stage is defined from the onset of Au (0) to the break in the slope of Au (0) increase (see Fig. 4.6). The duration of the nucleation stage strongly decreased when the TIPS concentration increased (Table 4.4). On the other hand, it is interesting to note that the percentage of Au (0) involved in the nucleation stage does not varied too much with the TIPS concentration, from 40 % for [TIPS]= 62 mM to 54 % for [TIPS]= 1M. Interestingly, the Au(I) concentration remained fairly constant at ~ 15 % during the growth stage, independently of the reducing agent concentration.

[TIPS]	**Onset of Au (0) (s)**	**Nucleation rate ($*10^{-3}$) (mol. L^{-1}. s^{-1})**	**% [Au (I)]$_{max}$**	**Time at which [Au (I)]$_{max}$**	**Duration of the nucleation stage (s)**	**% [Au (0)] after nucleation**
62 mM	178 ± 2	5.0 ± 0.4	50	200 s	74	40
125 mM	78 ± 2	-	50	82 s	58	48
250 mM	39 ± 3	9 ± 2	40	47 s	54	45
500 mM	24 ± 1	15 ± 3	30	32 s	35	50
1 M	7.6 ± 1	26 ± 6	36	15 s	12	54

Table 4.4 The summary of the Au (0) onset, nucleation rate, [Au (I)]$_{max}$ and the time at which it is observed, duration of the nucleation stage and [Au (0)] in the nucleation stage obtained from the XAS spectra measured *in situ* during the reaction using [TIPS] from 62 mM to 1 M

In figure 4.7.a-b, the induction time and nucleation rate were plotted as a function of $[TIPS]^{-1}$ and [TIPS], respectively. The plot of the induction time as a function of $[TIPS]^{-1}$ is fitted well with a linear function ($\chi^2 = 0.995$) (figure 4.7.a). From this graph, the induction time is found proportional to the $[TIPS]^{-1}$ with a slope of 11 s. mol. L^{-1}. On the other hand, the plot of the evolution of the nucleation rate with respect to the [TIPS] demonstrates linearity ($\chi^2 = 0.997$) (figure 4.7.b). From this plot, we can deduce that the nucleation rate is proportional to the [TIPS] with a slope of 0.03 s^{-1}.L.mol^{-1}.

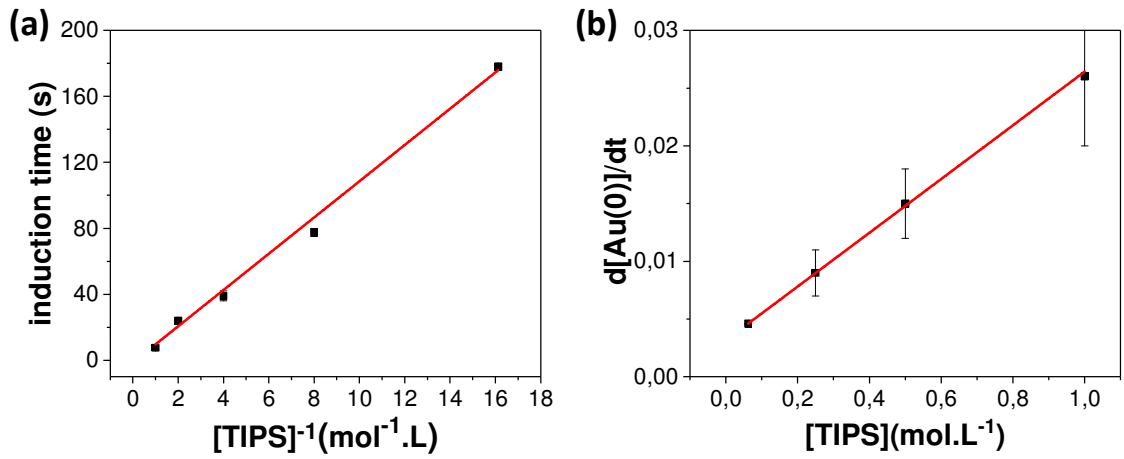

Figure 4.7 (a) The time of Au (0) onset as a function of $[TIPS]^{-1}$, (b) The nucleation rate (s^{-1}) as a function of [TIPS] obtained from the XAS spectra. Black squares : experimental point, Red line : linear fit

4.4 Comparison of the onset and the reaction rate determined from XAS and UV-Vis

Using two different in-situ techniques, we could determine the critical time, or onset, at which the reaction start to proceed, and some reaction rate. The agreement between UV-Vis and XAS regarding the onset time was really good and evidenced that it is inversely proportional to the TIPS concentration. Some questions however remained concerning the reaction rates we could deduce from the two techniques. XAS clearly allow us to determine the rate at which the Au (0) forms. Concerning the UV-Vis measurements, we do not directly probe the concentration of Au (0) but the evolution of the signal absorbance. As detailed in the chapter 2, we have considered the specific wavelength of λ = 520 nm, assuming that it allowed to probe Au(0) even though the plasmon band was not clearly visible. To be able to convert the absorbance into a concentration using the Beer Lambert's law (Abs = ε. L. c), one should determine both ε and the optical path (L). Due to the possible fluctuation

in the microfluidic channel width, we renormalized the absorbance a posteriori, fixing the final Au(0) concentration determined by XAS as *c* and therefore determining the $\varepsilon \times L$ factor. Since this factor is independent of the reaction time, we could then apply this factor to normalize the whole time evolution of the UV-Vis and thus obtain the [Au (0)].

In figure 4.8, are given the resulting Au (0) relative concentrations as a function of time using the two different technics. For every TIPS concentration probed, the agreement between the XAS and UV-Vis is remarkable. The results obtained at the laboratory using UV-Vis absorption spectroscopy reproduce with a great fidelity the time evolution obtained from synchrotron measurements. Therefore, the direct measurement of the Au(0) concentration by UV-Vis is possible, providing a calibration that can be given by the XAS data, or by a standard colloidal suspension with a well-known concentration.

In a near future, the use of another polymer to fabricate the microfluidic chip could allow to follow as well the relative Au(III) and Au (I), providing that it's transparent in the characteristic UV region.

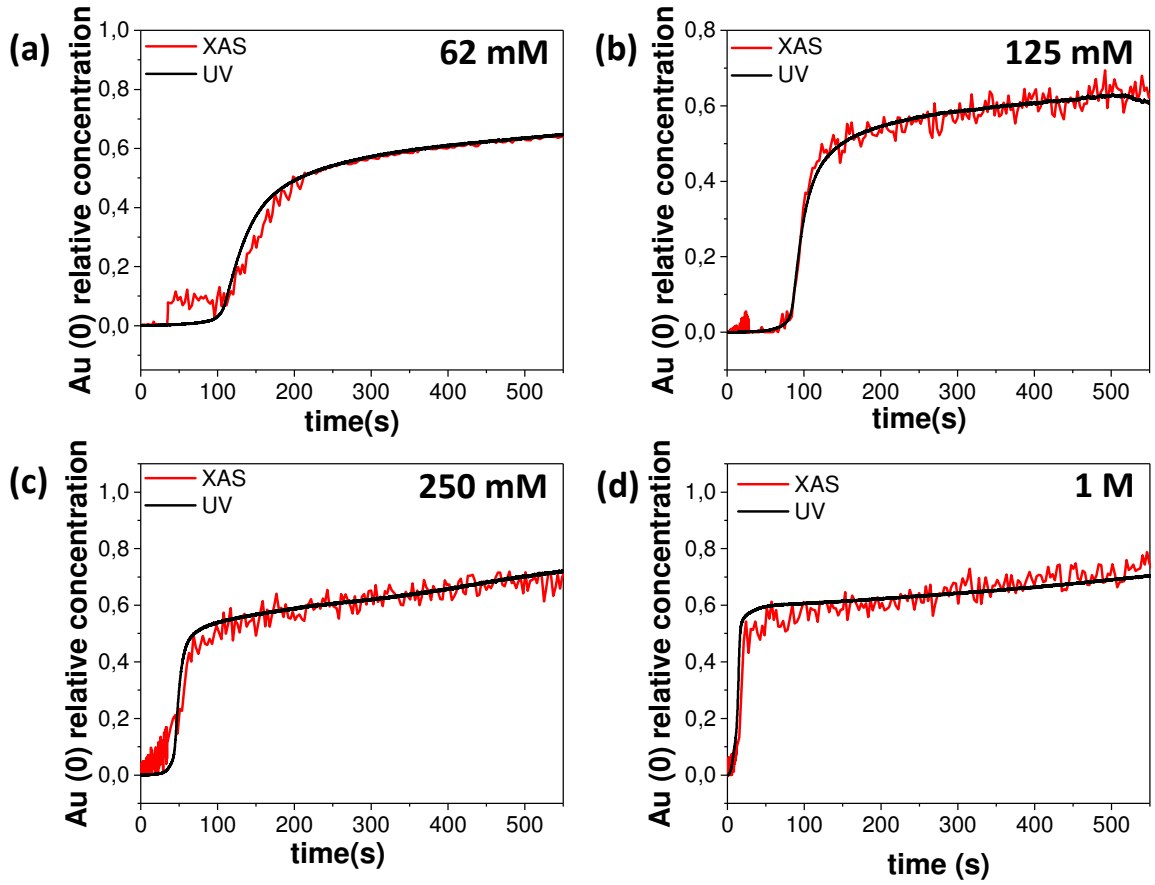

Figure 4.8 Comparing of relative Au (0) concentration obtained from UV-vis absorption spectroscopy and X-ray absorption spectroscopy for the [TIPS] (a) 62 mM, (b) 125 mM, (c) 250 mM and (d) 1 M.

4.5 *In situ* SAXS: influence of [TIPS]

In situ SAXS experiments were carried out to follow the reduction of the gold precursor into Au NPs at different TIPS concentrations. Figure 4.9 shows the time variation of the *in situ* SAXS patterns recorded during the synthesis of nanoparticles with [TIPS]= 62 mM and 250 mM concentrations. For all cases, the presence of scattering objects which are the pre-nucleation clusters (PNCs) were detected at short times. Indeed, the dissolution of $HAuCl_4$ in hexane thanks to the presence of OY results in the formation of clusters containing Au (III) complexes as previously reported in the chapter 3. The mean size of these clusters was estimated around 4 nm.

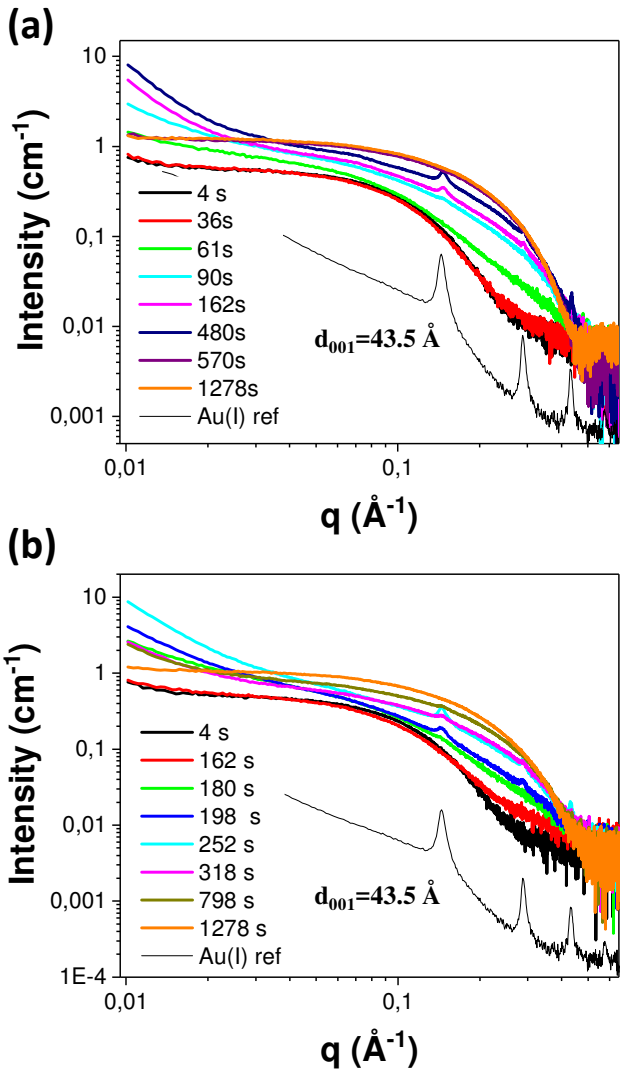

Figure 4.9. Time-resolved *in situ* synchrotron SAXS patterns recorded during the synthesis of Au nanoparticles in OY/hexane solution with different TIPS concentrations: (a) [TIPS] = 250 mM and (b) [TIPS] = 62 mM. The black line corresponds to the peaks of a lamellar phase with an arbitrary line broadening and an interlayer distance d_{001} = 43.5 Å.

The scattering intensity remained fairly constant during the induction stage showing that the size of the PNCs is almost constant. The induction stage lasts ~ 15 s for [TIPS] = 1 M, ~ 36 s for [TIPS]= 250 mM and up to 3 min for 62 mM. During this induction stage, the Au (III) complexes are partially reduced into Au(I), as previously explained in the XAS section, without any significant size modification.

At the end of this induction stage, the "knee position" of the scattering intensity profiles shifted towards higher *q*, revealing a decrease of the scattering objects' mean size. The shift was very fast with the highest [TIPS]= 1 M concentration as shown in the previous chapter. For the [TIPS]= 250 mM and 62 mM, the shift is more progressive, as evidenced in figure 4.9. This shift was interpreted as the onset of the small Au nanoparticles in the medium, *i.e.* the beginning of the nucleation.

At the same time, Bragg peaks along with an increased intensity at small *q* were clearly observed with [TIPS] = 62 and 250 mM. The positions of the two Bragg peaks, at q_1 = 0.1445 $Å^{-1}$ and q_2 = 0.289 $Å^{-1}$, can be interpreted as a lamellar phase with an interlayer distance d_{001} of 43.5 Å.

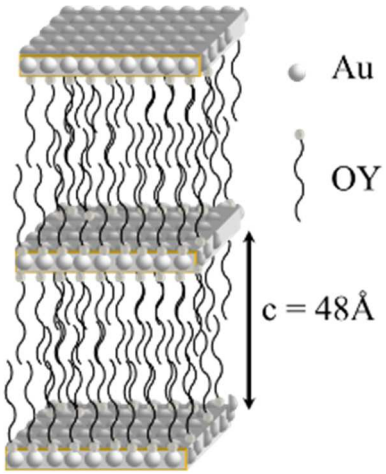

Figure 4.10 Representative picture of the lamellar phase ([OY-Au^{I}Cl]) with an interlayer distance d_{001} = 48 Å, reprinted from[1]

This distance is slightly smaller than the 48 Å previously reported in a [OY-Au^{I}-Cl] complex obtained reacting $HAuCl_4$ in pure oleylamine for 48h at 25°C (figure 4.10).[1] Considering the 2 nm length of a fully extended oleylamine, the interlayer distance d_{001} = 43.5 Å found here is still in agreement with a lamellar structure composed of Au planes separated by two molecules of oleylamine. The increases at small *q* revealed the appearance of large objects corresponding to the lamellar phase.

With time, the signature of the lamellar phase vanishes (the intensity of the Bragg peaks decreases). The time interval during which the lamellar phase was observed lasts from 200 to 800 s for [TIPS] = 62 mM and from 90 s to 480 s for [TIPS]= 250 mM. In contrast, the Bragg peaks were hardly detected for faster reaction carried out with [TIPS] = 1 M, as shown previously.

4.6 Characterization of the lamellar phase

4.6.1 *In situ* study and chemical analysis

In order to characterize the lamellar phase that appeared during the synthesis with the low TIPS concentrations, we decided to isolate it. For this purpose, $HAuCl_4$ was reduced in presence of OY with the same ratio OY/Au = 2.5 but using a TIPS concentration that was deliberately limited to a sub-stoichiometric value, *i.e.* 10 mM, to avoid the formation of metallic particles.

The reaction of 20 mM of Au (III) with 10 mM of TIPS is indeed expected to give a mixture of 50 % Au (III) and 50 % Au(I), considering the equation 1, previously described in the chapter 1:

$$HAuCl_4 + \frac{3}{2}R_3SiH + \frac{5}{2}C_{18}H_{35}NH_2 \rightarrow Au(0) + \frac{3}{2}R_3SiCl + \frac{5}{2}C_{18}H_{35}NH_3^+Cl^-$$

The reaction was followed *in situ* by SAXS (Figure 4.11). Up to 10 min, the characteristic signal of PNCs was observed. After about 12 min, the$(00l)$ Bragg peaks characteristic of a lamellar phase appeared. This phase exhibited the same interlayer distance of 43.5 Å as in the *in situ* kinetics with [TIPS] = 62 and 250 mM. The intensity at small-*q* values increased with time, concomitantly with the Bragg peaks' intensities. This high intensity at low *q* may come from the form factor of the lamellar phase. After 50 min of reaction, the SAXS pattern did not further evolved, indicating a fairly stable lamellar phase.

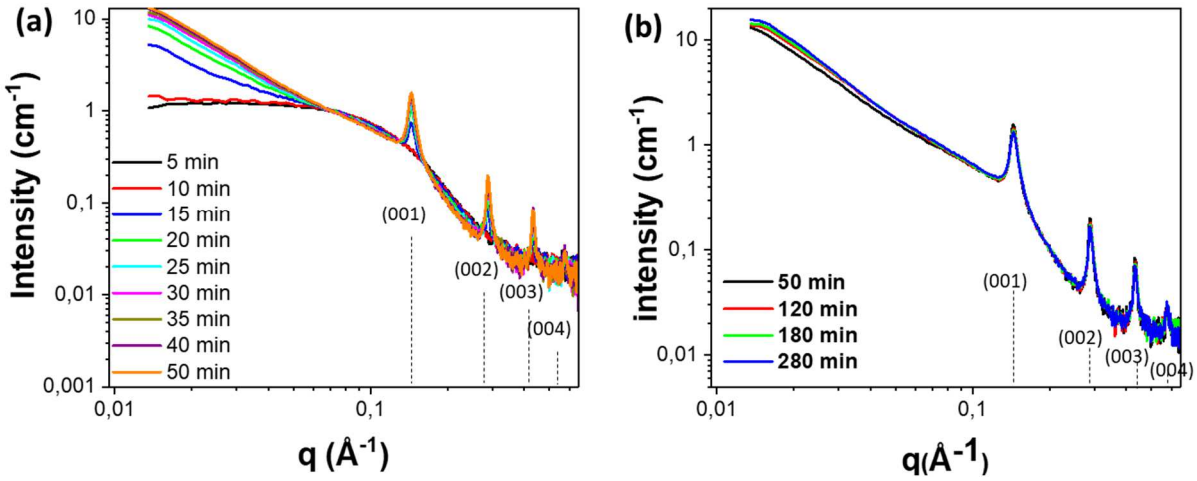

Figure 4.11. In situ SAXS patterns recorded during the partial reduction of $HAuCl_4$ using 0.5 eq. of TIPS at 25°C (the dashed lines correspond to the peaks of a lamellar phase with an interlayer distance (00*l*) d_{001} = 43.5 Å)

The lamellar phase was then prepared in large amount in a vial using the same reaction conditions as for the *in situ* SAXS. After 90 min of reaction, the white precipitate which formed was isolated by centrifugation, washed several times with hexane to remove the excess of Au (III) precursor and OY and then dried under vacuum. The chemical composition of this white phase was analyzed combining chemical analysis and X-Ray Photon Spectroscopy (XPS).

Chemical analysis provides the weight % of C, H and N. The experimental results were in very good agreement with the formula of the OY-Au(I)-Cl complex, *i.e.* $AuC_{18}H_{37}NCl$ as summarized in Table 4.5.

XPS is a well-known technique to determine the chemical state of the elements. Unfortunately, the Au complex was partially reduced under the X-ray beam: the white lamellar phase turned to pink. Thus, we could not confirm the potential Au(I) state in the complex. However, XPS allows quantifying the relative N/Cl and Au/Cl ratios, which were in both case close to 1 as expected for a OY-Au(I)-Cl complex (Table 4.5).

element	OY-Au(I)-Cl theory			experimental			
	wgt %	# atoms	ratio	wgt %	# atoms	ratio	technique
C	43,2	18		42,9	17,9		**chemical analysis**
H	7,4	37		7,1	35,7		
N	2,8	1		2,7	1		
Cl	7,1	1	N/Cl = 1	-	1	N/Cl = 1	**XPS**
Au	39,4	1	Au/Cl =1	-	0,9	Au/Cl =0,9	

Table 4.5 Elemental composition of the lamellar phase formed *in situ* determined by chemical and XPS analysis

4.6.2 Reduction of the Au(I) lamellar phase

In order to precise the role of the lamellar phase in the crystallization of the Au NPs, the direct reduction of this OY-Au(I)-Cl complex, once redispersed in hexane, was carried out with a large excess of TIPS. The concentration of Au and TIPS in the mixture was 20 mM and 1 M, respectively, as in the direct nanoparticle synthesis. The color change, which is a good indicator of the reduction of Au precursor to Au (0) NPs, was observed after about 10 min instead of the ~15 s needed when starting classically from the Au (III) precursor. Figure 4.12 shows a representative TEM image of the NPs obtained after 3h of reaction, revealing a very broad size distribution with particle size up to 6 nm, thus much larger than the NPs directly obtained classically. A first population is found with a size less than 2 nm. The second population which is the major one is obtained around 5 nm particle size up to 8 nm.

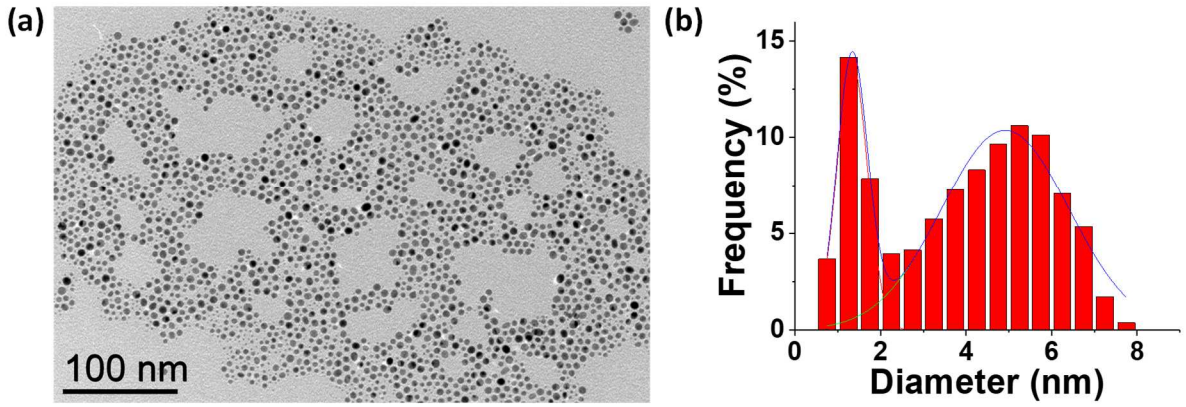

Figure 4.12. (a) TEM image of Au nanoparticles prepared by reduction of the lamellar phase OY-Au(I)-Cl with [TIPS] = 1 M. (b) number-weighted size distribution determined from the TEM image analysis.

After that, we have performed SAXS experiment to know more precisely the size and polydispersity of the final NPs. The 1.5 mm glass capillaries were filled with the colloidal suspensions directly obtained after 3h of reaction, without any further purification. Figure 4.13 shows the SAXS patterns of the as-prepared Au nanoparticle suspensions. At first sight, two step curves were observed indicating the presence of a bimodal distribution of nanoparticles. The main difference compared to the NPs obtained from the direct reduction concerns the relative ratio proportion of the ultra-small NPs (24% vs. 87%), which are in that case the minor population, and the very broad polydispersity observed (σ/dm ~ 33 % vs 15%) (table 4.6).

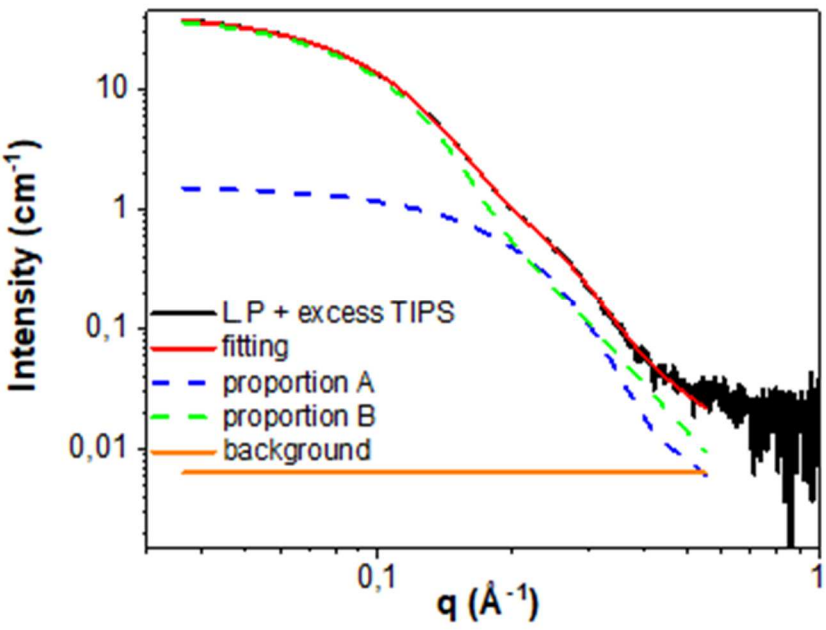

Figure 4.13 SAXS pattern of suspension of Au nanoparticles obtained by reduction of the lamellar phase (L.P) OY-Au(I)-Cl with [TIPS] = 1 M. In black: experimental data; red: the corresponding fit considering two populations of nanosphere (blue and green dashed lines) and a constant background (orange).

Type of reaction	**Population A**				**Population B**				
	d_m	**σ/d_m**	**% vol.**	**scale**	**d_m**	**σ/d_m**	**% vol.**	**scale**	**Total scale**
LP+ 1M TIPS	1.8	0.25	24	$6.4x10^{-4}$	3.3	0.33	76	$2x10^{-4}$	$8.4x10^{-4}$
Precursor + 1 M TIPS	1.7	0.15	87	$2.7x10^{-4}$	2.6	0.23	13	$4.0x10^{-5}$	$3.1x10^{-4}$

Table 4.6 Summary of the adjustable parameters of the two gaussian distribution used to properly adjust the experimental SAXS pattern of Au nanoparticle suspensions obtained after 3h of reaction starting from the lamellar phase or directly from the precursor solution. Mean diameter, d_m, and polydispersity expressed as σ/d_m, with σ the standard deviation of the gaussian distribution.

4.7 TIPS in the stoichiometric condition (1.5 eq)

Except for the preparation of the OY-Au(I)-Cl complex, all the experiments were performed in presence of an excess of TIPS compared to the stoichiometric conditions (62 mM or above). Considering all the information we now gained on our system, we tried to reduce the gold precursor $HAuCl_4$ using a [TIPS]/[Au] ratio of 1.5. Due to accessibility issues of SAXS, we could only study the final NPs using conventional TEM.

By adding [TIPS]= 30 mM, the pale-yellow solution characteristic of the Au (III) precursor turned to a cloudy brown suspension in ~ 5 min. Such cloudy phase is typical of the lamellar phase. After ~ 8 min, the solution was totally dark. The TEM image of the NPs obtained after 3h of reaction is given in figure 4.14. Large NPs with a mean diameter of d_m= 5.6 nm and a fairly broad size distribution were obtained. These particles look pretty similar to the NPs prepared by the direct reduction of the lamellar phase. They are on the contrary very different from the ultra-small NPs of ~1.7 nm prepared in presence of an excess of TIPS.

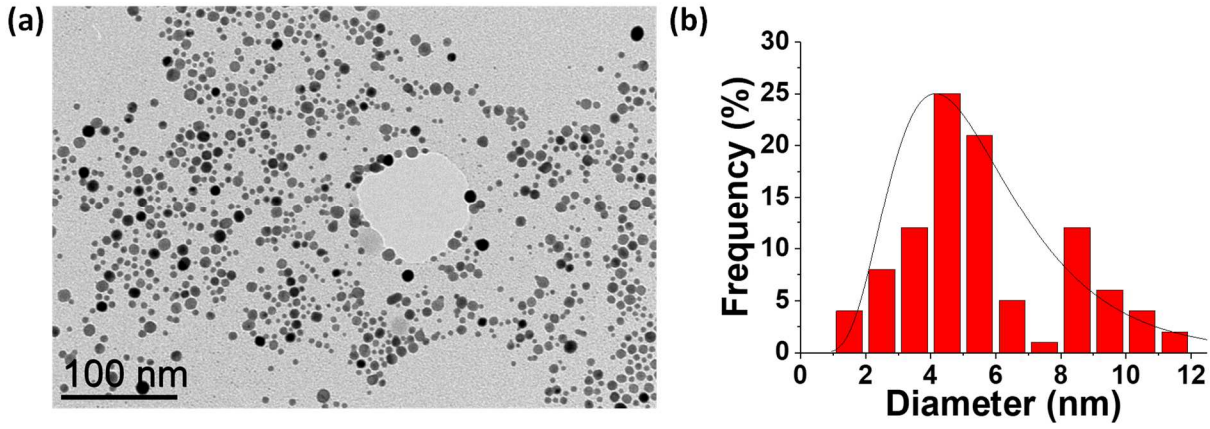

Figure 4.14 (a) TEM image of Au nanoparticles prepared with [TIPS] = 30 mM, (b) a number-weighted size distribution determined from the TEM image analysis.

4.8 Structural Study

4.8.1 Ultra-small Au NPs

The structural analysis of the ultra-small Au NPs prepared with [TIPS]= 62 mM, 250 mM and 1 M were carried out using *in situ* high energy XRD (HEXRD). Figure 4.15 shows the representative XRD patterns measured on the as-prepared Au nanoparticles in their mother liquor. As already described in the chapter 3, the very broad diffraction peaks revealed a crystalline structure different from the bulk *fcc* Au. The main band found at q = 2.795 Å^{-1} is shifted to high q values compared to the expected (111) peak of *fcc* Au (q = 2.668 Å^{-1}) and the additional feature at q = 3.37 Å^{-1} also is observed for every sample.

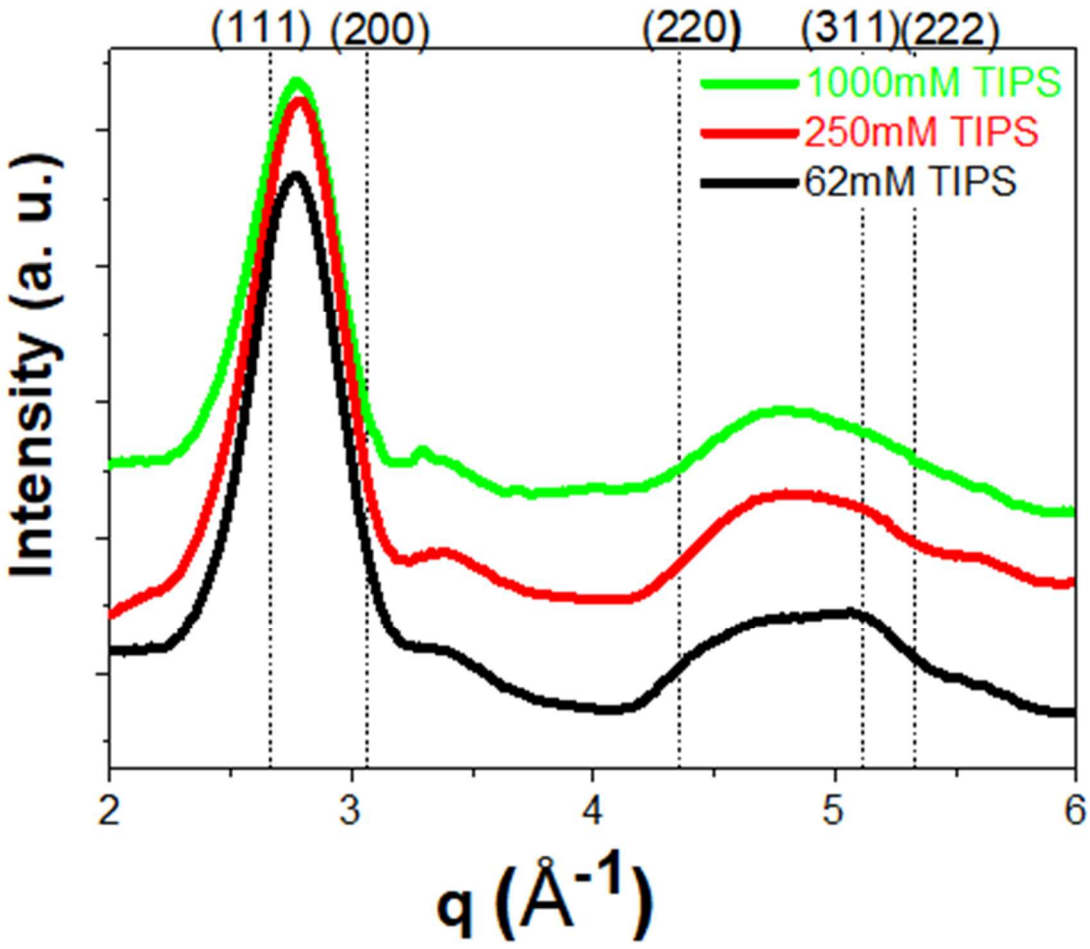

Figure 4.15 X-Ray Diffraction patterns of the final NPs obtained with different TIPS concentration (green = 1M, red = 250mM, black = 62 mM). The dash black line corresponds to the theoretical XRD pattern of *fcc* Au.

Regarding the different pair distribution function (PDF) extracted, there is no strong difference at first sight (figure 4.16.a). In every case, the physical oscillations in the PDF extend in the *r*-space to a distance of around 1.7 nm, which can be considered as a length of structural coherence for the Au NPs (highlighted by the dashed orange line in Figure 4.16a). This is close to the mean NP diameter measured by SAXS.

The experimental PDF of the NPs prepared with [TIPS]= 62 mM is compared with the same cuboctahedron and the icosahedron models used in the chapter 3 for [TIPS]= 1M (figure 4.16.b). Once more, a fairly good matching is obtained with the icosahedron model containing 309 atoms. Thus, the crystalline structure seems not to be strongly affected by the concentration of the reducing agent when [TIPS] $\geq$ 62 mM, despite the modification of the size distribution observed by SAXS.

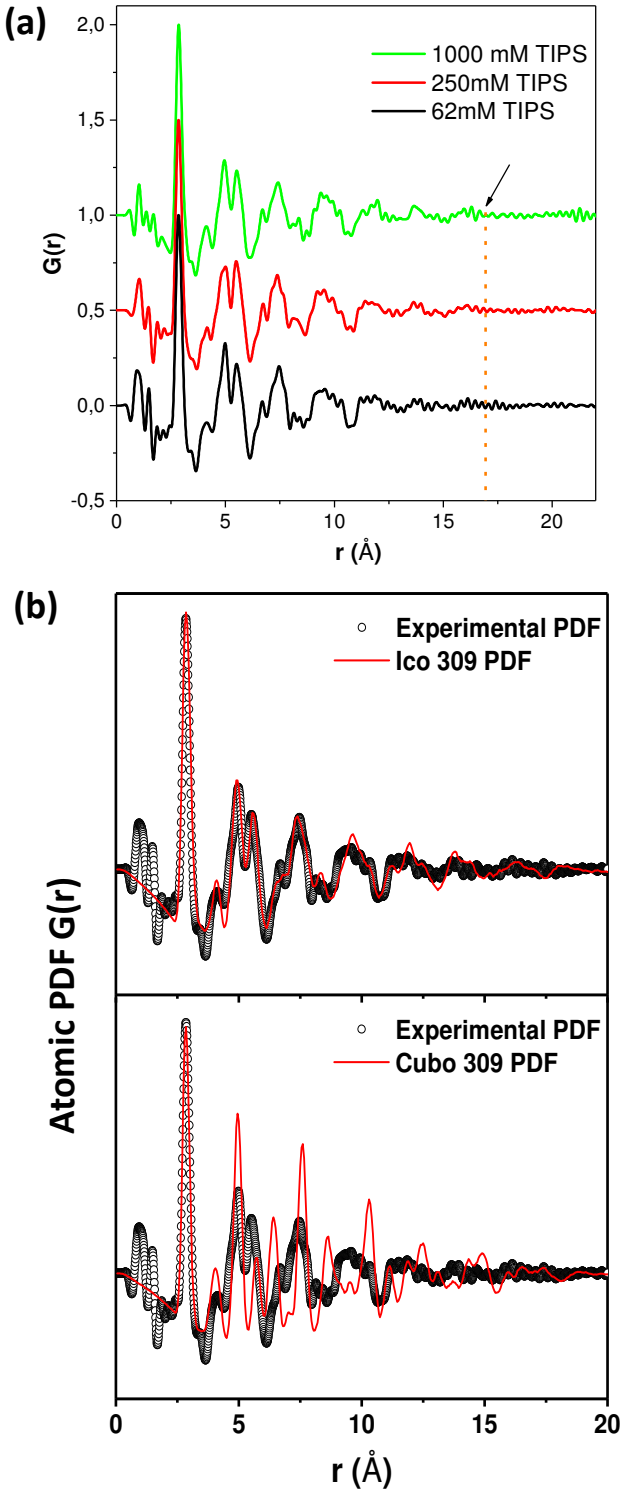

Figure 4.16 (a) *In situ* atomic pair distribution functions of Au NPs prepared with [TIPS]= 62 mM (black line), 250 mM (red line) and 1000 mM (green line). The dash orange line shows the place at which the oscillation is loss, (b) Comparison between experimental PDF of Au NPs (black circle) prepared with [TIPS]= 62 mM with ICO (up) and CBO (bottom) atomic models of 309 atoms.

4.8.2 Au NPs prepared from the Au(I) lamellar phase

The XRD pattern of particles prepared either by direct reduction of the lamellar phase OY-Au(I)-Cl using a large excess of TIPS, or by the classical reaction using TIPS in stoichiometric amount are given in figure 4.17. The pattern obtained for NPs prepared with [TIPS] = 62 mM is reprinted for comparison ease. The XRD patterns are this time consistent with a *fcc* crystal structure: all the peaks are falling on the expected (*hkl*) lines of *fcc* Au.

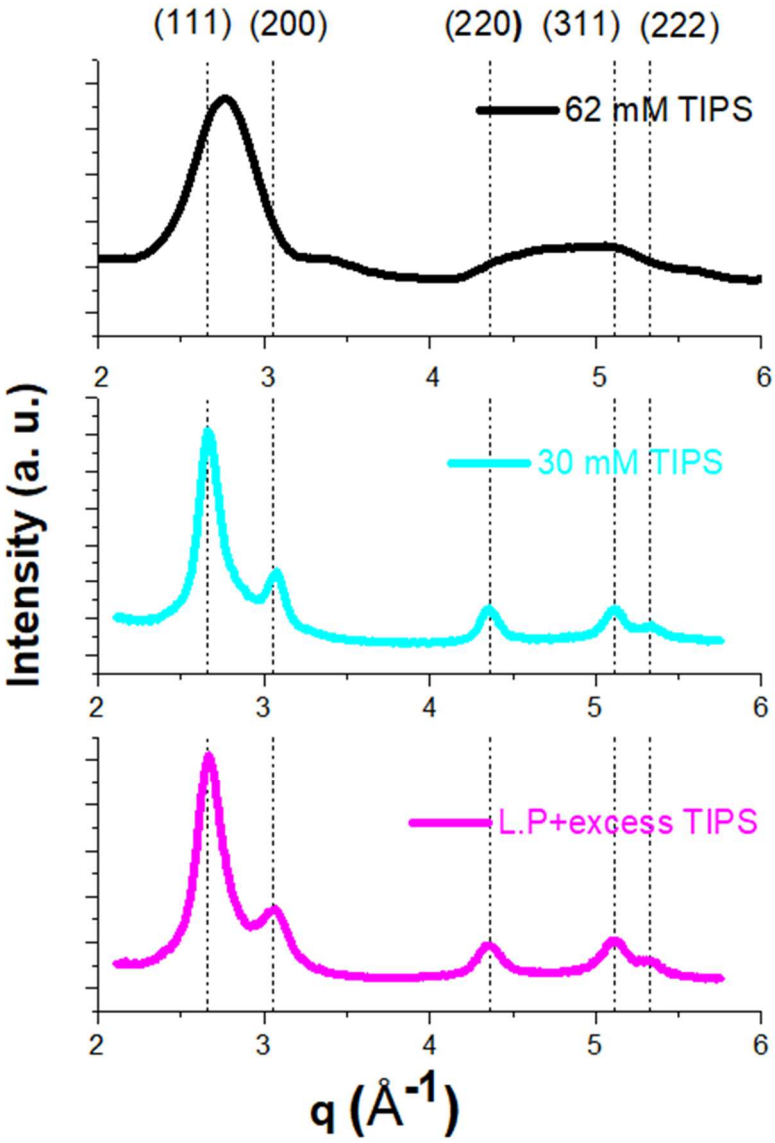

Figure 4.17 X-Ray Diffraction patterns of the final NPs prepared by direct reduction of the precursor in presence of [TIPS]= 62 mM (black) and 30 mM (cyan) or from the lamellar phase OY-Au(I)-Cl with a large excess of TIPS (1 M) (magenta). Dashed black lines : theoretical XRD pattern of *fcc* Au.

One can however notice that the (111) peak is dissymmetric. This could be due to the presence of small icosahedra along with the larger *fcc* NPs. We calculate the crystallite size (L) of the larger NPs using the Scherrer equation:

$$L = \frac{\mathrm{K}.\lambda}{\mathrm{B}.\cos\theta} \qquad \text{Eq.4.1}$$

where *K* is the Scherrer constant (0.94 for spheres), λ is the XRD radiation of wavelength (here λ_{Co} = 0.1789 nm) and *B*, expressed in radian, is the full width at half maximum of the peak considered. For the Au NPs prepared by the direct reduction of the lamellar phase, a crystallite size of 4.4 nm was determined, which is very close to the size determined by TEM. For the particles prepared with 30 mM TIPS, the crystallite size is 5.5 nm, once more in good agreement with the TEM mean size (5.6 nm). In both cases, the crystallite size is very close to the mean dimeter of the particles determined by TEM, revealing that the NPs are single-crystalline.

4.9 Summary of the results

We have reported here the first study on the impact of the reducing agent concentration (TIPS) on the synthesis of ultra-small Au nanoparticles. Thanks to in-situ XAS and UV-Vis studies, we have evidenced that the TIPS concentration was playing an important role on the reduction rate. The induction period was inversely proportional to the TIPS concentration while the slope of the Au(0) concentration in what we called nucleation stage was proportional to the [TIPS] concentration.

For the slow reactions, the crystallization of the OY-Au(I)-Cl lamellar phase was observed. This lamellar phase is in direct competition with the nucleation/growth of the Au icosahedral NPs.

For the stoichiometric TIPS concentration, corresponding to a very slow reaction rate, NPs with a mean diameter of d_m= 5.6 nm and 5 nm with a quite broad size distribution were obtained. These NPs are fairly similar to the NPs prepared by the direct reduction of the lamellar phase. In both cases, the NPs exhibit a fcc structure, very different from the icosahedral structure observed by the direct reduction of the precursor in presence of an excess of TIPS, even as small as 62 mM.

Thus, to obtain ultra-small monodisperse Au NPs with a non *fcc* structure, one should favor fast reaction rate in order to avoid or at least reduce the formation of the OY-Au(I)-Cl lamellar phase. The effect of the different parameters on the size and structure is summarized in the figure 4.18.

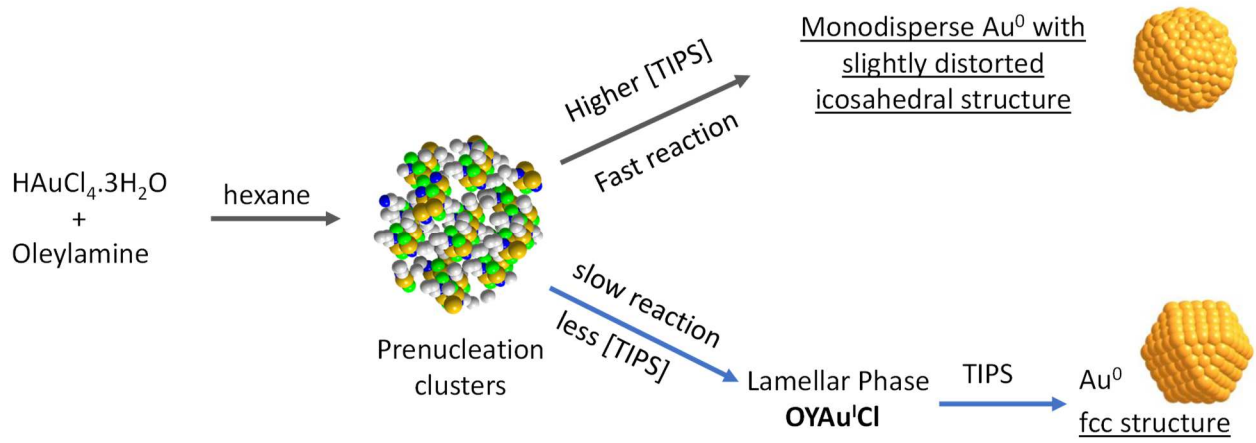

Figure 4.18. Schematics of the competition between the direct pathway leading to the crystallization of monodisperse ultra-small Au NPs with the icosahedral structure and the one involving the lamellar phase OY-Au(I)-Cl and leading to bigger particles with the *fcc* structure.

Bibliography

(1) Loubat, A.; Lacroix, L.-M.; Robert, A.; Impéror-Clerc, M.; Poteau, R.; Maron, L.; Arenal, R.; Pansu, B.; Viau, G. Ultrathin Gold Nanowires: Soft-Templating versus Liquid Phase Synthesis, a Quantitative Study. *J. Phys. Chem. C* **2015**, *119* (8), 4422–4430. https://doi.org/10.1021/acs.jpcc.5b00242.

Chapter 5 Optimization of Monodisperse Ultra-Small Au NPs

In the previous chapter, we have studied the effect of the TIPS concentration on the Au NP size, size distribution and structure. Depending on the TIPS concentration, we have obtained different nucleation and growth rates. When the TIPS concentration was low (≤ 250 mM), a slow reaction occurred during which an OY-Au(I)-Cl phase was observed. The direct reduction of this intermediate phase using a large excess of TIPS yields particles of ~ 5 nm, exhibiting a *fcc* structure. On the contrary, when we have used larger TIPS concentration (≥ 500 mM), the reaction was fast and let to ultra small Au NPs with the icosahedral structure.

In order to optimize the preparation of monodisperse ultra-small Au NPs, one should prevent the formation of OY-Au(I)-Cl. Since the Au (I) intermediate solid phase was not detected in presence of [TIPS] = 1M, *i.e.* for a fast reaction, we studied the effect of two other parameters: i) the reaction temperature and ii) the strength of the reducing agent.

5.1 Influence of the temperature

As the reactions were carried out in hexane, the temperature range was limited. In this section we compare the particles prepared at 25 °C (already described in the last chapter) with particles prepared at higher temperature, up to 40 °C. We have focused this study on the synthesis with low TIPS concentration since with [TIPS] = 1 M the particles were already monodisperse. Two concentrations are reported below: [TIPS] = 30 mM, i.e. the stoichiometric concentration according to Eq. 3.1, and a concentration slightly higher [TIPS] = 62 mM.

5.1.1 [TIPS]= 30 mM

As explained in the previous chapter, for [TIPS]= 30 mM we have obtained particles with a mean size of 5.6 nm crystallizing with the *fcc* structure. The onset of the dark red color appeared after 8 min.

When we have performed this experiment at 40°C, keeping the Au, OY and TIPS concentrations constant at 20 mM, 50 mM and 30 mM, respectively, the reaction became faster. The onset of the dark color appeared after ~5 min. The final particles obtained after 3h of reaction were observed by TEM (Figure 5.1a). Two populations were found: a population of ultra-small Au NPs exhibiting a mean diameter of 1.9 nm and a relative standard deviation σ/d = 19% (Figure 5.1b) along with larger particles with a mean diameter of 8.9 nm and a relative standard deviation σ/d = 26 % (Figure 5.1.c).

Then, we have performed SAXS experiment to know more precisely the size and polydispersity of the final NPs. The 1.5 mm glass capillaries were filled with the colloidal suspensions directly obtained after 3h of reaction. Figure 5.1.d shows the SAXS patterns of the as-prepared Au nanoparticle suspensions. When we look at the appearance of the SAXS pattern, two step curves were observed showing the presence of a bimodal distribution of nanoparticles. The experimental curve was well fitted considering two gaussian distributions: a major one (population A) with a mean diameter of d_m = 1.7 nm, and a second one (population B) with a larger diameter d_m= 3.6 nm. The mean size, d_m, the relative standard deviation σ/d_m and scales are shown in Table 5.1. For this sample we performed a normalization with water and/or hexane. So, the total scale was found consistent with the theoretical volume fraction of [Au]= 20 mM.

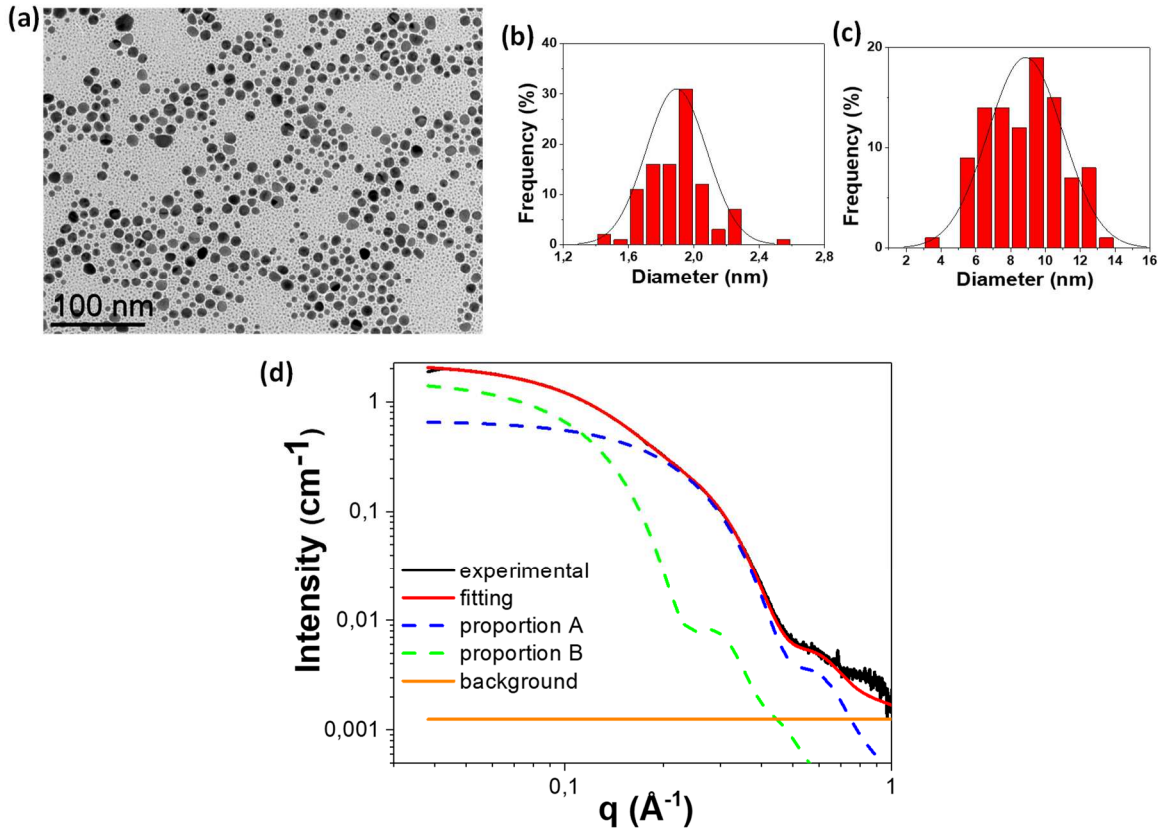

Figure 5.1 (a) TEM image of Au NPs obtained after 3h of reaction at T= 40°C with [TIPS]= 30 mM, the corresponding particle size distribution histograms of (b) small and (c) big particles and (d) SAXS patterns of suspensions of Au nanoparticles prepared by reduction of $HAuCl_4.3H_2O$ in OY/hexane ([Au] = 20 mM; [OY] = 50 mM) using TIPS as reducing agent ([TIPS] = 30 mM) at T = 40°C (Black: experimental data, red: best fits including two populations of nanospheres, population A (dashed blue), population B (dashed green), and a constant background (orange).

Population A				Population B				
d_m	σ/d_m	% vol.	scale	d_m	σ/d_m	% vol.	scale	Total scale
1.7	0.17	76	$1.3x10^{-4}$	3.6	0.15	24	$0.4x10^{-4}$	$1.7x10^{-4}$

Table 5.1 Summary of the adjustable parameters of the two gaussian distributions (A and B) used to fit the experimental SAXS pattern of Au nanoparticle suspensions obtained after 3h of reaction using [TIPS]= 30 mM at 40°C: the mean diameter, d_m, the polydispersity expressed as σ/d_m, (with σ the standard deviation of the gaussian distribution), and the relative volume fraction of both populations, *% vol*.

The XRD patterns of the NPs obtained at 40°C is displayed in Figure 5.2 and compared with the ones prepared at 25°C. The peaks of the *fcc* structure are still observed but the (111) peak appears broader and asymmetric compared to the (111) peak of the particles prepared at 25 °C.

The asymmetry of the main peak can be due to the presence of small icosahedra. The additional feature at q = 3.33 $Å^{-1}$, highlighted by the blue arrow, is the characteristic sign of the icosahedral structure. It is however much weaker compared to the one observed in the XRD pattern of Au NPs prepared with [TIPS] = 1 M for example (figure 5.2 blue line). All these observations are in good agreement with a sample made up of a mixture of small particles crystallizing with the icosahedral structure and big particles crystallizing with the *fcc* structure.

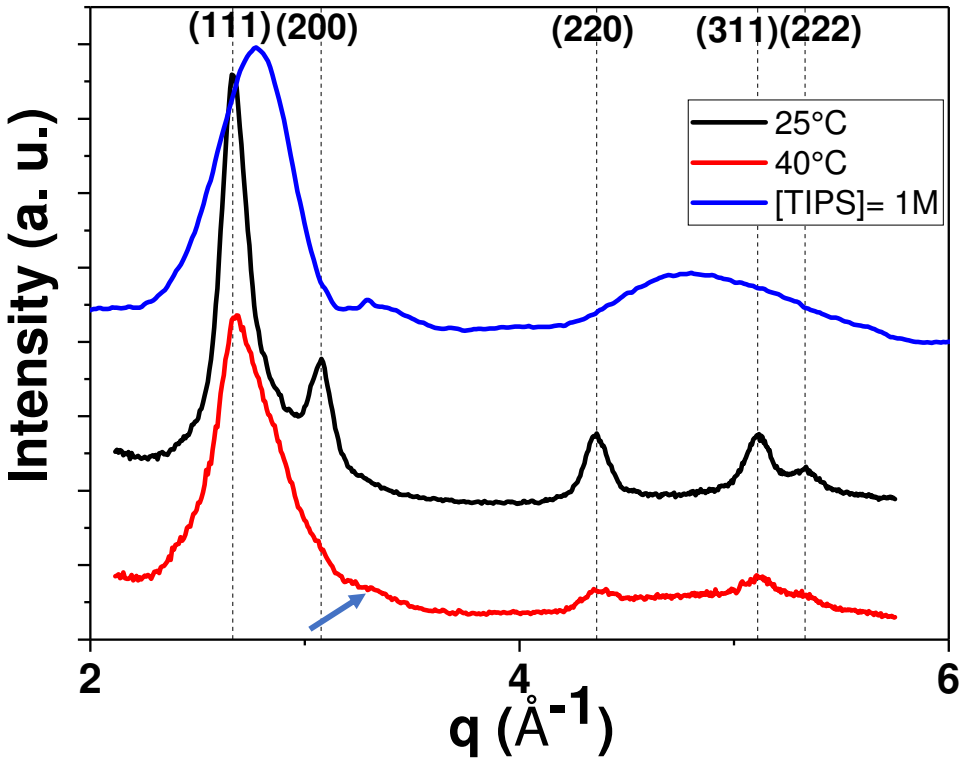

Figure 5.2 X-Ray Diffraction patterns of the final NPs obtained with 30 mM TIPS at 40°C (red line), 25°C (black line) and 1 M TIPS at 25°C (blue line). The dash black line corresponds to the theoretical XRD pattern of *fcc* Au. The blue arrow indicates the characteristic additional feature at q = 3.33 $Å^{-1}$.

By increasing the temperature from 25 °C to 40 °C, we increased the number of ultra-small particles. So, we can say that, the temperature is an effective parameter on the reaction. However, the effect was not sufficient to prepare monodisperse ultra-small particles.

5.1.2 [TIPS]= 62 mM: Effect of T varying from 25°C to 40 °C

The study on the influence of the temperature was extended to the slight excess of TIPS, *i.e.* 62 mM. The Au and OY concentrations were kept constant at 20 mM and 50 mM, respectively. The two vials containing the $HAuCl_4$ and OY solution and the TIPS solution were thermalized in a temperature controlled water bath to have a same and homogeneous temperature. The mixing was also done in

the bath to ensure a controlled temperature and the reaction then let undisturbed to proceed during 3 h.

Working at higher temperature decreased the onset time at which the solution turned red, from 180 s at T = 25°C down to 60 s at T = 40 °C.

Figure 5.3 shows the SAXS patterns of the as-prepared Au nanoparticle suspensions after 3h of reaction at 30 °C, 35 °C and 40 °C. As we know from the previous chapter, the two-step curves indicate the presence of a bimodal distribution of nanospheres as it was observed clearly for the NPs prepared with 62 mM TIPS at 25 °C. The two-step curves progressively smoothened with increasing temperature. At 40 °C, the oscillations at high q, characteristic of fairly monodisperse NPs, were observed (Fig. 5.3.c). All the experimental curves were nicely fitted considering two gaussian distributions: a major one (population A) with a mean diameter of d_m = 1.8 - 2 nm, and a second one (population B) with a larger diameter d_m= 3.3 - 3.8 nm. The mean size, d_m, the relative standard deviation σ/d_m and scales are given in Table 5.2. The total scale, corresponding to the Au volume fraction, is the same for the four different temperatures which means that there is no effect of the temperature on the reduction yield. The relative volume fraction of the two populations depends on the temperature, as evidenced by the figure 5.3.d which represents the volume-weighted size distribution determined by SAXS. The proportion of the smallest nanoparticles (population A), increased significantly with the temperature: from 64 % for T = 25 °C to 92 % for T = 40 °C. Thus, even if the temperature was varied in a fairly small range, from 25 to 40 °C, it has a strong effect on the size distribution of the particles.

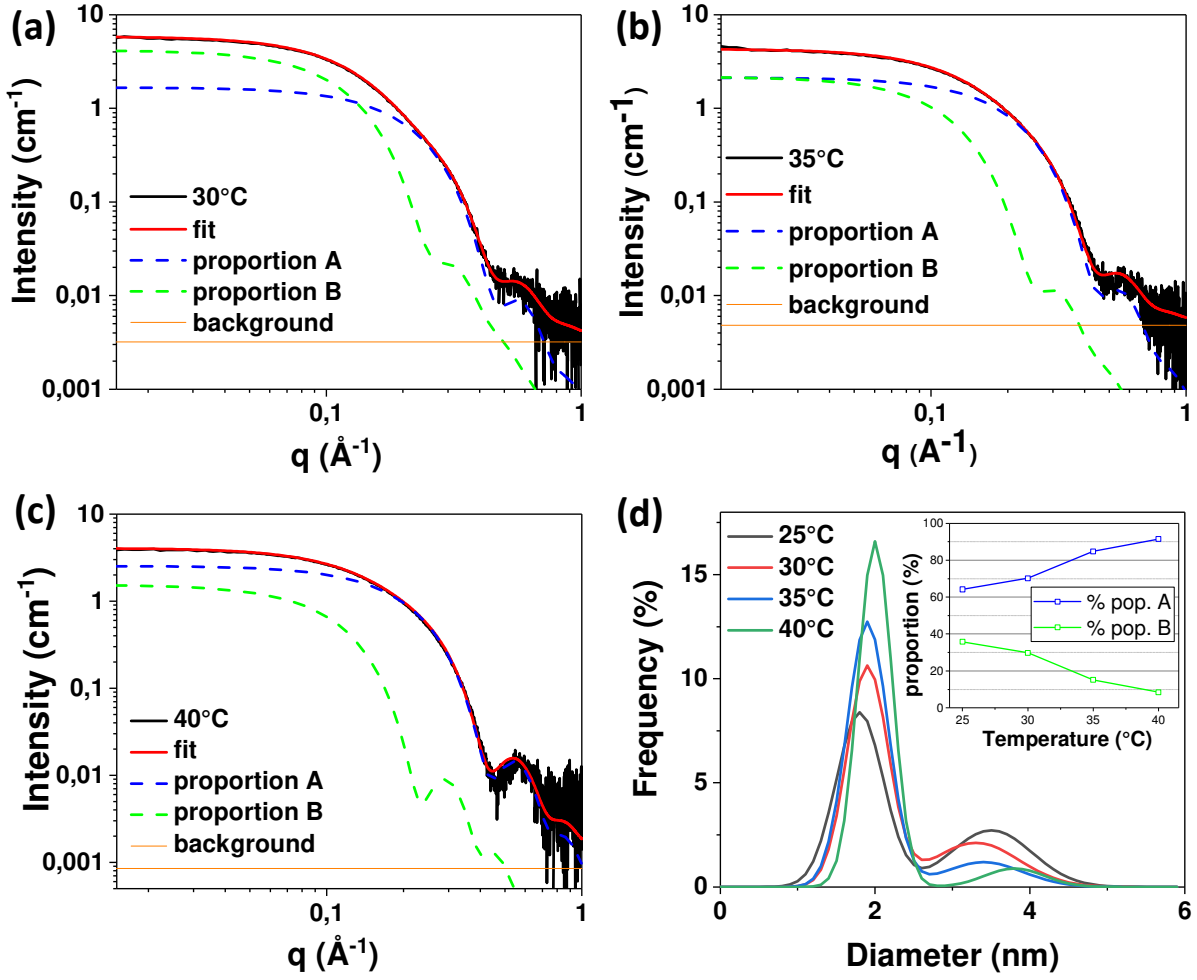

Figure 5.3 (a) SAXS patterns of suspensions of Au nanoparticles prepared by reduction of $HAuCl_4.3H_2O$ in OY/hexane ([Au] = 20 mM; [OY] = 50 mM) using TIPS as reducing agent ([TIPS] = 62 mM) at (a) T = 30°C, (b) T= 35°C, (c) T= 40°C Black: experimental data, red: best fits including two populations of nanospheres, population A (dashed blue), population B (dashed green), and a constant background (orange) (d) Volume-weighted size distribution determined by SAXS of the particles prepared at different temperatures. *Inset*: relative proportion of the two populations A and B *vs* reaction temperature.

T °C	Population A				Population B				
	d_m	σ/d_m	% vol.	scale	d_m	σ/d_m	% vol.	scale	Total scale
25 °C	1.8	0.17	64	$2.6x10^{-4}$	3.5	0.15	36	$1.4x10^{-4}$	$4x10^{-4}$
30 °C	1.9	0.14	70	$2.9x10^{-4}$	3.3	0.17	30	$1.2x10^{-4}$	$4.1x10^{-4}$
35 °C	1.9	0.14	85	$3.3x10^{-4}$	3.4	0.15	15	$6x10^{-5}$	$3.9x10^{-4}$
40°C	2.0	0.11	92	$3.7x10^{-4}$	3.8	0.10	8	$3.4x10^{-5}$	$4x10^{-4}$

Table 5.2 Summary of the adjustable parameters of the two gaussian distributions (A and B) used to fit the experimental SAXS pattern of Au nanoparticle suspensions obtained after 3h of reaction using [TIPS]= 62 mM at different reaction temperatures: the mean diameter, d_m, the polydispersity expressed as σ/d_m, (with σ the standard deviation of the gaussian distribution), and the relative volume fraction of both populations, *% vol*.

5.1.3 Discussion on the temperature effect

In the presence of a stoichiometric concentration of TIPS or of a slight excess, the temperature seems to favor ultra-small particles. In the framework of the competitive pathway between a direct reduction and the crystallization of the OY-Au(I)-Cl lamellar phase proposed in chapter 4, we can suppose that the temperature plays a key role on the intermediate. Unfortunately, we didn't have the chance to follow these reactions using in-situ SAXS during a synchrotron campaign.

However, we studied specifically the OY-Au(I)-Cl intermediate in presence of sub-stoichiometric TIPS concentration using the SAXS available at LGC.

The partial reduction of 20 mM of $HAuCl_4$ with 10 mM of TIPS was performed at T = 40 °C following the same protocol as in the section 4.6.1. Interestingly, the SAXS recorded *in situ* did not show any Bragg peaks but only an increase of the intensity at small *q* (figure 5.4.a). After 15 min, we observed a power law of $q^{-0.81}$ at low-q region, which is close to the value of q^{-1}. This exponent demonstrates that elongated rod-like aggregates form in the solution[1]. The increase of the intensity at small *q* may due to this aggregation.

Thus, increasing the reaction temperature by only 15 °C prevents the crystallization of the lamellar phase. The absence of the lamellar phase at 40°C doesn't mean that the intermediate OY-Au(I)-Cl precursor is not formed. Indeed, when cooling down the sample prepared at 40°C leads to the crystallization of the lamellar phase (figure 5.4.b).

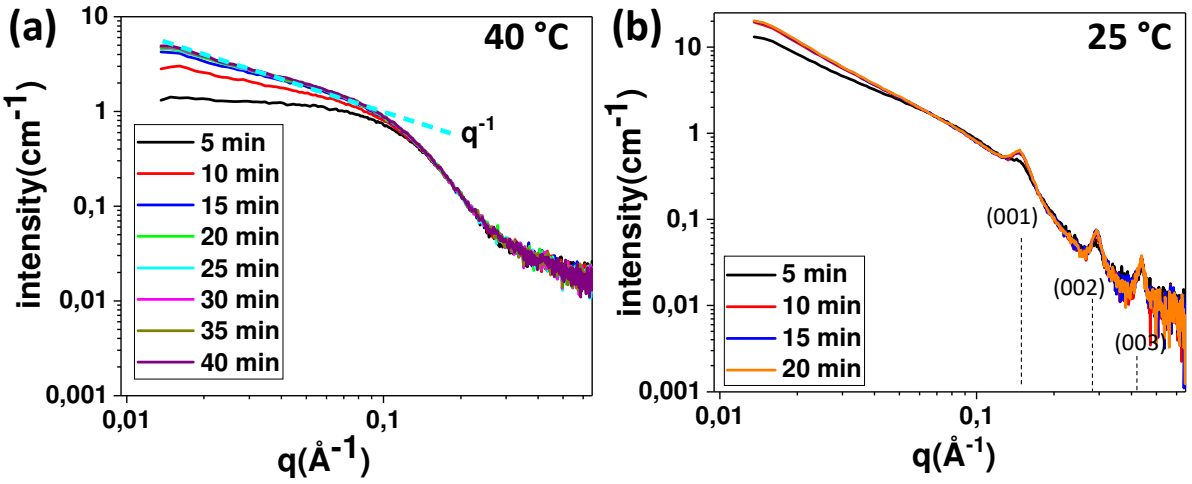

Figure 5.4 (a) *In situ* SAXS patterns recorded during the partial reduction of $HAuCl_4$ using 0.5 eq. of TIPS at 40 °C ([Au] = 20 mM, [TIPS] = 10 mM), (b) In situ SAXS pattern recorded at 25°C on the sample aged 40 min at 40°C then cooled at 25°C. Dashed line: power law q^{-1}.

To confirm this result, we prepared the OY-Au(I)-Cl intermediate at 25 °C. After around 1 h at 25 °C, we heat the capillary to 40 °C. The evolution of the SAXS signal is reported in the figure 5.5. The lamellar phase quickly vanishes, the Bragg peaks being no longer observed after few minutes. The lamellar phase thus exhibits a melting temperature in the range 25°C-40°C.

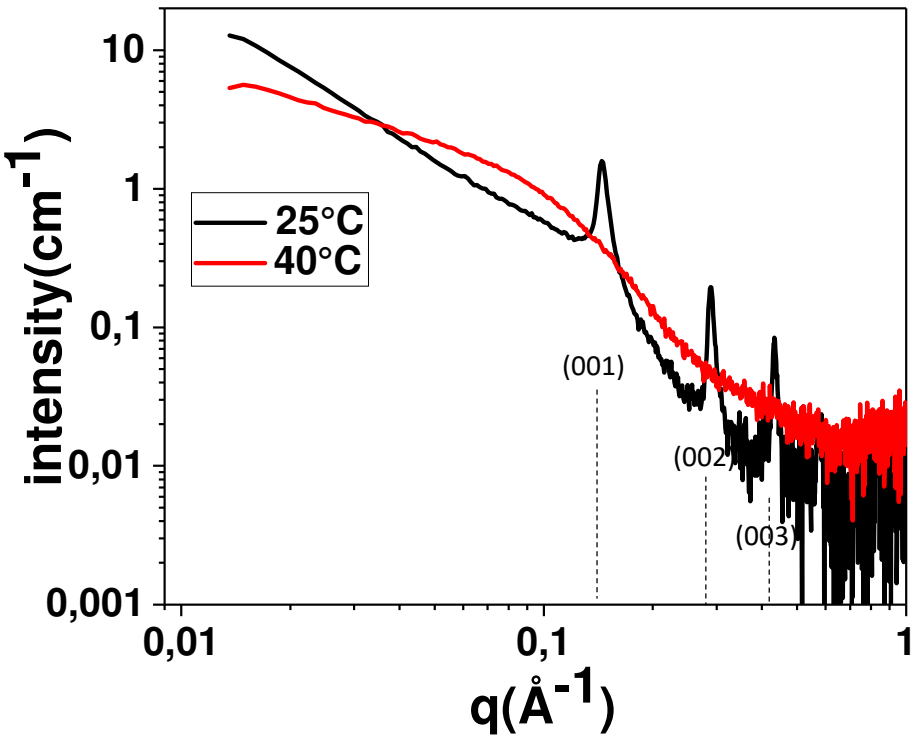

Figure 5.5 *In situ* SAXS patterns recorded during the partial reduction of $HAuCl_4$ using 0.5 eq. of TIPS ([Au] = 20 mM, [TIPS] = 10 mM) at 25 °C (black line) and *in situ* SAXS pattern (red line) recorded at 40°C on the sample aged 1 h at 25°C then heated at 40°C.

The higher temperature (T = 40°C) prevents the crystallization of the lamellar phase and favors the smallest nanoparticles. Their relative volume fraction indeed increases from 64 % for T = 25 °C to 92 % for T = 40 °C. These results agree with the proposed competition between the two-reaction pathway, as described in chapter 4, the limiting step being not only the formation of the OY-Au(I)-Cl compound but its crystallization into a stable lamellar phase.

5.2 Influence of the trialkylsilane

While TIPS is the most commonly used silane for the synthesis of gold nanowires[2], other silanes such as triethylsilane (TES) and tris(trimethylsilyl)silane (TTMS) have been used for gold nanoparticles[3,4] or ultrathin copper nanowires synthesis[5], respectively. The chemical formulas of these silanes are given in figure 5.6.

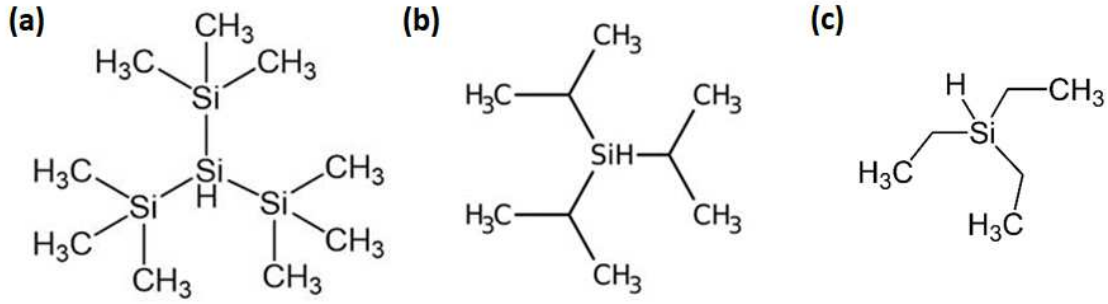

Figure 5.6: (a) Tris(trimethylsilyl)silane (TTMS), (b) Triisopropylsilane (TIPS) and (c) Triethylsilane (TES)

In the following Au NPs syntheses were carried out at T = 25°C using triethylsilane (TES) as reducing agent, keeping the same experimental conditions as before ([Au] = 20 mM; [OY] = 50 mM). As the ethyl chains of TES are less bulky than the isopropyl chains of TIPS, a lower steric hindrance was expected which could favor the coordination to the gold complexes and therefore, increase the reduction rate.

5.2.1 UV-Vis absorption

To show the influence of the nature of the trialkylsilane, we compare first the kinetic followed by UV-vis of the reactions with TES and TIPS at the concentration of 62 mM.

With [TES] = 62 mM the solution turned red only a few seconds after the addition, much faster than the 185 ± 5 s observed with [TIPS] = 62 mM. The absorbance of the solution at 520 nm measured as a function of time on the *in situ* UV-vis curves is displayed on Figure 5.7. The onset of Au (0) is around 10 s, a value similar to the one observed with [TIPS] = 1 M. The slope of the curve Abs = f(t) was found

0.12 s^{-1} for the reaction with [TES] 62 mM which is 10 times faster than with [TIPS] = 62 mM. Au (0) NPs were formed very quickly, supporting our assumption on the higher reactivity of TES.

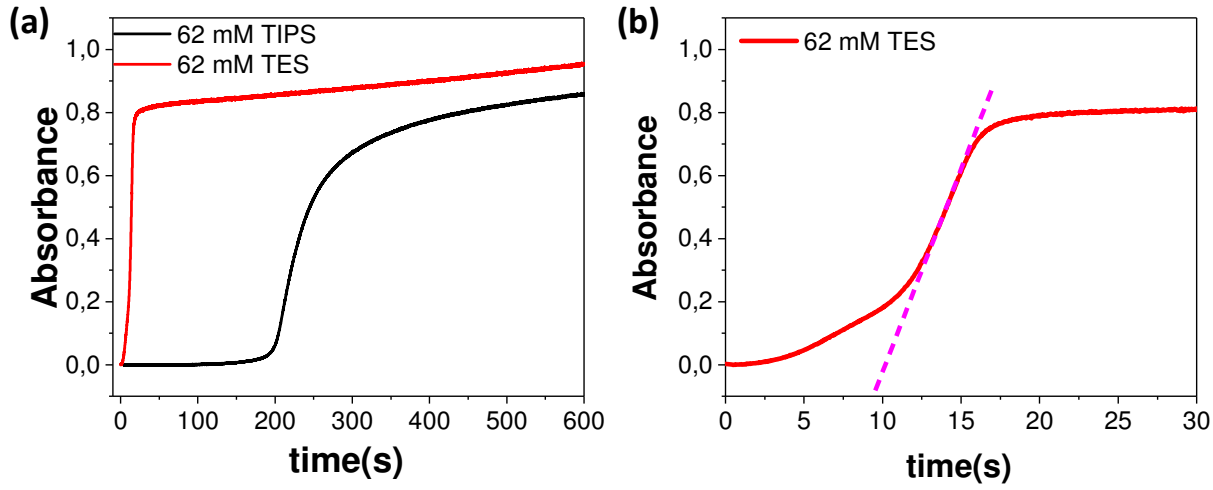

Figure 5.7 (a) UV-vis absorbance at λ = 520 nm vs time measured in the channel of a microfluidic chip during the reduction of $HAuCl_4$ (20 mM) with [TIPS]= 62 mM (black line) and [TES]= 62 mM (red line) and (b) zoom on the first 30 s. The pink dashed line allows to define the time on the Au(0) onset and the slope in the first stage of the reduction.

5.2.2 Effect of the TES concentration on the particle size

Au NPs were synthesized varying the concentrations of TES between 62 mM and 1M. The NPs obtained after 3h of reaction were characterized by SAXS (Figure 5.8). Interestingly, the curves were smooth and exhibit oscillations at high *q*, revealing the presence of monodisperse nanoparticles for every TES concentration. In the case of TIPS, two-step curves were on the contrary observed at low concentration. The experimental patterns were nicely fitted with two populations of spheres with a large proportion (~90%) of small NPs (d_m < 2 nm) highly monodisperse (σ/d_m = 8%) (Table 5.3). The second population (~10%) corresponds to particles with a mean diameter of 3 to 3.5 nm (Table 5.3).

As already faced in chapter 4, the total scale deduced from the fit is higher than the theoretical volume fraction of Au NPs (3.2 ± 0.3 x 10^{-4} vs 2 x 10^{-4}). However, if we look at the table 5.3, the total scale is fairly independent of the TES concentration. Therefore, one can assume that the Au volume fraction in the sample does not depend on the TES concentration, *i.e.* that the yield was 100 %.

TES concentration does slightly impact the mean diameter of the ultra-small NPs which was decreased from 2 nm for [TES] = 62 nm down to 1.7 nm for [TES] = 1M. The results were highly reproducible, confirming this slight trend on the mean diameter (Table 5.3).

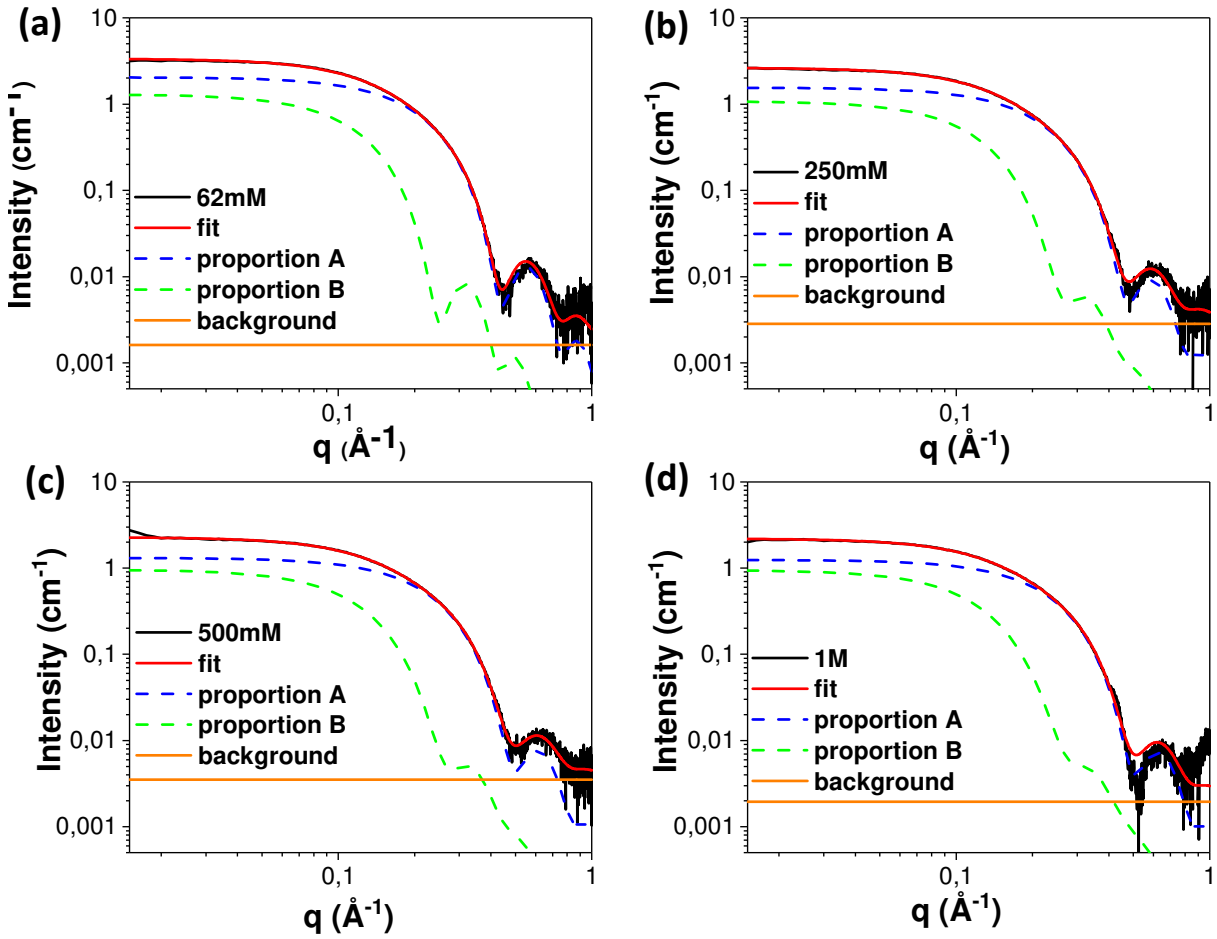

Figure 5.8 (a) SAXS patterns of suspensions of Au nanoparticles prepared by reduction of $HAuCl_4.3H_2O$ in OY/hexane ([Au] = 20 mM; [OY] = 50 mM) using TES as reducing agent in different concentrations: (a) [TES]= 62 mM, (b) [TES]= 250 mM, (c) [TES]= 500 mM, (d) [TES]= 1 M Black: experimental data, red: best fits including two populations of nanospheres, population A (dashed blue), population B (dashed green), and a constant background (orange)

[TES]	Population A				Population B				
	d_m	σ/d_m	% vol.	scale	d_m	σ/d_m	% vol.	scale	Total scale
62 mM	2	0.08	89	$3{,}1\times10^{-4}$	3.5	0.08	11	3.7×10^{-5}	3.5×10^{-4}
250 mM	1.9	0.10	89	2.9×10^{-4}	3.2	0.14	11	3.5×10^{-5}	3.2×10^{-4}
500 mM	1.8	0.11	90	$2{,}8\times10^{-4}$	3.2	0.14	10	3.2×10^{-5}	3.1×10^{-4}
1 M	1.7	0.10	90	$2{,}8\times10^{-4}$	3.0	0.17	10	3.3×10^{-5}	3.1×10^{-4}

Table 5.3 Summary of the adjustable parameters of the two gaussian distributions (A and B) used to fit the experimental SAXS pattern of Au nanoparticle suspensions obtained after 3h of reaction using TES at different concentrations: the mean diameter, d_m, the polydispersity expressed as σ/d_m, (with σ the standard deviation of the gaussian distribution), and the relative volume fraction of both populations, *% vol*.

5.2.3 XAS with different TES concentrations

To have a better assessment of the successive reduction steps and understand the difference between the two reducing agents, the Au NP syntheses were followed *in situ* by X-ray absorption spectroscopy (XAS). The time-resolved XAS spectra (figure 5.9) were fitted by a linear combination (LCA) of three components, Au (III), Au (I) and Au (0), as described previously. In the following, we compare at first, TIPS and TES at the same concentration of 62 mM, and then the different TES concentrations in the range 62 mM and 1 M.

The same sequence of the three successive stages could be determined for [TES]= 62 mM: induction, nucleation and growth (figure 5.9.a). However significant differences were observed compared to the reduction with TIPS. The induction and the nucleation stages were much shorter compared to TIPS: $t_{induction}$ 13.5 s vs 178 s and $t_{nucleation}$ = 22.5 s vs 74 s, respectively (table 5.4). For [TES]= 62 mM, the concentration of the Au(I) species reached also a maximum value at the Au (0) onset, i.e. at the beginning of the nucleation stage, but this value was lower than with TIPS, 25 % vs 50 %.

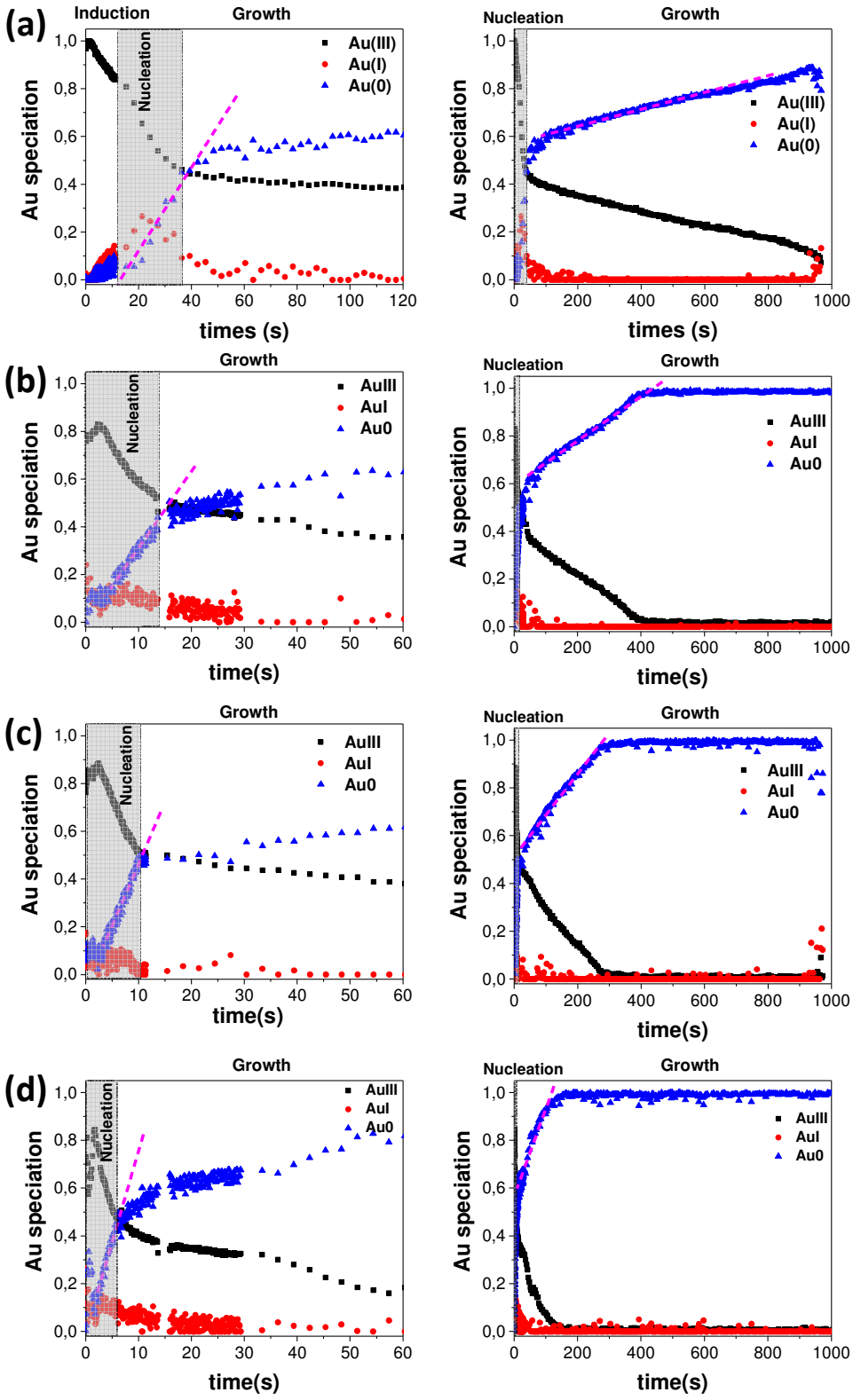

Figure 5.9 Relative Au (III), Au (I) and Au (0) concentrations deduced from the linear combination analysis of the XAS spectra measured in situ during the reaction using different [TES] (a) 62 mM, (b) 250 mM, (c) 500 mM and (d) 1 M. Pink and green dashed lines: linear fit of the first and second Au (0) slope to determine the nucleation and growth rate, respectively.

For the other concentrations, the reaction is much faster. Despite its specific design, our microfluidic chip did not allow to capture the induction time if existing: the beginning of the nucleation stage is directly seen (figure 5.9.b-c-d). For this reason, we could not define any induction stage for [TES]>62 mM, but the nucleation and the growth stage are clearly visible.

In the figure 5.10.a, the nucleation rate was plotted as a function of [TES]. The plot is fitted well with a linear function (χ^2 = 0.994), revealing that the nucleation rate is proportional to the [TES]. The nucleation rate is increasing by a factor of 5 over the whole concentration range. The proportionality slope is 2.5 times larger than the one observed with TIPS (0.074 vs. 0.03 $s^{-1}.L.mol^{-1}$).

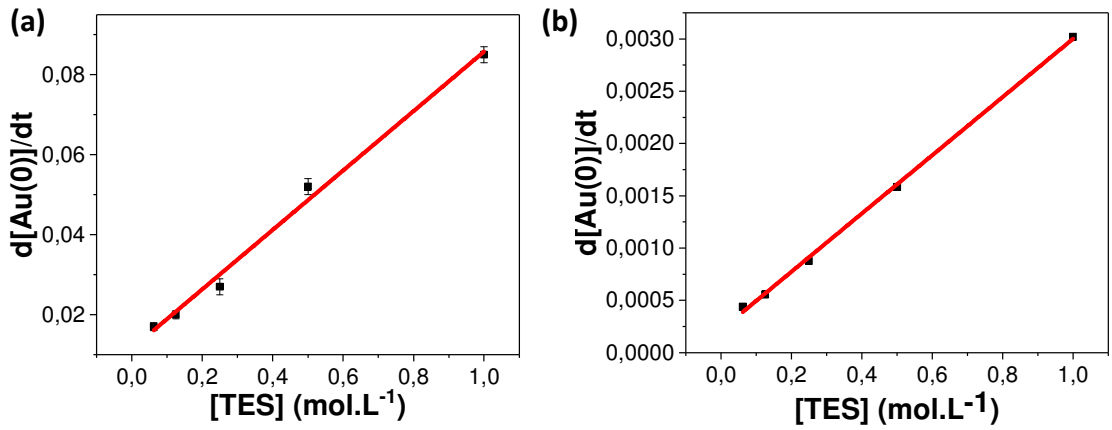

Figure 5.10 (a) Nucleation and (b) growth rate as a function of [TES] obtained from the XAS spectra

With the TES concentration increase, the maximum of Au (I) ($[Au(I)]_{max}$ in table 5.4) is decreasing from 25 % to 10 %. The concentration of Au(I) tends then rapidly to 0 during the nucleation stage. It took only 45 s, 30 s, 10 s and few seconds for [TES] = 62, 250, 500 mM and 1M; while Au(I) was still observed after 30 min in presence of TIPS.

Then, [Au(I)] remained equal to zero all over the growth stage while [Au (III)] and [Au (0)] varied linearly (χ^2 = 0.999) as shown in figure 5.10.b. From this plot, we can deduce that the growth rate is found proportional to the [TES] with the rate 0.003 $s^{-1}.L.mol^{-1}$. If we consider a simple model with two successive reduction steps: Au (III)→Au(I)→Au (0), the low concentration of Au(I) observed with TES shows that the reduction of Au(I) →Au (0) is much faster than the reduction that Au (III)→Au(I). We can say that whatever the TES concentration, a zero-order reaction was observed during the growth stage.

[TES]	Onset of Au (0)	Nucleation rate (mol. L^{-1}. s^{-1})	$[Au(I)]_{max}$ (%)	Time at which $[Au(I)]_{max}$	End of the duration of nucleation stage (s)	Growth rate (mol. L^{-1}. s^{-1})
62 mM TIPS	178 ± 2	0.0050 ± 0.0004	50	200 s	252	-
62 mM	13.5 s	0.017 ± 0.001	25	21 s	36	$4.4x10^{-4}$
125 mM	-	0.020 ± 0.001	20	10 s	27	$5.6x10^{-4}$
250 mM	-	0.027 ± 0.001	18	8 s	14	$8.8x10^{-4}$
500 mM	-	0.052 ± 0.002	12	7 s	10	$2x10^{-3}$
1 M	-	0.085 ± 0.002	10	3 s	6	$3x10^{-3}$

Table 5.4 The summary of the Au (0) onset, nucleation and growth rates, $[Au(I)]_{max}$ and the time at which it is observed, the time at which the nucleation stage ends obtained from the XAS spectra measured *in situ* during the reaction using [TES] from 62 mM to 1 M

Since, during the nucleation stage, the concentration of Au(I) tends rapidly to 0, the intermediate OY-Au(I)-Cl complex cannot crystallize and thus do not get involved in the Au (0) NP nucleation and growth, contrarily to the reaction performed in presence of TIPS. The presence in a large majority of ultrasmall NPs with TES further strengthened our hypothesis of two competitive pathways.

5.3 Structural studies on the final Au NPs

The structural analysis of the ultra-small Au NPs were performed using *in situ* high energy XRD (HE-XRD) and structure modelling. The Au nanoparticles prepared at 25 °C with [TES] = 62 mM or [TIPS] = 1 M, and at 40 °C with [TIPS] = 62 mM were measured as prepared, in the mother liquor.

Figure 5.11.a shows the representative *in situ* XRD patterns of these samples. The XRD patterns of the ultra-small particles, which do not correspond to the *fcc* structure, look pretty similar but some slight differences can be seen depending on the synthesis conditions.

For the particles prepared at 40 °C, the peaks are broader and the second peak is shifted to q = 3.48 $Å^{-1}$ compared to the value of q = 3.31 $Å^{-1}$ found for the two samples prepared at 25 °C (Figure 5.11.a). The *in situ* HE-XRD patterns of these three samples were transformed to atomic PDFs (Figure 5.11.b). The physical oscillations in the PDF of the two samples prepared at 25 °C (with [TES] = 62 mM or [TIPS] = 1 mM) extend in the *r*-space to a distance of about 1.7 nm, which is considered as the length of structural coherence for the studied NPs. This size is in good agreement with the mean NP diameter measured by SAXS, showing the good crystallinity of the NPs. In addition to this, the oscillations of the PDF for the sample prepared at 40 °C with [TIPS] = 62 mM appear to be damped to zero at smaller *r* values. It corresponds to a reduced coherent length of about 1.3 nm, which is below the 2.0 nm mean size determined by TEM.

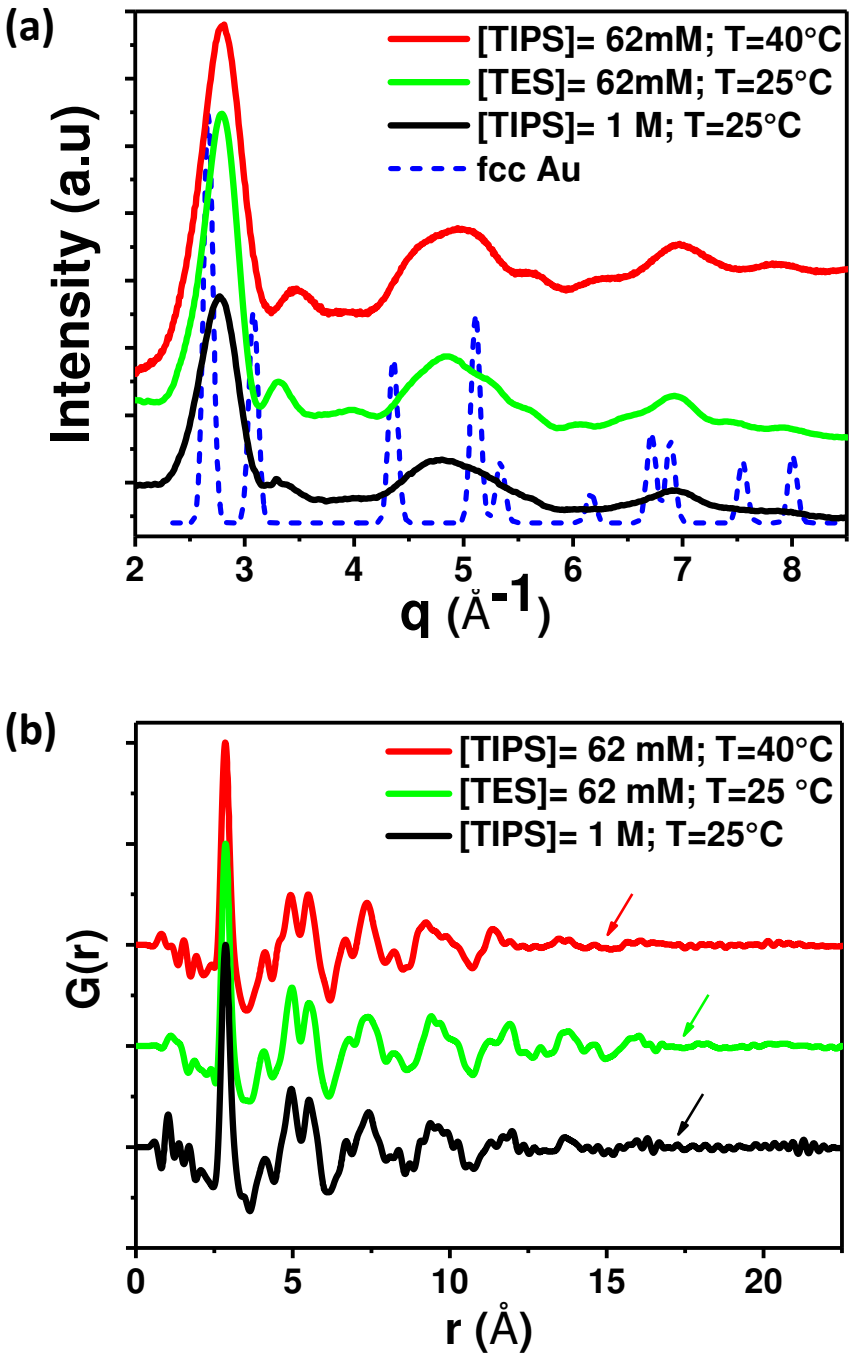

Figure 5.11. (a) *In situ* high-energy X-ray diffraction and (b) the corresponding *G*(*r*) oscillations of monodisperse gold nanoparticles prepared at T = 25 °C with [TES] = 62 mM (green line) or [TIPS] = 1 M TIPS (black line) or at 40°C with [TIPS] = 62 mM (red line). The dash blue line corresponds to the theoretical XRD pattern of *fcc* Au with an arbitrary peak broadening. An arrow on the PDF shows the loss of oscillation and thus the length of structural coherence.

To display the atomic structure of Au NPs, the *in situ* atomic PDFs were compared first with the two theoretical PDFs of 309 atom clusters (1.7 nm in size) previously used in the chapter 3 and 4: a cuboctahedron with the *fcc* structure (CBO) and an icosahedron (ICO) (Figure 5.12). Our reference for the *fcc* structure is CBO which is the *fcc* polyhedra. It has six equal squares and eight equal triangles as faces. The reference for the icosahedron which is ICO has twenty triangles as faces and exhibits 5-fold axes. The 5-fold axes is a non-crystallographic symmetry. The comparison clearly indicates that the CBO does not generate the experimental PDFs (Figure 5.12 top), which verifies that the particles have a non *fcc* structure. On the contrary, the PDF of the 309 atoms ICO reproduces fairly well the experimental data (Figure 5.12 middle). In order to improve the agreement with the experimental data, and in particular the amplitude of the peaks, a model of a distorted icosahedron was developed by adding a layer of atoms to some of the NP facets of the 309 perfect ICO, without touching its icosahedral 5-fold symmetry. After that the changing of the positions of the all these atoms in the undistorted ICO lattice was allowed to have a local structural disorder ICO (Inset in Figure 5.12 bottom). The computed PDFs of this new model matched with the experimental PDFs in finest detail.

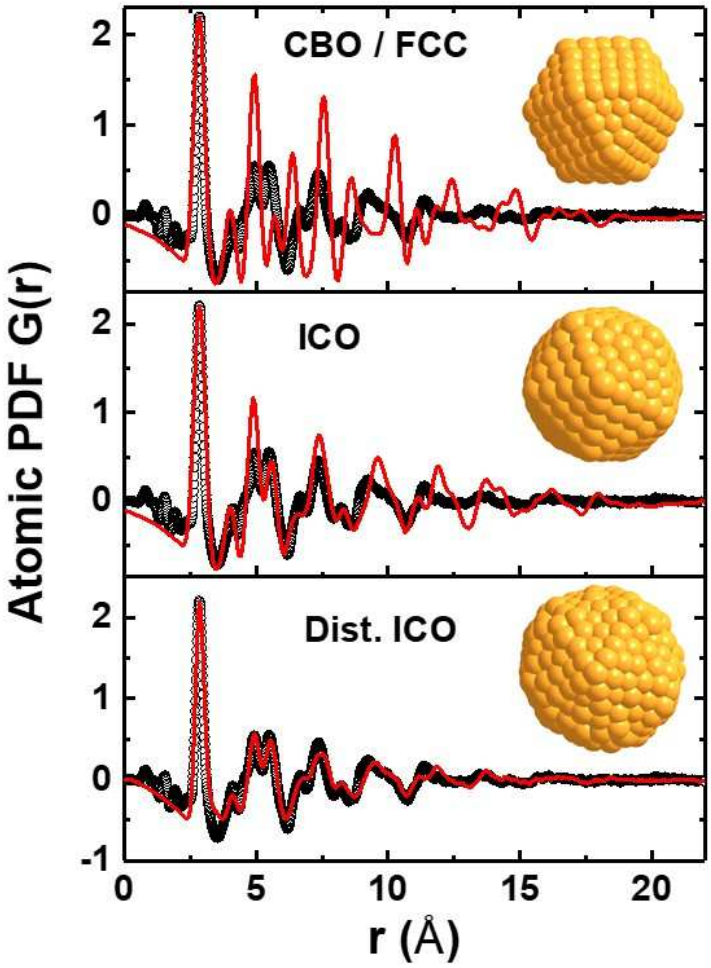

Figure 5.12. Comparison between experimental PDF of Au NPs prepared by reduction with [TIPS] = 62 mM at 40 °C (black circle) and different computed atomic PDFs (red line). CBO is a 309 atoms cuboctahedron with *fcc* structure, ICO is a 309 atoms icosahedron and Dist. ICO is 435 atoms distorted icosahedron. *Inset*: images of the structural models.

5.4 Self-assembly of ultra small NPs, Au (0) superlattices

The spontaneous assembly of NPs into superlattices has been intensively studied due to the peculiar collective properties that can arise.[6] It is known to be observed only with monodisperse NPs. Having a method to prepare highly monodisperse icosahedral Au NPs using [TES] = 62 mM in hand, we studied their spontaneous organization under solvent evaporation. The NPs self-assemble into crystalline superlattices once deposited on TEM grids or silicon substrates. The SAXS signal of Au NPs assemblies

exhibited well defined Bragg peaks that were indexed as the first three (*hkl*) reflections of a *bcc* superlattice with a unit cell parameter *a* = 5.25 nm (Figure 5.13.a). In a *bcc* structure the distance center to center between two adjacent particles is $d_{NP-NP} = a\frac{\sqrt{3}}{2}$, taking the value of 4.55 nm in the present case. The Au core of the particles was 2.0 nm, according the SAXS. Thus, the distance edge to edge between two adjacent particles was $e = d_{NP\text{-}NP} - d_m$ = 2.55 nm. Considering that the fully extended OY chain length is *L* = 2.1 nm,[7] *e* is in between *L* and 2*L*. NP superlattices were also observed on the TEM grids. A representative example of area showing a stack of a few NP layers is given in Figure 5.13.b. In every case, the superlattice was indexed as a *bcc* structure in the [011] zone axis where the unit cell parameter agrees with the a= 5.25 nm determined by SAXS.

It has been largely reported that the structure of NP superlattices depends on the diameter of the metal core, d_m, and on the thickness of the ligand shell coating the metal core. A *fcc* structure is generally found when the metal core is large compared to the ligand shell while a *bcc* structure is observed for small metal cores and thick ligand shells[8]. Pansu *et al.* proposed the structure diagrams of thiolated Au NP superlattices as a function of the Au core size and the number of atoms in the thiol chain or the ligand fully extended length *L*[9]. In these diagrams, a transition threshold L/R > 1.2 was reported to stabilize the *bcc* structure. In our case, the particles exhibit a core radius $R = d_m/2$ = 1.0 nm and are stabilized by a 18 carbon chain amine of *L* = 2.1 nm, leading to a *L*/*R* ratio of 2.1, well above the transition threshold. Therefore, the Au NP superlattice prepared from ultra small icosahedral NPs falls in the *bcc* structure region of Pansu's diagram. The validity of the structure diagram for the bcc superlattice seems to be extended to long chain amine as well.

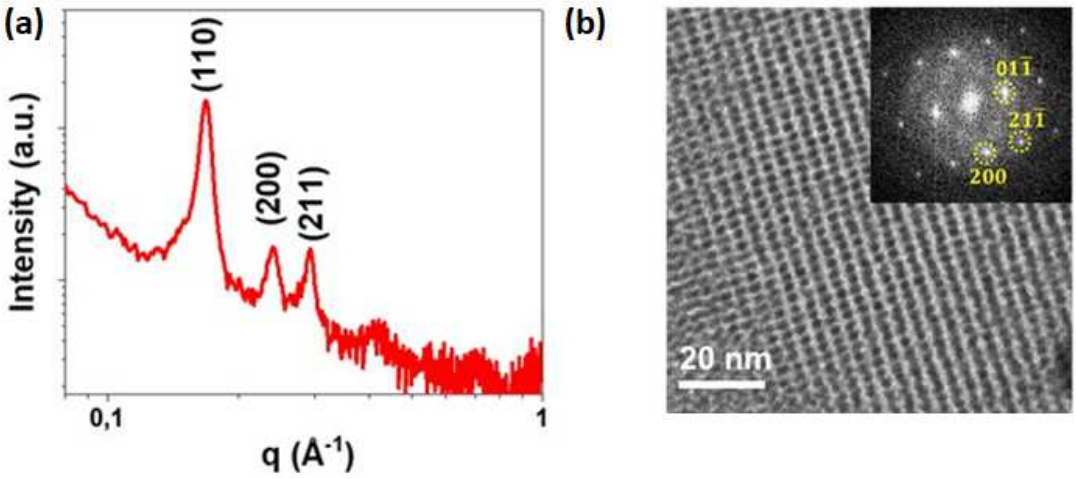

Figure 5.13. (a) SAXS of dried assembly of ultra-small particles prepared with [TES] = 62 mM at 25 °C; (b) TEM image of an assembly of NPs. Inset: the corresponding FFT indexed as a *bcc* structure in the [011] zone axis.

5.5. Discussion on the icosahedra formation

In this chapter we have established that the temperature and the nature of the trialkylsilane play a key role on the monodispersity of the Au particles. We have shown that compared to the standard synthesis involving [TIPS] = 62 mM at 25 °C, the size distribution was improved by three means: (i) increasing the TIPS concentration to 1 M as shown in the chapter 3, (ii) increasing the reaction temperature to 40 °C or (iii) using TES as reducing agent instead of TIPS.

The effect of the temperature and the TES was to increase the reduction rate, avoiding the crystallization of a OY-Au(I)-Cl lamellar phase which is in direct competition with the nucleation/growth of the Au icosahedral NPs. In the figure 5.14, the model of two competitive pathway has been completed with the different parameters one can play with: the reaction temperature, the concentration and the nature of the reducing agent.

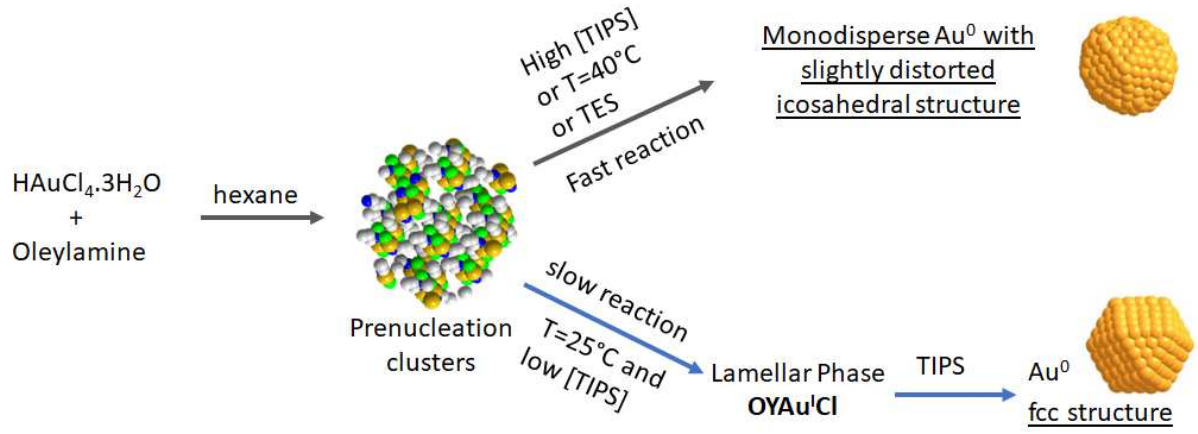

Figure 5.14. Schematics of the competition between the direct pathway leading to the crystallization of ultra-small Au NPs with the icosahedral structure and the one involving the lamellar phase OY-Au(I)-Cl and leading to bigger particles with the *fcc* structure.

Bibliography

(1) Lombardo, D.; Munaò, G.; Calandra, P.; Pasqua, L.; Caccamo, M. T. Evidence of Pre-Micellar Aggregates in Aqueous Solution of Amphiphilic PDMS–PEO Block Copolymer. *Phys. Chem. Chem. Phys.* **2019**, *21* (22), 11983–11991. https://doi.org/10.1039/C9CP02195G.

(2) Loubat, A.; Impéror-Clerc, M.; Pansu, B.; Meneau, F.; Raquet, B.; Viau, G.; Lacroix, L.-M. Growth and Self-Assembly of Ultrathin Au Nanowires into Expanded Hexagonal Superlattice Studied by in Situ SAXS. *Langmuir* **2014**, *30* (14), 4005–4012. https://doi.org/10.1021/la500549z.

(3) Sugie, A.; Somete, T.; Kanie, K.; Muramatsu, A.; Mori, A. Triethylsilane as a Mild and Efficient Reducing Agent for the Preparation of Alkanethiol-Capped Gold Nanoparticles. *Chem. Commun. Camb. Engl.* **2008**, 3882–3884. https://doi.org/10.1039/b806251j.

(4) Sugie, A.; Song, H.; Horie, T.; Ohmura, N.; Kanie, K.; Muramatsu, A.; Mori, A. Synthesis of Thiol-Capped Gold Nanoparticle with a Flow System Using Organosilane as a Reducing Agent. *Tetrahedron Lett.* **2012**, *53* (33), 4457–4459. https://doi.org/10.1016/j.tetlet.2012.06.056.

(5) Cui, F.; Yu, Y.; Dou, L.; Sun, J.; Yang, Q.; Schildknecht, C.; Schierle-Arndt, K.; Yang, P. Synthesis of Ultrathin Copper Nanowires Using Tris(Trimethylsilyl)Silane for High-Performance and Low-Haze Transparent Conductors. *Nano Lett.* **2015**, *15* (11), 7610–7615. https://doi.org/10.1021/acs.nanolett.5b03422.

(6) Boles, M. A.; Engel, M.; Talapin, D. V. Self-Assembly of Colloidal Nanocrystals: From Intricate Structures to Functional Materials. *Chem. Rev.* **2016**, *116* (18), 11220–11289. https://doi.org/10.1021/acs.chemrev.6b00196.

(7) Mourdikoudis, S.; Liz-Marzán, L. M. Oleylamine in Nanoparticle Synthesis. *Chem. Mater.* **2013**, *25* (9), 1465–1476. https://doi.org/10.1021/cm4000476.

(8) Goodfellow, B. W.; Yu, Y.; Bosoy, C. A.; Smilgies, D.-M.; Korgel, B. A. The Role of Ligand Packing Frustration in Body-Centered Cubic (Bcc) Superlattices of Colloidal Nanocrystals. *J. Phys. Chem. Lett.* **2015**, *6* (13), 2406–2412. https://doi.org/10.1021/acs.jpclett.5b00946.

(9) Pansu, B.; Goldmann, C.; Constantin, D.; Impéror-Clerc, M.; Sadoc, J.-F. Softness-Driven Complexity in Supercrystals of Gold Nanoparticles. *Soft Matter* **2021**, *17* (26), 6461–6469. https://doi.org/10.1039/D1SM00617G.

Chapter 6 Pre-Nucleation Clusters (PNCs)

For many years, the formation of metal nanoparticles in liquid phase has been explained by the classical nucleation theory. However, some studies focused on the possibility of non-classical nucleation pathways depending on the reaction parameters[1]. A precise information about the nucleation mechanisms is crucial in order to control the particle size and morphology[2]. Capturing experimentally the homogeneous nucleation stage is quite challenging because of its stochastic nature. In the previous chapters, we have collected many data on the kinetic of nucleation and growth of Au NPs using silanes as reducing agent. The scope of this last chapter is to summarize these results and try to draw some conclusions on the nucleation/growth mechanism.

6.1 Classical vs non-classical scenarii

In the classical nucleation theory (CNT), the nucleation corresponds to the overcome of the activation energy barrier, i.e. the free energy of the nuclei, which results from the volume and surface contributions (see chapter 1). Applied to the formation of metal nanoparticles, the CNT implies the formation of first zero-valent metal atoms which are the monomers for the further formation of the embryos and nuclei. When the concentration of these atoms exceeds the supersaturation threshold, the nucleation occurs, the critical size of the embryos is reached, stable nuclei resulting from the crystallization of metal atoms appear and start to grow. The nucleation stage consumes monomers and once the concentration of the monomer decreases below the supersaturation limit, the nucleation finishes and only the growth can continue. If one considers an atom by atom growth, the final particle size is only dictated by the number of stable seeds formed during the nucleation stage and thus depend only on the nucleation rate. Abecassis et al.[3] and Chen et al.[4] reported in-situ studies on the synthesis of Au nanoparticles using SAXS, UV-vis or XAS with results in agreement with the classical nucleation theory. The Au NPs were prepared by the reduction of gold chloride using borohydride or borane. Depending on the experimental conditions, the size of the particles was found in the range 1.4 nm to 5.9 nm.

Recent studies reported that non-classical nucleation processes could be involved in the crystallization of solids and nanoparticles.[3,4] These mechanisms happen via some more complex free-energy landscapes than the single barrier of the classical nucleation theory. The nucleation can involve stable pre-nucleation clusters, for example $CaCO_3$[5], or metastable intermediate states with amorphous structure, such as YVO_4:Eu[6]. Li et al.[7,8] have reported study about the nucleation mechanism of the two phases Brust synthesis with showing the formation of inverse micelles [TOA][Au(I)X_2]. They have concluded that there was a competition between reduction of complexes in the inverse micelles and

formation of a lamellar phase ($[AuSR]_n$). To confirm that, they have isolated this polymeric chain $[AuSR]_n$ and prepared NPs by reduction of this phase. They have obtained larger NPs (2.26 nm ± 0.39 nm). They have observed that this polymeric $[AuSR]_n$ is not good precursor to produce homogeneous ultrasmall Au NPs, and the presence of this complex increases the polydispersity of the synthesized Au NPs.

In 2020 we also proposed that such a non-classical nucleation theory could explain our first in-situ studies on the synthesis of ultra-small gold nanoparticles by the reduction of gold chloride in presence of oleylamine and a large excess of triisopropylsilane[9], as detailed in chapter 3. The presence of pre-nucleation clusters (PNCs) was clearly evidenced by the combined SAXS and XAS studies.

Since then, we have extended the study. In the chapters 4 and 5 kinetic data were extracted from the XAS and UV-vis studies for different trialkylsilanes and with different concentrations. In Chapter 4, we have shown the excellent reproducibility of the UV-vis and XAS kinetic data. We therefore have reliable data that can help to go further in the discussion of the nucleation mechanism. In the following, these data are examined to see if they fit with the CNT or, on the contrary if they can help to discard the CNT.

6.2 Comparison of the kinetic studies with TIPS and TES

As a reminder, all the XAS data shown in the chapters 4 and 5 obtained with TIPS and TES present the same features. To illustrate this, we compare in the Figure 6.1 the Au speciation for [TIPS] and [TES] of 62 mM, 250 mM and 1 M. In all cases, after an induction time during which Au(III) is gradually reduced to Au(I), Au(0) appears and increases very rapidly in a second stage. This second stage has been called the nucleation stage based on the comparison of the XAS and SAXS data of chapter 3 and confirmed in chapter 4 that showed that the first Au NPs appears in SAXS at the same time as the fast increase of Au(0) in XAS .

The end of the nucleation stage is characterized by a clear break in the slope of the Au(0) = f(t) curve. After this break, the Au(0) increase is much lower than during the nucleation stage. This third stage has been called the growth stage.

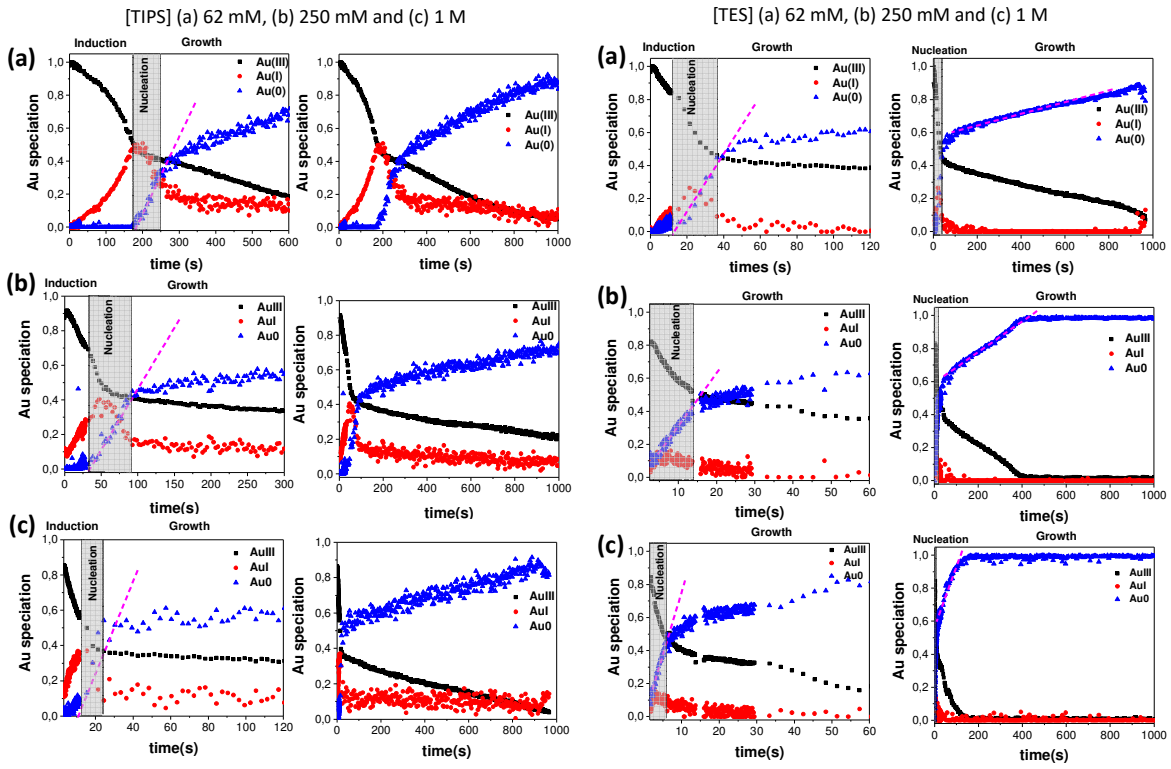

Figure 6.1. Au speciation calculated from the time-resolved XAS data with TIPS (left panel) and TES (right panel) at the concentrations of 62 mM, 250 and 1M.

The onset of Au(0) depends on the reduction rate. In other words, the duration of the induction stage depends on the nature of the trialkylsilane and its concentration. The induction time, t*, is shorter when the concentration of the reducing agent increases and it is shorter with TES than with TIPS, showing the higher reactivity of TES and higher reduction rate. In the case of TIPS, t* is inversely proportional to the TIPS concentration (Fig. 4.7a). In the case of TES, t* is extremely short and it was difficult to measure it precisely for [TES] > 125 mM because of the noise in the data at short times.

The nucleation rate also depends on the nature of the trialkylsilane and its concentration. It is faster with TES and, in both cases, TES and TIPS, the nucleation rate is proportional to the silane concentration (Figure 4.7 and 5.9). In figure 6.2 are plotted together the nucleation rate at the different concentrations of TIPS and TES. In this figure we have included a line showing that below a given nucleation rate the size distribution is bimodal and above it is more monodisperse. The reason for such a difference was clearly established in chapter 4, when the reduction rate is slow the increasing concentration of Au(I) (observed by XAS) favors the formation of the lamellar phase OY-Au(I)-Cl (observed by SAXS). Two pathways are then in competition: 1) the reduction of the PNC forming Au(0)

nuclei and 2) the crystallization of the lamellar phase. This competition is responsible for the bimodal distribution.

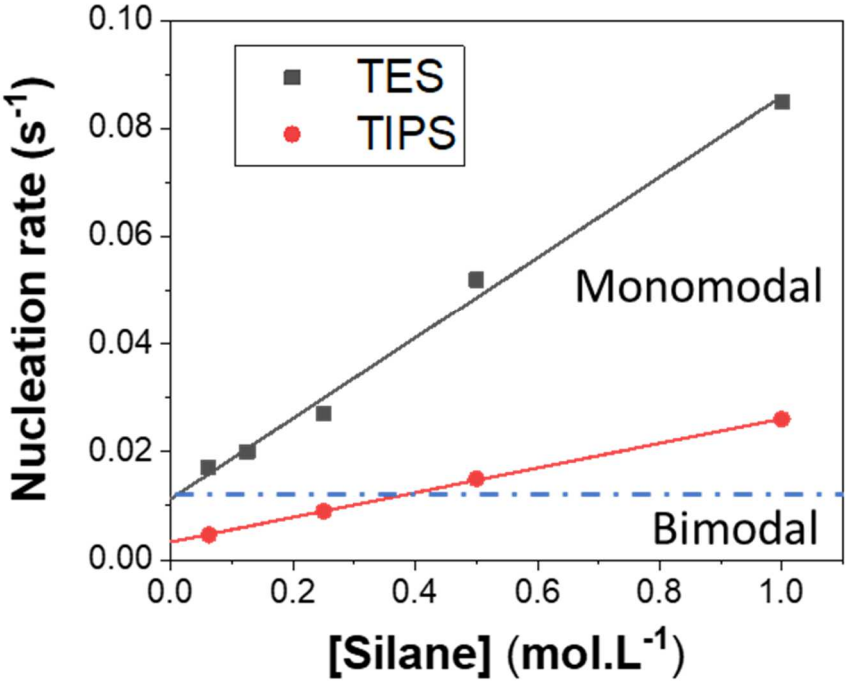

Figure 6.2. Nucleation rate as a function of the TES and TIPS concentration

As a consequence, the set of experiments carried out with TES and the ones with the highest TIPS concentrations (500 mM and 1M) appear more like a "model system" compared to the experiments carried out with the low TIPS concentration.

6.3 Discussion on the syntheses with TES

As shown in the Figure 6.2, the nucleation rate is proportional to the TES concentration and it increases of a factor 5 over the whole range of concentration studied.

Surprisingly, this linear relationship does not intercept the origin, as if the nucleation could occur without any addition of TES which is not the case experimentally. In absence of TES the PNCs transform very slowly into Au(I) but in general at room temperature we do not observe any Au(0) particles. This point is not understood and should be clarified in the future.

Considering now the variation of the particle mean size with the TES concentration, we have observed that the mean diameter is almost constant. The mean diameter decreased from 2 to 1.7 nm when the TES concentration was varied between 62 mM to 1 M (Figure 6.3a) which correspond to a decrease of a factor 1.6 of the mean volumes (Figure 6.3b). If we include in the same graph the mean diameter of the particles prepared with [TIPS]= 500 mM and 1 M (red dot in the graphs), we can conclude that there is no relationship between the nucleation rate and the final particle size.

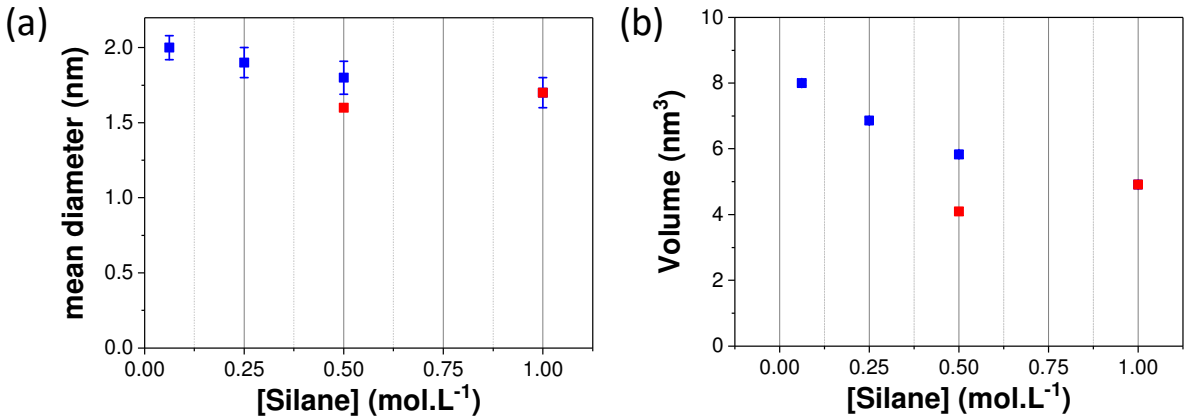

Figure 6.3. Au NP mean size (a) and mean volume (b) plotted as a function of the TES (blue) or TIPS (red) concentration.

In addition, as we can see in the Figure 6.1 (right panel for TES and values reported in the Table 5.3), the nucleation stage always stopped when the relative concentration of Au(0) reached the value of 50 %, whatever the TES concentration. This value of 50 % is also observed with [TIPS] = 500 mM and 1 M (see Fig. 6.1, left panel bottom). It means that the percentage of Au atoms involved in the nucleation stage is independent of the nucleation rate and independent of the duration of the nucleation stage as well.

According to the classical nucleation theory, the size of the nuclei is proportional to the surface tension of the solid particle in the liquid γ and inversely proportional to ln*S*, *S* being the supersaturation concentration, as it has been reminded in the chapter 1:

$$r^* = \frac{2\gamma v_m}{kT ln S} \qquad \text{(Eq. 1.4)}$$

with v_m the molar volume.

By varying the TES concentration from 62 mM to 1 M the nucleation rate was varied of a factor 5, so with [TES] = 1 M the concentration should reach a supersaturation ratio much higher than with [TES] = 62 mM since 50% of Au atoms are involved in the nucleation. Smaller nuclei in higher number are therefore expected with [TES] = 1M leading to a smaller final particle size.

As the final size slightly varies with [TES], one might think that this conclusion is a bit questionable. However, if we also include the results obtained with [TIPS] = 500 mM and 1 M, we can definitively rule out the CNT to explain the final particle size. Indeed, with these concentrations the mean diameters were 1.6 and 1.7 nm, respectively (Figure 6.3 and Table 4.2). The nucleation rates were much smaller than with TES while 50% of Au was involved (Figure 6.2).

The average diameter of the final particles measured by SAXS is around 1.8 nm. On the other hand, an icosahedron of 309 atoms fitted well the experimental PDF. Considering the “magic” multi-shell icosahedra, the number of atoms are 13, 55, 147 and 309 atoms in the 1-, 2-, 3- and 4-shell icosahedra, respectively[10]. Thus, in a 309 atoms icosahedron, the proportion of surface atoms is around 50 %[11]. As mentioned above, in all experiments around 50 % of Au atoms are involved in the nucleation stage and 50 % in the growth stage. We can reasonably state that in all experiments the nucleation stage generates gold particles containing approximately 150 atoms and this number increases to 300 atoms at the end of the growth stage. The size of gold particles of 150 and 300 atoms are estimated at 1.5 nm and 2 nm.

As mentioned in chapters 3 and 4, the precursor solution of all our syntheses results from the dissolution of $HAuCl_4$ in hexane thanks to the presence of oleylamine. The SAXS studies showed that the Au(III) complexes are involved in pre-nucleation clusters of size around 4 nm. Considering that this size is independent of the reduction conditions, one can suspect that the nucleation occurs inside the PNC. Having a better idea of the PNCs nature and estimating the number of Au(III) atoms in the PNCs is therefore important for a full understanding of the mechanism.

6.4 Chemistry of the Pre-Nucleation Clusters (PNCs)

The effect of the oleylamine concentration on the precursor solution was studied. Different precursor solutions were prepared by dissolving $HAuCl_4.3H_2O$ ([Au] = 20 mM) in hexane in presence of [OY] varying from 40 mM to 400 mM, i.e for a ratio OY/Au varying from 2 to 20 (i.e. for the conditions used for the synthesis of the ultrasmall nanospheres to the ultrathin Au nanowires).

6.4.1 Evolution of the precursor nature : state of the art

It is important to have in mind that below 2 equivalents of OY, it is not possible to dissolve completely $HAuCl_4$ in hexane. With 2 equivalents the dissolution is possible but take times and requires stirring and sonication. It is a little bit easier with 2.5 equivalents (conditions classically used for the synthesis of the Au ultra-small nanospheres) and much faster with higher concentration of OY. Once dissolved, the $HAuCl_4$ solution shows fairly different colors, varying from pale yellow to orange color as shown on figure 6.4. The color is pale yellow from 2 to 4 eq. of oleylamine and the transition to the orange color is observed abruptly for the OY/Au ratio = 4.

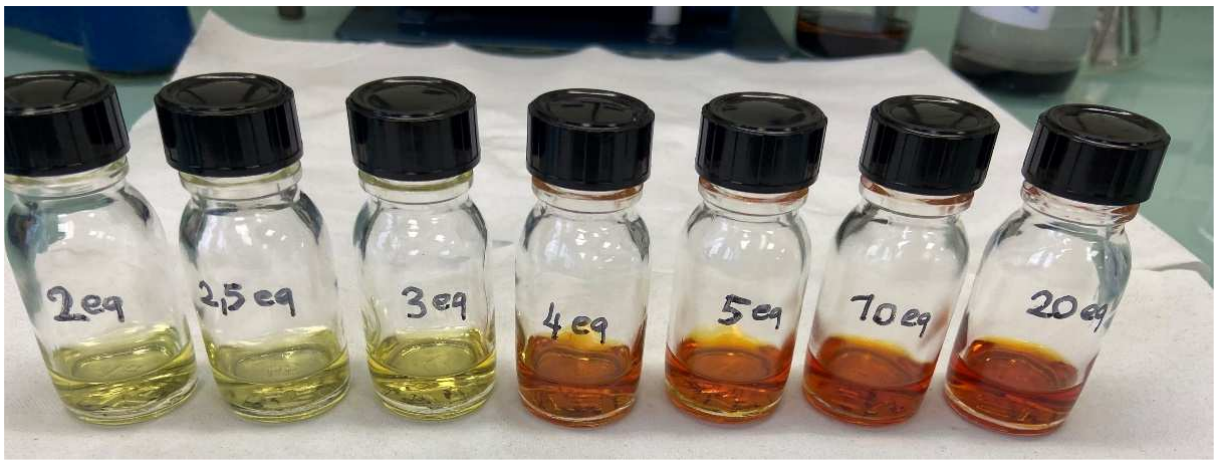

Figure 6.4. Vials containing $HAuCl_4$, 3 H_2O (20 mM) dissolved in hexane solution containing oleylamine at different concentrations from 40 mM (2 eq.) to 400 mM (20 eq.)

From the color of the solutions it is possible to have some information about the coordination chemistry. The pale yellow solution observed for 2 < OY/Au < 4 is characteristic of a Au(III) complex with a square planar geometry in which the Au(III) centers are coordinated by four weak σ-donor ligands. This is the color of the complex $[AuCl_4]^-$ obtained by dissolution of $HAuCl_4$ in water. This is also the color of the amino- complexes $[Au(III)enCl_2]^+$ and $[Au(III)en_2]^{3+}$ with en = ethylene diamine reported by Zhu et al[12].

The first step in the dissolution of $HAuCl_4$ in hexane thanks to OY is certainly the formation of the ion pair RNH_3^+ $[AuCl_4]^-$ by the acid-base reaction, OY capturing the proton of $HAuCl_4$ according to Eq. 6.1 :

$$HAuCl_4 + RNH_2 \rightarrow RNH_3^+ [AuCl_4]^- \quad \text{(Eq. 6.1)}$$

By adding a second equivalent of OY, the substitution of one chloride ion of the A_U(III) coordination sphere by one OY molecule to form the neutral amino complex, RNH_2-$AuCl_3$, according to Eq. 6.2, may occur:

$$HAuCl_4 + 2\ RNH_2 \rightarrow RNH_3^+Cl^- + RNH_2\text{-}AuCl_3 \quad \text{(Eq. 6.2)}$$

Chloride and amino are all weak σ-donor ligands. The pale-yellow color can correspond to the ion pair $RNH_3^+[AuCl_4]^-$ with 4 chloride in the Au(III) coordination sphere or to the amino-chloride complex RNH_2-$AuCl_3$. However, as mentioned above, 1 equivalent of OY is not enough to solubilize the gold precursor. The ion pair RNH_3^+ $[AuCl_4]^-$ is probably not soluble enough in hexane. On the other hand, we have checked that oleyl ammonium chloride is soluble in hexane. So, the formation of the neutral amino complex, RNH_2-$AuCl_3$, and the oleylammonium chloride according to Eq. 6.2 is the most probable.

For the ratio OY/Au ≥ 4 the dissolution of $HAuCl_4$ is much faster and the solution takes an orange color. We know from the literature that this orange color is characteristic of the formation of an amido complex[13,14]. The amines can coordinate Au(III) as amido ligand releasing a proton in the medium. So with 4 eq. of OY, the Au(III) complexation can be written as :

$$HAuCl_4 + 4\ RNH_2 \rightarrow 2\ RNH_3^+Cl^- + RNH\text{-}Au(RNH_2)Cl_2 \quad \text{(Eq. 6.3)}$$

According to Eq. 6.3 the neutral Au(III) complex is formed with 1 amino-, 1 amido- and two chloride ions in the coordination sphere. Four equivalents of OY are necessary since two oleylammonium chloride are formed, one taking the proton of $HAuCl_4$ and the second one with the proton released by the amido ligand. The amido ligand is a stronger σ-donor ligand. The color change is well explained by the presence of this ligand in the Au(III) coordination sphere.

Some articles reported that it is possible to have four amido ligands in the Au(III) coordination sphere[15]. So, in our case we can imagine that by increasing the OY concentration in the medium, we can form the following complexes:

$$HAuCl_4 + 6\ RNH_2 \rightarrow 3\ RNH_3^+Cl^- + (RNH)_2\text{-}Au(RNH_2)Cl \quad \text{(Eq. 6.4)}$$

$$HAuCl_4 + 8\ RNH_2 \rightarrow 4\ RNH_3^+Cl^- + (RNH)_3\text{-}Au(RNH_2) \quad \text{(Eq. 6.5)}$$

In this assumption, according the Eqs. 2-6, all the gold complexes formed in hexane are neutral.

In the chapter 1, we have mentioned that the reduction of the precursor of the gold nanowires was very slow (induction time t* of a few hours, even with a large excess of TIPS) contrarily to the reduction of the precursor of the gold nanospheres (induction time of a few seconds). The reason for such drastic difference is the nature of the precursor. The excess of OY in solution leads to the formation of the tris-amido complex which seems to be very stable toward the reduction by the trialkylsilanes.

6.4.2 Evolution of the precursor nature : EXAFS study

To confirm the nature of the coordination spheres of the Au(III) precursors with different concentration of OY, the EXAFS spectra of the different solution were analyzed by Dr. Raj Kumar Ramamoorthy in the article published in Nanoscale[9].

The XAS spectra of the precursor solutions are given in the figure 6.5. They all exhibit an intense white line peak, referred as A, at 11921.2 eV, which is the characteristic of Au complex in the +3-oxidation state (figure 6.5.a). However, slight differences can be seen as a function of [OY]. A small peak at 11934 eV, referred to as “C” in figure 6.2.a vanishes when the OY concentration increase. The maximum of the white line slightly shifts towards the higher energy with the oleylamine concentration.

The EXAFS spectra were Fourier transformed (FT) and fitted in “R”-space to evaluate the local changes of the Au coordination shell as shown in figure 6.5.b-c-d. For comparison, the amplitude and phase shift functions of Au–Cl and Au–N bonds were calculated from the structure of the amino-chloroaurate(III), $AuCl_3NH_3$ (crystallographic open database file no. 1532148, using FEFF8.4.[16]

For the OY concentration of 50 mM, 4 Cl atoms at the distance of R=2.23 Å are found in the first coordination shell of Au (table 6.1). Such Au–Cl bond distance is in agreement with the references : the bond length varies between 2.23 and 2.34 Å in the dimer Au_2Cl_6 in the solid state, and takes an average value of 2.277 and 2.274 Å in $NaAuCl_4$ and NR_4AuCl_4, respectively[17,18]. From these results we should conclude that in presence of [OY] = 50 mM, $[AuCl_4]^-OY^+$ ion pairs are formed.

This conclusion is in disagreement with the need to have at least 2 equivalents of OY to completely solubilize $HAuCl_4$, as described above. This point should be clarified in the future. To further understand the chemistry of the precursor and conclude on the presence of $[AuCl_4]^-OY^+$ ion pairs or on the neutral amino complex, RNH_2-$AuCl_3$, further experiments are mandatory. Preliminary NMR experiments have been done but unfortunately too late to be fully analyzed and included in the manuscript.

With increasing [OY], the progressive replacement of the chlorine atoms by nitrogen in the coordination shell was observed. Indeed, for [OY]= 100 mM (OY/Au = 5), a mixed Cl/N coordination shell was found, with a R_{Au-N} bond length of 2.02 Å. For [OY]= 400 mM (OY/Au = 20), all the chlorine have been replaced : 4 N atoms are found as first neighbors. The R_{Au-N} bond length increases to 2.06 Å. If we compare with the $AuCl_3NH_3$ reference[19,20], this bond length is slightly longer. However, it is similar to the bond length determined by EXAFS and previously reported by F. Pschunder et al. on a solution of $HAuCl_4$ in hexane in the presence of an excess of oleylamine[19]. In hexane it is very unlikely to have four amino ligands in the Au(III) coordination sphere since it would form a cation with a charge +3. It is this much more probable to form the neutral tris-amido complex $(RNH)_3$-$Au(RNH_2)$ as predicted by Eq. 6.5. The Debye-Waller factor, σ^2, which indicates the ordering parameter of the local environment didn't change with increasing of [OY].

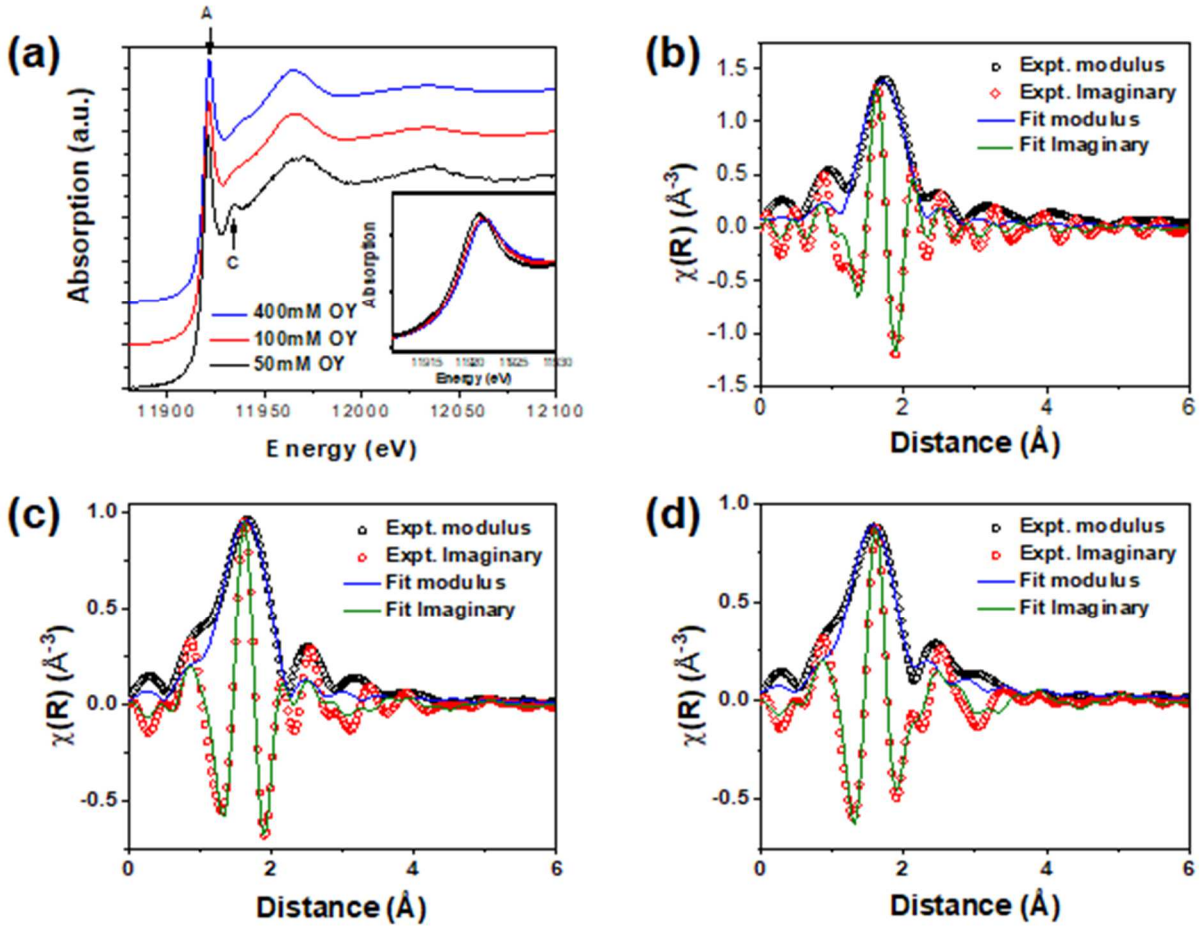

Figure 6.5 (a) In situ XAS spectra at the Au L_{III}-edge of $HAuCl_4.3H_2O$ ([Au]=20 mM) in solution of oleylamine (OY) in hexane at different OY concentration (black: 50 mM; red: 100 mM; blue: 400 mM); (b-d) Experimental real and imaginary components of the Fourier transform of the k^2-weighted EXAFS signal χ(k) (open dots) and best fits (full lines) for OY concentration of (b) 50 mM, (c) 100 mM and (d) 400 mM.

[OY]	N_{Au-Cl}	R_{Au-Cl}(Å)	σ^2_{Au-Cl}(Å^2)	N_{Au-N}	R_{Au-N}(Å)	σ^2_{Au-N}(Å^2)
50 mM	4.1	2.23	0.005	-	-	-
100 mM	1.5	2.28	0.005	2.5	2.02	0.005
400 mM	-	-	-	4.1	2.06	0.006

Table 6.1 Coordination number, N, bond length, R, and Debye-Waller factor, σ^2, of the first coordination shell around Au fitted to EXAFS spectra of Au (III) precursors.

6.5. Analysis of the PNCs using SAXS

In the following we focus now only on the PNCs prepared with OY/Au = 2.5, *i.e* those involved in the nanospheres synthesis. The idea is to combine the SAXS data and the information related to the chemistry of $HAuCl_4$ in solution of OY in hexane, to determine the number of Au(III) ions involved in each PNC.

In chapter 3, we reported the SAXS characterization of the precursor solution with 50 mM OY showing the presence of PNCs in the precursor solution (Figure 3.14a). The SAXS signal of the PNCs was fitted using the Beaucage model to extract the size of the PNCs (Figure 3.14b). Assuming isotropic objects, their mean size was calculated from the radius of gyration, $D_{SAXS} = 2\sqrt{5/3}\,R_g$. During the induction stage the value D_{SAXS} of the PNCs was found in the range 4 - 4.4 nm (Table 3.3).

The PNCs are supramolecular association of the gold(III) complex in the hexane solution. According to the previous section, we can assume that these molecular clusters are the association of the ion pair RNH_3^+ $[AuCl_4]^-$ or of the neutral gold complex RNH_2-$AuCl_3$. In the chapter 3, the molecular volume of these two complexes were estimated to be 0.679 nm^3 (Table 3.2). According to the mean volume of the PNCs, $\frac{4\pi}{3}{R_{SAXS}}^3$, we can estimate the number of Au(III) complexes per PNC at 50 to 65 for a diameter of PNCs of 4 and 4.4 nm, respectively (corresponding volumes of 33.5 and 44.6 nm^3).

This calculation assumes that the PNC are aggregates of the Au(III) complexes and that these scattering objects are homogeneously filled with the long alkyl chain of the amine or ammonium and the polar head NH_2-$AuCl_3$ or $[AuCl_4]^-$. Actually, another reasonable hypothesis is to consider that the long alkyl hydrophobic chains of the complex point toward the hexane solvent like in inverse micelles, the core of the PNCs containing mainly Au (III) complexes and the water molecules. In the case of the Brust synthesis described in Chapter 1, where the first step consists in extracting the gold complex in toluene using tetra octyl ammonium bromide (TOAB), mechanistic studies have shown the formation of reverse micelles in toluene by association of TOA^+ and $[AuCl_4]^-$.[7,8] In this hypothesis, the scattering objects are the core of the micelles because the electron density contrast between hexane and oleylamine is very weak (Table 3.2).

The calculation of the number of Au atoms contained in the PNCs requires to know the chemical composition and the density (or molecular volume) of the molecular units contained in the core of the PNCs. If we consider that the PNC core is occupied by {$AuCl_4$, 3 H_2O} we can estimate the volume of this molecular unit. According to the Table 3.2 we can take $V_M(AuCl_4)$ = 0.14 nm^3. For the 3 water molecules a first approximation is to use the density of liquid water (1g.cm^{-3}) which gives a volume of

0.03 nm^3 per water molecule. Considering the {$AuCl_4$, 3 H_2O} molecular volume of 0.224 nm^3, the total number of Au(III) complexes per PNC is 150 and 200 for the PNCs diameter of 4 and 4.4 nm, respectively.

The latter molecular volume is probably underestimated because the molecular volume of water is certainly higher than in the dense liquid water. So, a value comprised between 50 and 150 seems more reasonable. Further studies are needed to conclude definitively but these calculations show that the assumption of a nucleation occurring inside PNCs should be seriously considered.

However several questions have not been addressed yet :

- we do not know what is the proportion of the gold complexes involved in the PNCs;
- If it is 100 %, i.e. there is no free Au(III) complex in solution, why only 50 % PNC react during the nucleation stage.

6.6 The role of the trialkylsilane

Another question is the role of the reducing agent. In all the study we have used trialkysilanes, TIPS or TES, to reduce Au(III) and Au(I) to Au(0), leading mostly to icosahedral NPs. Au nanoparticles exhibiting an ultrasmall diameter and a *fcc* structure were however previously reported in the literature using different reducing agents like sodium borohydride or amino borane[21,22].

Therefore, we wanted to know if starting with PNCs as gold precursor, other reducing agents would lead to NPs with similar size and structure as with silanes. To have a direct comparison, Au NPs were prepared using tert-butyl amino borane (BTB) as reducing agent, following the same protocol as for the particles prepared with TIPS. $HAuCl_4.3H_2O$ was dissolved in hexane with OY and mixed with the solution of BTB in hexane. The standard concentrations were [Au] = 10 mM or 20 mM, [BTB]/[Au] = 50 and [OY]/[Au] = 2.5. The Au (III) complex was immediately reduced to Au (0) by BTB resulting in a dark red suspension.

According to the TEM images (figure 6.6a) we have observed that the particles exhibit a spherical shape with a mean diameter d_m = 2.5 nm and are quite homogeneous in size (σ/d_m = 13%). Surprisingly, despite a very fast reaction, the particle mean size is a little bit bigger than with the silanes.

After that, we have performed SAXS experiment to know more precisely the size and polydispersity of the final NPs. The 1.5 mm glass capillaries were filled with the colloidal suspensions directly obtained after 3h of reaction, without any further purification. Figure 6.6b indicates the SAXS patterns of the as-prepared Au nanoparticle suspensions. We have succeeded to fit the experimental curve with the one population which shows the ultra-small NPs with a mean size dm= 2.6 nm and the polydispersity (σ/dm ~ 18). The total scale is found 1.7 x 10^{-3}. The mean particle size is found consistent with the size observed by TEM.

The *ex situ* XRD pattern of the nanospheres prepared with tert-butyl amino borane (BTB) is given in figure 6.6c. Broad peaks are observed in agreement with the small diameter of the particles. The comparison with the peak positions of *fcc* Au shows that each band falls close to the expected 2θ angle of the (111), (200), (220), (311) and (222) reflections. The NPs prepared with BTB therefore exhibit a structure which is much closer to the expected *fcc* structure of bulk Au than the small particles prepared with silanes. PDF analysis will be interesting to carry out in the future to conclude definitively because slight differences are however observed. The main peak which is a little bit shifted to high angles compared to the (111) peak and the relative intensity of the second peak is weak if we compare with the expected relative intensity I(200)/I(111) of the *fcc* Au.

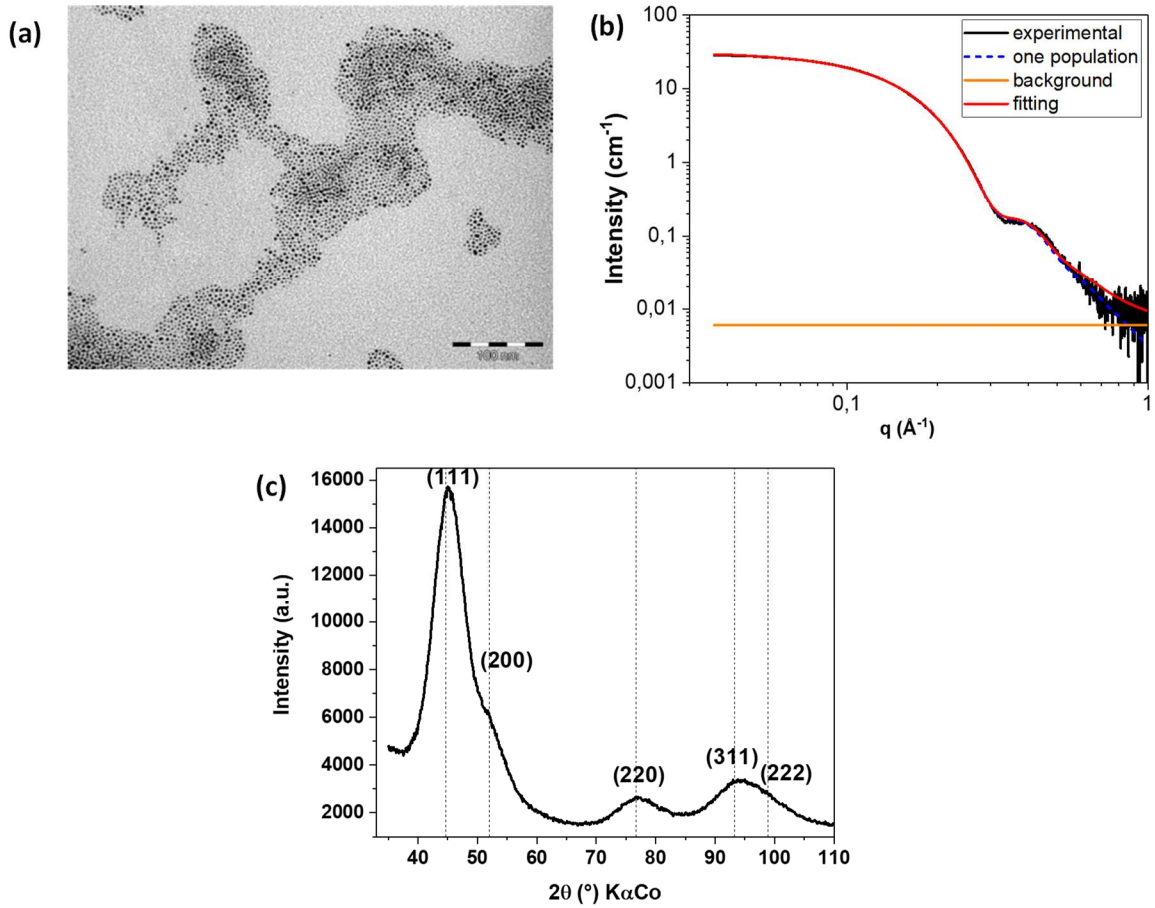

Figure 6.*6*. (a) TEM image of nanoparticles synthesized with BTB (b) SAXS pattern of suspension of Au nanoparticles obtained by reduction of $HAuCl_4.3H_2O$ in OY/hexane ([Au] = 20 mM; [OY] = 50 mM) using BTB ([BTB]= 1 M) as reducing agent In black: experimental data; red: the corresponding fit considering one populations of nanosphere (blue dashed lines) and a constant background (orange); (c) Ex situ XRD pattern of Au nanoparticles synthesized with BTB. The dashes black line corresponds to the XRD peaks of *fcc* bulk Au.

The use of silanes as reducing agent seems to be fairly specific, leading to small icosahedral NPs independently of the nucleation rate, while slightly larger NPs were observed in presence of BTB, a stronger reducing agent.

6.7 Conclusion

In this chapter, we have tried to demonstrate that the formation of the Au NPs by the reduction of $HAuCl_4$ dissolved in solution of oleylamine in hexane and using trialkylsilanes as reducing agent cannot be explained in the framework of the classical nucleation theory (CNT).

Our strongest argument for ruling out CNTs is that by decreasing/increasing the reaction rate, we should increase/decrease the critical radius of the nuclei and change the particle size, which we do not observe. On the contrary, by varying nature and the concentration of the silane, the reaction rate can be fastened without any strong changes in the particle size (dm = 1.7 -2 nm) and structure (icosahedral). The stability of the mean size is in agreement with the XAS data showing that we have always 50 % of Au atoms involved in the nucleation stage.

We have a strong presumption that nucleation takes place within the PNCs. We have tried to estimate the number of Au atoms inside the PNCs. A good order of magnitude is 100 but a more precise assessment is needed. A hundred of atoms is also what is estimated for the number of atoms in the nuclei.

However, some points remain to be clarified in the future :

- If the PNCs are involved in the nucleation, why did we observe a size increase when we used an amino borane as reducing agent ? Extending this study to other reducing agents could also be interesting for example to gaseous H_2 to see if a slow diffusion of molecular hydrogen could also favor the mild transformation of the PNCs into particles.
- What determines that 50 % of Au atoms are involved in the nucleation ?
- What is the coordination chemistry of the Au(III) precursor (ion pair or amino complex) and what is the structure of the PNCs ? Does the inverse micelles scheme apply ?

Bibliography

(1) Thanh, N. T. K.; Maclean, N.; Mahiddine, S. Mechanisms of Nucleation and Growth of Nanoparticles in Solution. *Chem. Rev.* **2014**, *114* (15), 7610–7630. https://doi.org/10.1021/cr400544s.

(2) Shevchenko, E. V.; Talapin, D. V.; Schnablegger, H.; Kornowski, A.; Festin, Ö.; Svedlindh, P.; Haase, M.; Weller, H. Study of Nucleation and Growth in the Organometallic Synthesis of Magnetic Alloy Nanocrystals: The Role of Nucleation Rate in Size Control of CoPt3 Nanocrystals. *J. Am. Chem. Soc.* **2003**, *125* (30), 9090–9101. https://doi.org/10.1021/ja029937l.

(3) Gebauer, D.; Cölfen, H. Prenucleation Clusters and Non-Classical Nucleation. *Nano Today* **2011**, *6* (6), 564–584. https://doi.org/10.1016/j.nantod.2011.10.005.

(4) Karthika, S.; Radhakrishnan, T. K.; Kalaichelvi, P. A Review of Classical and Nonclassical Nucleation Theories. *Crystal Growth & Design* **2016**, *16* (11), 6663–6681. https://doi.org/10.1021/acs.cgd.6b00794.

(5) Demichelis, R.; Raiteri, P.; Gale, J. D.; Quigley, D.; Gebauer, D. Stable Prenucleation Mineral Clusters Are Liquid-like Ionic Polymers. *Nat Commun* **2011**, *2* (1), 590. https://doi.org/10.1038/ncomms1604.

(6) Fleury, B.; Neouze, M.-A.; Guigner, J.-M.; Menguy, N.; Spalla, O.; Gacoin, T.; Carriere, D. Amorphous to Crystal Conversion as a Mechanism Governing the Structure of Luminescent YVO4:Eu Nanoparticles. *ACS Nano* **2014**, *8* (3), 2602–2608. https://doi.org/10.1021/nn4062534.

(7) Li, Y.; Zaluzhna, O.; Tong, Y. J. Critical Role of Water and the Structure of Inverse Micelles in the Brust–Schiffrin Synthesis of Metal Nanoparticles. *Langmuir* **2011**, *27* (12), 7366–7370. https://doi.org/10.1021/la201158v.

(8) Li, Y.; Zaluzhna, O.; Xu, B.; Gao, Y.; Modest, J. M.; Tong, Y. J. Mechanistic Insights into the Brust−Schiffrin Two-Phase Synthesis of Organo-Chalcogenate-Protected Metal Nanoparticles. *J. Am. Chem. Soc.* **2011**, *133* (7), 2092–2095. https://doi.org/10.1021/ja1105078.

(9) Ramamoorthy, R. K.; Yildirim, E.; Barba, E.; Roblin, P.; Vargas, J. A.; Lacroix, L.-M.; Rodriguez-Ruiz, I.; Decorse, P.; Petkov, V.; Teychené, S.; Viau, G. The Role of Pre-Nucleation Clusters in the Crystallization of Gold Nanoparticles. *Nanoscale* **2020**, *12* (30), 16173–16188. https://doi.org/10.1039/D0NR03486J.

(10) Baletto, F.; Ferrando, R. Structural Properties of Nanoclusters: Energetic, Thermodynamic, and Kinetic Effects. *Rev Mod Phys* **2005**, *77* (1), 371–423. https://doi.org/10.1103/RevModPhys.77.371.

(11) Kaatz, F. H.; Bultheel, A. Magic Mathematical Relationships for Nanoclusters. *Nanoscale Research Letters* **2019**, *14* (1), 150. https://doi.org/10.1186/s11671-019-2939-5.

(12) Zhu, S.; Gorski, W.; Powell, D. R.; Walmsley, J. A. Synthesis, Structures, and Electrochemistry of Au(III)-Ethylenediamine Complexes and Interactions with Guanosine 5'-Monophosphate. *Inorg Chem* **2006**, *45* (6), 2688–2694. https://doi.org/10.1021/ic051411p.

(13) Cao, L.; Jennings, M. C.; Puddephatt, R. J. Amine−Amide Equilibrium in Gold(III) Complexes and a Gold(III)−Gold(I) Aurophilic Bond. *Inorg. Chem.* **2007**, *46* (4), 1361–1368. https://doi.org/10.1021/ic061911y.

(14) Baddley, W. H.; Basolo, F.; Gray, H. B.; Nolting, C.; Poe, A. J. Acidodiethylenetriaminegold(III) Complexes: Preparation, Solution Chemistry, and Electronic Structure. *Inorg. Chem.* **1963**, *2* (5), 921–928. https://doi.org/10.1021/ic50009a011.

(15) Oyaizu, K.; Ohtani, Y.; Shiozawa, A.; Sugawara, K.; Saito, T.; Yuasa, M. Highly Stable Gold(III) Complex with a Hydantoin Ligand in Alkaline Media. *Inorg. Chem.* **2005**, *44* (20), 6915–6917. https://doi.org/10.1021/ic050515x.

(16) Ankudinov, A. L.; Nesvizhskii, A. I.; Rehr, J. J. Dynamic Screening Effects in X-Ray Absorption Spectra. *Phys. Rev. B* **2003**, *67* (11), 115120. https://doi.org/10.1103/PhysRevB.67.115120.

(17) Jones, P. G.; Hohbein, R.; Schwarzmann, E. Anhydrous Sodium Tetrachloroaurate(III). *Acta Cryst C* **1988**, *44* (7), 1164–1166. https://doi.org/10.1107/S0108270188002756.

(18) Serpell, C. J.; Cookson, J.; Ozkaya, D.; Beer, P. D. Core@shell Bimetallic Nanoparticle Synthesis via Anion Coordination. *Nat Chem* **2011**, *3* (6), 478–483. https://doi.org/10.1038/nchem.1030.

(19) Pschunder, F.; Puig, J.; Giovanetti, L. J.; Huck-Iriart, C.; Requejo, F. G.; Buceta, D.; Hoppe, C. E.; Ramallo-López, J. M. New Insights into the Growth Mechanism of Ultrathin Au Nanowires from Combined in Situ EXAFS and SAXS Studies. *The Journal of Physical Chemistry C* **2018**, *122* (50), 29051–29061.

(20) Strähle, J.; Gelinek, J.; Kölmel, M.; Nemecek, A.-M. Die Kristallstruktur Der Salze K2Au2I6 Und Cs2AgxAuI1-XAuIIIBr6. Ein Beitrag Zur Kristallchemie Der Alkalihexahalogenoaurate(I,III) / Crystal Structure of the Salts K2Au2I6 and Cs2AgxAuI1-XAuIIIBr6. A Contribution to the Crystal Chemistry of the Alkali Hexahalogeno Aurates(I,III). *Zeitschrift für Naturforschung B* **1979**, *34* (8), 1047–1052. https://doi.org/10.1515/znb-1979-0801.

(21) Abécassis, B.; Testard, F.; Spalla, O.; Barboux, P. Probing in Situ the Nucleation and Growth of Gold Nanoparticles by Small-Angle X-Ray Scattering. *Nano Lett* **2007**, *7* (6), 1723–1727. https://doi.org/10.1021/nl0707149.

(22) Chen, X.; Schröder, J.; Hauschild, S.; Rosenfeldt, S.; Dulle, M.; Förster, S. Simultaneous SAXS/WAXS/UV–Vis Study of the Nucleation and Growth of Nanoparticles: A Test of Classical

Nucleation Theory. *Langmuir* **2015**, *31* (42), 11678–11691. https://doi.org/10.1021/acs.langmuir.5b02759.

Conclusions

At the very beginning of this PhD, discussions between researchers in nanochemistry of LPCNO and researchers in chemical engineering of LGC underlined the interest of a collaboration to elucidate interesting questions about the nucleation and growth of nanoparticles in the liquid phase. LPCNO's team would bring model systems to study and the LGC's team the tools to study and model them. This work is the direct result of those discussions.

Nucleation studies are one of the most challenging goal in nanochemistry and, more generally, in crystallization of solids particles. Nucleation is often very fast and involves very small amount of matter. For these two reasons it is very difficult to catch it experimentally. Furthermore, there is always an overlap between nucleation and particle growth, even if the final particles are highly monodisperse. In nanochemistry, the systems can even be complexified by the surfactants introduced in the system to control the growth. Indeed, these surfactants can play several roles in the whole chemical process, among which act as ligand for the precursor. In most studies dealing with metal nanoparticle synthesis, the considerations about the nucleation and growth of nanoparticles are deduced from the size, size distribution, shape and structure of the final particles. However, to have a clear picture of the nucleation and growth mechanism, one needs to study with a good accuracy the evolution of the reaction mixture in-situ and in real time combining different techniques.

In this work we were interested in the synthesis of gold particles using trialkylsilanes as reducing agents. The syntheses were performed in an apolar solvent, hexane, containing oleylamine. The interest of combining trialkylsilanes and oleylamine had been previously demonstrated: it is a fairly simple synthesis under very mild conditions which can lead to particles of very original shape and structure. Ultrafine nanowires and nanospheres of icosahedral structure were obtained depending on the oleylamine concentration.

Taking advantage of the opportunity to collaborate with Sébastien Teychené and Isaac Rodriguez-Ruiz of LGC we decided to develop the proper microfluidic tools to study the nucleation and growth mechanism of such gold nanoparticles. This is a rather fundamental research work, however the synthesized objects will eventually serve in catalysis or microelectronics due to their enhanced properties, and the microfluidic tools will be further used in a near future to study other systems involving very fast reactions.

The microfluidic chips that have been designed and fabricated involves indeed an efficient mixer at the beginning of the channel allowing for the fast mixing of the reactant solutions. Thus, very short reaction times can be caught. Moreover, these chips can be used either in continuous flow or in stopped flow, giving access to a broad time range from sub seconds up to hours. We have shown in the chapters 3 and 4 that these chips were very well suited to follow the crystallization of the Au nanoparticles, even though improvements can still be made to address the shortest times, especially for the XAS data. This should be a perspective of the following works.

The other interest of these microfluidic chips is that they are compatible with the synchrotron radiations. Thanks to the high brilliance of the X-rays lines and to the high quality of the detectors, synchrotrons are extremely useful for such kind of studies because of the very short acquisition times and the small amount of matter required to have a good signal. In this work we carried out in-situ and time resolved small angle X-ray scattering and X-ray absorption measurements at synchrotron facilities. These studies were very complementary of the characterizations that have been done at the laboratory such as in situ UV-visible kinetic studies, XRD characterizations and in situ SAXS to follow the structure and the size of the final particles, respectively.

The syntheses of Au nanoparticles using the reduction by trialkylsilane of a Au(III) precursor in solution of oleylamine in hexane have several interests :

- When the nucleation and growth is well controlled, the size distribution is narrow, with a mean size of about 2 nm, and the nanoparticle crystalize with an icosahedral structure;
- The particle grow from a solution containing pre-nucleation clusters of Au(III) and not from a homogeneous solution. This let us think that the nucleation could follow a non-classical mechanism.

The main results of the kinetic studies are the following:

- XAS helped us to define the best conditions to obtain monodisperse NP with the icosahedral structure. The reduction of Au(III) complexes to Au(0) nanoparticles involves two steps, the reduction of Au(III) to Au(I) and the reduction of Au(I) to Au(0). Thanks to the time-resolved Au speciation we concluded that the key is that the Au(I) $\rightarrow$ Au(0) reduction step is much faster than the Au(III) $\rightarrow$ Au(I) reduction step. The first Au(III) $\rightarrow$ Au(I) reduction must be the limiting step of the reaction. In this case there is indeed no accumulation of Au(I) in the medium, the formation of the OY-Au(I)-Cl lamellar phase is therefore prevented. The competition between the reduction of the Au complexes involved in the pre-nucleation clusters and in the lamellar phase does not apply, allowing for monodisperse icosahedral nanoparticles to be formed. This result led us to extend the synthesis conditions improving the control of the synthesis. We

showed that small changes in the experimental conditions favored the formation of monodisperse NP: an increase of the reaction temperature of only 15 °C (from 25°C to 40°C), or a lesser steric hindrance of the alkyl chains of the silane (change of triisopropylsilane to triethylsilane).

- The SAXS studies evidenced the competition between the direct reduction of the PNCs or the crystallization of an intermediate OY-Au(I)-Cl lamellar phase in case of slow reduction (chapters 3 and 4). In case of the direct reduction of the PNCs the first results showing the shrinkage of the size were very new. However, because of the presence of the PNCs in the starting solution it is difficult to fit the SAXS data with a mixture of PNCs and Au NPs because we don't know if the size of the PNC is constant. Therefore, it is difficult to follow precisely the size variation of the Au nanoparticles in the very first stage of the nucleation. From the comparison of the time resolved XAS and SAXS we have a good description of the three stages observed with both techniques, i.e. induction, nucleation and growth.
- Finally, all the XAS and SAXS studies were summarized in the chapter 6 to question the classical nucleation theory in the case of the formation of the icosahedral NPs. A main difference with the CNT is the nature of the precursor solution which is not homogeneous and contain aggregates of complex called PNCs. Moreover, a strong argument was the non-dependence of the particle size when the reaction rate (both the nucleation and growth rates) was increased of a factor 5.

Due to the difficulty to have a complete and exact picture of the nucleation and growth, there are of course still numerous interesting questions to address, in particular, concerning the structure of the particles:

- Is the icosahedral structure only due to the very small particle size ?
- Is it due to the oleylammonium chloride coating ?
- or do the confinement of the nucleation inside the PNCs has a role in the formation of the icosahedral structure ?
- Is it due to a specific role of the silane ?

The preliminary results obtained with BTB as reducing agent seems to show that despite the presence of the PNCs, the 2.5 nm NP finally obtained did present a structure which seems more *fcc*.

In addition, further developments of this work would be interesting to follow:

- For kinetic studies in the microfluidic chips and using the UV-visible absorption, we were limited to the signal of Au(0) due to the absorbing properties of the ostemer in the UV. In the future, the use of another polymer such as epoxy to fabricate the microfluidic chip could permit to follow the relative Au(III) and Au(I) concentrations, providing it is transparent in the UV region.
- Recently, we have found that the monodisperse icosahedral NPs could be used as starting materials to get controlled decahedra after an aging process (see figure below). In the literature, decahedra have been used as seeds to prepare nanorods thanks to their peculiar 5-fold axis. The aim of this synthesis could be the preparation of magnetic nanorods using gold decahedral particles as seeds for a controlled heterogeneous nucleation and growth.
- Finally, this fairly simple synthesis using silane could be extended to other metals. Silver icosahedra were recently prepared in a very reproducible way using the same method. This reaction could be simpler to study since only two oxidation state of silver are involved, this is part of the thesis of Rohan Parmar that has started recently.

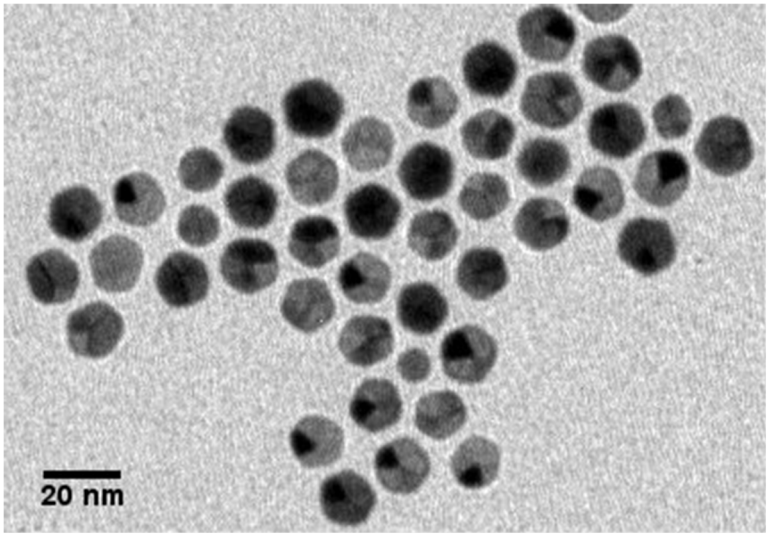

Figure Decahedral NP obtained after ageing of monodisperse icosahedral NPs

Résumé Français

Les récents efforts de réduction de la taille des nanoparticules métalliques ont donné naissance à une grande variété d'objets dont la morphologie et les propriétés peuvent être modifiées. Outre la taille et la forme des nanoparticules, le contrôle des structures cristallines est également très important pour régler correctement les propriétés physiques ou chimiques des nanoparticules. En particulier, la préparation de nanoparticules métalliques monodisperses avec une structure cristalline à faible symétrie est très importante d'un point de vue fondamental et technologique pour leurs propriétés primordiales qui les qualifient pour des applications optiques, catalytiques et électroniques.

Des clusters de taille sélectionnée avec des structures atomiques contrôlées, telles que des icosaèdres, des décaèdres ou des cuboctaèdres, ont été préparés par des méthodes de synthèse en phase gazeuse. Les particules icosaédriques sont particulièrement intéressantes pour la catalyse car elles présentent 20 facettes triangulaires et un axe de symétrie double, triple et quintuple. Ces particules, énergétiquement favorisées seulement à de très petites tailles en raison de l'importante déformation induite, pourraient être obtenues spécifiquement grâce à la sélection de taille mais seulement en quantités limitées.

En revanche, la synthèse chimique en phase liquide permet de produire de grandes quantités de nanoparticules en un seul lot. Grâce à des recherches intensives au cours des dernières décennies, des nanoparticules de taille et de forme assez contrôlées ont pu être obtenues grâce à l'ajout approprié de ligands. Ces molécules aident à stabiliser les nanoparticules en modifiant l'énergie de surface et donc la taille à laquelle une structure cristalline donnée peut devenir stable.

Les ligands ne stabilisent pas seulement les nanoparticules finales, mais ils peuvent aussi interférer avec le précurseur métallique pour former des complexes stables, ce qui affecte considérablement la cinétique de la réaction. Ainsi, pour préparer des nanoparticules monodisperses avec une structure

atomique spécifique, il faut identifier correctement les complexes formés in-situ et comprendre en profondeur le mécanisme de nucléation et de croissance impliqué.

Jusqu'à présent, la formation de nanoparticules métalliques a été décrite par la théorie de la nucléation classique (CNT). Selon la CNT, lorsque les atomes en solution dépassent la limite de solubilité, ils s'agrègent et génèrent des noyaux stables après avoir franchi la barrière énergétique imposée par les énergies de volume et de surface. Ensuite, ils croissent par un processus d'addition atome par atome. La taille de la nanoparticule finale est inversement proportionnelle au rapport de sursaturation qui est le rapport entre la concentration réelle et la concentration à l'équilibre des précurseurs. Mais des observations récentes, utilisant des techniques de caractérisation avancées, ont mis en évidence l'existence d'états intermédiaires non cristallins tels que des oligomères ou des clusters de pré-nucléation (PNC).

Parmi les différents métaux d'intérêt, nous nous sommes concentrés sur l'or. Assez résistantes à l'oxydation, les NPs d'Au présentent de bonnes propriétés catalytiques, électroniques et optiques. Des études antérieures réalisées dans le groupe ont montré que des nanofils ultrafins pouvaient être facilement obtenus par la réduction d'un sel de chlorure d'or en présence d'une amine à longue chaîne (oleylamine) dans un solvant organique. Ces fils, d'un diamètre inférieur à 2 nm et d'une longueur micrométrique, possèdent une structure cristalline tétragonale fermée, qui diffère fortement de la structure fcc.

Il est intéressant de noter qu'en faisant varier le rapport oleylamine/or, des nanoparticules ultra petites de moins de 2 nm ont pu être produites quantitativement. En combinant la diffraction des rayons X à haute énergie in situ et la microscopie électronique à transmission à balayage, il a été prouvé que les particules présentaient une structure icosaédrique, mais la voie de réaction n'était pas connue.

Dans cette thèse, nous avons étudié la synthèse de NPs d'Au icosaédriques ultra petites grâce à des études in situ résolues en temps, à savoir la diffusion de rayons X aux grands angles, la spectroscopie

d'absorption des rayons X (XAS) et la spectroscopie UV-Visible en utilisant une configuration microfluidique dédiée afin d'accéder à des temps de réaction courts.

La thèse de doctorat présentera les principaux résultats de notre étude et est divisée en 6 chapitres.

Le chapitre 1 présente un aperçu partiel des travaux de recherche étendus sur les méthodes de synthèse des Au NPs. Un accent particulier est mis sur les études mécanistiques utilisant des techniques in-situ. La théorie classique de la nucléation (CNT) est brièvement introduite ainsi que les voies non classiques récemment proposées. Enfin, notre système étudié qui consiste en la synthèse de NPs d'Au en utilisant des silanes comme agent réducteur en présence d'oleylamine est détaillé.

Le chapitre 2 donne une description des outils microfluidiques spécifiques développés et des techniques de caractérisation utilisées pour étudier la synthèse des Au NPs. L'accès à des temps de réaction courts, typiquement de l'ordre de quelques secondes, était essentiel pour capturer les tout premiers événements de la réaction et en particulier l'étape de nucléation.

Le chapitre 3 étudie la synthèse de nanoparticules d'Au préparées avec un grand excès de triisopropylsilane (TIPS), qui était couramment utilisé comme agent réducteur dans ces systèmes. Après avoir caractérisé les nanoparticules finales obtenues d'un point de vue morphologique et structurel, des études résolues dans le temps combinant la diffusion des rayons X aux petits angles (SAXS) et la spectroscopie des rayons X (XAS) ont été réalisées. Alors que des résultats préliminaires ont été obtenus dans des capillaires, l'utilisation des puces microfluidiques a permis d'avoir une vision plus claire des trois étapes impliquées dans la réaction, à savoir les étapes d'induction, de nucléation et de croissance.

Le chapitre 4 présente l'effet de la concentration de l'agent réducteur sur la formation des NPs d'Au. Pour la première fois, la présence d'une phase intermédiaire qui tend à cristalliser sous une réaction lente est mise en évidence. La relation entre cette phase lamellaire stable, qui contient des espèces d'Au(I), et la présence de plus grandes NPs est proposée.

Le chapitre 5 présente l'optimisation des paramètres de réaction pour obtenir des NP d'Au monodisperses et ultra-petites. Pour accélérer la cinétique de réaction et ainsi prévenir la cristallisation de la phase lamellaire, l'influence de la température de réaction et de la force de l'agent réducteur a été étudiée. Il est intéressant de noter que des NP hautement monodisperses présentant la structure icosaédrique ont pu être préparées en utilisant un agent réducteur moins volumineux, à savoir le triéthoxysilane (TES).

Le chapitre 6 propose une discussion générale sur l'ensemble des résultats obtenus et une confrontation avec la théorie classique de la nucléation est proposée. Bien qu'il s'agisse encore d'une hypothèse, des voies non classiques pourraient s'appliquer à la formation de NPs d'Au en utilisant du silane. Dans ce cadre, le rôle des clusters de pré-nucléation, ainsi que leur chimie, leur nature et leur taille sont discutés.

Enfin, une conclusion et quelques perspectives de ce travail sont données.

L'objectif du chapitre 1 est de décrire l'état de l'art sur la synthèse de NPs d'Au dans un solvant organique en utilisant le silane comme agent réducteur. L'originalité de la forme et de la structure atomique des particules obtenues par ces méthodes sera présentée et le rôle de l'OY et du silane discuté. Cette section est basée sur les études précédentes rapportées dans la littérature et dans notre groupe ainsi que sur les résultats préliminaires que j'ai obtenus lors de mon stage de Master au LPCNO.

Notre méthode est très simple et offre une grande variété de formes en changeant les paramètres de réaction tels que la concentration du précurseur Au, la concentration de OY ou le solvant. Comme il sera décrit ci-dessous, un grand intérêt de cette méthode est que des particules monodisperses peuvent être produites en utilisant une concentration assez élevée d'or, typiquement 10 ou 20 mM. Par conséquent, une grande quantité de particules peut être produite en un seul lot et ces grandes concentrations facilitent les études in situ, permettant de réduire le temps d'acquisition.

Les silanes constituent une catégorie particulière d'agents réducteurs qui ne sont pas si souvent utilisés pour la synthèse de nanoparticules métalliques, contrairement au borohydrure de sodium ou à l'amino

borane. La formule générale des silanes est R_3SiH (R = alkyle). Ces molécules sont solubles dans les solvants organiques. Les silanes peuvent être considérés comme des hydrures, ainsi chaque silane peut être oxydé et libérer 2 électrons et un proton pour former le cation R_3Si^+. Il est cependant peu probable qu'un tel cation se forme dans les solvants organiques. Il est plus probable que le silane se transforme en un chlorure de silicium R_3SiCl. La première étape de la réduction peut être considérée comme l'échange de la liaison Si-H par une liaison Si-Cl. La réduction de Au (III) en Au (0), qui nécessite 3 électrons, doit impliquer 1,5 éq. de R_3Si-H. Le Cl en excès conduira à la formation de chlorure d'oleylammonium, nécessitant ainsi 2,5 éq. d'oleylamine comme réactif.

La réduction peut être écrite comme suit :

$$HAuCl_4 + \frac{3}{2}R_3SiH + \frac{5}{2}C_{18}H_{35}NH_2 \rightarrow Au(0) + \frac{3}{2}R_3SiCl + \frac{5}{2}C_{18}H_{35}NH_3^+Cl^-$$

En conclusion, la synthèse de nanoparticules d'Au à l'aide de triisopropylsilane dans des solvants non polaires contenant de l'OY est très simple à réaliser et a déjà prouvé son intérêt pour synthétiser des nanoparticules ultra petites avec une distribution de taille étroite. Une originalité de ces synthèses est la structure atomique inhabituelle des particules, très différente de la structure fcc du massif.

Si plusieurs aspects concernant la formation des particules et le rôle réel de OY dans la mise en forme des particules ont déjà été étudiés, certains points concernant le mécanisme de nucléation et de croissance méritent d'être abordés plus en détail. La croissance des nanofils a été étudiée uniquement par SAXS in situ. Suivre la synthèse des petites nanosphères préparées avec [OY] = 50 mM avec des techniques complémentaires telles que la spectroscopie d'absorption des rayons X in situ (XAS) ou la diffraction des rayons X in situ (XRD) pourrait donner des informations supplémentaires sur les différentes étapes chimiques de la réaction et la cristallisation des particules d'or.

D'un point de vue expérimental, la forte concentration d'or utilisée facilitera les études in situ, la sensibilité des différentes techniques n'étant pas une limitation. Cependant, la réaction est très rapide dans le cas de la nanosphère : le changement de couleur caractéristique est observé après seulement quelques secondes. Ainsi, pour étudier correctement in situ la cristallisation des nanosphères, un montage microfluidique spécial avec un mélange rapide est nécessaire. Dans le chapitre suivant, la conception et la réalisation d'une telle installation microfluidique artisanale seront expliquées.

Les principaux objectifs du travail présenté dans ce manuscrit étaient d'étudier la nucléation et la croissance de nanoparticules d'or obtenues par la réduction d'un précurseur d'or avec un trialkylsilane en présence d'oleylamine. Comme il a été décrit dans le chapitre précédent, la réduction du précurseur Au (III) par un silane en milieu organique est fortement affectée par la concentration en amine, allant de quelques secondes pour une faible concentration à quelques heures pour un fort excès. Pour obtenir une image claire du mécanisme de nucléation et de croissance, il est nécessaire d'étudier avec une bonne précision l'évolution du mélange réactionnel in-situ et en temps réel en combinant différentes techniques.

Dans le chapitre 2, nous allons tout d'abord présenter brièvement les bases de trois de ces techniques : la diffusion des rayons X aux petits angles (SAXS) pour déterminer la taille et la forme de la particule formée ; la spectroscopie d'absorption des rayons X (XAS) pour suivre in-situ la spéciation de l'or et la spectroscopie UV-visible pour suivre l'apparition des NPs d'Au (0) dans le milieu en utilisant des installations internes.

Pour la formation de nanofils, la réaction est très lente et des installations classiques telles que des capillaires en verre peuvent être utilisées. En revanche, pour les nanosphères préparées avec une concentration stochiométrique d'amine, la réduction est très rapide. Elle nécessite donc des montages spécifiques pour accéder à des temps très courts (quelques dizaines de millisecondes). Le développement de montages microfluidiques dédiés, compatibles avec un solvant organique agressif,

a constitué une barrière technologique majeure. Le processus de fabrication de la puce à base d'ostémère et les conceptions spécifiques pour assurer un rapport signal sur bruit suffisant pour chaque technique de caractérisation sont décrits dans la deuxième partie du chapitre.

Les cellules microfluidiques ont été largement développées au cours des dernières décennies pour réaliser le multiplexage et le tri à haut débit pour les applications biomédicales. L'efficacité du mélange, du transport et de la séparation des fluides dans des canaux à l'échelle microscopique était également très intéressante pour étudier la matière en combinant des méthodes de caractérisation avancées comme la spectroscopie d'absorption des rayons X (XAS), la diffusion des rayons X aux petits angles (SAXS) et la spectroscopie d'absorption UV-visible. Les systèmes microfluidiques présentent de nombreux avantages tels que :

- L'utilisation de petits volumes d'échantillons et de réactifs qui réduit la consommation de produits chimiques.

- Une exposition limitée aux produits chimiques dangereux.

- Mélange efficace et précis

- Mesures précises grâce à une haute résolution spatiale combinée à des techniques de caractérisation sensibles.

En général, la fabrication de la puce microfluidique peut être ajustée en fonction des exigences expérimentales telles que :

i) les méthodes de caractérisation qui peuvent nécessiter un chemin optique plus large,

ii) les substances chimiques utilisées qui imposent des restrictions sur le polymère pour la fabrication de la puce,

iii) la cinétique de la réaction qui peut nécessiter des éléments de mélange ultra-rapides et efficaces et une résolution temporelle inférieure à la seconde.

Dans la plupart des cas, les puces microfluidiques sont préparées à l'aide de techniques de lithographie douce et de moulage en tenant compte de toutes les contraintes expérimentales.

Ensuite, une pompe est bien sûr obligatoire pour pousser la solution dans la puce, d'importantes forces capillaires étant rencontrées dans les canaux microfluidiques.

Récemment, des personnes ont utilisé des puces microfluidiques pour réaliser des études cinétiques sur la synthèse chimique, en combinant des techniques de caractérisation avancées, soit en interne, soit dans des installations synchrotron. De nombreuses études ont été rapportées sur le processus de cristallisation utilisant la microfluidique à base de gouttelettes. Par exemple, Pham et. al. ont travaillé sur la cristallisation des protéines dans des gouttelettes aqueuses dans l'huile. En utilisant seulement quelques mg de protéines, ils ont pu étudier un grand nombre de conditions de cristallisation et les étudier par SAXS.

Dans le chapitre 3, nous décrirons la synthèse de particules d'or en utilisant un grand excès de triisopylsilane (TIPS). Nous commençons par décrire les premières études cinétiques in situ réalisées dans des capillaires ou dans des flacons, puis nous poursuivons avec les expériences réalisées à l'aide des puces microfluidiques.

Le chapitre est organisé comme suit : les conditions expérimentales de la synthèse, la caractérisation de la taille et de la structure des particules finales sont données en premier, puis les différentes études XAS et SAXS in situ résolues en temps sont présentées. Dans la dernière section, nous comparerons les résultats obtenus avec les puces microfluidiques décrites au chapitre 2 avec ceux obtenus avec des procédures de mélange classiques.

Les mesures XAS et SAXS nous ont permis de définir trois étapes dans la formation des NPs d'Au, les étapes d'induction, de nucléation et de croissance. Selon la spécificité de chaque méthode, les trois étapes ont été définies différemment.

- Avec les mesures XAS, le stade d'induction est la période pendant laquelle nous avons observé uniquement la réduction de Au (III) en Au(I). L'étape de nucléation commence avec l'apparition de Au (0) et se poursuit avec l'augmentation rapide de [Au (0)]. Nous avons considéré que l'étape de nucléation s'arrête lorsque nous avons observé une rupture de la pente avec un taux de réduction beaucoup plus faible. L'étape de nucléation s'est étendue de 10 s à 22 s lorsque la puce est utilisée alors qu'avec le T-mixer/cuvette PMMA elle s'est étendue de 15 à 30 s.

- Dans les expériences SAXS, seule une très légère variation du signal SAXS a été observée pendant l'étape de nucléation. L'étape de nucléation commence par le déplacement du signal SAXS vers les valeurs élevées de q. Pendant la phase de croissance des NP d'Au, l'intensité de la diffusion augmente et le signal est légèrement décalé vers les valeurs à faible q en raison d'une légère augmentation de la taille moyenne des particules.

Dans la figure 1, nous avons reporté sur la même figure la taille mesurée par SAXS et les différents stades identifiés par XAS :

- stade d'induction : Premièrement, des clusters de prénucléation (PNC) non réduits se sont formés. Ensuite, les atomes d'Au (III) dans les PNCs ont été progressivement réduits en Au (I), conduisant à des précurseurs de PNCs Au (III) - Au (I), sans affecter la taille des PNCs.

-L'étape de nucléation : Un rétrécissement rapide de la taille des PNCs a été observé, conduisant à de petits noyaux de métal Au(0). Ce rétrécissement est interprété comme la transition entre les clusters moléculaires et les PNC métalliques.

-Stade de croissance : Une augmentation lente de la taille moyenne des NPs métalliques est observée. Les NP d'Au (0) finales ont été formées par la réduction des PNC d'Au (III) et d'Au (I).

A partir de nos études in-situ sur la formation des nanoparticules d'or, nous avons montré que la théorie classique de nucléation peut être remise en question. Abecassis et al. et Chen et al. ont étudié la réduction chimique du chlorure d'or, en utilisant le borohydrure ou le borane comme agents

réducteurs. Ils ont rapporté que les monomères libres d'Au(0) étaient progressivement associés en petits clusters d'Au(0), conduisant finalement à des noyaux stables d'Au(0) en accord avec la théorie de la nucléation classique. Dans notre cas, la solution de départ n'est pas une solution classique de monomères puisque ce complexe d'or forme ces agrégats qui donnent un signal fort en SAXS et que nous avons appelés clusters de pré-nucléation. Le rétrécissement des amas de pré-nucléation en petites particules de métal Au (0) semble indiquer que la nucléation est une réduction interne au sein des amas de pré-nucléation. Dans les chapitres suivants, nous avons étendu cette étude à différentes conditions expérimentales en faisant varier la concentration de l'agent réducteur et/ou sa nature afin d'avoir plus de données pour comparer nos synthèses avec la théorie classique de la nucléation.

Un des objectifs de ce chapitre était de comparer le montage microfluidique avec les conditions de mélange classiques. Les expériences réalisées avec les puces microfluidiques ont bien reproduit les expériences réalisées dans les capillaires et dans les cuvettes mais la résolution temporelle a été augmentée. Cependant, à des temps très courts (inférieurs à 2,5s), nous avons remarqué un artefact dans la spéciation de l'Au calculée à partir des expériences XAS. Cela peut être dû à un problème de mélange dans le grand canal de la puce. Ce problème devra être analysé en détail à l'avenir.

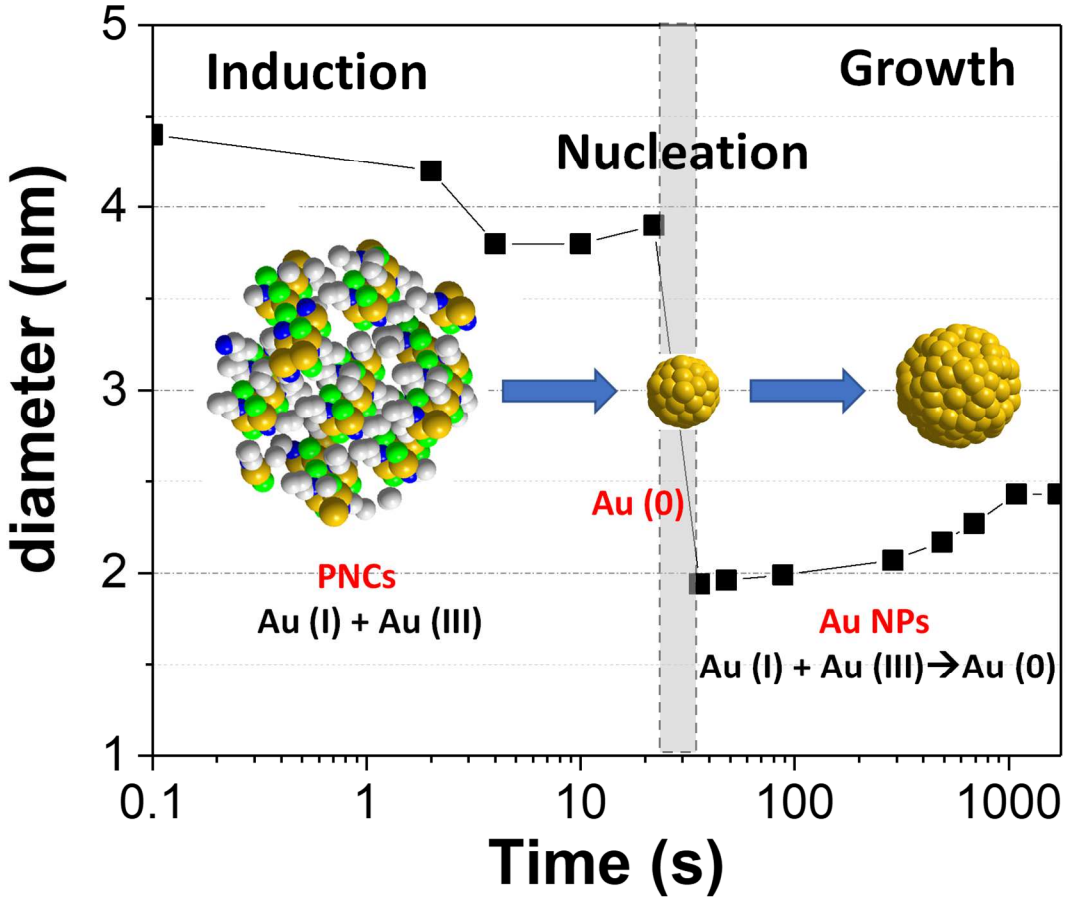

Figure 1. Évolution temporelle de la taille moyenne des particules, déterminée par SAXS, ainsi que l'évolution de la spéciation de l'Au, déterminée par XAS. La zone grisée montre la période de nucléation, déterminée à partir des résultats XAS.

Nous avons décrit dans le chapitre 3 la synthèse d'ultra petites NP d'Au à partir de la réduction d'une solution de $HAuCl_4.3H_2O$ dans l'hexane ([Au] = 20 mM) en présence d'une concentration stœchiométrique de OY (50 mM) et d'un large excès de TIPS (1M). Cette synthèse est assez simple à réaliser d'un point de vue expérimental mais présente un chemin réactionnel complexe avec la présence de clusters de pré-nucléation dans la solution d'Au(III) de départ.

Comme décrit dans le chapitre 1, des études précédentes ont montré que la concentration en OY joue un rôle clé sur le contrôle de la forme des NPs : des nanosphères ultra petites sont obtenues à faible

concentration en OY ([OY] < 100 mM) alors que des nanofils ultra fins sont stabilisés en présence d'un excès de OY. L'objectif du chapitre 4 est d'étudier l'effet de la concentration de l'agent réducteur dans la condition de formation des nanosphères (OY/Au = 2,5), qui est jusqu'à présent inconnue. Par conséquent, des synthèses avec différentes concentrations de TIPS ont été réalisées et caractérisées :

- Premièrement, à l'état final, pour étudier l'impact sur la morphologie, la taille et la distribution de taille des NPs finales, en utilisant TEM et SAXS.

- Deuxièmement, pendant la réaction, en utilisant les techniques in-situ UV-Vis, XAS et SAXS pour comprendre l'influence de la concentration de l'agent réducteur sur la formation des NP.

Nous avons rapporté ici la première étude sur l'impact de la concentration de l'agent réducteur (TIPS) sur la synthèse de nanoparticules d'Au ultra-petites. Grâce à des études XAS et UV-Vis in-situ, nous avons mis en évidence que la concentration en TIPS jouait un rôle important sur le taux de réduction. La période d'induction était inversement proportionnelle à la concentration en TIPS tandis que la pente de la concentration en Au(0) dans ce que nous appelons l'étape de nucléation était proportionnelle à la concentration en [TIPS].

Pour les réactions lentes, la cristallisation de la phase lamellaire OY-Au(I)-Cl a été observée. Cette phase lamellaire est en compétition directe avec la nucléation/croissance des NPs icosaédriques d'Au.

Pour la concentration stœchiométrique de TIPS, correspondant à un taux de réaction très lent, des NPs d'un diamètre moyen de dm= 5.6 nm et 5 nm avec une distribution de taille assez large ont été obtenues. Ces NPs sont assez similaires aux NPs préparées par la réduction directe de la phase lamellaire. Dans les deux cas, les NPs présentent une structure fcc, très différente de la structure icosaédrique observée par la réduction directe du précurseur en présence d'un excès de TIPS, même aussi faible que 62 mM.

Ainsi, pour obtenir des NP d'Au monodisperses ultra-petites avec une structure non fcc, il faut favoriser une vitesse de réaction rapide afin d'éviter ou au moins de réduire la formation de la phase lamellaire OY-Au(I)-Cl. L'effet des différents paramètres sur la taille et la structure est résumé dans la figure 2.

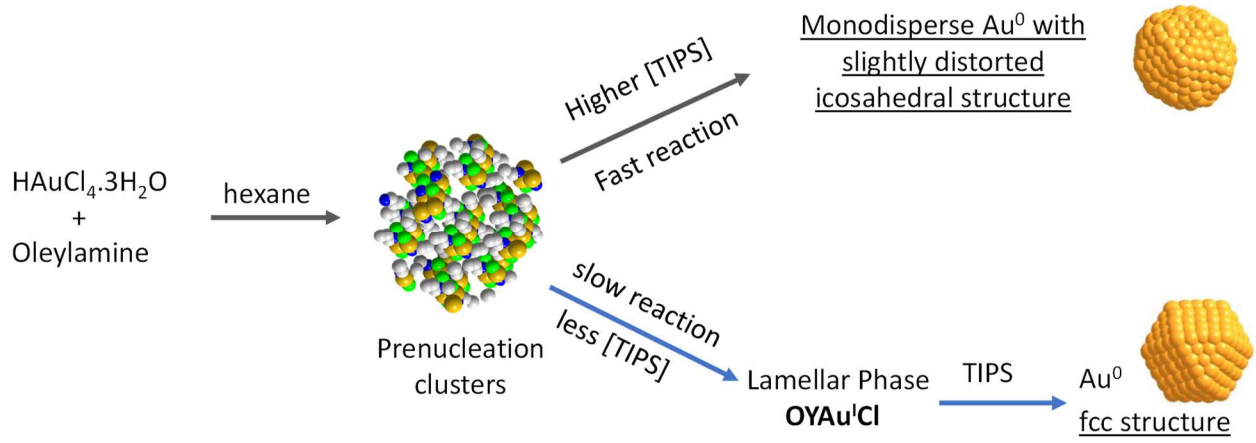

Figure 2. Schémas de la compétition entre la voie directe menant à la cristallisation de NPs d'Au monodisperses ultra petits avec la structure icosaédrique et celle impliquant la phase lamellaire OY-Au(I)-Cl et menant à des particules plus grandes avec la structure fcc.

Dans le chapitre précédent, nous avons étudié l'effet de la concentration en TIPS sur la taille, la distribution de taille et la structure des NP d'Au. En fonction de la concentration en TIPS, nous avons obtenu différents taux de nucléation et de croissance. Lorsque la concentration en TIPS était faible (< 250 mM), une réaction lente s'est produite au cours de laquelle une phase OY-Au(I)-Cl a été observée. La réduction directe de cette phase intermédiaire en utilisant un grand excès de TIPS donne des particules de ~ 5 nm, présentant une structure fcc. Au contraire, lorsque nous avons utilisé une plus

grande concentration de TIPS (≥ 500 mM), la réaction a été rapide et a permis d'obtenir des NP d'Au ultra petites avec une structure icosaédrique.

Afin d'optimiser la préparation de NP d'Au ultra petites et monodisperses, il faut empêcher la formation de OY-Au(I)-Cl. Comme la phase solide intermédiaire Au (I) n'a pas été détectée en présence de [TIPS] = 1M, c'est-à-dire pour une réaction rapide, nous avons étudié l'effet de deux autres paramètres : i) la température de réaction et ii) la force de l'agent réducteur.

Dans le chapitre 5, nous avons établi que la température et la nature du trialkylsilane jouent un rôle clé sur la monodispersité des particules d'or. Nous avons montré que par rapport à la synthèse standard impliquant [TIPS] = 62 mM à 25 °C, la distribution de taille a été améliorée par trois moyens : (i) en augmentant la concentration de TIPS à 1 M comme montré dans le chapitre 3, (ii) en augmentant la température de réaction à 40 °C ou (iii) en utilisant TES comme agent réducteur au lieu de TIPS.

L'effet de la température et du TES était d'augmenter le taux de réduction, évitant la cristallisation d'une phase lamellaire OY-Au(I)-Cl qui est en compétition directe avec la nucléation/croissance des NPs icosaédriques d'Au. Dans la figure 3, le modèle de deux voies compétitives a été complété avec les différents paramètres avec lesquels on peut jouer : la température de réaction, la concentration et la nature de l'agent réducteur.

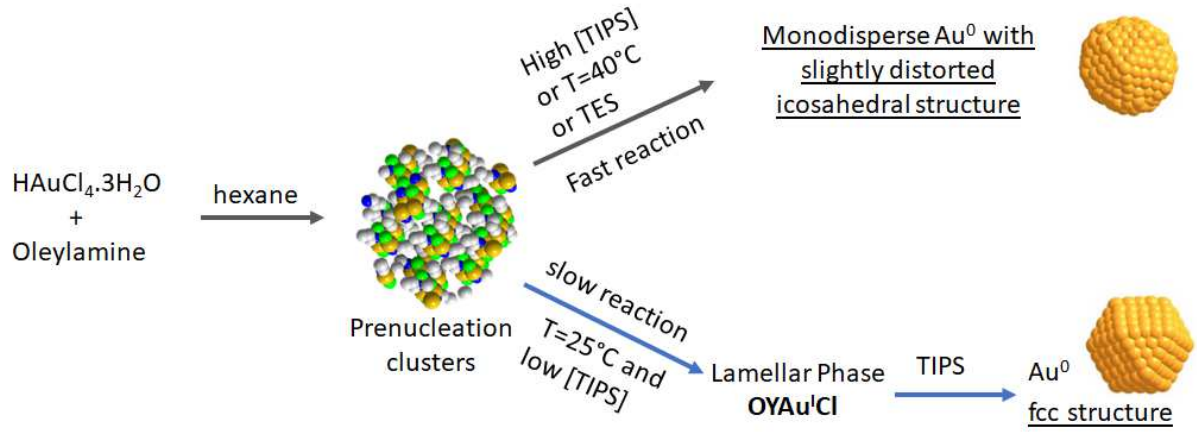

Figure 3. Schémas de la compétition entre la voie directe menant à la cristallisation d'ultra petites NP d'Au avec la structure icosaédrique et celle impliquant la phase lamellaire OY-Au(I)-Cl et menant à des particules plus grandes avec la structure fcc.

Pendant de nombreuses années, la formation de nanoparticules métalliques en phase liquide a été expliquée par la théorie classique de la nucléation. Cependant, certaines études se sont concentrées sur la possibilité de voies de nucléation non classiques en fonction des paramètres de réaction. Une information précise sur les mécanismes de nucléation est cruciale afin de contrôler la taille et la morphologie des particules. La capture expérimentale de l'étape de nucléation homogène est assez difficile en raison de sa nature stochastique. Dans les chapitres précédents, nous avons recueilli de nombreuses données sur la cinétique de nucléation et de croissance des NPs d'Au en utilisant des silanes comme agent réducteur. Le chapitre 6 a pour but de résumer ces résultats et d'essayer de tirer quelques conclusions sur le mécanisme de nucléation/croissance.

Dans ce chapitre, nous avons essayé de démontrer que la formation des NPs d'Au par la réduction de $HAuCl_4$ dissous dans une solution d'oleylamine dans l'hexane et en utilisant des trialkylsilanes comme agent réducteur ne peut pas être expliquée dans le cadre de la théorie classique de la nucléation (CNT).

Notre argument le plus fort pour exclure les NTC est qu'en diminuant/augmentant le taux de réaction, on devrait augmenter/diminuer le rayon critique des noyaux et changer la taille des particules, ce que nous n'observons pas. Au contraire, en faisant varier la nature et la concentration du silane, le taux de réaction peut être accéléré sans que la taille des particules (dm = 1,7 -2 nm) et leur structure (icosaédrique) ne soient fortement modifiées. La stabilité de la taille moyenne est en accord avec les données XAS montrant que nous avons toujours 50 % d'atomes d'Au impliqués dans l'étape de nucléation.

Nous avons une forte présomption que la nucléation a lieu à l'intérieur des PNCs. Nous avons essayé d'estimer le nombre d'atomes d'Au à l'intérieur des PNCs. Un bon ordre de grandeur est 100 mais une évaluation plus précise est nécessaire. Une centaine d'atomes est également ce qui est estimé pour le nombre d'atomes dans les noyaux.

Cependant, certains points restent à éclaircir à l'avenir :

- Si les PNCs sont impliqués dans la nucléation, pourquoi avons-nous observé une augmentation de taille lorsque nous avons utilisé une amine borane comme agent réducteur ? Il pourrait être intéressant d'étendre cette étude à d'autres agents réducteurs, par exemple à l'H_2 gazeux, pour voir si une diffusion lente de l'hydrogène moléculaire pourrait également favoriser la transformation douce des PNCs en particules.

- Qu'est-ce qui détermine que 50 % des atomes d'Au sont impliqués dans la nucléation ?

- Quelle est la chimie de coordination du précurseur Au(III) (paire d'ions ou complexe aminé) et quelle est la structure des PNCs ? Le schéma inverse des micelles s'applique-t-il ?

Au tout début de cette thèse, les discussions entre les chercheurs en nanochimie du LPCNO et les chercheurs en génie chimique du LGC ont souligné l'intérêt d'une collaboration pour élucider des questions intéressantes sur la nucléation et la croissance des nanoparticules en phase liquide. L'équipe du LPCNO apporterait des systèmes modèles à étudier et l'équipe du LGC les outils pour les étudier et les modéliser. Ce travail est le résultat direct de ces discussions.

L'étude de la nucléation est l'un des objectifs les plus difficiles en nanochimie et, plus généralement, dans la cristallisation des particules solides. La nucléation est souvent très rapide et implique une très petite quantité de matière. Pour ces deux raisons, il est très difficile de la saisir expérimentalement. En outre, il y a toujours un chevauchement entre la nucléation et la croissance des particules, même si les particules finales sont hautement monodisperses. En nanochimie, les systèmes peuvent même être complexifiés par les tensioactifs introduits dans le système pour contrôler la croissance. En effet, ces tensioactifs peuvent jouer plusieurs rôles dans l'ensemble du processus chimique, dont celui de ligand pour le précurseur. Dans la plupart des études traitant de la synthèse de nanoparticules métalliques, les considérations sur la nucléation et la croissance des nanoparticules sont déduites de la taille, de la distribution de taille, de la forme et de la structure des particules finales. Cependant, pour avoir une image claire du mécanisme de nucléation et de croissance, il faut étudier avec une bonne précision l'évolution du mélange réactionnel in-situ et en temps réel en combinant différentes techniques.

Dans ce travail, nous nous sommes intéressés à la synthèse de particules d'or en utilisant des trialkylsilanes comme agents réducteurs. Les synthèses ont été réalisées dans un solvant apolaire, l'hexane, contenant de l'oleylamine. L'intérêt de combiner les trialkylsilanes et l'oleylamine avait été démontré précédemment : il s'agit d'une synthèse assez simple dans des conditions très douces qui peut conduire à des particules de forme et de structure très originales. Des nanofils ultrafins et des nanosphères de structure icosaédrique ont été obtenus en fonction de la concentration en oleylamine.

Profitant de l'opportunité de collaborer avec Sébastien Teychené et Isaac Rodriguez-Ruiz du LGC, nous avons décidé de développer les outils microfluidiques appropriés pour étudier le mécanisme de

nucléation et de croissance de ces nanoparticules d'or. Il s'agit d'un travail de recherche plutôt fondamental, mais les objets synthétisés serviront éventuellement en catalyse ou en microélectronique en raison de leurs propriétés améliorées, et les outils microfluidiques seront utilisés dans un avenir proche pour étudier d'autres systèmes impliquant des réactions très rapides.

Les puces microfluidiques qui ont été conçues et fabriquées comportent en effet un mélangeur efficace au début du canal, permettant le mélange rapide des solutions réactives. Ainsi, des temps de réaction très courts peuvent être obtenus. De plus, ces puces peuvent être utilisées soit en flux continu, soit en flux arrêté, donnant accès à une large gamme de temps allant de quelques secondes à plusieurs heures. Nous avons montré dans les chapitres 3 et 4 que ces puces étaient très bien adaptées pour suivre la cristallisation des nanoparticules d'Au, même si des améliorations peuvent encore être apportées pour traiter les temps les plus courts, notamment pour les données XAS. Ceci devrait être une perspective des travaux suivants.

L'autre intérêt de ces puces microfluidiques est qu'elles sont compatibles avec le rayonnement synchrotron. Grâce à la haute brillance des raies de rayons X et à la haute qualité des détecteurs, les synchrotrons sont extrêmement utiles pour ce type d'études en raison des temps d'acquisition très courts et de la faible quantité de matière nécessaire pour obtenir un bon signal. Dans ce travail, nous avons effectué des mesures in-situ et résolues en temps de la diffusion des rayons X aux petits angles et de l'absorption des rayons X dans des installations synchrotron. Ces études ont été très complémentaires des caractérisations qui ont été faites au laboratoire telles que les études cinétiques UV-visible in situ, les caractérisations XRD et SAXS in situ pour suivre la structure et la taille des particules finales, respectivement.

Les synthèses de nanoparticules d'Au utilisant la réduction par trialkylsilane d'un précurseur d'Au(III) en solution d'oleylamine dans l'hexane présentent plusieurs intérêts :

- Lorsque la nucléation et la croissance sont bien contrôlées, la distribution de taille est étroite, avec une taille moyenne d'environ 2 nm, et les nanoparticules cristallisent avec une structure icosaédrique ;

- Les particules croissent à partir d'une solution contenant des clusters de pré-nucléation d'Au(III) et non à partir d'une solution homogène. Ceci nous laisse penser que la nucléation pourrait suivre un mécanisme ne suivant pas la CNT.

Les principaux résultats des études cinétiques sont les suivants :

- La XAS nous a aidé à définir les meilleures conditions pour obtenir des NP monodisperses avec la structure icosaédrique. La réduction des complexes Au(III) en nanoparticules Au(0) implique deux étapes, la réduction de Au(III) en Au(I) et la réduction de Au(I) en Au(0). Grâce à la spéciation de l'Au résolue en temps, nous avons conclu que la clé est que l'étape de réduction de Au(I)→ Au(0) est beaucoup plus rapide que l'étape de réduction de Au(III)→ Au(I). La première réduction Au(III) → Au(I) doit être l'étape limitante de la réaction. Dans ce cas, il n'y a en effet pas d'accumulation de Au(I) dans le milieu, la formation de la phase lamellaire OY-Au(I)-Cl est donc empêchée. La compétition entre la réduction des complexes d'Au impliqués dans les amas de pré-nucléation et dans la phase lamellaire ne s'applique pas, permettant la formation de nanoparticules icosaédriques monodisperses. Ce résultat nous a conduit à étendre les conditions de synthèse en améliorant le contrôle de la synthèse. Nous avons montré que de petits changements dans les conditions expérimentales favorisaient la formation de NP monodisperses : une augmentation de la température de réaction de seulement 15 °C (de 25°C à 40°C), ou un encombrement stérique moindre des chaînes alkyles du silane (passage du triisopropylsilane au triéthylsilane).

- Les études SAXS ont mis en évidence la compétition entre la réduction directe des PNCs ou la cristallisation d'une phase lamellaire intermédiaire OY-Au(I)-Cl dans le cas d'une réduction lente (chapitres 3 et 4). Dans le cas de la réduction directe des PNCs, les premiers résultats montrant le rétrécissement de la taille étaient très récents. Cependant, en raison de la présence de PNCs dans la

solution de départ, il est difficile d'ajuster les données SAXS avec un mélange de PNCs et de NPs d'Au car nous ne savons pas si la taille du PNC est constante. Par conséquent, il est difficile de suivre précisément la variation de taille des nanoparticules d'Au dans la toute première étape de la nucléation. La comparaison de la XAS et de la SAXS résolues en temps nous permet de bien décrire les trois étapes observées avec les deux techniques, c'est-à-dire l'induction, la nucléation et la croissance.

- Enfin, toutes les études XAS et SAXS ont été résumées dans le chapitre 6 pour remettre en question la théorie classique de la nucléation dans le cas de la formation des NPs icosaédriques. Une différence principale avec les NTC est la nature de la solution précurseur qui n'est pas homogène et contient des agrégats de complexes appelés PNCs. De plus, un argument fort était la non-dépendance de la taille des particules lorsque le taux de réaction (à la fois le taux de nucléation et le taux de croissance) était augmenté d'un facteur 5.

En raison de la difficulté d'avoir une image complète et exacte de la nucléation et de la croissance, il reste bien sûr de nombreuses questions intéressantes à traiter, en particulier concernant la structure des particules :

- La structure icosaédrique est-elle seulement due à la très petite taille des particules ?

- Est-elle due à l'enrobage de chlorure d'oleylammonium ?

- ou le confinement de la nucléation à l'intérieur des PNCs joue-t-il un rôle dans la formation de la structure icosaédrique ?

- Est-ce dû à un rôle spécifique du silane ?

Les résultats préliminaires obtenus avec le BTB comme agent réducteur semblent montrer que malgré la présence des PNCs, les NP de 2.5 nm finalement obtenues présentent une structure qui semble plus fcc.

En outre, il serait intéressant de suivre les développements ultérieurs de ce travail :

- Pour les études cinétiques dans les puces microfluidiques et en utilisant l'absorption UV-visible, nous avons été limités au signal de Au(0) en raison des propriétés d'absorption de l'ostémère dans l'UV. Dans le futur, l'utilisation d'un autre polymère tel que l'époxy pour fabriquer la puce microfluidique pourrait permettre de suivre les concentrations relatives d'Au(III) et d'Au(I), à condition qu'il soit transparent dans la région UV.

- Récemment, nous avons découvert que les NPs icosaédriques monodisperses pouvaient être utilisées comme matériaux de départ pour obtenir des décaèdres contrôlés après un processus de vieillissement (voir figure 4 ci-dessous). Dans la littérature, les décaèdres ont été utilisés comme graines pour préparer des nanorods grâce à leur axe particulier à 5 plis. L'objectif de cette synthèse pourrait être la préparation de nanorods magnétiques en utilisant des particules décaédriques d'or comme graines pour une nucléation et une croissance hétérogènes contrôlées.

- Enfin, cette synthèse assez simple utilisant le silane pourrait être étendue à d'autres métaux. Des icosaèdres d'argent ont récemment été préparés de manière très reproductible en utilisant la même méthode. Cette réaction pourrait être plus simple à étudier puisque seuls deux états d'oxydation de l'argent sont impliqués.

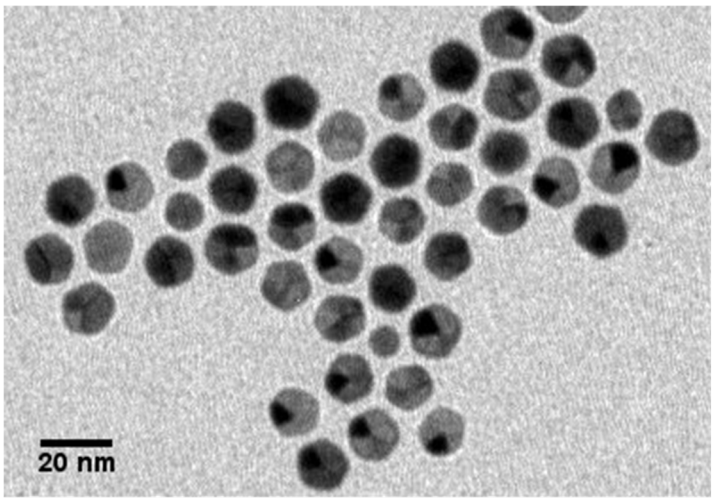

Figure 4 NP décaédrique obtenue après vieillissement de NP icosaédriques monodisperses